THE UNIVERSITY *of* EDINBURGH

Reciprocity-based imaging using multiply scattered waves

Matteo Ravasi

Thesis presented for the degree

Doctor of Philosophy

THE UNIVERSITY
of EDINBURGH

School of GeoSciences

2015

Ph.D. Thesis
01/02/2012– 29/05/2015

Submission 29/05/2015
Viva Voce 06/07/2015
Final Version 20/07/2015

University of Edinburgh
School of GeoSciences

Matteo Ravasi
M.Ravasi@sms.ed.ac.uk

B.Sc. Telecommunication Engineering 2009
Politecnico di Milano

M.Sc. Telecommunication Engineering 2011
Politecnico di Milano

Supervisors

Prof. Andrew Curtis
Professor of Mathematical Geoscience

Dr. Giovanni Angelo Meles

Examiners

Prof. Anton Ziolkowski
Professor of Petroleum Geoscience

Prof. Kees Wapenaar
Professor of Applied Geophysics

A mamma e papà

Abstract

In exploration seismology, seismic waves are emitted into the structurally complex Earth. Its response, consisting of a mixture of arrivals including primary reflections, conversions, multiples, and transmissions, is used to infer the internal structure and properties. Waves that interact multiple times with the inhomogeneities in the medium probe areas of the subsurface that are sometimes inaccessible to singly scattered waves. However, these contributions are notoriously difficult to use for imaging because multiple scattering turns out to be a highly nonlinear process. Conventionally, imaging algorithms assume singly scattered energy dominates data. Hence these require that energy that scatters more than once is attenuated.

The principal focus of this thesis is to incorporate the effect of complex nonlinear scattering in the construction of subsurface elastic images. Reciprocity theory is used to establish an exact relation between the full recorded data and the local (zero-offset, zero-time) scattering response in the subsurface which constitutes our image. Fully nonlinear, elastic imaging conditions are shown to lead to better illumination, higher resolution and improved amplitudes in pure-mode imaging. Strikingly it is also observed that when multiple scattering is correctly handled, no converted-wave energy is mapped to any image point. I explain this result by noting that conversions require finite time and space to manifest.

The construction of wavefield propagators (Green's functions) that are used to extrapolate recorded data from the surface to points in the Earth's interior is a crucial component of any imaging technique. Classical approaches are based on strong assumptions about the propagation direction of recorded data, and their polarization; preliminary steps of wavefield decomposition (directional and modal) are required to extract upward propagating waves at the recording surface and separate different wave modes. These algorithms also generally fail to explain the trajectories of multiply scattered and converted waves, representing a major problem when constructing nonlinear images as we do not know where such energy interacted with the scatterers to be imaged. A secondary aim of this thesis is to improve on the practice of wavefield extrapolation or redatuming by taking advantage of the different nature of multi-component data compared with single-mode acoustic data. Two-way representation theorems are used to define novel formulations in elastic media which allow both up- and downward propagating fields to be back-propagated correctly without ambiguity in the direction, and such that no cross-talk between wave modes is generated. As an application of directional extrapolation, the acoustic counterpart of the new approach is tested on an ocean-bottom cable field dataset acquired over the Volve field, North Sea. Interestingly, the process of redatuming sources to locations beneath a complex overburden by means

of multi-dimensional deconvolution also requires preliminary wavefield separation to be successful: I propose to use the two-way convolution-type representation as a way to combine full pressure and particle velocity recordings. Accurate redatumed wavefields can then be obtained directly from multi-component data without separation.

Another major challenge in seismic imaging is to construct detailed velocity models through which recorded data will be extrapolated. Nowadays the information contained in the extension of subsurface images along either the time or space axis is commonly exploited by velocity model building techniques acting in the image domain. Recent research has shown that when both extensions are taken into account, it is possible to estimate the data that would have been recorded if a small, local seismic survey was conducted around any image point in the subsurface. I elaborate on the use of non-linear elastic imaging conditions to construct such so-called extended image gathers: missing events, incorrect amplitudes, and spurious energy generated from the use of only primary arrivals are shown to be mitigated when multiple scattering is included in the migration process. Finally, having access to virtual recordings in the subsurface is also very useful for target-oriented imaging applications. In the context of one-way representation, I apply the novel methodology of Marchenko redatuming to the Volve field dataset as a way to unravel propagation effects in the overburden structure. Constructed wavefields are then used to synthesize local, subsurface reflection responses that are only sensitive to local heterogeneities, and detailed images of target areas of the subsurface are ultimately produced.

Overall the findings of this thesis demonstrate that, while incorporating multiply scattered waves as well as multi-component data in imaging may be not a trivial task, such information is vital for achieving high-resolution and true-amplitude seismic imaging.

Lay summary

As a man standing near a cliff can simply use the echo of his voice to locate the position of the cliff, sound waves emitted and recorded on the Earth's surface are commonly used to detect oil and gas reservoirs through a process called imaging or migration. If many cliffs are present along a coastline, waves that bounce multiple times on those structures tend to contain additional information about the shape of the coastline. At the same time, they are harder to interpret. A similar phenomenon occurs every time waves travel within the Earth and encounter various heterogeneities.

The principal focus of this thesis is to incorporate the effect of such complex waves in imaging techniques. The theory of reciprocity is used to obtain a mathematical relation between the waves recorded along the Earth's surface and the propagation phenomena occurring in the subsurface. Such relation can aid the construction of images with better illumination, higher resolution and improved amplitudes, ultimately helping us to improve our understanding of the Earth structure.

Since the Earth is a solid body, two types of waves arise during propagation: waves that travel faster and reach the recording devices first, called primary waves, and slower waves that arrive later, called secondary waves. Another fundamental step of any imaging algorithm is the projection of the recorded data down into the subsurface where waves have travelled. Classical approaches assume that only one type of waves travel in the Earth, and fail to simultaneously handle primary and secondary waves. In this thesis I propose a novel method where, by exploiting the information contained in measurements from additional instruments, both types of waves can be accounted for and used to provide complementary information of the Earth properties.

Finally, recent research has shown that imaging algorithms can be used to construct new data that would have been recorded if a small, local seismic survey was conducted around any point of interest in the subsurface. Using the techniques developed in this thesis, I improve upon the construction of such virtual data. Methods that estimate velocity models of the subsurface and characterize oil and gas reservoirs using image amplitudes may benefit from these advancements.

Overall the findings of this thesis demonstrate that, while incorporating in imaging the waves that have interacted multiple times within the subsurface as well as additional data may be not a trivial task, such information is vital for improving our imaging results.

8

Declaration

I declare that this thesis has been composed solely by myself and that it has not been submitted, either in whole or in part, in any previous application for a degree. Except where otherwise acknowledged, the work presented is entirely my own.

Parts of this work have been submitted and/or published in Ravasi and Curtis (2013a,b); Ravasi et al. (2014), and Ravasi et al. (2015b,c,d,e).

Matteo Ravasi
20/07/2015

Acknowledgment

This thesis goes far beyond documenting the outcome of almost four years of intense scientific work, it is rather the story of the journey that has transformed a young, curious engineer into the scientist I am today. Along this journey I have met many outstanding individuals who have dedicated their time, passion, and experience to my education, and I can easily admit that I owe most of where I am today to them.

First, I would like to thank my supervisor Andrew Curtis for giving me this amazing opportunity despite my very limited initial knowledge of geophysics, and for guiding me through the intricate maze of applied seismology. His contagious enthusiasm and continuous advice have been a fantastic source of inspiration that will be never forgotten. I am also deeply grateful to him for giving me so much freedom of research and for helping me in establishing collaborations with industry sponsors and other academic research groups.

I am also immensely fortunate to have met Ivan Vasconcelos. With his genuine dedication towards the education and growth of young scientists, he has become for me another exceptional supervisor and mentor. I feel that every hour spent in his office at Schlumberger Cambridge Research has represented an immense source of inspiration for my research. Our scientific relationship has turned into a friendship that I am sure will last for a long time.

I would like to express my gratitude to Alexander Kritski. His involvement in my project and his commitment in finding a suitable dataset which I could apply my theories and techniques to has been a key factors to the success of my Ph.D. During my visit to Statoil, he went far beyond his role of supervisor by being a fantastic host and making me feel at home, and by providing me with many invaluable scientific advices.

Since none of this would have happened without my initial internship at WesternGeco, I am very grateful to Dirk-Jan van Manen and Massimiliano Vassallo for introducing me to the fascinating world of scientific research and for pointing me into the direction of this Ph.D. project. It has also been an immense pleasure to work alongside Nizare El Yadari and Yousif Kamil during my second placement at WesternGeco. My thanks are extended to Ed Kragh and James Rickett in Schlumberger, Odd Arve Solheim, Marianne Houbiers, and Severine Lescoffit in Statoil for welcoming me to their teams and for their guidance and support. I finally thank the sponsors of the Edinburgh Interferometry Project (EIP) for insightful comments on my work.

Much of the results of this thesis have been published in peer reviewed journals. I would like to thank Deyan Dragnanov, Johan Robertsson, Roald Van Borsalen, Dirk-Jan van Manen, Joost van der Neut, Kees Wapanaar and several anonymous reviewers

for insightful comments that helped improve the work in this thesis. A special thank goes to my examiners Anton Ziolkowski and Kees Wapenaar, whose great feedbacks helped me to further polish up this manuscript. I am also grateful to Dieter Werthmuller, a former Ph.D. student in the department of GeoSciences, for sharing his LaTeXsource file which I found very useful in the writing of this manuscript.

When it comes to my research group, I could have not asked for a better guidance than that of Giovanni Meles. He was the first to receive me in Edinburgh. He made me feel at home as soon as I landed in Edingurgh, and he introduced me to the obscure world of seismic interferometry. His door was always open for insightful scientific discussions that sometimes rescued me from moments of desperation, amusing chats about our rival football teams and the political situation of our home country. I am grateful to several fellow students Erica, Katrin, Lizzie, Matt, Claire, Zara, Sjoerd, Flora, Sven, Cederic, Jurg, Shihao, and Momoh for being great companions during all these years. A special mention goes to Carlos da Costa, it has been a pleasure to work with him and share moments of happiness and desolation while writing (many) lines of code together. I wish him all the best for the following of his career. Lastly, I thank Liu for making my supervision of his undergraduate project a rather easy and amusing task, and for his helpful inputs.

A special thank you goes to Claire. While filling my days with happiness, she has given me extra confidence in the most challenging months of my Ph.D. Now I wish her good luck with her Ph.D. and I look forward to becoming Doctor^2 (and I promise that I will stay away from microseismics!).

Finally, the biggest of my thanks goes to my Mum, Dad, and Giulia. Their encouragements and never ending support towards my dreams, their 'keep studying and do not worry about money!' has shaped me into the person and the scientist I am today. I know how much they have enjoyed Scotland and Edinburgh, with every excuse being a good one to visit me and sample some of the best food and whiskeys in town... but I am sure Norway will become soon their new second home too — vi aspetto!

Contents

List of Figures

Symbols and Abbreviations

Symbols

Variables that are repeatedly used throughout the thesis are specified for convenience in the following list. SI and SI-derived units are used in accordance with the guidelines for correct use of the International System of Units (SI) that can be found at the Bureau International des Poids et Mesures, http://www.bipm.org/en/si.

Symbol	Description	Units
ω	**Angular frequency**	rad/s
c_{ijkl}	**Compliance**	m/N
ρ	**Density**	kg/m^3
z	**Depth**	m
u	**Displacement field**	m
h	**External deformation rate (quadrupole) source**	1/s
f	**External volume force (dipole) source**	N/m^3
q	**External volume injection rate (monopole) source**	1/s
F	**Focusing function**	-
G	**Green's function**	-
I	**Image**	–
	superscripts nl and l for nonlinear and linear image.	
$\mathbf{x}_I$	**Image point**	m
j	**Imaginary unit**, $j = \sqrt{-1}$.	–
$\mathbf{n}$	**Normal vector**	–
	subscripts S and R for source and receiver boundary.	
ξ	**Obliquity factor**	kg / (m^2 s)
δ	**Offset**	m
χ	**Perturbation operator**	rad/(s Pa)
Φ	**Potential field**	Pa
p	**Pressure field**	Pa

Symbol	Description	Units
$\mathbf{x}_r$	**Pseudoreceiver position**	m
$\mathbf{x}_s$	**Pseudosource position**	m
$\mathbf{x}_R$	**Receiver position**	m
R	**Reflection operator or Reflectivity**	-
$\mathbf{x}_S$	**Source position**	m
s_{ijkl}	**Stiffness**	N/m
τ	**Stress field**	Pa
∂D	**Surface integration boundary**	-
	subscripts S and R for source and receiver boundary.	
t	**Time**	s
V	**Velocity**	m/s
	subscripts P and S for P- and S-wave velocities.	
v	**Velocity field**	m/s
$\mathbf{x}_{VS}$	**Virtual source position**	m
k	**Wavenumber**	rad/m

Table 1: Variables names and definitions.

Formulae

1D Fourier transform pair

$$F(\omega) = \int_{-\infty}^{\infty} f(t) e^{-j\omega t} \, \mathrm{d}t$$

$$f(t) = \int_{-\infty}^{\infty} F(\omega) e^{j\omega t} \, \mathrm{d}\omega$$

2D Fourier transform pair

$$F(k_x, \omega) = \int_{-\infty}^{\infty} f(x, t) e^{-j(\omega t - k_x x)} \, \mathrm{d}t\mathrm{d}x$$

$$f(x, t) = \int_{-\infty}^{\infty} F(k_x, \omega) e^{j(\omega t - k_x x)} \, \mathrm{d}\omega\mathrm{d}k_x$$

Convolution

$$f(t) * h(t) = \int_{-\infty}^{\infty} f(t') h(t - t') \, \mathrm{d}t' \Leftrightarrow F(\omega) H(\omega)$$

Correlation

$$f(t)\bar{*}h(t) = f(t) * h(-t) = \int_{-\infty}^{\infty} f(t+t')h(t')\,\mathrm{d}t' \Leftrightarrow F(\omega)H^*(\omega)$$

Parseval's theorem

$$E_f = \int_{-\infty}^{\infty} |f(t)|^2\,\mathrm{d}t = \int_{-\infty}^{\infty} |F(\omega)|^2\,\mathrm{d}\omega$$

ℓp norm

$$\| \mathbf{x} \|^p = \left(\sum_{i=1}^{N} |x_i|^p \right)^{1/p}$$

Einstein's summation

$$f_i h_i \Leftrightarrow \sum_i f_i h_i = f_x h_x + f_y h_y + f_z h_z$$

Gauss's theorem

$$\int_V \partial_i f_i(x)\,\mathrm{d}^3x = \int_{\partial V} f_i(x) n_i\,\mathrm{d}^2x$$

Abbreviations

AVO	Amplitude-Versus-Offset
CIG	Common-Image Gather
EI	Extended Image
FWI	Full-Waveform Inversion
IC	Imaging Condition
ISS	Inverse Scattering Series
MDD	Multidimensional Deconvolution
OBC	Ocean-Bottom Cable
OBN	Ocean-Bottom Node
OBS	Ocean-Bottom Seismometer
PRM	Permanent Reservoir Monitoring
PSF	Point Spread Function
RTM	Reverse-Time Migration
SRI	Source-Receiver Interferometry
SRME	Surface Related Multiple Elimination
VA	Vector-Acoustic

Thesis

1

Introduction

Today's noise is tomorrow's signal.

Geophysicists' perception of what constitutes signal and noise has remained nearly static for many decades, but today it is radically changing. It was the commonly held belief that much of the information recorded in a seismic experiment (e.g., surface waves and multiples) was noise, and therefore the interpreter's bane which should be accurately separated and removed from the signal (the primary reflections). However, over the past decade, this view has been challenged. Understanding the additional role that noise may have in the study of the interior of the Earth requires:

i) the recognition that every portion of seismic recordings represent waves that sense the subsurface in a particular fashion. Nothing should be discarded. Instead most of the data could be used to aid the imaging and characterization of the Earth's interior.

ii) the identification of novel processing, imaging, and inversion techniques that can accommodate current noise and turn it into useful signal, unravelling features of the subsurface that could not have been identified otherwise.

Pioneering steps have been made in a variety of different directions, for example showing that surface waves tell us more about the near surface properties (Socco et al., 2010; Strobbia et al., 2011; Haney and Douma, 2012; Boiero et al., 2013), multiple reflections can increase the illumination and imaging resolution of the deep subsurface (Muijs et al., 2007; Wong et al., 2010; Whitmore et al., 2010; Davydenko and Verschuur, 2012; Lu et al., 2014), and even that the Earth's ambient vibrations from ocean swells and storms can be turned into useful signal by cross-correlation techniques (Campillo and Paul, 2003; Shapiro et al., 2005; Brenguier et al., 2007; Bussat and Kugler, 2011; de Ridder and Dellinger, 2011; Mordret et al., 2013). This thesis focuses on improving the theory and practice of seismic imaging with respect to free-surface effects, internal multiples,

and rapidly decaying (or evanescent) waves. We begin by introducing the concepts that will be explored herein.

1.1 Seismic imaging and the single-scattering assumption

Seismic imaging represents one of the most challenging tasks of seismology and exploration geophysics (Bleistein et al., 2001; Biondi, 2006). The goal is to determine the characteristics of the interior of a body (the Earth) where it is impossible or impractical to make observations directly, based only on measurements made remotely on some boundary surface (usually the Earth's surface). Despite its theoretical complexity, the underlying principle of seismic imaging is reasonably simple. Waves propagate from the seismic source into the Earth's subsurface; they scatter or reflect from heterogeneities which act as secondary sources in the medium and radiate energy towards the receivers. By projecting the recorded scattered energy backwards into the subsurface and understanding where it focusses, the focus point reveals the positions of the secondary sources and a map of the scattering structure is constructed.

This thesis will consider a particular class of imaging techniques, the so-called wave-equation migration methods — e.g., Reverse-Time Migration (RTM)— which can generally be described as composed of three main steps (Figure 1.1a). First, an incident wavefield (the source-side wavefield) is modelled numerically by firing a source at any physical source location within an estimate of the Earth velocity model (herein referred to as *background* or *reference model*). Second, *redatuming* of the receiver array (also known as *extrapolation* of the recorded wavefield) is performed via synthetic backward propagation in time through the reference velocity model of the seismic data recorded at the surface, producing the receiver-side wavefield. This is followed by the application of an *imaging condition* (IC) (Claerbout, 1971) — an equation that detects at which point in the medium source- and receiver-side wavefields coincide. Since they should coincide at the locations at which the source field scattered into the receiver field, this constructs an estimate of the subsurface structure (the so-called *seismic image*).

Seismic imaging as described so far is based on a single-scattering assumption: waves interact only once with heterogeneities of the medium as they propagate from the source to the receiver. These arrivals are referred to as the *linear* part of the seismic wavefield because of their first order dependence on the medium perturbation to the reference model. Wave propagation is however a much more complex process than the one depicted in Figure 1.1a, as many heterogeneities can be found in the subsurface and seismic waves interact multiple times with those heterogeneities before reaching the Earth's surface. Additionally to primary arrivals (Figure 1.1a), the recorded data are

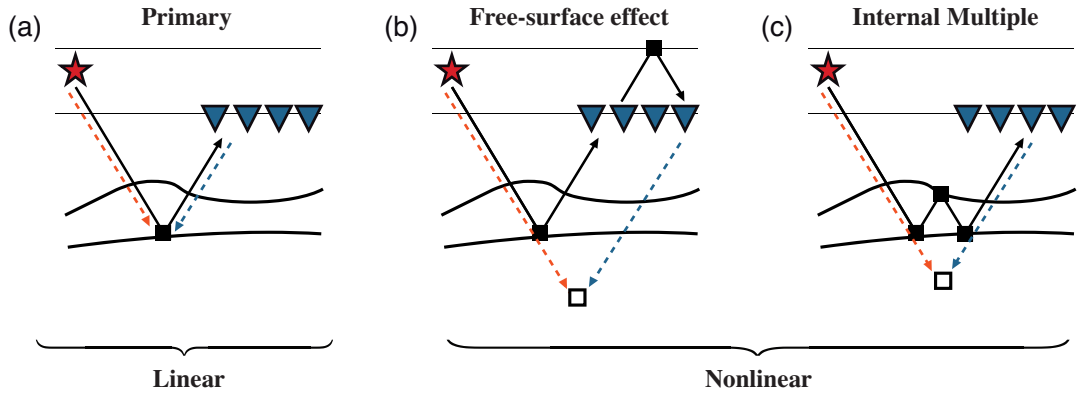

Figure 1.1: Schematic representation of wave-equation migration of (a) a primary arrival, (b) a free-surface effect, and (c) an internal reverberation. In each plot, a black ray represents a wavefield due to a source (red star) and recorded at a receiver (blue triangle), while black squares refer to the location where scattering events have occurred. The incident part of the arrival is directly modelled from the source (dashed red ray), while the scattered part of the arrival is projected into the subsurface from the receiver (dashed blue ray). The recorded energy is therefore mapped at the location in the subsurface where these wavefields coincide in time and space. This is equivalent to the true scattering point for the primary arrival in (a), while it is incorrect for the nonlinear events in (b) and (c) as indicated by white squares.

composed of events that experience one or multiple bounces on the free-surface (Figure 1.1b) as well as internal reverberations within the subsurface (Figure 1.1c). Given their higher order relation with the subsurface heterogeneities, we refer to these arrivals as the *nonlinear* part of the seismic wavefield.

Tracing the propagation path of multiply scattered waves is much more challenging than it is for primary arrivals. This in fact may require embedding discontinuities in the synthetic medium used to compute the source- and receiver-side wavefields, such that recorded energy can be focused at each scattering point involved in the subsurface propagation. Conventional migration techniques tend to ignore the nonlinear contribution, by assuming it to be small compared to the linear one. When this approximation is made, migration is performed under the so-called single-scattering, or first-order Born approximation (Stolt and Weglein, 1985; Oristaglio, 1989), and the seismic data are assumed to be a linear function of model contrasts. Since primary events like those depicted in Figure 1.1a are the only portion of the seismic data that is linear with respect to the model contrasts, conventional migration can handle only these waves correctly. Nonlinear events are instead misinterpreted by such algorithms and generate spurious structure in the seismic image, as indicated by white squares in Figure 1.1b and c (see also Malcolm et al., 2007; Liu et al., 2011). In an attempt to mitigate these artefacts, the seismic community has historically been primarily focused on the implementation of procedures that aim to remove the effect of multiply scattered waves from the recorded

data.

Since the Earth is a solid medium, conversions from P to S or from S to P wave energy occur at any scattering or reflection point as illustrated in Figure 1.2. Another degree of complexity is therefore created by the presence of both compressional and shear wave modes in recorded seismic data. When the imaging procedure discussed above is applied using the elastic wave equation, *both* P- and S-waves are generated erroneously in the extrapolation of each recorded P or S wave arrival (Sun and McMechan, 1986; Chang and McMechan, 1994; Yan and Sava, 2008). These errors further affect the quality of the seismic image.

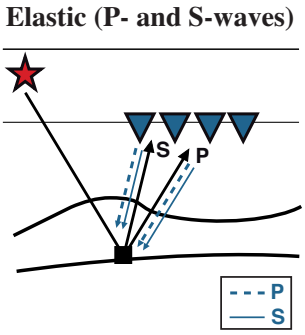

Figure 1.2: Illustration of seismic wavefield extrapolation in the elastic Earth. In the physical propagation within the Earth, two events are generated for each interaction of the seismic wavefield with the medium heterogeneities: a compressional (P-wave) arrival and a shear (S-wave) arrival. For each recorded arrival, both a P-wave (dashed blue ray) and an S-wave (solid blue ray) are synthetically backward propagated into the subsurface. Key as in Figure 1.1.

1.2 Handling multiply scattered waves in imaging

The industry trend towards more complex exploration areas and more difficult plays has recently led to the rise of the following question. Do primaries contain enough information for successful imaging of complex geologies, or would multiples add information and improve our imaging products? By reaching areas of the subsurface that are sometimes inaccessible to singly scattered waves, multiply scattered arrivals contain complementary information about medium heterogeneities to that carried by primaries. Multiply scattered waves are therefore becoming more recognised as a consistent part of our data. Standard imaging algorithms have thus recently been adapted for ad-hoc treatment of one or other type of nonlinear event (e.g., free-surface or internal multiples) and novel imaging paradigms have been formulated with the aim of handling different nonlinearities of the seismic wavefield at the same time.

Approaches to handle free-surface effects like those in Figure 1.1b as part of the imaging process have been proposed by Vasconcelos (2011, 2013); Blanch (2012) and Amundsen and Robertsson (2014). The idea is to jointly use pressure and particle velocity data in the extrapolation of the seismic wavefield, because these recordings carry different information about the directionality of the wavefield arriving at the acquisition array.

More specifically, subsurface reflections (the *up-going field*) and waves that reach the acquisition surface after experiencing their last bounce with the free-surface (the *down-going field*) have the same polarity in the geophone recording, but they show inverted polarity in the hydrophone recording. As a result, each recorded arrival is backward propagated only towards its direction of arrival, rather then both above and below the receiver array as occurs in standard extrapolation techniques. By avoiding the injection of down-going wavefields directly into the subsurface it is thus possible to reduce the number of artefacts in the seismic image. In Chapter 3, I further extend such an approach to elastic media where compressional (P) and shear (S) waves are also handled without ambiguity. This enables the propagation of the correct mode towards the correct direction and suppresses all the other unwanted events that generally affect the extrapolated wavefields. The first application of the acoustic version of this technique to a field ocean-bottom multi-component dataset is the subject of Chapter 7.

Two different routes have been taken for imaging using internal multiples. On the one hand, model-based approaches rely on a preliminary estimate of the heterogeneities in the subsurface (e.g., sharp reflecting interfaces) (Malcolm et al., 2011; Davydenko and Verschuur, 2012; Fleury, 2013). This prior model is used to predict seismic wavefields in the subsurface, including multiple interactions with estimated heterogeneities. On the other hand, the data-based approach (one of which is generally referred to as *autofocusing* or *Marchenko redatuming*) is based on the inverse scattering theory in mathematical physics. It iteratively solves a set of coupled Marchenko equations (Rose, 2002; Broggini et al., 2012, 2014; Wapenaar et al., 2013, 2014a), hence providing a mapping between the first arriving wave at a point in the background model of the subsurface and the multiply scattered wavefields in the true subsurface. As wavefields can be estimated at any image point independently, this strategy is particularly interesting for imaging of target areas of the subsurface as pursued in Chapter 8.

An overall improvement in the resolution of the subsurface image represents another advantage of imaging the Earth's structure nonlinearly. *Resolution* is the principal notion in imaging which describes the smallest details in an object that the imaging methods can differentiate from a neighbouring object (Simonetti, 2006). Under the Born approximation, the classical diffraction or Rayleigh resolution limit precludes the possibility of resolving details of a wave-scattering object that are less than $\lambda/2$ apart (Elmore and Heald, 1969; Born and Wolf, 1999) where λ is the wavelength of the seismic field. As recent research in microwave and ultrasound sensing has demonstrated (Simonetti, 2006; Simonetti et al., 2007; Lerosey et al., 2007; Fink, 2008), imaging with multiple scattering is the key to extract subwavelength information from measurements obtained away from the scattering object (i.e., in the far-field). In fact, when a wave is incident on an object, the scattered field in the proximity of the object (i.e., in the near-field)

contains both propagating waves that radiate away from the object and evanescent fields whose amplitude decays rapidly away from the object. While the content of such non-propagating waves originating from single scattering is lost unless a sensor is placed in the proximity of the perturbation, multiply scattered waves encode subwavelength information in the far-field. The contribution of evanescent waves from the first scattering event interacts with other scattering objects and is converted back into radiating energy which does reach the recording array in the far-field (Simonetti et al., 2008). The ability of an imaging algorithm to use multiply scattered waves in order to resolve structure at a fraction of the classical resolution limits is known in the literature as *super-resolution*. Fleury and Vasconcelos (2012) and Vasconcelos (2013) adapted this concept to seismic imaging by showing that high-resolution images can be achieved by adding a second contribution to the imaging condition that uses the nonlinear part of the seismic data in combination with correct full wavefield extrapolators. In Chapter 2, I build on the acoustic theory of Fleury and Vasconcelos (2012) and propose an extension to elastic media for imaging of multiply scattered compressional and shear waves (and their mutual conversions).

1.3 Reciprocity-based imaging

As mentioned earlier, the aim of migration techniques is to construct an image of the contrasts in the physical properties of the Earth. The classic approach to wave-equation migration is based on the concept of adjoint-state methods (Plessix, 2006). The image is obtained as a result of a single iteration of the gradient-based optimization process used in inversion-type imaging (Tarantola, 1984; Tromp et al., 2005). Given that a linearisation of the functional is applied at the start of the optimization process around the reference (initial) velocity model, migration has sometimes been considered a linear problem in which nonlinearities do not occur, unless the whole inversion process is carried out.

Describing the migration process in terms of reciprocity and representation theorems (de Hoop, 1988; Fokkema and van den Berg, 1993; Wapenaar et al., 2008a) represents an alternative framework where nonlinearities are naturally taken into account. Based on the fact that a representation theorem expresses a wavefield quantity at some point in a medium in terms of boundary (and volume) integrals, an image can thus be defined directly in terms of scattered field or reflectivity operator excited and recorded within the subsurface (Vasconcelos et al., 2010).

Scattering-based imaging is the first approach based on reciprocity that will be used in this thesis, and it relies on a two-way wavefield representation (Wapenaar,

2004; Wapenaar and Fokkema, 2006). The image is found by collapsing the recorded scattered wavefield onto an image point and is interpreted as the predicted experiment at depth with co-located sources and receivers (referred to as *pseudosources* and *pseudoreceivers*) at time equal zero (see Figure 1.3a). Vasconcelos (2008) has shown that scattering-based integral relations, originally derived for seismic interferometry (Vasconcelos et al., 2009b), lead to an explicit mathematical representation of the physical intuition on which Claerbout's imaging condition is based. The scattering-based imaging condition is composed of two terms, the first being the linear contribution and the second contributing to mapping the effect of nonlinearities back to the image point (Fleury and Vasconcelos, 2012):

$$\begin{aligned} I(\mathbf{x}_I) = p^S(\mathbf{x}_I, \mathbf{x}_I, t=0) = &\int_{-\infty}^{+\infty} \left(\oint_{\partial D_S} p^S(\mathbf{x}_I, \mathbf{x}_S, \omega) G^{0*}(\mathbf{x}_I, \mathbf{x}_S, \omega)\, \mathrm{d}^2\mathbf{x}_S \right) d\omega \\ &+ \int_{-\infty}^{+\infty} \left(\oint_{\partial D_S} p(\mathbf{x}_I, \mathbf{x}_S, \omega) G^{S*}(\mathbf{x}_I, \mathbf{x}_S, \omega)\, \mathrm{d}^2\mathbf{x}_S \right) d\omega, \end{aligned} \tag{1.1}$$

where p and p^S represent the full and scattered components of the pressure wavefields, respectively. G^0 is the wavefield propagator computed in the reference model, and G^S is the scattered wavefield propagator obtained as the difference of the full and reference propagators: $G^S = G - G^0$. Surface integration is carried out along the boundary ∂D_S of available sources $\mathbf{x}_S$, $\mathbf{x}_I$ identifies the image point, and $*$ represents complex conjugation in frequency domain (time-reversal in time domain) with ω denoting the angular frequency. The main advantage of this formalism lies in the fact that the sought field $p^S(\mathbf{x}_I, \mathbf{x}_I, t=0)$ is explicitly expressed in terms of correlation-type integrals. Its numerical computation requires the crosscorrelation of the required fields either in time or frequency domain, and does thus not use any deconvolution or inversion step. Moreover, two-way representation theorems account for all directions of propagation including evanescent fields, making the energy mapped at each image point $\mathbf{x}_I$ sensitive to the model perturbation all around the point (Figure 1.3a). Non-propagating waves (depicted as a double wiggle in Figure 1.3a) are especially beneficial in improving the resolution of the image as discussed above.

On the other hand, theory dictates that boundaries of sources (as well as receivers for wavefield extrapolation — see Halliday and Curtis, 2010; Vasconcelos, 2013) completely enclose the locations of interest in the subsurface. Analysis carried out in the field of seismic interferometry for both reflected and scattered body waves has revealed that when the source and/or receiver distributions are limited, a significant error is introduced, infecting the retrieved response with so-called *nonphysical waves* (Snieder et al., 2006; King and Curtis, 2012; Meles and Curtis, 2013; Loer et al., 2014). Our numerical experiments in Chapters 2, 5 and 6 confirm that these observations also

appear to hold in an imaging context.

The original formulation of **reflectivity-based imaging** relies instead on one-way representation (Wapenaar and Grimbergen, 1996; Wapenaar et al., 2004). The vertical axis is chosen to be the preferred direction of propagation and the fields are expressed in terms of their up- and down-going constituents, p^- and p^+ (Figure 1.3b). The first and most important difference with the scattering-based approach lies in the definition of an image. While the two-way image satisfies the wave-equation for scattered fields (Vasconcelos et al., 2009b, 2010), the one-way image is the zero-offset, zero-time sample of the kernel operator R of the following integral relation (Wapenaar et al., 2008a):

$$p^-(\mathbf{x}_I + \boldsymbol{\delta}, \mathbf{x}_S, \omega) = \int_{\partial D_I} R(\mathbf{x}_I, \mathbf{x}_I + \boldsymbol{\delta}, \omega) p^+(\mathbf{x}_I, \mathbf{x}_S, \omega)\, \mathrm{d}^2\mathbf{x}_I, \tag{1.2}$$

where $R(\mathbf{x}_I, \mathbf{x}_I + \boldsymbol{\delta}, t)$ is commonly referred to as reflection operator or reflectivity. It is interpreted as the finite-time up-going reflectivity response to the down-going field p^+ from a pseudosource at $\mathbf{x}_I + \boldsymbol{\delta}$ to a pseudoreceiver $\mathbf{x}_I$ within a modified subsurface model that is heterogeneous and with the same properties as the true medium below the depth level ∂D_I, but homogeneous above it (the reflector above ∂D_I in Figure 1.3b is therefore represented by a dashed rather than solid line). A second difference can be found in the fact that a convolution-type theorem is used (so the integrand in equation 1.2 is a convolution not a correlation). This leads to an important advantage: an enclosing boundary of sources is not required (i.e., one-sided illumination may be sufficient). However, the computation of a reflectivity-based image is significantly more costly than its scattering-based counterpart. The imaging condition in equation 1.2 that recover R is in fact the result of a multidimensional deconvolution (MDD) process (Wapenaar and van der Neut, 2010; Wapenaar et al., 2011). The reflectivity function is not directly accessed by correlation or convolution of different fields, but it is rather one of the two terms involved in the integral relation and needs to be inverted for, given the other two constituents of the equation.

In this formulation, multiply scattered waves are embedded in the up- and down-fields and effectively used in the estimate process, as a natural way to regularize the deconvolution step because of their additional coverage and complementary illumination with respect to primaries (Vasconcelos and Rickett, 2013; van der Neut et al., 2013b). On the other hand, the use of a one-way representation does not allow evanescent fields and waves with large angles of incidence to be included in the MDD process. They are thus generally filtered out from the input data to avoid unstable behaviour. This imposes a limit to the maximum obtainable spatial resolution (Berkhout and van Wulfften Palthe, 1979). In Chapter 4, I suggest an extension of source redatuming by MDD to two-way representation theorems where full pressure and velocity fields are used in spite of up-

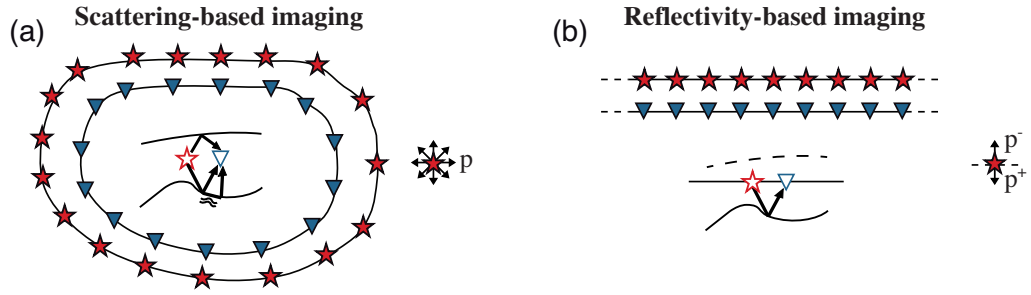

Figure 1.3: Schematic illustration of the geometry used for (a) scattering-based and (b) reflectivity-based imaging. Solid red stars are sources while receivers are indicated by solid blue triangles. Open red stars and blue triangles represent pseudosources and pseudoreceivers in the subsurface, while black rays (and double wiggles) identify the components of the wavefield that are mapped at the image point from the discontinuities around it. On the right side of each plot, a source is depicted alongside the direction of waves that are accounted for by two- and one-way representation theorems, respectively.

and down-going fields, and no assumptions about the preferred direction of propagation has to be made.

Finally, one more important thing to point out is that the imaging approaches discussed here are also naturally suited for the computation of so-called *extended images* (de Bruin et al., 1990; Vasconcelos et al., 2009a, 2010; Sava and Vasconcelos, 2011). As depicted in both cartoons of Figure 1.3, two-way and one-way imaging conditions can produce time- and space-varying responses around each image point of interest when a certain space-lag $\boldsymbol{\delta}$ is allowed between the two points of the scattered wavefield $p^S(\mathbf{x}_I, \mathbf{x}_I + \boldsymbol{\delta}, t)$ and/or reflectivity operator $R(\mathbf{x}_I, \mathbf{x}_I + \boldsymbol{\delta}, t)$, and when they are evaluated for a finite amount of time rather than at $t = 0$ only. By interpreting those gathers as seismic surveys between sources and receivers located within the subsurface, without actually requiring such equipment to be installed there, the reconstructed events can contain useful information for both velocity analysis (Symes, 2008; Yang and Sava, 2011b; Fleury and Perrone, 2012) and reservoir characterization (Thomson, 2012; Vasconcelos and Rickett, 2013). In Chapter 6 I discuss the computation of extended image gathers by means of nonlinear elastic scattering-based imaging, and I provide a detailed analysis of the added value that multiply scattered and transmitted waves bring to the computation of such gathers.

1.4 Thesis plan

In overview I begin with theoretical Chapters 2 through 4 in which I focus on the development of reciprocity-based imaging techniques that take advantage of multiply

scattered waves. I then discuss applications of this theory from Chapters 5 to 8.

In **Chapter 2**, I describe a set of elastic imaging conditions for scattering-based imaging which are based on two-way, full wavefield representation theorems. They are shown to be able to deal with the nonlinear nature of the seismic wavefield as well as all directions of arrival of seismic wavefronts. Imaging of pure-mode compressional waves (i.e., PP imaging) confirms the claim of Fleury and Vasconcelos (2012) for acoustic imaging: that the correct focusing of multiple-scattering effects in the form of both propagating fields (e.g., multiples) and evanescent fields is responsible for increased illumination, higher resolution, and equalized amplitudes. When the very same imaging framework is instead applied to converted waves, a striking conclusion is reached: PS imaging leads to a null image because no converted energy can be mapped at zero-time and zero-offset.

Chapter 3 extends the theory of scattering-based imaging to wavefield extrapolation of elastic data. By introducing an extrapolation scheme based on the correlation-type elastic representation theorem that correctly honours the physics of wave propagation, I achieve directional and modally-selective injection of the recorded data without the need for elastic wavefield separation. Up- and down-going waves are separated on-the-fly and injected only towards their direction of arrival, whereas P- and S- waves are injected such that only the correct mode back-propagates into the subsurface.

In **Chapter 4**, I focus on the retrieval of acoustic reflectivity functions by means of multi-dimensional deconvolution of two-way representation theorems. This study represents an extension of conventional reflectivity-based processing and imaging approaches which rely on one-way representations and up/down separated fields. One-way equations are in fact only strictly valid for vertically propagating waves, so they tend not to be as accurate for steeply dipping arrivals, and they also do not include evanescent waves. The formulation based on two-way reciprocity theoretically accounts for waves reaching the recording surface at any angle of incidence, as well as all rapidly decaying fields. Numerical examples of source redatuming show the effectiveness of two-way MDD in scenarios where receivers are physically placed in the subsurface avoiding the preliminary step of wavefield separation.

Chapter 5 combines the findings of Chapter 2 and Chapter 3 in an attempt to define a comprehensive scattering-based imaging framework in elastic media that can ultimately lead to nonlinear images of the subsurface. I test this methodology on a benchmark model that emulates deep water subsalt prospects as found in the Gulf of Mexico, and analyse the additional value provided by multiply scattered and transmitted waves. Finally, I discuss a number of approaches that may be used in practical applications to provide the fields required by nonlinear imaging.

In **Chapter 6**, I adapt the scattering-based imaging framework to estimate spatio-temporal responses between offset subsurface sources and receivers. When such extended image gathers are computed by means of linear imaging using partial boundaries of sources and receivers, the quality of their reconstruction is affected by missing events, incorrect amplitudes, and spurious energy which may mislead their interpretation. I prove that more reliable estimates can be produced by adding nonlinear terms and transmitted waves (the latter available if surface and borehole seismic data are jointly acquired or estimated by means of autofocusing), and by applying frequency-wavenumber (f-k) filtering procedures to reduce artefacts from near-horizontally propagating waves. I finally show that reflections and transmissions have a different sensitivity with respect to velocity errors and I suggest a new objective function that may lead to more robust velocity analysis methods.

Chapter 7 and **Chapter 8** are dedicated to the application of acoustic directional wavefield extrapolation and target-oriented imaging by means of Marchenko redatuming respectively, to an ocean-bottom multi-component dataset acquired over the Volve field, North Sea. This represents the first time that either approach has been applied to a field dataset. I describe the processing sequences that are applied to recorded data, and discuss imaging results and their implications. Challenges and open questions that still need to be answered before these techniques may become mainstream are also highlighted.

Chapter 9 recommends areas for future work arising from the studies presented in this thesis. They include an optimization-based approach to elastic imaging where, by ensuring the converted-wave image to be null everywhere in the subsurface, the quality of compressional wave imaging could be enhanced. Given the impossibility to record shear stress energy, various strategies for the application of scattering-based elastic wavefield extrapolation, are also discussed. Moreover, I propose a modified version of the correlation-type representation theorem that combines recorded data with data modelled along the portion of the source boundary where sources are not physically available. This may give rise to a subsurface-domain metric to quantify model errors.

Finally, in **Chapter 10** I summarise the main conclusions that can be drawn from this thesis.

Figure 1.4 visually summarizes some of the main findings of this thesis. Its meaning will become clear as the reader progresses.

1.5 Publications

All chapters of the thesis have been published in, submitted to, or are in preparation for peer-reviewed journals*.

Chapter 2 is published as:
- **M. Ravasi** and A. Curtis. [2013] Nonlinear scattering based imaging in elastic media: theory, theorems and imaging conditions. *Geophysics*, 78(3), pp. S137-S155.

Chapter 3 is published as:
- **M. Ravasi** and A. Curtis. [2013] Elastic imaging with exact wavefield extrapolation for application to ocean-bottom 4C seismic data. *Geophysics*, 78(6), pp. S265-S284.

Chapter 4 is in published as:
- **M. Ravasi**, G. Meles, A. Curtis, Z. Rawlinson and L. Yikuo. [2015] Seismic interferometry by multi-dimensional deconvolution without wavefield separation. *Geophysical Journal International*, 202(1), pp. 1-16.

Chapter 5 is published as:
- **M. Ravasi**, I. Vasconcelos and A. Curtis. [2014] Beyond conventional migration: non-linear elastic subsalt imaging with transmissions and two-sided illumination. *Geophysical Journal International*, 198(2), pp. 1187-1199.

Chapter 6 is in press as:
- **M. Ravasi**, I. Vasconcelos, A. Curtis and G. Meles [2015] Elastic extended images and velocity-sensitive objective functions using multiple reflections and transmissions. *Geophysical Journal International*.

Chapter 7 is in press as:
- **M. Ravasi**, I. Vasconcelos, A. Curtis and A. Kritski [2015] Vector-Acoustic reverse time migration of Volve OBC dataset without up/down decomposed wavefields. *Geophysics*.

Chapter 8 is in preparation as:
- **M. Ravasi**, I. Vasconcelos, A. Kritski, A. Curtis, C. da Costa and G. Meles [2015] Target-oriented Marchenko imaging of a North Sea field. *Geophysical Research Letters*.

*Minor changes have been introduced to the text and equations to provide a consistent notation in the different chapters of the thesis.

In addition to the publications included in this thesis, I have also contributed to the following publications:

- C. da Costa, **M. Ravasi**, A. Curtis, and G. Meles. [2014] Elastodynamic Green's function retrieval through single-sided Marchenko inverse scattering. *Physical Review E*, 90, 063201.
- G. Meles, K. Loer, **M. Ravasi** and A. Curtis, C. A. da Costa Filho.[2014] Internal multiple prediction and removal using Marchenko autofocusing and seismic interferometry. *Geophysics*, 80(1), pp. A7-A11
- C. da Costa, **M. Ravasi** and A. Curtis [2014] Imaging with primaries and internal multiples in elastic media using autofocusing. In Press in *Geophysics*.

The following conference abstracts have resulted from this study:

- **M. Ravasi**, I. Vasconcelos, A. Kritski, A. Curtis, C.A. da Costa Filho, and G. Meles. [2015] Marchenko imaging of Volve field, North Sea. 77th Annual International Conference and Exhibition, EAGE.
- **M. Ravasi**, I. Vasconcelos, A. Curtis, and A. Kritski. [2015] Multi-dimensional free-surface multiple elimination and source deblending of Volve OBC data. 77th Annual International Conference and Exhibition, EAGE.
- **M. Ravasi**, I. Vasconcelos, A. Curtis, and A. Kritski. [2015] A practical approach to vector-acoustic imaging of primaries and free-surface multiples. 77th Annual International Conference and Exhibition, EAGE - Workshop 06: Seismic Imaging, Latest Developments.
- **M. Ravasi**, I. Vasconcelos, A. Curtis, and A. Kritski. [2014] Vector-Acoustic reverse-time migration of Volve OBC dataset without up/down decomposed wavefields. Second EAGE/SBGf Workshop.
- **M. Ravasi**, I. Vasconcelos, A. Curtis, and A. Kritski. [2014] Directional & modally-selective wavefield extrapolation without up/down or P/S separation. 84th SEG - Workshop: W-18 New Advances in Migration.
- I. Vasconcelos, **M. Ravasi**, and J. van der Neut. [2014] An interferometry-based, subsurface-domain objective function for targeted waveform inversion. 76th Annual International Conference and Exhibition, EAGE.
- **M. Ravasi**, I. Vasconcelos, and A. Curtis. [2014] Beyond conventional migration: nonlinear subsalt imaging with transmissions and two-sided illumination. 76th Annual International Conference and Exhibition, EAGE.

- **M. Ravasi**, and A. Curtis. [2013] Exact Wavefield Extrapolation for Elastic Reverse-Time Migration. 75th Annual International Conference and Exhibition, EAGE.
- **M. Ravasi**, and A. Curtis. [2013] Nonlinear Scattering-based Imaging in Elastic Media. 75th Annual International Conference and Exhibition, EAGE.

■

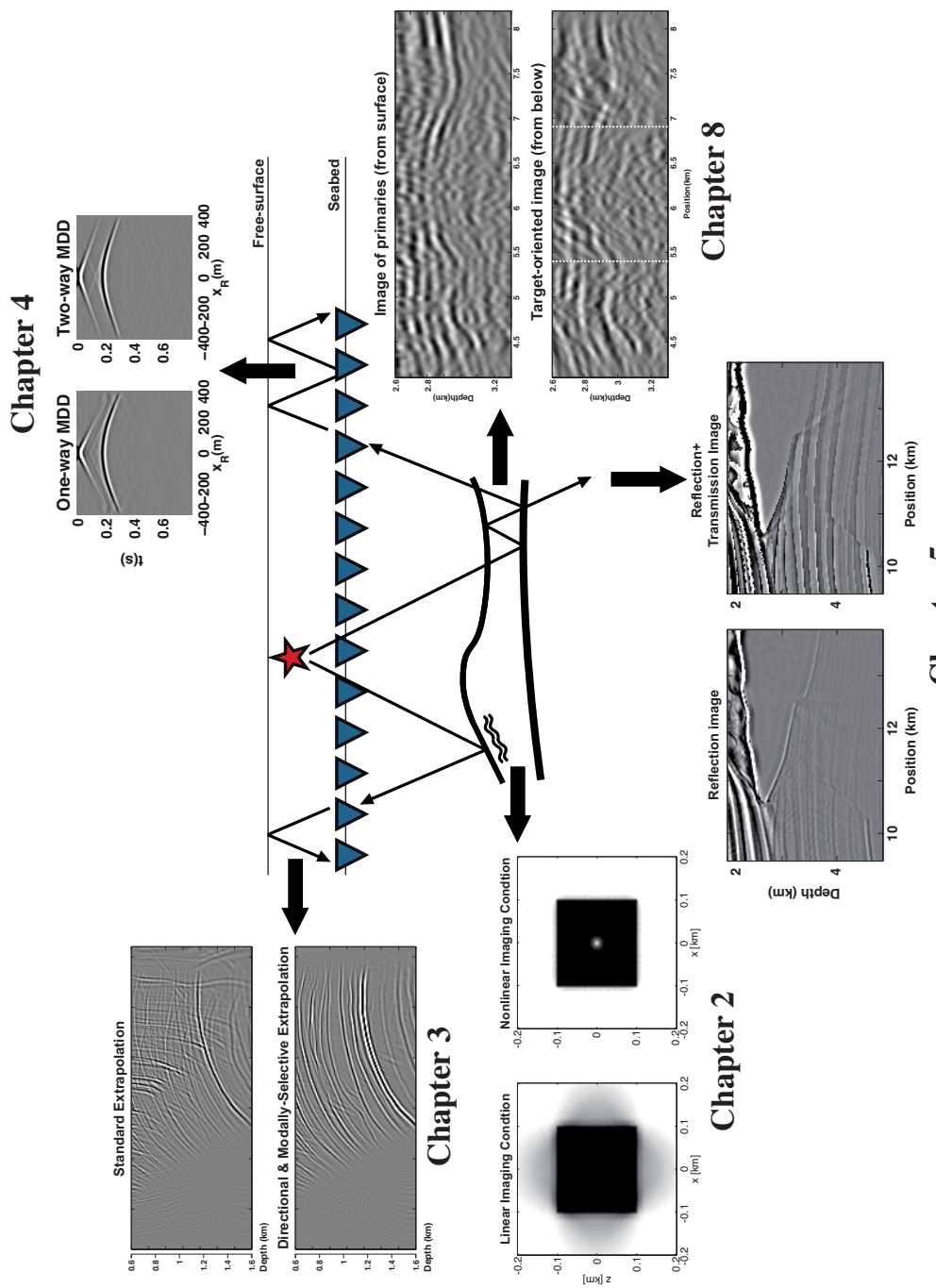

Figure 1.4: Visual summary of the various nonlinear migration techniques discussed in this thesis.

2

Nonlinear scattering-based imaging conditions in elastic media

With the more widespread introduction of multicomponent recording devices in land and marine ocean-bottom seismic acquisition, elastic imaging may become mainstream in coming years. We have derived a set of elastic imaging conditions able to deal with nonlinear multiple-scattering effects (e.g., migration of multiples, amplitude-preserving migration). A correlation-type representation theorem for perturbed elastic media, commonly used in seismic interferometry to explain how a scattered wave response between two receivers may be predicted given a boundary of sources, can be considered as a starting point for the derivation. Here, we use this theorem to derive and interpret imaging conditions for wave-equation elastic migration. Some approximations lead to a known, heuristically derived imaging condition that crosscorrelates P- and S-wave potentials that are separated in the subsurface after full-wavefield extrapolation. This formal connection reveals that the non-approximated correlation-type representation theorem can be interpreted as a nonlinear imaging condition, that accounts also for multiply scattered and multiply converted waves, properly focusing such energy at each image point. We present a synthetic data example and demonstrate the importance of nonlinearities in pure- and converted-mode imaging. In PP imaging, they result in better illumination and artefact reduction, whereas in PS imaging they show how zero time-lag and zero space-lag crosscorrelation imaging conditions are not ideal for imaging of converted-mode waves because no conversion arises from zero-offset experiments.

2.1 Introduction

The earliest forms of migration involved moving (migrating) energy around seismic time sections to estimate the true subsurface position of spatial changes of the medium parameters (the reflectivity) — see Yilmaz (1989). Migration is commonly based on a linearized, single-scattering approximation called the Born approximation (Oristaglio, 1989). Only energy from primary reflections or diffractions is therefore properly focused by migration; multiples and higher-order scattering events must generally be attenuated at an early stage of data processing to prevent the distortion of seismic images.

More sophisticated forms of migration aim at preserving amplitudes in the data (Gray, 1997) to produce so-called 'true-amplitude images' (images where reflectivity estimates are directly related to the values of elastic rock-physics parameters) of complex geologic regions. This is desirable because careful synthesis of reflection amplitudes is crucial for velocity model building, estimation of elastic subsurface parameters, and determination of specific reservoir characteristics using Amplitude-Versus-Offset (AVO) analysis. Wave-equation migration techniques are one promising tool to achieve this goal because they are based on the full wave equation, in principle requiring no single-scattering approximation. Nevertheless, they employ imaging conditions that are borrowed from the earliest forms of imaging and do not allow us to image beyond single-scattering (Weglein, 2014).

An explicit link has recently been established between seismic interferometry and reverse-time imaging in acoustic media. This has allowed various acoustic imaging conditions to be reinterpreted in terms of physical wave propagation phenomena, and to be reformulated in a nonlinear fashion using representation theorems (Vasconcelos et al., 2009b, 2010; Vasconcelos, 2011; Vasconcelos et al., 2012; Halliday and Curtis, 2010; Sava and Vasconcelos, 2011; Fleury and Vasconcelos, 2012). In this chapter, we focus our attention on elastic RTM, and we use a correlation-type representation theorem for perturbed elastic media to identify a new set of true-amplitude, nonlinear imaging conditions.

Seismic interferometry usually refers to the synthesis of the wavefield that would propagate between two receiver locations, as if one receiver was replaced by a source (Figure 2.1a). This is obtained by crosscorrelating the wavefields observed at each receiver location due to an enclosing boundary of energy sources (Wapenaar, 2004; van Manen et al., 2005, 2006; Wapenaar and Fokkema, 2006). Introductions, tutorials, and reviews are given in Curtis et al. (2006); Wapenaar et al. (2010a,c) and Galetti and Curtis (2012). Slob et al. (2007) showed that crossconvolution can also be used to construct interreceiver wavefields (in the geometry of Figure 2.1b), and Vasconcelos and

Snieder (2008a,b) first used deconvolution to perform interferometry. By reciprocity it was shown that the Green's function between two sources can also be estimated given their recordings on a boundary of receivers (as in Figure 2.1c — also Hong and Menke (2006); Curtis et al. (2009)). Finally, if we have a boundary of sources and a boundary of receivers, Curtis (2009); Curtis and Halliday (2010) and Curtis et al. (2012) demonstrated that the Green's function between a physical source and physical receiver that are not on either boundary can be constructed using appropriate crosscorrelation and/or crossconvolution operations (Figure 2.1d). The latter method is referred to as source-receiver interferometry (SRI).

Vasconcelos et al. (2009a) and Sava and Vasconcelos (2011) found a connection between the zero time-lag and zero space-lag crosscorrelation imaging condition invoked by most wave-equation-based imaging methods (e.g., Claerbout (1985)), and the theory and practice of seismic inter-receiver interferometry. In the context of inter-receiver interferometry, Fleury and Vasconcelos (2012) define for the first time a nonlinear imaging condition that may be suitable for practical applications, which takes into account amplitude corrections necessary to migrate multiply scattered waves (e.g., reflection multiples). This imaging condition was shown to produce an image that is approximately the zero-time, scattered-wave response generated by zero-offset pseudo experiments between a source and a receiver located exactly at each and every image point. Finally, Halliday and Curtis (2010) used the theory of source-receiver interferometry to generalize that connection by deriving a new form of integral that describes the recovery of scattered waves propagating between a real source and a real receiver. They included terms that describe the propagation of wavefields from a boundary of sources to any image point, and to a boundary of receivers from the image point. Thus, they were able to create an explicit analytic link between this form of seismic interferometry and inverse scattering seismic imaging theory: by using a single-scattering Born approximation, they present an alternative derivation of Oristaglio's inverse-scattering formula (Oristaglio, 1989; Thorbecke and Wapenaar, 2007) which is equivalent to many currently used migration algorithms, and which they derive directly from source-receiver interferometry. By removing the Born approximation, they obtain a nonlinear imaging theorem that accounts for multiple scattering, and the correct distribution of energy in the scattered waves as is described by the optical theorem of physics (Snieder et al., 2008; Halliday and Curtis, 2009).

Over recent decades, acquisition technologies have improved with the introduction of multicomponent recording devices for land, ocean-bottom, and marine seismic surveys. They record not only the vertical component of particle velocity (or particle acceleration) but also the horizontal components. New geophysical techniques have been developed to take advantage of these acquisition developments, especially in data pro-

cessing such as noise attenuation, signal reconstruction, and interpolation or multiple attenuation. On the other hand, even though multicomponent imaging has been an active research area for many years, multicomponent data are not usually processed with specifically designed imaging techniques.

For isotropic media, the most straightforward way to process these data is based on the assumption that P- and S-waves can be separated on the recording surface from multicomponent data, and each can be imaged independently with procedures borrowed from acoustic wave equation imaging algorithms, using P- and S-wave velocities, respectively. Early attempts at multicomponent imaging used the Kirchhoff integral and separated waves on the Earth's free surface, and involved computing traveltimes for PP and PS reflections and summing data along those trajectories (e.g., Wapenaar and Haimé (1990). Yan and Sava (2008) suggest an alternative procedure that employs the entire vector wavefield for wavefield reconstruction, then separates P- and S-waves after extrapolating the full vector wavefield into the subsurface, just before the imaging condition is applied. They also formulate a new set of imaging conditions that combine the various incident and reflected wave modes.

The recently increasing interest in recording multicomponent wavefields, and in seismic scattering and imaging based on the elastic wave equation, indicates that the interferometric nonlinear imaging conditions proposed so far in the acoustic case could usefully be extended to the elastic case. Here, we first consider the correlation- type representation theorem in elastic media (van Manen et al., 2006; Wapenaar and Fokkema, 2006) and explicitly express the construction of only the scattered wavefield. We manipulate this formula to obtain a new set of imaging conditions that crosscorrelate P- and S-wave potentials separated in the subsurface after a full-wavefield extrapolation. These are suitable for use with land and marine ocean-bottom seismic acquisition. We then show how one can approximate and linearize our expressions to obtain an imaging condition that is identical to that proposed by Yan and Sava (2008). This suggests that, without these approximations, the correlation-type representation theorem can be regarded as a nonlinear, true-amplitude version of the latter imaging condition, that accounts also for multiply scattered and converted waves.

We demonstrate this with a synthetic example, in which two different acquisition geometries are used. First, a full boundary of sources allows for a perfect construction of the scattered-wave Green's function at each and every image point: its zero-time value is the elastic image. Then the effect of more practical source coverage and partial illumination is investigated by using only a portion of the source boundary for the image construction. These examples highlight many interesting issues; for instance, how partial illumination affects nonlinear imaging, and why there is debate about how to

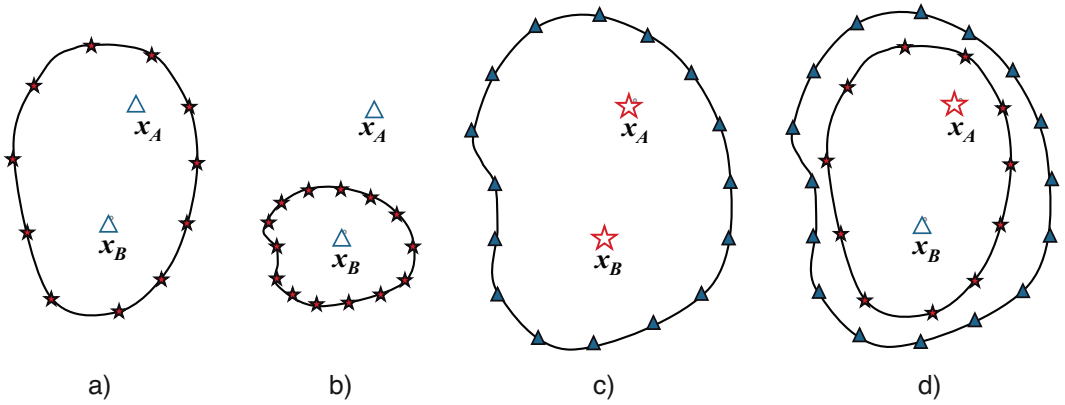

Figure 2.1: Configurations for (a) inter-receiver correlational interferometry, (b) inter-receiver convolutional interferometry, (c) inter-source correlational interferometry, and (d) source-receiver interferometry using two correlational integrals. Solid stars and triangles indicate sources and receivers on the boundaries. Interferometry is used to construct the wavefield between the open stars and the open triangles.

choose signs in PS-wave imaging conditions (see the Discussion section). In fact, we show that PS imaging is only possible using previous zero-offset ICs because of the incompleteness of the source boundary, and hence works only because the full theory breaks down.

2.2 Representation theorems for perturbed elastic media

Given an elastic lossless arbitrarily inhomogeneous anisotropic medium, our starting point for the derivation of reciprocity and representation theorems are the equation of motion and the linear stress-strain relation (Aki and Richards, 1980; Snieder, 2002), which in the frequency domain (where ω denotes the angular frequency) can be written as

$$j\omega\rho(\mathbf{x})v_i(\mathbf{x},\omega) - \partial_j\tau_{ij}(\mathbf{x},\omega) = f_i(\mathbf{x},\omega) \tag{2.1}$$

and

$$-j\omega c_{ijkl}(\mathbf{x})\tau_{kl}(\mathbf{x},\omega) + (\partial_j v_i(\mathbf{x},\omega) + \partial_i v_j(\mathbf{x},\omega))/2 = h_{ij}(\mathbf{x},\omega), \tag{2.2}$$

where $v_i(\mathbf{x},\omega)$ is the i-th component of the particle velocity vector at position $\mathbf{x}$, $\tau_{ij}(\mathbf{x},\omega)$ is the ij-th component of the stress tensor, $f_i(\mathbf{x},\omega)$ is the i-th component of the volume force density, $h_{ij}(\mathbf{x},\omega)$ is the ij-th component of the deformation rate density, ∂_j is the spatial partial derivative with respect to the x_j coordinate ($\partial_j g = \frac{\partial g}{\partial x_j}$),

$c_{ijkl}(\mathbf{x})$ is the elasticity tensor or compliance (the inverse of stiffness $s_{ijkl}(\mathbf{x})$), and $\rho(\mathbf{x})$ is the density. Note that Einstein's summation convention for repeated indices is used throughout this chapter.

Given two wave states A and B, where a *state* means a combination of medium parameters, field quantities, source quantities, boundary conditions, and initial conditions that satisfy the wave equation, a Betti-Rayleigh reciprocity theorem of the correlation-type can be derived from the following interaction quantity

$$-\partial_j\{v_i^A\tau_{ij}^{B*} + v_i^{B*}\tau_{ij}^A\} = 0, \tag{2.3}$$

where the complex conjugate stress tensor for state B is multiplied by v_i^A and the stress tensor for state A is multiplied by v_i^{B*}, their results are subtracted, and a partial derivative in the i-th direction is applied. Integrating over a volume D with closed boundary ∂D, and using Gauss's theorem to convert volume integrals into surface integrals (Aki and Richards, 1980; Snieder, 2002) we obtain

$$\oint_{\partial D}\{-v_i^{B*}\tau_{ij}^A - v_i^A\tau_{ij}^{B*}\}n_j\,\mathrm{d}^2\mathbf{x} = \int_D\{v_i^A f_i^{B*} + v_i^{B*}f_i^A - \tau_{ij}^A h_{ij}^{B*} - \tau_{ij}^{B*}h_{ij}^A\}\,\mathrm{d}^3\mathbf{x}, \tag{2.4}$$

where we have assumed the medium to be lossless and identical in both states, and we have accounted for the symmetry properties of the elasticity tensor ($c_{ijkl} = c_{klij}$) to derive equation 2.4 from equation 2.3. Note that n_j is the j-th component of the outward normal vector to the boundary ∂D.

If we now assume that $h_{ij}^A = h_{ij}^B = 0$, and we introduce the Green's function for states A and B by taking f_i^A as an impulsive point source of force at location $\mathbf{x}_A$ in the fixed n-th direction ($f_i^A = \delta_{in}\delta(\mathbf{x}-\mathbf{x}_A)$) and f_i^B as a source of the same type at location $\mathbf{x}_B$ in the fixed m-th direction ($f_i^B = \delta_{im}\delta(\mathbf{x}-\mathbf{x}_B)$), the general field quantities $v_i^A(\mathbf{x})$, $v_i^B(\mathbf{x})$, $\tau_{ij}^A(\mathbf{x})$, and $\tau_{ij}^B(\mathbf{x})$ turn into specific Green's functions (by definition)

$$\begin{aligned} v_i^A(\mathbf{x}) &= G_{(i,n)}^{(v,f)}(\mathbf{x},\mathbf{x}_A) \qquad & v_i^B(\mathbf{x}) &= G_{(i,m)}^{(v,f)}(\mathbf{x},\mathbf{x}_B) \\ \tau_{ij}^A(\mathbf{x}) &= G_{(ij,n)}^{(\tau,f)}(\mathbf{x},\mathbf{x}_A) \qquad & \tau_{ij}^B(\mathbf{x}) &= G_{(ij,m)}^{(\tau,f)}(\mathbf{x},\mathbf{x}_B) \end{aligned} \tag{2.5}$$

where the two superscripts between brackets on the G terms represent the observed quantity and the source type, respectively, and the subscripts identify the selected components (similar to the notation of Wapenaar and Fokkema (2006)). Substituting into equation 2.4, assuming $\mathbf{x}_A$ and $\mathbf{x}_B$ are situated in D, and using source-receiver

reciprocity gives

$$
\begin{aligned}
&G^{(v,f)}_{(m,n)}(\mathbf{x}_B,\mathbf{x}_A) + G^{(v,f)*}_{(m,n)}(\mathbf{x}_B,\mathbf{x}_A) = \\
&-\oint_{\partial D}\{G^{(v,h)}_{(n,ij)}(\mathbf{x}_A,\mathbf{x})G^{(v,f)*}_{(m,i)}(\mathbf{x}_B,\mathbf{x}) + G^{(v,f)}_{(n,i)}(\mathbf{x}_A,\mathbf{x})G^{(v,h)*}_{(m,ij)}(\mathbf{x}_B,\mathbf{x})\}n_j\,\mathrm{d}^2\mathbf{x},
\end{aligned}
\tag{2.6}
$$

where h identifies the external deformation rate source, which is reciprocal to the stress receiver τ. This is the correlation-type representation theorem for elastic media (van Manen et al., 2006; Wapenaar and Fokkema, 2006). This equation shows that the sum of the Green's function and its complex conjugate (so-called homogeneous Green's function) can be computed (represented) between two points $\mathbf{x}_A$ and $\mathbf{x}_B$ everywhere inside the volume D if responses to force and deformation sources between the enclosing boundary ∂D and each of these points are known.

The propagation domain can be considered to be composed of an unperturbed medium with elasticity tensor $c^0_{ijkl}(\mathbf{x})$ and density $\rho^0(\mathbf{x})$, and a perturbation defined by $c^S_{ijkl}(\mathbf{x}) = c_{ijkl}(\mathbf{x}) - c^0_{ijkl}(\mathbf{x})$, and $\rho^S(\mathbf{x}) = \rho(\mathbf{x}) - \rho^0(\mathbf{x})$. We write for the Green's functions $G = G^0 + G^S$, where the superscript 0 indicates the wavefield in the reference medium and superscript S indicates the wavefield perturbation caused by medium changes, the latter usually being referred to as the scattered component of the wavefield. Substituting each Green's function for the sum of its reference and scattered components into the right-hand side (RHS) of equation 2.6 gives

$$
\begin{aligned}
&G^{(v,f)}_{(m,n)}(\mathbf{x}_B,\mathbf{x}_A) + G^{(v,f)*}_{(m,n)}(\mathbf{x}_B,\mathbf{x}_A) = \\
&-\oint_{\partial D}\{G^{0(v,h)}_{(n,ij)}(\mathbf{x}_A,\mathbf{x})G^{0(v,f)*}_{(m,i)}(\mathbf{x}_B,\mathbf{x}) + G^{0(v,f)}_{(n,i)}(\mathbf{x}_A,\mathbf{x})G^{0(v,h)*}_{(m,ij)}(\mathbf{x}_B,\mathbf{x})\}n_j\,\mathrm{d}^2\mathbf{x} \leftarrow l_{00} \\
&-\oint_{\partial D}\{G^{S(v,h)}_{(n,ij)}(\mathbf{x}_A,\mathbf{x})G^{0(v,f)*}_{(m,i)}(\mathbf{x}_B,\mathbf{x}) + G^{S(v,f)}_{(n,i)}(\mathbf{x}_A,\mathbf{x})G^{0(v,h)*}_{(m,ij)}(\mathbf{x}_B,\mathbf{x})\}n_j\,\mathrm{d}^2\mathbf{x} \leftarrow l_{0S} \\
&-\oint_{\partial D}\{G^{0(v,h)}_{(n,ij)}(\mathbf{x}_A,\mathbf{x})G^{S(v,f)*}_{(m,i)}(\mathbf{x}_B,\mathbf{x}) + G^{0(v,f)}_{(n,i)}(\mathbf{x}_A,\mathbf{x})G^{S(v,h)*}_{(m,ij)}(\mathbf{x}_B,\mathbf{x})\}n_j\,\mathrm{d}^2\mathbf{x} \leftarrow l_{S0} \\
&-\oint_{\partial D}\{G^{S(v,h)}_{(n,ij)}(\mathbf{x}_A,\mathbf{x})G^{S(v,f)*}_{(m,i)}(\mathbf{x}_B,\mathbf{x}) + G^{S(v,f)}_{(n,i)}(\mathbf{x}_A,\mathbf{x})G^{S(v,h)*}_{(m,ij)}(\mathbf{x}_B,\mathbf{x})\}n_j\,\mathrm{d}^2\mathbf{x} \leftarrow l_{SS},
\end{aligned}
\tag{2.7}
$$

where l_{00}, l_{0S}, l_{S0}, and l_{SS} denote each of the four terms on the RHS of equation 2.7 as shown. The first term on the RHS of equation 2.7 constitutes one side of the correlation-type representation theorem for the reference medium, thus it equals the reference homogeneous Green's function ($l_{00} = G^{0(v,f)}_{(m,n)}(\mathbf{x}_B,\mathbf{x}_A) + G^{0(v,f)*}_{(m,n)}(\mathbf{x}_B,\mathbf{x}_A)$). If we bring this term over to the left-hand side (LHS) and we subtract the reference homogeneous

Green's function from the total homogeneous Green's function, we obtain

$$
\begin{aligned}
&G^{S(v,f)}_{(m,n)}(\mathbf{x}_B,\mathbf{x}_A) + G^{S(v,f)*}_{(m,n)}(\mathbf{x}_B,\mathbf{x}_A) = \\
&-\oint_{\partial D}\{G^{S(v,h)}_{(n,ij)}(\mathbf{x}_A,\mathbf{x})G^{0(v,f)*}_{(m,i)}(\mathbf{x}_B,\mathbf{x}) + G^{S(v,f)}_{(n,i)}(\mathbf{x}_A,\mathbf{x})G^{0(v,h)*}_{(m,ij)}(\mathbf{x}_B,\mathbf{x})\}n_j\,\mathrm{d}^2\mathbf{x} \leftarrow l_{0S} \\
&-\oint_{\partial D}\{G^{0(v,h)}_{(n,ij)}(\mathbf{x}_A,\mathbf{x})G^{S(v,f)*}_{(m,i)}(\mathbf{x}_B,\mathbf{x}) + G^{0(v,f)}_{(n,i)}(\mathbf{x}_A,\mathbf{x})G^{S(v,h)*}_{(m,ij)}(\mathbf{x}_B,\mathbf{x})\}n_j\,\mathrm{d}^2\mathbf{x} \leftarrow l_{S0} \\
&-\oint_{\partial D}\{G^{S(v,h)}_{(n,ij)}(\mathbf{x}_A,\mathbf{x})G^{S(v,f)*}_{(m,i)}(\mathbf{x}_B,\mathbf{x}) + G^{S(v,f)}_{(n,i)}(\mathbf{x}_A,\mathbf{x})G^{S(v,h)*}_{(m,ij)}(\mathbf{x}_B,\mathbf{x})\}n_j\,\mathrm{d}^2\mathbf{x} \leftarrow l_{SS}.
\end{aligned}
\tag{2.8}
$$

This is the correlation-type representation theorem for perturbed elastic media (Lu et al., 2011): the scattered homogeneous Green's function between $\mathbf{x}_A$ and $\mathbf{x}_B$ is given by the sum of three different surface integrals that contain crosscorrelations of reference and perturbed and only perturbed wavefields between the enclosing boundary ∂D and each of these points. A related result, the derivation of which is based on the theory of reciprocity for perturbed elastic media, can be found in Vasconcelos (2008) and Gaiser and Vasconcelos (2010). Their equations differ by the fact that only the causal scattered Green's function is constructed (so-called 'one-sided theorems') using a combination of surface and volume integrals.

Equation 2.8 is of great importance for practical applications like imaging because each of the integrals can be computed numerically, and the related contribution can be added together to give a nonlinear imaging condition as we show below.

Example 1: 2D elastic point scatterer

We here apply the theory presented in the previous section for perturbed elastic media to a simple example. An isotropic homogeneous medium with density $\rho = 1000\,kg/m^3$, compressional wave-velocity $V_P = 1500\,m/s$, and shear wave-velocity $V_S = 800\,m/s$ is used as reference medium, and a high-density point perturbation is added to the background medium. Two receivers are surrounded by a square boundary of sources (the distance between sources is $dx_S = 2\,m$) as shown in Figure 2.2.

We are initially interested in the band-limited scattered Green's function $G^{S(v,f)}_{(x,x)}(\mathbf{x}_B,\mathbf{x}_A,t)$, excited by a horizontal body-force source at location $\mathbf{x}_A$ and recorded by a horizontal particle velocity receiver at location $\mathbf{x}_B$. In this context, *band-limited* means that a source wavelet is applied to the Green's function as detailed below. We expect to see reflections (PP and SS) and conversions (PS and SP) between the two receiver locations due to the point scatterer. Because a body-force density source excites P-waves as well as S-waves, this Green's function is in fact mainly composed of four events:

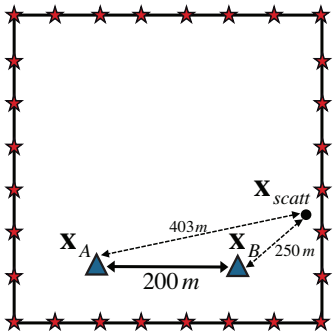

Figure 2.2: Geometry used for the numerical example of interferometry in perturbed elastic media. Stars indicate sources on the boundary ∂D, triangles indicate receivers, and a point scatterer is represented by a black dot. The background medium is an elastic isotropic homogeneous medium with density $\rho = 1000\ kg/m^3$ and velocities $V_P = 1500\ m/s$ and $V_S = 800\ m/s$. The scatterer ($\rho = 2000\ kg/m^3$) is added to the density model.

the first and the fourth events are due to the PP and SS pure scattering, whereas the second and the third events are the PS and SP conversions (Figure 2.3 - red line). To construct such response, two separate forward modelling runs are carried out using the unperturbed background and perturbed velocity models, and the resulting wavefields are subtracted.

We then run the forward model also from each source along the boundary to receivers at $\mathbf{x}_A$ and $\mathbf{x}_B$. Each time series, as well as the response in between the two receivers, are frequency-band limited from 0 to 60 Hz using a Ricker wavelet with a center frequency $f_c = 30\ Hz$. Forward modelling simulations are performed using a staggered-grid, 2D elastic finite-difference algorithm (Robertsson et al., 1994). Outgoing (i.e., radiation or absorbing) boundary conditions are applied just outside the surface enclosing the points of interest to truncate the computational domain. Because we consider the 2D elastodynamic wave equation, at least two forward simulations must be accomplished for each source location — one for each point-force source in mutually orthogonal directions. Derivatives of the Green's functions with respect to source locations on the boundary must also be computed to obtain external deformation rate sources required in equation 2.8. Alternatively we note that, using reciprocity, these terms can be interpreted as the stress measured on the enclosing boundary resulting from point force sources emitted at receiver locations. Since stresses are computed directly in the finite-difference modelling because the code is based on a velocity-stress formulation, the entire set of fields in equation 2.8 could be computed by firing two sets of orthogonal sources at $\mathbf{x}_A$ and $\mathbf{x}_B$, respectively.

After these wavefields are computed, we implement the interferometric integrals and deconvolve the source wavelet from the resulting trace such that their frequency content will be the same of that of the directly modelled response. The trace obtained by the crosscorrelations of reference and perturbed wavefields (Figure 2.3) shows eight events at positive times, exactly twice the number of events we expect from the physical events. Four of them are physical events with traveltime equal to the sum of any combination of P- and S-waves traveling from $\mathbf{x}_A$ to the scatterer and from the scatterer to $\mathbf{x}_B$ (Figure

2.4), whereas the others are spurious or nonphysical events with traveltimes equal to the difference of any combination of P- and S-waves traveling from $\mathbf{x}_A$ to the scatterer and from the scatterer to $\mathbf{x}_B$ (Figure 2.5). However, because the correlation-type representation theorem for perturbed elastic media in equation 2.8 is mathematically exact, we expect the crosscorrelation of only perturbed waves to cancel out these nonphysical waves. The seismic trace in Figure 2.6a fits the true scattered Green's function perfectly. This time series presents the weakest event at earliest time due to the PP wave (traveltime $t^{PP}_{\mathbf{x}_A\to\mathbf{x}_B} = t^{P}_{\mathbf{x}_A\to\mathbf{x}_{scatt}} + t^{P}_{\mathbf{x}_B\to\mathbf{x}_{scatt}} \approx 0.44s$), and the strongest event at latest time due to the SS wave ($t^{SS}_{\mathbf{x}_A\to\mathbf{x}_B} = t^{S}_{\mathbf{x}_A\to\mathbf{x}_{scatt}} + t^{S}_{\mathbf{x}_B\to\mathbf{x}_{scatt}} \approx 0.82s$); the two intermediate events come from conversion of a P-wave into an S-wave ($t^{PS}_{\mathbf{x}_A\to\mathbf{x}_B} = t^{P}_{\mathbf{x}_A\to\mathbf{x}_{scatt}} + t^{S}_{\mathbf{x}_B\to\mathbf{x}_{scatt}} \approx 0.58s$) and vice versa ($t^{SP}_{\mathbf{x}_A\to\mathbf{x}_B} = t^{S}_{\mathbf{x}_A\to\mathbf{x}_{scatt}} + t^{P}_{\mathbf{x}_B\to\mathbf{x}_{scatt}} \approx 0.67s$). We repeat the same procedure to obtain the three other components of the particle velocity Green's tensor $G^{S(v,f)}_{(z,x)}(\mathbf{x}_B,\mathbf{x}_A,t)$, $G^{S(v,f)}_{(x,z)}(\mathbf{x}_B,\mathbf{x}_A,t)$, and $G^{S(v,f)}_{(z,z)}(\mathbf{x}_B,\mathbf{x}_A,t)$ (Figure 2.6). Note how the different source-radiation patterns are reproduced accurately. The cancellation of nonphysical energy occurs in exactly the same way as above for each of these terms.

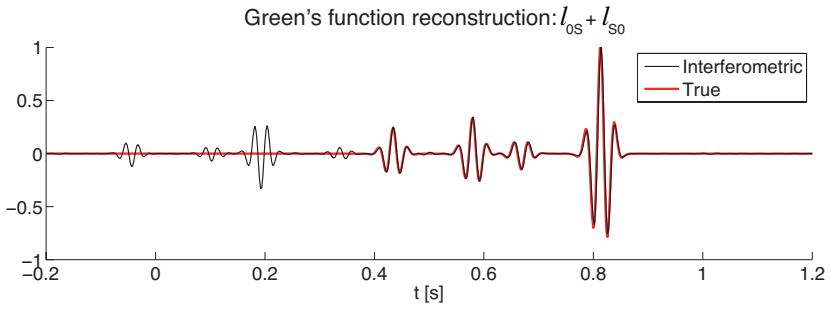

Figure 2.3: Partial reconstruction of the particle velocity Green's function $G^{S(v,f)}_{(x,x)}(\mathbf{x}_B,\mathbf{x}_A,t)$ with only crosscorrelation of reference and perturbed wavefields (black line), and the true scattered Green's function (red line). The partial reconstruction shows four strong nonphysical events at traveltimes $t^{P/S}_{\mathbf{x}_A\to\mathbf{x}_{scatt}} - t^{P/S}_{\mathbf{x}_B\to\mathbf{x}_{scatt}}$ as explained by Figure 2.5.

2.3 Representation theorems for perturbed elastic media for P- and S-waves

As shown above, the final reconstructed Green's functions can be understood in terms of P- and S-waves and their conversions. A similar understanding of the internal process of crosscorrelation within the integrals of equation 2.8 might be tractable if we understood how P- and S-waves interact within these integrals. We therefore now derive a correlation-type representation theorem in perturbed elastic media in terms of P- and

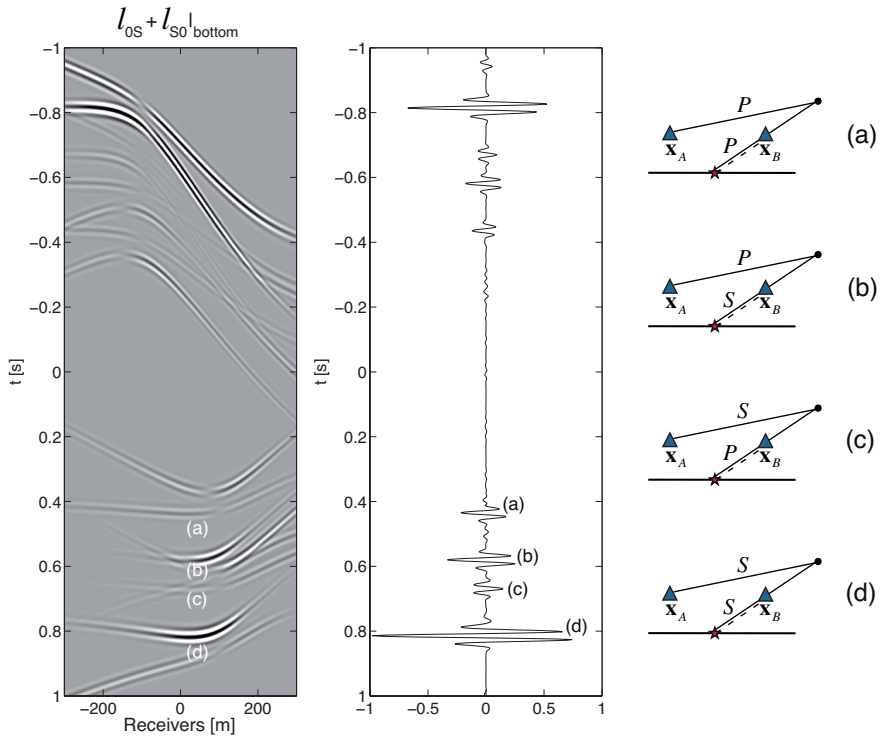

Figure 2.4: Integrand and stationary points in the crosscorrelation of reference and perturbed wavefields ($l_{0S} + l_{S0}$) that contribute to the generation of physical events in Figure 2.3. They have a traveltime equal to the sum of (a) P-waves traveling from $\mathbf{x}_A$ to the scatterer and from the scatterer to $\mathbf{x}_B$, (b) P-waves traveling from $\mathbf{x}_A$ to the scatterer and S-waves traveling from the scatterer to $\mathbf{x}_B$, (c) S-waves traveling from $\mathbf{x}_A$ to the scatterer and P-waves traveling from the scatterer to $\mathbf{x}_B$, and (d) S-waves traveling from $\mathbf{x}_A$ to the scatterer and from the scatterer to $\mathbf{x}_B$.

S-waves, rather than only in terms of particle velocity-type Green's functions as above (equation 2.8).

Taking advantage of the P- and S-wave Green's functions defined by Wapenaar and Haimé (1990) and Wapenaar and Fokkema (2006), we recall that the P- and S-wave components of the wavefield can be expressed as a sum of partial derivatives of the particle velocity

$$G^{(\Phi,f)}_{(P,n)}(\mathbf{x}_B,\mathbf{x}_A) = -\rho(\mathbf{x}_B)V_P^2(\mathbf{x}_B)\partial_i G^{(v,f)}_{(i,n)}(\mathbf{x}_B,\mathbf{x}_A) \tag{2.9}$$

$$G^{(\Phi,f)}_{(S_k,n)}(\mathbf{x}_B,\mathbf{x}_A) = -\rho(\mathbf{x}_B)V_S^2(\mathbf{x}_B)\varepsilon_{kji}\partial_j G^{(v,f)}_{(i,n)}(\mathbf{x}_B,\mathbf{x}_A) \tag{2.10}$$

where Φ in the superscripts refers to potential fields, and V_P and V_S are the local P-wave and S-wave velocities at $\mathbf{x}_B$, respectively. $G^{(\Phi,f)}_{(P,n)}(\mathbf{x}_B,\mathbf{x}_A)$ is thus the Green's function representing the P-wave at $\mathbf{x}_B$, $G^{(\Phi,f)}_{(S_k,n)}(\mathbf{x}_B,\mathbf{x}_A)$ is the equivalent Green's function representing the S-wave at $\mathbf{x}_B$ polarized in the plane with normal n_k, and ε_{kjl} is

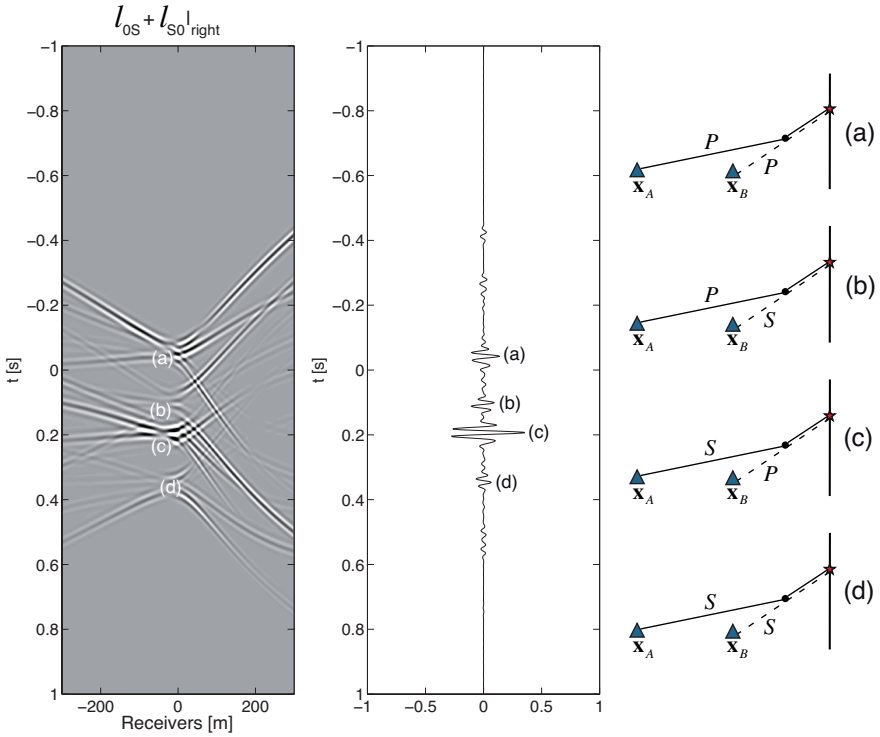

Figure 2.5: Integrand and stationary points in the crosscorrelation of reference and perturbed wavefields ($l_{0S} + l_{S0}$) that contribute to the generation of non-physical events in Figure 2.3. They have a traveltime equal to the difference of (a) P-waves traveling from $\mathbf{x}_A$ to the scatterer and from the scatterer to $\mathbf{x}_B$, (b) P-waves traveling from $\mathbf{x}_A$ to the scatterer and S-waves traveling from the scatterer to $\mathbf{x}_B$, (c) S-waves traveling from $\mathbf{x}_A$ to the scatterer and P-waves traveling from the scatterer to $\mathbf{x}_B$, and (d) S-waves traveling from $\mathbf{x}_A$ to the scatterer and from the scatterer to $\mathbf{x}_B$.

the alternating tensor (or Levi-Civita tensor). In the following we also use the compact notation $G^{(\Phi,f)}_{(K,n)}(\mathbf{x}_B, \mathbf{x}_A)$ to indicate a generic potential response. $K = P$ refers to the P-wave and $K = S_1$,S_2, or S_3 refers to the S-wave with orthogonal orientations, assuming that appropriate P or S velocities are used in equations 2.9 and equation 2.10. Note that, to interpret these equations as P- and S-waves, we are assuming that the medium is homogeneous and isotropic locally around the receiver point $\mathbf{x}_B$. Furthermore, even though the application of the divergence and curl to the full particle velocity vector is always valid, their respective definition as P- and S-waves (and their conversions) is only valid in the far-field region (Wu and Ben-Menahem, 1985).

Equations 2.9 and 2.10 are weighted sums of the spatial derivatives of particle velocity receiver (or point force source) responses and can be used to express P- and S-wave source and receiver Green's functions by taking derivatives of equation 2.8 (Halliday

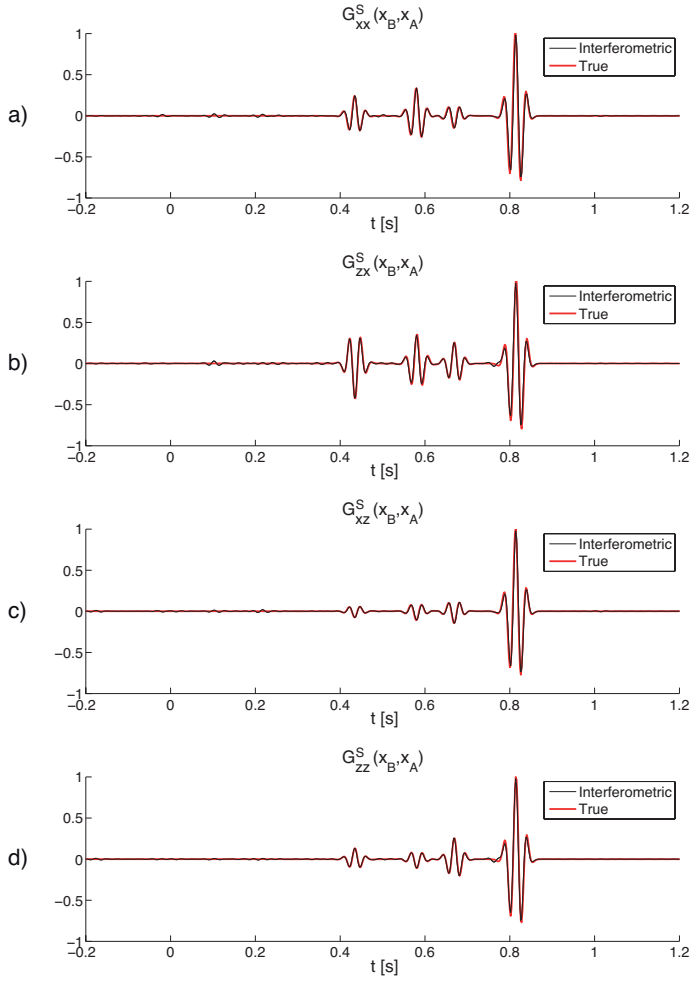

Figure 2.6: Particle velocity Green's functions reconstructed with the full interferometric integrals in equation 2.8 (black line) compared to the true scattered Green's function components (red line): (a) $G^{S(v,f)}_{(x,x)}(\mathbf{x}_B,\mathbf{x}_A,t)$ (b) $G^{S(v,f)}_{(z,x)}(\mathbf{x}_B,\mathbf{x}_A,t)$, (c) $G^{S(v,f)}_{(x,z)}(\mathbf{x}_B,\mathbf{x}_A,t)$, (d) $G^{S(v,f)}_{(z,z)}(\mathbf{x}_B,\mathbf{x}_A,t)$.

et al., 2012)

$$
\begin{aligned}
&G^{S(\Phi,\Phi)}_{(M,N)}(\mathbf{x}_B,\mathbf{x}_A)+G^{S(\Phi,\Phi)*}_{(M,N)}(\mathbf{x}_B,\mathbf{x}_A)=\\
&-\oint_{\partial D}\{G^{S(\Phi,h)}_{(N,ij)}(\mathbf{x}_A,\mathbf{x})G^{0(\Phi,f)*}_{(M,i)}(\mathbf{x}_B,\mathbf{x})+G^{S(\Phi,f)}_{(N,i)}(\mathbf{x}_A,\mathbf{x})G^{0(\Phi,h)*}_{(M,ij)}(\mathbf{x}_B,\mathbf{x})\}n_j\,\mathrm{d}^2\mathbf{x}\\
&-\oint_{\partial D}\{G^{0(\Phi,h)}_{(N,ij)}(\mathbf{x}_A,\mathbf{x})G^{S(\Phi,f)*}_{(M,i)}(\mathbf{x}_B,\mathbf{x})+G^{0(\Phi,f)}_{(N,i)}(\mathbf{x}_A,\mathbf{x})G^{S(\Phi,h)*}_{(M,ij)}(\mathbf{x}_B,\mathbf{x})\}n_j\,\mathrm{d}^2\mathbf{x}\\
&-\oint_{\partial D}\{G^{S(\Phi,h)}_{(N,ij)}(\mathbf{x}_A,\mathbf{x})G^{S(\Phi,f)*}_{(M,i)}(\mathbf{x}_B,\mathbf{x})+G^{S(\Phi,f)}_{(N,i)}(\mathbf{x}_A,\mathbf{x})G^{S(\Phi,h)*}_{(M,ij)}(\mathbf{x}_B,\mathbf{x})\}n_j\,\mathrm{d}^2\mathbf{x}.
\end{aligned}
\tag{2.11}
$$

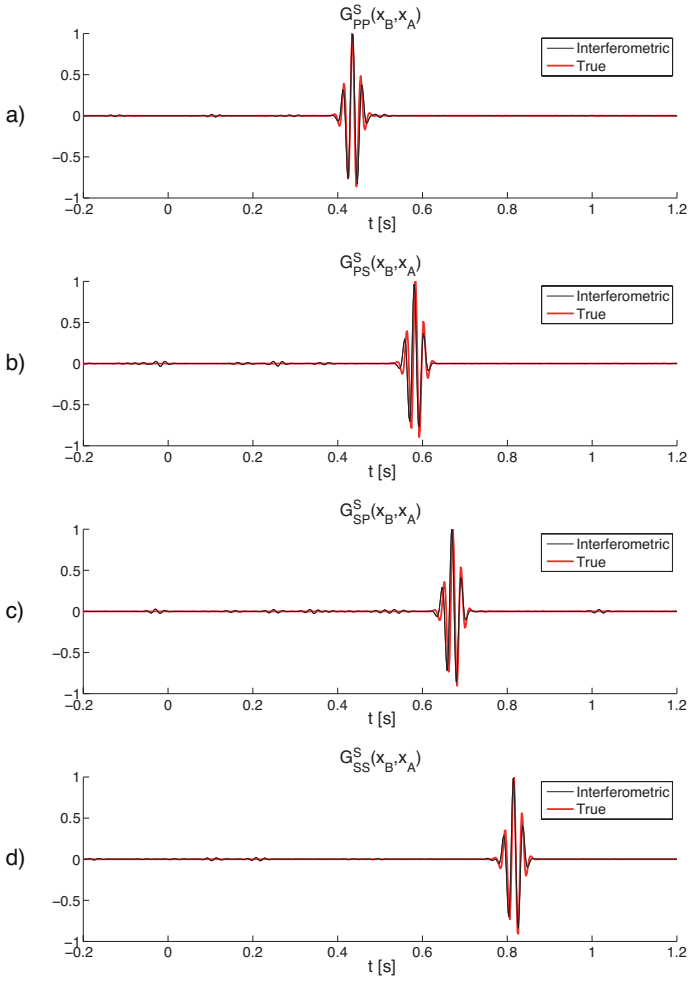

Figure 2.7: P- or S-wave scattered Green's functions due to P- or S-wave sources, reconstructed with the full interferometric integrals in equation 2.11 (black line) compared to the true scattered Green's functions (red line): (a) $G^{S(\Phi,\Phi)}_{(P,P)}(\mathbf{x}_B,\mathbf{x}_A,t)$ (b) $G^{S(\Phi,\Phi)}_{(P,S)}(\mathbf{x}_B,\mathbf{x}_A,t)$, (c) $G^{S(\Phi,\Phi)}_{(S,P)}(\mathbf{x}_B,\mathbf{x}_A,t)$, (d) $G^{S(\Phi,\Phi)}_{(S,S)}(\mathbf{x}_B,\mathbf{x}_A,t)$.

This representation theorem for perturbed elastic media shows how $G^{S(\Phi,\Phi)}_{(M,N)}(\mathbf{x}_B,\mathbf{x}_A)$, the Green's function representing the P- or S-wave component of the scattered wavefield at $\mathbf{x}_B$ due to a P- or S-wave source at $\mathbf{x}_A$, can be recovered from reference and perturbed Green's functions between $\mathbf{x}_i$ $(i = A, B)$ and the enclosing boundary ∂D representing the P- or S-wave components of the wavefield due to force and deformation point sources at boundary points $\mathbf{x} \in \partial D$.

In land acquisition, the most advanced multicomponent seismic survey gives a total of nine components for analysis (9C data). This uses one vertical and two orthogonal S-wave vibrators (or one triaxial vibrator) as sources, and records P-waves and S-waves by deploying multicomponent receivers that measure particle velocities in three

perpendicular orientations. This configuration is well-suited to use the representation theorem for perturbed elastic media (equation 2.11) because using the appropriate combination of recordings (e.g., for a P-wave generated by a vertical point force, use $G^{0/S(\Phi,f)}_{(P,z)}(\mathbf{x}_A,\mathbf{x})$) we can estimate any combination of P- and S-waves (PP, PS, SP, and SS) propagating between the two receiver locations $\mathbf{x}_A$ and $\mathbf{x}_B$. For example, considering again the geometry in Figure 2.2, we compute P- or S-wave recordings at $\mathbf{x}_A$ and $\mathbf{x}_B$, from vertical and horizontal sources on boundary ∂D. These recordings are combined to compute the scattered wave representing the P- or S-wave components of the wavefield at $\mathbf{x}_B$ due to a P- or S-wave source at $\mathbf{x}_A$ and the reconstruction is nearly perfect (Figure 2.7 — differences are due to numerical errors only). Of course, in practical applications, the estimate is limited by only having sources on the Earth's surface (rather than on an enclosing boundary) so the reconstruction will be affected by some nonphysical artefacts. Nevertheless, equation 2.11 does show how P- or S-waves are constructed from force and deformation point sources, and allows the effect of a depletion of the surface integrals to span only the Earth's surface, to be analysed for land seismic surveys.

In a marine environment, on the other hand, water cannot transmit shear wave energy. Marine multicomponent recording of shear energy is only feasible using ocean-bottom seismometers (OBSs). Furthermore, marine seismic airguns can generate only P-wave energy. According to these constraints, the representation theorem for perturbed elastic media (equation 2.11) cannot be used directly. We use the transformation proposed by Wapenaar and Fokkema (2006) to change source quantities on ∂D to be P- and S-wave sources. Assuming that the medium outside of ∂D is homogeneous, isotropic, and unperturbed, by expressing force and deformation sources in term of sources of P- and S-wave potentials, we obtain

$$
\begin{aligned}
&G^{S(\Phi,\Phi)}_{(M,N)}(\mathbf{x}_B,\mathbf{x}_A)+G^{S(\Phi,\Phi)*}_{(M,N)}(\mathbf{x}_B,\mathbf{x}_A)=\\
&\quad\oint_{\partial D}\frac{2}{j\omega\rho(\mathbf{x})}\{\partial_j G^{S(\Phi,\Phi)}_{(N,K)}(\mathbf{x}_A,\mathbf{x})G^{0(\Phi,\Phi)*}_{(M,K)}(\mathbf{x}_B,\mathbf{x})\}n_j\,\mathrm{d}^2\mathbf{x}\\
&+\oint_{\partial D}\frac{2}{j\omega\rho(\mathbf{x})}\{\partial_j G^{0(\Phi,\Phi)}_{(N,K)}(\mathbf{x}_A,\mathbf{x})G^{S(\Phi,\Phi)*}_{(M,K)}(\mathbf{x}_B,\mathbf{x})\}n_j\,\mathrm{d}^2\mathbf{x}\\
&+\oint_{\partial D}\frac{2}{j\omega\rho(\mathbf{x})}\{\partial_j G^{S(\Phi,\Phi)}_{(N,K)}(\mathbf{x}_A,\mathbf{x})G^{S(\Phi,\Phi)*}_{(M,K)}(\mathbf{x}_B,\mathbf{x})\}n_j\,\mathrm{d}^2\mathbf{x}.
\end{aligned}
\tag{2.12}
$$

This equation still requires the availability of monopole and dipole P- and S-wave source responses. If only monopole responses are available, we approximate the dipole response using $\partial_j G^{0/S(\Phi,f)}_{(N,K)}(\mathbf{x}_B,\mathbf{x})n_j \approx -(j\omega/V_K(\mathbf{x}))G^{0/S(\Phi,f)}_{(N,K)}(\mathbf{x}_B,\mathbf{x})$, where V_K is either the P-

or S-wave velocity as appropriate, to obtain

$$
\begin{aligned}
&G^{S(\Phi,\Phi)}_{(M,N)}(\mathbf{x}_B,\mathbf{x}_A) + G^{S(\Phi,\Phi)*}_{(M,N)}(\mathbf{x}_B,\mathbf{x}_A) \approx \\
&\quad \oint_{\partial D} \frac{2}{\rho(\mathbf{x})V_K(\mathbf{x})}\{G^{S(\Phi,\Phi)}_{(N,K)}(\mathbf{x}_A,\mathbf{x})G^{0(\Phi,\Phi)*}_{(M,K)}(\mathbf{x}_B,\mathbf{x})\}\,\mathrm{d}^2\mathbf{x} \\
&+ \oint_{\partial D} \frac{2}{\rho(\mathbf{x})V_K(\mathbf{x})}\{G^{0(\Phi,\Phi)}_{(N,K)}(\mathbf{x}_A,\mathbf{x})G^{S(\Phi,\Phi)*}_{(M,K)}(\mathbf{x}_B,\mathbf{x})\}\,\mathrm{d}^2\mathbf{x} \\
&+ \oint_{\partial D} \frac{2}{\rho(\mathbf{x})V_K(\mathbf{x})}\{G^{S(\Phi,\Phi)}_{(N,K)}(\mathbf{x}_A,\mathbf{x})G^{S(\Phi,\Phi)*}_{(M,K)}(\mathbf{x}_B,\mathbf{x})\}\,\mathrm{d}^2\mathbf{x}.
\end{aligned}
\tag{2.13}
$$

The Green's function representing the scattered P- or S-wave component of the wavefield at $\mathbf{x}_B$ due to a P- or S-wave source at $\mathbf{x}_A$ ($G^{S(\Phi,\Phi)}_{(M,N)}(\mathbf{x}_B,\mathbf{x}_A)$) can be recovered using only Green's functions from a boundary of P- or S-wave sources at $\mathbf{x}\in\partial D$ representing the unperturbed and perturbed P- or S-wave components of the wavefield at $\mathbf{x}_i\,(i=A,B)$ (Gaiser and Vasconcelos, 2010). Equation 2.13 can be used for instance to examine the effects of depleting the boundary sources to be P-sources only, as is required in marine seismic surveys.

2.4 Generalized form of imaging condition with scalar and vector potentials

As introduced in Chapter 1, seismic migration algorithms that use numerical solutions of the wave equation to produce an image of the subsurface generally consist of two consecutive steps: subsurface wavefield reconstruction (both source- and receiver-side), followed by the application of an imaging condition. For prestack depth migration, source and receiver wavefields must be reconstructed at all locations in the subsurface given the true recorded receiver and injected source fields in the actual survey. Using recorded data as boundary conditions, an imaging condition is then applied at all locations in the subsurface, which is supposed to discriminate places where the up- and downgoing wavefields (actually by assumption, the incident and scattered wavefields) are directly related (through local perturbations to the medium), and those where they are not. Thus we obtain an 'image' of the perturbations.

The simplest imaging conditions are based on crosscorrelation or deconvolution of the reconstructed wavefields (Claerbout, 1971, 1985). Vasconcelos et al. (2009a) and Halliday and Curtis (2010) pointed out that there is a connection between the wavefield correlations performed in seismic imaging and those performed in the theory and practice of seismic interferometry. In particular, acoustic representation theorems for the scattered field contain surface integrals similar to those in seismic imaging. Because an

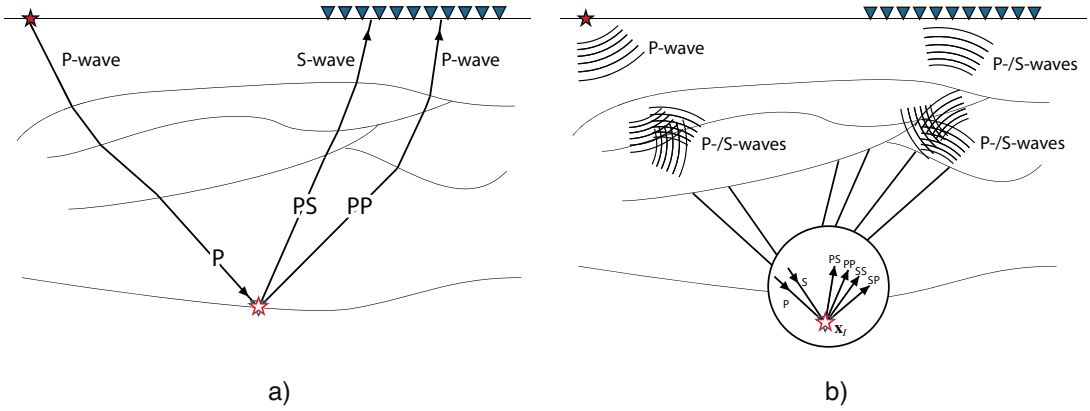

Figure 2.8: Sketches depicting conventional (scalar-based) imaging methods for multicomponent data and the full-wavefield imaging method. (a) Conventional imaging methods for multicomponent data separate wave modes at the acquisition surface and depth-extrapolate them by solving the scalar wave equation. The imaging condition focuses energy coming only from the crosscorrelation of pure-wave modes that do not experience any conversion on the wavepath along either source or receiver sides of the main reflection/conversion event. In a marine environment, where the source wavefield can only be a P-wave, crosscorrelation between the source P-wave and the receiver P-wave gives the PP reflectivity function, and crosscorrelation between the source P-wave and the receiver S-wave gives the PS reflectivity function. (b) In the full-wavefield imaging condition 2.15, wavefields are depth-extrapolated by solving the elastic wave equation. The imaging condition focuses more energy than that focused by the migration procedures that image P- and S-waves independently because every kind of reflection and conversion in the subsurface is taken into account during the wavefield extrapolation procedure.

image of a scatterer can be obtained by extrapolating the recorded scattered wavefield back to the scatterer location and evaluating it at zero-time (Vasconcelos et al., 2009a), a formulation based on scattering representations can be used to interpret the imaging condition in the context of seismic interferometry. However, typical implementations of two-way imaging by, for example, reverse-time migration do not use complete formulations of such an imaging condition. The gradient terms in the surface integrands above, that require data to be acquired with monopole and dipole sources and receivers, are approximated by invoking the far-field approximation ($\partial_i G n_i = (j\omega/V)G$). Moreover, the volume integrals that account for dynamic and kinematic effects associated with transmission effects and multiple scattering or nonlinear interactions of the fields G^0 and G^S with the scattering potential χ are not implemented in usual imaging methods.

We now examine the relation between the elastic representation theorems above and existing elastic imaging conditions. Starting from equation 2.11, we apply approximations similar to those in Vasconcelos et al. (2009a) and Halliday and Curtis (2010) to show that the elastic imaging condition with scalar and vector potentials proposed by Yan and Sava (2008) is just an approximated version of the more general representation

theorems for perturbed elastic media for P- and S-waves. This is important as it means that the full theory above can be used to understand why the latter algorithm produces imperfect results, and second to indicate ways elastic imaging might be implemented in future.

First, we define a point in the subsurface $\mathbf{x}_I = \mathbf{x}_A = \mathbf{x}_B$ at which we would like to construct an image. The representation theorem for perturbed elastic media (equation 2.11) becomes

$$\begin{aligned}
&\tilde{G}^{S(\Phi,\Phi)}_{(M,N)}(\mathbf{x}_I) + \tilde{G}^{S(\Phi,\Phi)*}_{(M,N)}(\mathbf{x}_I) = \\
&- \oint_{\partial D} \{d^{S(\Phi,h)}_{(N,ij)}(\mathbf{x}_I,\mathbf{x}) G^{0(\Phi,f)*}_{(M,i)}(\mathbf{x}_I,\mathbf{x}) + d^{S(\Phi,f)}_{(N,i)}(\mathbf{x}_I,\mathbf{x}) G^{0(\Phi,h)*}_{(M,ij)}(\mathbf{x}_I,\mathbf{x})\} n_j \, \mathrm{d}^2\mathbf{x} \\
&- \oint_{\partial D} \{d^{0(\Phi,h)}_{(N,ij)}(\mathbf{x}_I,\mathbf{x}) G^{S(\Phi,f)*}_{(M,i)}(\mathbf{x}_I,\mathbf{x}) + d^{0(\Phi,f)}_{(N,i)}(\mathbf{x}_I,\mathbf{x}) G^{S(\Phi,h)*}_{(M,ij)}(\mathbf{x}_I,\mathbf{x})\} n_j \, \mathrm{d}^2\mathbf{x} \\
&- \oint_{\partial D} \{d^{S(\Phi,h)}_{(N,ij)}(\mathbf{x}_I,\mathbf{x}) G^{S(\Phi,f)*}_{(M,i)}(\mathbf{x}_I,\mathbf{x}) + d^{S(\Phi,f)}_{(N,i)}(\mathbf{x}_I,\mathbf{x}) G^{S(\Phi,h)*}_{(M,ij)}(\mathbf{x}_I,\mathbf{x})\} n_j \, \mathrm{d}^2\mathbf{x},
\end{aligned} \tag{2.14}$$

where $\tilde{G}^{S(\Phi,\Phi)}_{(M,N)}(\mathbf{x}_I) = \tilde{G}^{S(\Phi,\Phi)}_{(M,N)}(\mathbf{x}_I,\mathbf{x}_I,\omega)$ is the scattered Green's function at $\mathbf{x}_I$, that is, the received scattered P- or S-wave recorded at point $\mathbf{x}_I$ due to a P- or S-wave source also located at $\mathbf{x}_I$. To evaluate the integral expression on the RHS of equation 2.14, we must first compute the subsurface-domain extrapolated wavefields present in the integrands. The source wavefields (e.g., $G^{0/S(\Phi,f)}_{(M,i)}(\mathbf{x}_I,\mathbf{x})$) are numerically modelled from the surface ($\mathbf{x}$) to $\mathbf{x}_I$: these are found in practice by solving the initial-value problem for the elastic wave equation where the initial condition is a body force (or deformation rate) source. The receiver wavefields (e.g., $d^{0/S(\Phi,f)}_{(N,i)}(\mathbf{x}_I,\mathbf{x})$) are depth-extrapolated numerically by solving a boundary-value problem for the elastic wave equation where the boundary condition (BC) consists of the full (or scattered), time-reversed acquired common shot data, as extensively discussed in Chapter 3. Finally, for both extrapolations, the separation of P- and S-wave potentials is performed in the subsurface. Here, we have substituted G with d in the receiver wavefields to emphasise their dependence on the acquired data. In other words, since data can be seen as the convolution of the source wavelet $s(\omega)$ with the Green's propagator G, receiver wavefields are thus also shaped by the source wavelet. Note that if data (or receiver wavefields) are not deconvolved for the source wavelet, the scattered Green's function $\tilde{G}$ that we are after is also a band-limited response.

The value of $\tilde{G}^{S(\Phi,\Phi)}_{(M,N)}(\mathbf{x}_I)$ at zero-time is the instantaneous scattered wave created by a source at $\mathbf{x}_I$. This can only be nonzero if there is a medium perturbation at $\mathbf{x}_I$. Hence, this zero-time value is a good candidate to be used as an imaging condition. Note that, because P- and S-waves (and their conversions) are fully defined only in the far-field, $\tilde{G}^{S(\Phi,\Phi)}_{(M,N)}(\mathbf{x}_I)$ can be considered only as a near-field projection of the far-field P-

and S-waves travelling toward (or leaving) $\mathbf{x}_I$, that we crosscorrelate to construct the Green's function at $\mathbf{x}_I$. Integrating over frequencies (ω) to get the zero-time response, we obtain

$$
\begin{aligned}
&I^{nl}_{NM}(\mathbf{x}_I) = \tilde{G}^{S(\Phi,\Phi)}_{(M,N)}(\mathbf{x}_I,\mathbf{x}_I,t=0) = 2\int_0^{+\infty} Re\{\tilde{G}^{S(\Phi,\Phi)}_{(M,N)}(\mathbf{x}_I)\}\,\mathrm{d}\omega = \\
&-\int_0^{+\infty}\left(\oint_{\partial D}\{d^{S(\Phi,h)}_{(N,ij)}(\mathbf{x}_I,\mathbf{x})G^{0(\Phi,f)*}_{(M,i)}(\mathbf{x}_I,\mathbf{x}) + d^{S(\Phi,f)}_{(N,i)}(\mathbf{x}_I,\mathbf{x})G^{0(\Phi,h)*}_{(M,ij)}(\mathbf{x}_I,\mathbf{x})\}n_j\,\mathrm{d}^2\mathbf{x}\right)\mathrm{d}\omega \\
&-\int_0^{+\infty}\left(\oint_{\partial D}\{d^{0(\Phi,h)}_{(N,ij)}(\mathbf{x}_I,\mathbf{x})G^{S(\Phi,f)*}_{(M,i)}(\mathbf{x}_I,\mathbf{x}) + d^{0(\Phi,f)}_{(N,i)}(\mathbf{x}_I,\mathbf{x})G^{S(\Phi,h)*}_{(M,ij)}(\mathbf{x}_I,\mathbf{x})\}n_j\,\mathrm{d}^2\mathbf{x}\right)\mathrm{d}\omega \\
&-\int_0^{+\infty}\left(\oint_{\partial D}\{d^{S(\Phi,h)}_{(N,ij)}(\mathbf{x}_I,\mathbf{x})G^{S(\Phi,f)*}_{(M,i)}(\mathbf{x}_I,\mathbf{x}) + d^{S(\Phi,f)}_{(N,i)}(\mathbf{x}_I,\mathbf{x})G^{S(\Phi,h)*}_{(M,ij)}(\mathbf{x}_I,\mathbf{x})\}n_j\,\mathrm{d}^2\mathbf{x}\right)\mathrm{d}\omega.
\end{aligned}
\tag{2.15}
$$

This equation can be regarded as a nonlinear, true-amplitude (under ideal acquisition geometries) imaging condition, that accounts also for multiply scattered waves and multiple conversions. It is suitable for land seismic acquisition where body-force density sources directed along x- or z-axes can be used, and deformation rate source can be estimate from spatial derivatives of the available data along the source coordinates. Note that here and throughout this thesis, *true-amplitude* is used to indicate an imaging algorithm which properly retrieves amplitudes that represent the zero-time, zero-offset (elastic) response.

Because the formulation with force and deformation sources is not practical for marine ocean-bottom applications as only P-wave sources are usually available, equation 2.13 is also recast in an imaging context

$$
\begin{aligned}
&I^{nl}_{NM}(\mathbf{x}_I) = \\
&\quad\int_0^{+\infty}\left(\oint_{\partial D}\frac{2}{\rho(\mathbf{x})V_P(\mathbf{x})}\{d^{S(\Phi,\Phi)}_{(N,P)}(\mathbf{x}_I,\mathbf{x})G^{0(\Phi,\Phi)*}_{(M,P)}(\mathbf{x}_I,\mathbf{x})\}\,\mathrm{d}^2\mathbf{x}\right)\mathrm{d}\omega \\
&+\int_0^{+\infty}\left(\oint_{\partial D}\frac{2}{\rho(\mathbf{x})V_P(\mathbf{x})}\{d^{0(\Phi,\Phi)}_{(N,P)}(\mathbf{x}_I,\mathbf{x})G^{S(\Phi,\Phi)*}_{(M,P)}(\mathbf{x}_I,\mathbf{x})\}\,\mathrm{d}^2\mathbf{x}\right)\mathrm{d}\omega \\
&+\int_0^{+\infty}\left(\oint_{\partial D}\frac{2}{\rho(\mathbf{x})V_P(\mathbf{x})}\{d^{S(\Phi,\Phi)}_{(N,P)}(\mathbf{x}_I,\mathbf{x})G^{S(\Phi,\Phi)*}_{(M,P)}(\mathbf{x}_I,\mathbf{x})\}\,\mathrm{d}^2\mathbf{x}\right)\mathrm{d}\omega.
\end{aligned}
\tag{2.16}
$$

Equation 2.16 can be considered to be a second, nonlinear (almost) true-amplitude imaging condition, suitable for marine ocean-bottom seismic acquisition. The word 'almost' reminds us that, because only monopole (P-wave) sources are used, the boundary ∂D must be approximately spherical with a large radius to make equation 2.16 deliver true amplitudes in images. This is obviously not the case, so some amplitude artefacts can still arise in the elastic images.

Basic imaging algorithms based on the separation of P- and S-waves on the recording surface followed by independent P- and S-wave imaging using procedures borrowed from acoustic wave equation imaging algorithms do not take into account the process of P-to-S or S-to-P conversion along reflectors and at scatterers in the subsurface. Thus, the amount of energy that is properly focused by an imaging condition after wavefield extrapolation based on the acoustic (scalar) wave equation is relatively small, and is limited to wavepaths that do not involve any conversion (Figure 2.8a). Any P- or S-wave seismic energy recorded on the surface that comes from conversions in the subsurface is not focused by such an imaging condition, and hence creates artefacts in the final image.

Instead of separating wavefields into scalar wave modes on the acquisition surface, the imaging condition proposed by Yan and Sava (2008) uses the full vector fields for wavefield reconstruction. Wavefield separation of scalar and vector potentials is performed just before the imaging condition is applied, and thus it involves the crosscorrelation of pure P or S modes from the source and receiver wavefields. This methodology allows for wave-mode conversions in wavefield reconstruction because the elastic wave equation is used to depth-extrapolate the source and receiver wavefields, and the imaging condition focuses not only pure-modes coming from the source and the receiver wavefields but also waves that experienced wave-mode conversion during extrapolation on either the source or receiver side (Figure 2.8b).

The correlation-type representation theorems in equations 2.15 and 2.16 share the same advantages discussed for this second elastic imaging condition. Indeed, if we consider only the first surface integral in equation 2.16, we obtain

$$I^{l}_{NM}(\mathbf{x}_I) = \int_0^{+\infty} \left(\oint_{\partial D} \frac{2}{\rho(\mathbf{x}) V_P(\mathbf{x})} \{ d^{S(\Phi,\Phi)}_{(N,P)}(\mathbf{x}_I, \mathbf{x}) G^{0(\Phi,\Phi)*}_{(M,P)}(\mathbf{x}_I, \mathbf{x}) \} \, \mathrm{d}^2\mathbf{x} \right) \mathrm{d}\omega. \quad (2.17)$$

This is is the dynamically correct version of the heuristically-derived imaging condition of Yan and Sava (2008), where the $2/\rho(\mathbf{x})V_P(\mathbf{x})$ scaling correctly accounts for heterogeneities in velocity and density parameters around the source boundary. It shows that the image is created by crosscorrelating the source wavefield $G^{0(\Phi,\Phi)}_{(M,P)}(\mathbf{x}_I, \mathbf{x})$ and the receiver wavefield $d^{S(\Phi,\Phi)}_{(N,P)}(\mathbf{x}_I, \mathbf{x})$. Note that only after wavefield reconstruction, the wavefields are separated into scalar and vector potentials and the imaging condition is applied.

Thus, the imaging condition of Yan and Sava (2008) is shown to be a heuristic approximation to the exact, scattering-based imaging conditions offered by equations 2.15 and 2.16. To summarize, this approximation is obtained by assuming the medium to be homogeneous, isotropic, and unperturbed outside of ∂D, by neglecting the crosscorrela-

tion of reference and scattered fields in the first surface integral and the crosscorrelation of scattered fields in the third surface integral, by discarding S-wave sources, by approximating dipole P-wave sources with monopole sources, and by identifying divergence and curl as near-field P- and S-waves, respectively.

Example 2: Elastic imaging of a square

A simple synthetic example is proposed here to compare our new imaging conditions to that of Yan and Sava (2008). An isotropic homogeneous medium is used as the background medium, and a high-velocity square that contains a point scatterer at its center is embedded in the reference medium as the perturbation to be imaged (Figure 2.9). The P-wave velocity of the background medium is $V_P = 1.5 km/s$, the square represents a positive perturbation of $\Delta V_P = 1.3\, km/s$, and the point scatterer is represented by a negative perturbation of $\Delta V_P = -1.2\, km/s$ with respect to the latter. The S-wave velocity is a scaled version of the P-wave velocity, with $V_P/V_S = 2$. P-wave sources are distributed along a circular boundary with radius $r = 0.4\, km$ to illuminate the target. The images to be compared are obtained by applying the IC in equation 2.17 and the IC in equation 2.16 where S-wave sources are neglected. The source and receiver wavefields are computed using a staggered-grid, 2D elastic finite-difference algorithm (Virieux, 1986). Here, the receiver wavefields ($d^{0/S}$) are directly modeled rather than obtained by wavefield extrapolation, hence they represent the exact, noiseless scattering responses. This removes adverse effects due to a limited receiver geometry on the surface, allowing the two imaging conditions to be compared without additional confounding sources of error. Note that, because only P-wave sources are used, the S-wave component of the reference source wavefield ($G^{0(\Phi,\Phi)}_{(S,P)}(\mathbf{x}_I, \mathbf{x})$) is always zero. Hence, we compare the images produced by crosscorrelating the P-wave components of the source wavefield with the P- and S-wave components of the receiver wavefield (I_{PP}; I_{PS}). We interpret the additional contribution of the interaction between scattered wavefields and we analyse the effect of illumination on these images by considering complete illumination (all sources active) and partial illumination (only top sources active) — see Figure 2.9.

Complete illumination

In the ideal imaging experiment, the nonlinear imaging condition allows the perturbation to be imaged exactly: scattering objects are constructed at correct locations with correct amplitudes. A first comparison between the images describing the PP scattered

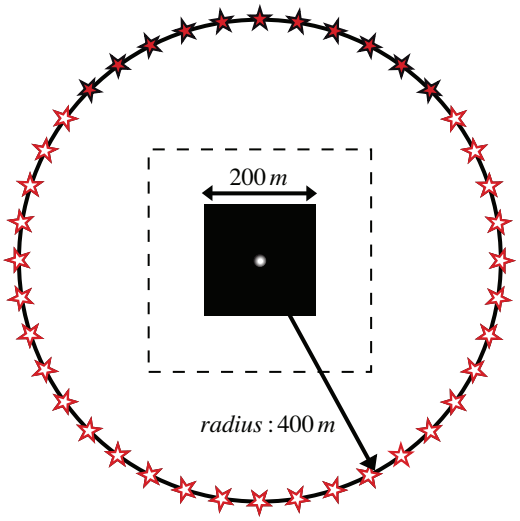

Figure 2.9: Geometry used for the imaging example. Images were created inside the dashed lines using a circular boundary of 40 P-wave sources. The sides and bottom sources (open stars) are active when the illumination is complete, and inactive when the illumination is partial, whereas the top sources (solid stars) are always active. The P-wave velocity of the background medium is $V_P = 1.5\ km/s$, the square represents a positive perturbation of $\triangle V_P = 1.3\ km/s$, and the point scatterer S represents a negative perturbation of $\triangle V_P = -1.2\ km/s$ with respect to the latter. The S-wave velocity is a scaled version of the P-wave velocity, with $V_P/V_S = 2$. A low-velocity point scatterer is located at the center of the square.

Green's function (Figure 2.10a and c) shows how the nonlinear imaging condition improves the images obtained from the heuristic imaging condition. The heuristic image (Figure 2.10a) in fact recovers only the square object; strong 'transmission artefacts' (i.e., artefacts due to interactions between the reference wavefield and forward scattered waves that traverse the square object, see Fleury and Vasconcelos (2012)) contaminate the image preventing a clear definition of its shape. The nonlinear imaging condition (Figure 2.10c) properly maps the square with the point scatterer at its center and artefacts are significantly reduced.

The heuristic image describing the PS scattered Green's function (Figure 2.10b) outlines the edges of the square with a polarity change between left and right sides (most obvious on the horizontal edges of the square). More strikingly, the nonlinear interaction between converted scattered waves (i.e., third integral in equation 2.16) perfectly matches the contributions of linear interactions between reference and scattered waves (i.e., first and second integrals in equation 2.16) and results in a final image that is almost perfectly null (Figure 2.10d), with the exception of some weak artefacts around the corners of the square. This result is consistent with the interferometic definition of the imaging condition in equation 2.16: I_{PS} is the zero time-lag and zero space-lag S-wave response due to a P-wave source. The impossibility of creating a conversion from a zero-offset experiment explains why the image is completely null (when the estimate of the total source power loss is accurate at every point thanks to having complete illumination, in contrast to results below).

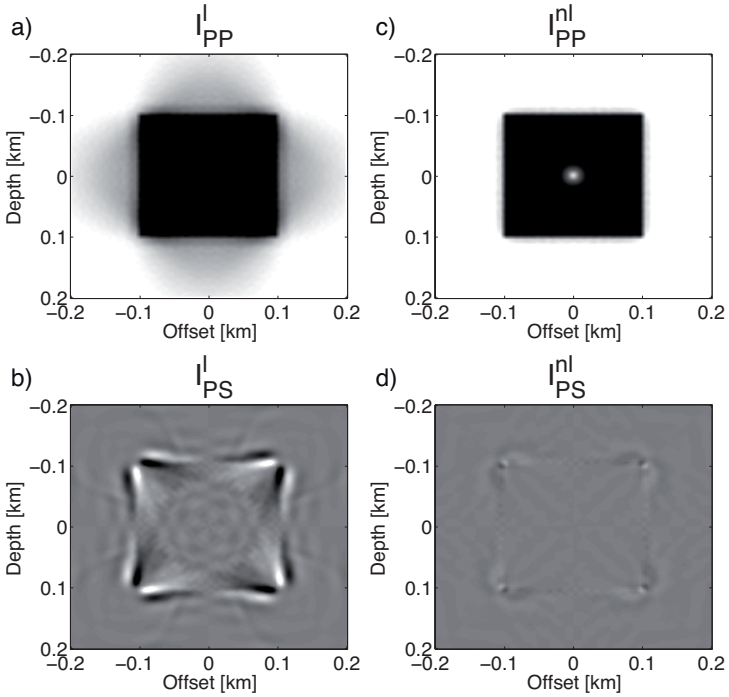

Figure 2.10: PP and PS images with complete illumination produced using a heuristically derived imaging condition in equation 2.17 that crosscorrelates P- and S-wave potentials separated in the subsurface after a full-wavefield extrapolation (Yan and Sava, 2008) on the left and our nonlinear imaging condition in equation 2.16 on the right. Images (a) and (c) are I_{PP}, whereas (b) and (d) are I_{PS}, where $I_{NM} = G^{S(\Phi,\Phi)}_{(M,N)}(\mathbf{x}_I, \mathbf{x}_I, t = 0)$. Acquisition geometry with complete illumination is shown in Figure 2.9 using all sources.

Partial illumination

We now use an experimental geometry that is closer to real seismic exploration where sources are located only on the earth's surface (i.e., one-sided illumination). The impact of such partial illumination is analysed by using only the top sources (closed stars in Figure 2.9) to image the target. The uneven illumination produces artefacts on both sides of and below the square for the heuristic PP image (Figure 2.11a). Although this breaks the power conservation that we use for the nonlinear imaging condition, the nonlinear image is still more accurate and the additional contribution of the interaction between scattered wavefields partially removes the artefacts (especially those on both sides of the square), and also identifies the point scatterer at its center (Figure 2.11c). Elastic imaging of PP waves thus shows a behavior similar to the acoustic case, even though we conjecture that now the nonlinear contribution focuses not only energy from single-mode multiply scattered waves but also P-wave energy from every kind of converted modes that have been multiply scattered. A more detailed analysis of nonlinear scattering-based purely acoustic imaging can be found in Fleury and Vasconcelos

(2012).

Imaging of PS-converted waves with an uneven illumination creates images (Figure 2.11b and d) with features that resemble other examples of elastic imaging presented in previous literature (e.g., Denli and Huang (2008); Lu et al. (2010)). Other than transmission artefacts, present also in the PP images and significantly attenuated by the application of a nonlinear imaging condition (Figure 2.11d), polarity reversals are evident. They are caused by the different polarizations of converted S-waves with respect to the incident P-wave. Therefore, the sign of the reflection coefficient of a converted P-to-S wave is a function of the P-wave incidence angle (Balch and Erdemir, 1994). Thus, when PS images with flipped polarities are stacked over all the shots, destructive interference occurs and degrades the migration results. This explains how the PS image stacks to exactly zero almost everywhere in Figure 2.10d; hence the image produced in Figure 2.11d only shows the structure because of the partial illumination. Thus, we observe that although the nonlinear imaging condition provides artefact reduction and illumination compensation for PP and PS images, it does not directly handle the polarity reversal occurring in PS images as is done in other imaging studies. So, to obtain an image using only PS data, further processing could be required before stacking over all the shots to avoid destructive interference as discussed in the next section.

2.5 Discussion

Multiply scattered and converted waves can be extremely sensitive to the properties of the medium through which they travel (Gret et al., 2006; Snieder, 2006b). They illuminate targets from a wider variety of directions than do primaries, and may be strongly affected by perturbations or errors in average velocity estimates because they have longer path lengths through the medium compared to primaries. This suggests that these waves could usefully be treated as signal rather than noise in imaging. Because multiply scattered waveforms are nonlinearly related to the scattering perturbations in a medium, nonlinear imaging methods are required to properly map their energy into models of subsurface scatterers.

Traditionally, a seismic image is obtained after three stages of processing: first, the smoothly varying part of the earth's velocity model (i.e., changes in properties over long length scales compared to the wavelength) is estimated by velocity analysis (Taner and Koehler, 1969; Neidell and Taner, 1971). Second, the initial velocity estimates are refined by traveltime tomography (Bishop, 1985; Stork, 1992) and/or waveform tomography (Pratt, 1999). Third, multiple-free seismic data are projected through the velocity model in an implementation of linearized imaging or migration. Discontinuities (i.e.,

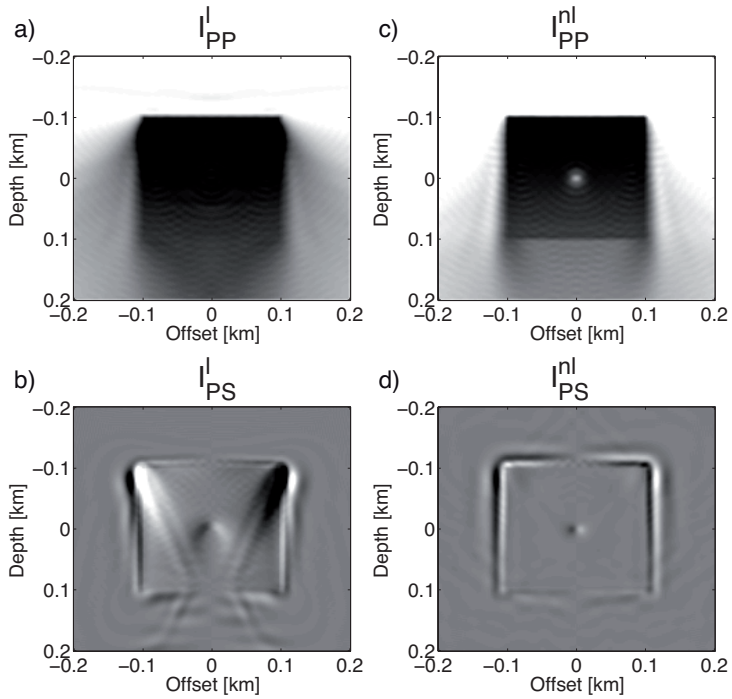

Figure 2.11: PP and PS images with only partial illumination produced using the heuristically derived imaging condition of (Yan and Sava, 2008) in equation 2.17 on the left, and our nonlinear imaging condition in equation 2.16 on the right. Images (a) and (c) are I_{PP}, whereas (b) and (d) are I_{PS}, where $I_{NM} = G^{S(\Phi,\Phi)}_{(M,N)}(\mathbf{x}_I, \mathbf{x}_I, t = 0)$. Acquisition geometry with partial illumination is shown in Figure 2.9 using only top sources.

changes in properties that occur over short length scales compared to the wavelength) are mapped only using linear interactions between the model and multiple-free data in this third stage. Nonlinear, scattering-based elastic imaging as presented herein can therefore be seen as a fourth stage of imaging, which does not currently exist in standard practice. It requires an a priori estimate of discontinuities, and it promises to sharpen images obtained after the usual three stages of imaging.

We have shown that the correlation-type representation theorem for perturbed elastic media with particle velocity (or P- and S-wave) sources and receivers, used to-date in seismic interferometry for constructing elastic scattered waves via crosscorrelations of observed wavefields for different types of media, can also be used to formulate new nonlinear elastic imaging methods. A first theorem derived above constructs any combination of P and S scattered waves propagating between two receiver locations, using multicomponent recordings for body-force density sources in every direction (so-called 9C data). In land acquisition, only the most advanced multicomponent seismic acquisition systems give a total of nine components for analysis, and for such data this new, exact expression for the reconstruction of full-wavefield P- and S-wave scattered fields

can be used for data analysis and imaging. On the other hand, common land seismic systems use only vertical vibrators and multicomponent receivers: in these cases, some terms within the reciprocity theorem must be discarded and only an approximate reconstruction can be accomplished. In addition, sources and receivers are usually constrained to the upper part of the bounding surface assumed in these theorems, leading to further approximations in their application. This should not be regarded as a weakness in the theory: on the contrary, the availability of this theory means that further studies and synthetic examples will help us to understand the effective contribution coming from the available data types, to test the potential improvements due to future new data types, and to be more aware of the errors that we should expect in the reconstructed Green's function due to the approximations that are necessarily employed.

Using reciprocity relations between only P- and S-wave Green's states, an alternative version of the representation theorem is proposed which is suitable for marine applications using ocean bottom systems. Because waves travel upward and downward at the source boundary (i.e., the medium is not homogeneous outside of ∂D as assumed in the P- and S-wave versions of the theory), the estimated scattered wavefield is only an approximated version of the true elastic response between two receivers at positions $\mathbf{x}_A$ and $\mathbf{x}_B$ along the seabed if the monopole approximation is used on the source side. This limitation can be overcome either by using source-side deghosting techniques, or by using the non-approximated theory with monopoles and dipoles sources (Robertsson et al., 2012). Similar expressions for full wavefields have been proposed by Halliday et al. (2012), developed using source-receiver interferometry (Curtis and Halliday, 2010) as a basis. They show how this form of interferometry can provide a generalized version of the $PP + PS = SS$ method introduced by Grechka and Tsvankin (2002). Combining our equations 2.11 or 2.13 with the theory of source-receiver interferometry could, for example, allow one to identify an expression that reconstructs the scattered SS response from PP and PS recordings. This again illustrates the value of having so comprehensive a theoretical understanding of potentially useful and applicable methods.

Elastic imaging is one of the main challenges in industrial geophysics, and from existing literature and practice it is still not clear which is the best way to use vector velocities or vector potentials to obtain an accurate image of the subsurface. An explicit relation between the recent practice of elastic wavefield-based seismic imaging and the theory of representation theorems has been derived in this chapter. Because representation theorems are exact expressions for wavefields, we conjecture that our equations 2.15 and 2.16 can guide future intuition to better combine scalar and vectorial potentials, obtained from different body-force density sources or P- and S-wave sources and separated in the subsurface. Thus, we identify full-wavefield imaging conditions that in the case of full

illumination from all directions produce true-amplitude images, accounting not only for every kind of nonlinear effect (e.g., multiples, and nonlinear scattering described by optical theorems — Snieder et al. (2008); Halliday and Curtis (2009); Margerin and Sato (2011)) but also for conversions occurring at different interfaces and diffractors. This is certainly true when an exact velocity model is used to obtain an estimate of scattering terms present in nonlinear imaging conditions; however, because the accuracy of these terms is affected when the velocity model is in error (short length-scale discontinuities will be mispositioned), further research into the sensitivity of imaging using multiple events in seismic data with respect to errors in the model estimate is necessary in future.

A simple synthetic example showed how the contribution coming from a previously published heuristically derived imaging condition (crosscorrelation between direct and scattered waves) and the nonlinear contribution from the autocorrelation of scattered waves are complementary. Combined together they create an image of the target that is consistent with the definition of the zero-time, scattered-wave response generated by a zero-offset pseudo experiment ($\tilde{G}^{S(\Phi,\Phi)}_{(M,N)}(\mathbf{x}_I, \mathbf{x}_I, t=0)$). Under ideal illumination (e.g., Figure 2.10), the nonlinear contribution for PP imaging removes artefacts otherwise observed around the perturbation and improves the definition of its edges. This term assumes more significance in PS imaging because it perfectly matches the contributions of linear interactions between reference and scattered waves and results in a final image that is perfectly null. Our definition of a reciprocity-based IC can explain this result, overcoming the intrinsic limitations of heuristically based ICs. The image is null because no conversion arises from a zero-offset experiment.

However, a zero time-lag and zero space-lag crosscorrelation IC creates a nonzero image for converted waves when evaluated using one-sided illumination. This fact has previously prevented a full understanding of the processes involved in converted wave imaging. Many attempts have been made to image reflectors and diffractors in the subsurface using converted-wave PS energy, and to mitigate the 'natural' destructive interference that occurs while stacking over all shots (see Yan and Sava (2008) and references therein). The fact that converted S-waves have different polarizations based on the P-wave incidence angle has led authors to preprocess (reverse) some converted wave polarizations before stacking. As a rule of thumb, we can assume that the polarity change occurs between either side of zero offset, and can be corrected by multiplying by -1 on one side of the shot position while keeping the other side unchanged (e.g., Figure 2.12). A more sophisticated procedure proposed by Balch and Erdemir (1994) corrects for this reversal in complex background velocity models by estimating the P-wave incidence angle for every image point using a ray approximation, and demonstrated its feasibility in a cross-borehole experiment. Denli and Huang (2008)

defined a wavefield-separation imaging condition based on the separation of wavefields with respect to a given direction using f-k filters after the elastic wavefields are downward propagated. Rosales et al. (2008) and Lu et al. (2010) suggested an approach in which the angle-domain common-image gathers (Sava and Fomel, 2003) are computed at every image point and the polarity is corrected in the angle domain before stacking. Finally, Du et al. (2012) introduced a sign factor to represent the polarity distribution of the S-wave component; this sign factor is computed using the energy flux density vector.

From our results above, we can conclude that if the zero-time scattered-wave response generated by zero-offset pseudo experiments is a good candidate to be used as an imaging condition for single-mode elastic waves, it may not be the best condition for imaging of converted-mode elastic waves. Every attempt to reduce or remove the destructive summation can now be seen as an attempt to obtain an image that does not resemble the zero-time, scattered-wave response generated by zero-offset pseudo experiments. We conjecture that a more appropriate context for imaging of converted waves is represented by extended images (Sava and Vasconcelos, 2011). The evaluation of an imaging condition at nonzero subsurface offset could effectively extract the energy coming from the conversion process at any discontinuity in the subsurface. Further studies will be carried out in this direction. Moreover, an IC that describes the received scattered P- or S-wave due to a co-located P- or S-wave source and receiver contradicts the fact that when using physical point sources the P- and S-waves can be defined only in the far-field. Although the application of divergence and curl to particle velocity recordings is still valid, the result of such an IC should be interpreted as a near-field projection of the far-field P- and S-waves crosscorrelated at the image point. For these reasons, only an elastic imaging condition based on the full elastic wavefield can truly express the local interaction in the subsurface, as if real unidirectional point force sources and particle velocity (or displacement) receivers were co-located at each image point. Such an IC can be obtained by writing equation 2.8 with $\mathbf{x}_I = \mathbf{x}_A = \mathbf{x}_B$ and integrating over frequencies (ω)

$$
\begin{aligned}
I^{nl}_{nm}(\mathbf{x}_I) &= \tilde{G}^{S(v,f)}_{(m,n)}(\mathbf{x}_I, \mathbf{x}_I, t=0) = 2\int_0^{+\infty} Re\{\tilde{G}^{S(v,f)}_{(m,n)}(\mathbf{x}_I)\}\,\mathrm{d}\omega \\
&- \int_0^{+\infty}\left(\oint_{\partial D}\{d^{S(v,h)}_{(n,ij)}(\mathbf{x}_I,\mathbf{x})G^{0(v,f)*}_{(m,i)}(\mathbf{x}_I,\mathbf{x}) + d^{S(v,f)}_{(n,i)}(\mathbf{x}_I,\mathbf{x})G^{0(v,h)*}_{(m,ij)}(\mathbf{x}_I,\mathbf{x})\}n_j\,\mathrm{d}^2\mathbf{x}\right)\mathrm{d}\omega \\
&- \int_0^{+\infty}\left(\oint_{\partial D}\{d^{0(v,h)}_{(n,ij)}(\mathbf{x}_I,\mathbf{x})G^{S(v,f)*}_{(m,i)}(\mathbf{x}_I,\mathbf{x}) + d^{0(v,f)}_{(n,i)}(\mathbf{x}_I,\mathbf{x})G^{S(v,h)*}_{(m,ij)}(\mathbf{x}_I,\mathbf{x})\}n_j\,\mathrm{d}^2\mathbf{x}\right)\mathrm{d}\omega \\
&- \int_0^{+\infty}\left(\oint_{\partial D}\{d^{S(v,h)}_{(n,ij)}(\mathbf{x}_I,\mathbf{x})G^{S(v,f)*}_{(m,i)}(\mathbf{x}_I,\mathbf{x}) + d^{S(v,f)}_{(n,i)}(\mathbf{x}_I,\mathbf{x})G^{S(v,h)*}_{(m,ij)}(\mathbf{x}_I,\mathbf{x})\}n_j\,\mathrm{d}^2\mathbf{x}\right)\mathrm{d}\omega.
\end{aligned}
\tag{2.18}
$$

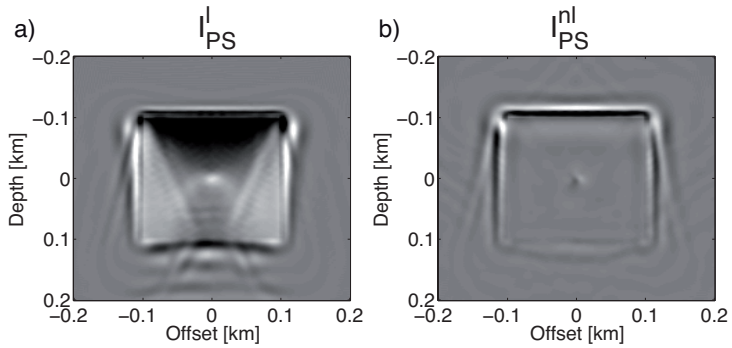

Figure 2.12: PS images with only the partial illumination in Figure 2.9 when polarity correction is applied before stacking for (a) linear and (b) nonlinear imaging. Nonlinear terms still contribute to reduce artefacts around the interfaces, and to sharpen up the entire image.

This imaging condition will be the subject of future investigation.

2.6 Conclusion

In this chapter, a correlation-type representation theorem for perturbed elastic media is derived. The interior workings of the elastic scattering representation theorem is illustrated using a simple elastic isotropic example through a stationary-phase analysis. We then derive alternative versions of this scattered-wave theorem for the cases where P- and S-wave sources and/or receivers are available. We suggest potential applications of these formulae in land and marine seismic acquisition.

Starting from a representation theorem with P- or S-wave receivers, we have proposed two nonlinear, true-amplitude imaging conditions. These account for multiply scattered waves and every kind of wavefield conversion in the subsurface, facilitating a fourth stage of nonlinear elastic imaging, when an estimate of the velocity model with short-scale discontinuities has already been provided by the usual three stages of velocity analysis, waveform tomography, and linear migration.

We have also shown that the imaging condition with P- or S-wave sources on the Earth's surface can be turned into a previously published elastic imaging condition that crosscorrelates pure modes separated in the subsurface after a fullwavefield extrapolation. However, this is only possible if our imaging conditions are severely approximated. Thus, our new full wavefield ICs are shown to be theoretically exact versions of the previous heuristically derived ICs. This result creates an explicit link between theory of seismic interferometry and elastic seismic imaging, and sheds new light on how to create true-amplitude elastic images.

3

Directional and modally-selective elastic wavefield extrapolation

A central component of imaging methods is the receiver-side wavefield backpropagation or extrapolation in which the wavefield from a physical source scattered at any point in the subsurface is estimated from data recorded by receivers located near or at the Earth's surface. Elastic reverse-time migration usually accomplishes wavefield extrapolation by simultaneous reversed-time injection of the particle displacements (or velocities) recorded at each receiver location into a wavefield modelling code. Here, we formulate an exact integral expression based on reciprocity theory that uses a combination of velocity-stress recordings and quadrupole-dipole backpropagating sources, rather than the commonly used approximate formula involving only particle velocity data and dipole backpropagating sources. The latter approximation results in two types of nonphysical waves in the scattered wavefield estimate: first, each arrival contained in the data is injected upward and downward rather than unidirectionally as in the true time-reversed experiment; second, all injected energy emits compressional and shear propagating modes in the model simulation (e.g., if a recorded P-wave is injected, both P and S propagating waves result). These artefacts vanish if the exact wavefield extrapolation integral is used. Finally, we show that such a formula may be suitable for extrapolation of ocean-bottom 4C data: when the fluid-solid boundary conditions hold at the seabed, the data recorded in standard surveys are sufficient to perform backpropagation using the exact equations. Synthetic examples provide numerical evidence of the importance of correcting such errors.

3.1 Introduction

Acquisition of the seismic wavefield directly at the seabed provides the only possible direct recordings of shear waves in marine seismics. Modern acquisition systems make use of 4C sensors consisting of a multicomponent geophone and a hydrophone, to record the elastic wavefield in the solid seabed and the acoustic wavefield in the water just above the seabed. They are usually connected to each other by, and are housed within, a so-called ocean-bottom cable (OBC), which transmits data to a recording system on a boat using wired telemetry, while a second boat fires a marine source around and over the sensors (Berg et al., 1994; Amal et al., 2005). Alternatively, remotely operated vehicles can be used to deploy individual sensor nodes (ocean-bottom node, OBN) on the seafloor allowing more flexible acquisition geometries (Ronen et al., 2003; Granger et al., 2005). Recording data in this way has certain advantages over conventional marine acquisition where streamers of hydrophones and multicomponent accelerometers are towed behind a vessel. Ocean-bottom seismics can in principle be used to acquire data in areas congested by platforms or other obstacles at the sea surface, to provide wide-azimuth illumination, improve repeatability, collect shear-wave (S-wave) as well as acoustic (P-wave) energy, and achieve higher resolution due to the shorter wavelengths of S-waves compared to P-waves (Maver, 2011).

Although the P-wave energy is often easier than S-waves to generate, record, and process in marine seismics, S-waves can provide additional information about the subsurface. Imaging with multicomponent seismic data can better describe the physics of wave propagation, and resulting seismic images more accurately characterize the subsurface (Zhu et al., 1999; Gaiser et al., 2001; Simmons and Backus, 2003; Stewart et al., 2003; Ravasi and Curtis, 2013b). Pure-mode (SS) or converted-mode (PS/SP) shear-wave images have many applications: for example, they provide useful information to discriminate gas-related from nonhydrocarbon-related reflection amplitude anomalies (Hughes et al., 2010), image through gas clouds where the P-wave signal is attenuated (Thomsen et al., 1997; Knapp et al., 2001), estimate density (Leiceaga et al., 2010), improve the ability to characterize lithology (Shahraeeni and Curtis, 2011; Shahraeeni et al., 2012), and detect fractures (Li, 1998).

Different schemes used for processing ocean-bottom data can be classified by the type of information used at the imaging stage to estimate the subsurface structure. The traditional way is to remove all free-surface multiples and image with only primary reflections (Yilmaz, 1989). A technique known as PZ summation (Barr and Sanders, 1989; Soubaras, 1996; Schalkwijk et al., 1999) attenuates strong free-surface multiples by combining the geophone and hydrophone recordings: it exploits the polarity dif-

ference between an isotropic measurement (pressure) and a directional measurement (velocity) to eliminate the receiver ghost and the water-column reverberations. A more sophisticated method is to deconvolve the up- and downgoing wavefields (Sonneland and Berg, 1987; Amundsen, 2001; Wang et al., 2009). This provides receiver- and source-side free-surface multiple attenuation but also deghosting and signature deconvolution in layered and complex media, although it puts strict requirements on the spatial density of source and receiver locations. This latter method has the further advantage that it can also be applied to the horizontal components and therefore allows a complete free-surface demultiple method for converted-wave (PS) data.

Alternatively, free-surface multiples (and additionally, internal multiples) can be treated as a useful signal and migrated together with the primaries: because they are formed by the same source signal as the primaries but travel along different paths through the medium, they contain information not contained in the primaries. Several authors have used the receiver ghost for migration of ocean-bottom data (Godfrey et al., 1998; Ronen et al., 2005; Grion et al., 2007; Dash et al., 2009). Muijs et al. (2007) make an early attempt to image using primary and free-surface multiples together: the final image however contains crosstalk artefacts; they are caused by interference of up- and downgoing waves not associated with the same subsurface reflector. Wong et al. (2010) define a joint, linear least-squares inversion framework that can migrate primary and ghost signals together, combining their structural information free from crosstalk. This method was then modified to account for the subsequent higher order multiples (Wong et al., 2011). Note that all of these techniques require the data to be decomposed into up- and downgoing components.

A distinction may also be made between methods that migrate (or assume the recorded wavefield comprises) only P-waves and those that image using the full elastic wavefield. Two possible avenues exist to make use of the extra elastic wavefield information contained in multicomponent ocean-bottom data at the imaging stage. The first is borrowed from the acoustic case: it uses a purely scalar wave equation for extrapolation. For such methods, wavefield decomposition into scalar and vector potentials is performed before extrapolation; the success of such a separation heavily depends on the estimation of ocean-bottom elastic properties, which is often inaccurate. After separation, up- and downgoing P- and S-wavefields are processed separately as scalar wavefields, using existing processing algorithms (multiple elimination, migration) developed for acoustic wavefields. The main disadvantage of such methods is that the wavefield is treated as purely P or purely S during extrapolation; thus, conversions that may occur during propagation between any image point and the receivers are ignored. The other avenue is to treat data in a vector form and use fully elastic RTM (Chang and McMechan, 1986, 1994; Sun and McMechan, 1986; Yan and Sava, 2008). Particle displacement (or

velocity) recordings are usually directly injected as a boundary condition in a numerical solution to the elastic wave equation; the separation into P- and S-waves is then performed just before the imaging condition is applied. Note that while accounting for all types and orders of conversions during extrapolation, this approach is however more sensitive to velocity errors (Wapenaar et al., 1991).

In this chapter, a more accurate boundary condition is proposed for wavefield injection, which accounts for velocity and stress or strain recordings. We begin by deriving an exact wavefield extrapolation integral expression based on reciprocity theory that uses a combination of velocity-stress recordings and quadrupole-dipole backpropagating sources (i.e., it performs tensorial wavefield extrapolation). This allows the extrapolation of receiver-side wavefields without the introduction of nonphysical waves that arise when wavefield extrapolation is accomplished by direct injection of particle velocity components at the receiver locations (vectorial wavefield extrapolation — Yan and Sava (2007)). Then we discuss how our tensorial wavefield extrapolation integral may become practical for backpropagation of recorded ocean-bottom 4C data: we show that, in the presence of hard seabed, only particle velocity and pressure recordings are required over the available portion of the seabed because of the incorporation of the physical boundary conditions that govern the fluid-solid boundary. Numerical examples are used to illustrate the advantages of tensorial wavefield extrapolation over common-practice vectorial extrapolation.

3.2 Elastic wavefield extrapolation

To evaluate any of the imaging conditions in Chapter 2, source and receiver wavefields must first be computed. Although the source-side wavefields (e.g., $G^{0/S(\Phi,\Phi)}_{(M,P)}(\mathbf{x}_I,\mathbf{x}_S)$) are easily obtained by forward modelling using the reference/full model of the subsurface and the survey's known acquisition geometry (usually, a P-wave source and vector potential receivers at $\mathbf{x}_I$ in the subsurface), the receiver-side wavefields (e.g., $d^{0/S(\Phi,\Phi)}_{(N,P)}(\mathbf{x}_I,\mathbf{x}_S)$) extrapolated to point $\mathbf{x}_I$ are not directly available. An accurate estimate of these wavefields is fundamental for the creation of an image without artefacts. In an ocean-bottom acquisition setup, this estimate is obtained by extrapolating the physically recorded data given by P-wave sources towed below the sea-air free-surface interface at position $\mathbf{x}_S$ and observed at all available receiver locations $\mathbf{x}_R$ along the seabed, backward in time to any desired subseabed image point $\mathbf{x}_I$ (Figure 3.1). Divergence and curl operators are then applied to the extrapolated wavefields to extract P- and S-waves in the subsurface.

In accord with the theory of elastic reciprocity in Wapenaar and Fokkema (2006), we now provide an exact integral expression for wavefield extrapolation in the form of boundary integrals controlled by recorded elastic data. This reciprocity-based wavefield extrapolation can be combined with the imaging conditions in Chapter 2 to define a theoretically exact source-receiver integral framework for imaging of land or ocean-bottom elastic data, as discussed in Chapter 5. This provides the basis for studies of new acquisition designs because it defines precisely the information that any proposed survey design would and would not provide about any image point in the subsurface.

As derived in Appendix A, and closely connected with the work of Mittet (1994), an exact integral expression for elastic receiver-side extrapolation with monopole sources and velocity-stress receivers is given in the frequency domain by

$$
\begin{aligned}
&d^{S(\Phi,\Phi)}_{(N,K)}(\mathbf{x}_I,\mathbf{x}_S) = \\
&-\oint_{\partial D_R}\{d^{S(\tau,\Phi)}_{(ij,K)}(\mathbf{x}_R,\mathbf{x}_S)G^{0(\Phi,f)*}_{(N,i)}(\mathbf{x}_I,\mathbf{x}_R)+d^{S(v,\Phi)}_{(i,K)}(\mathbf{x}_R,\mathbf{x}_S)G^{0(\Phi,h)*}_{(N,ij)}(\mathbf{x}_I,\mathbf{x}_R)\}n_{R_j}\,\mathrm{d}^2\mathbf{x}_R \\
&-\oint_{\partial D_R}\{d^{(\tau,\Phi)}_{(ij,K)}(\mathbf{x}_R,\mathbf{x}_S)G^{S(\Phi,f)*}_{(N,i)}(\mathbf{x}_I,\mathbf{x}_R)+d^{(v,\Phi)}_{(i,K)}(\mathbf{x}_R,\mathbf{x}_S)G^{S(\Phi,h)*}_{(N,ij)}(\mathbf{x}_I,\mathbf{x}_R)\}n_{R_j}\,\mathrm{d}^2\mathbf{x}_R,
\end{aligned}
\tag{3.1}
$$

where G terms represent wavefield propagators from receivers $\mathbf{x}_R$ to subsurface image points $\mathbf{x}_I$, d terms on the right hand side are recorded data from sources $\mathbf{x}_S$ to receivers $\mathbf{x}_R$, and the d term on the left hand side is the receiver wavefield used in Chapter 2 to define different imaging conditions. Moreover, we recall from the previous chapter that superscripts v and τ represent particle velocity and stress recordings and subscripts i/ij identify the i-th/ij-th component of the particle velocity vectors and stress tensors, respectively. Superscripts f and h indicate external volume force (dipole) sources and external deformation rate (quadrupole) sources, respectively, while subscripts i/ij identify the i-th/ij-th component of the external volume force vectors and external deformation rate tensors. Finally, Φ refers to potentials and is associated with subscript capital letters K and N, each of which can be substituted by P or S_k to identify P- or S-wave potentials.

The subscript K can be replaced by P when only P-wave sources are used in the physical (e.g., marine seismic) experiment:

$$
\begin{aligned}
&d^{S(\Phi,\Phi)}_{(N,P)}(\mathbf{x}_I,\mathbf{x}_S) = \\
&-\oint_{\partial D_R}\{d^{S(\tau,\Phi)}_{(ij,P)}(\mathbf{x}_R,\mathbf{x}_S)G^{0(\Phi,f)*}_{(N,i)}(\mathbf{x}_I,\mathbf{x}_R)+d^{S(v,\Phi)}_{(i,P)}(\mathbf{x}_R,\mathbf{x}_S)G^{0(\Phi,h)*}_{(N,ij)}(\mathbf{x}_I,\mathbf{x}_R)\}n_{R_j}\,\mathrm{d}^2\mathbf{x}_R \\
&-\oint_{\partial D_R}\{d^{(\tau,\Phi)}_{(ij,P)}(\mathbf{x}_R,\mathbf{x}_S)G^{S(\Phi,f)*}_{(N,i)}(\mathbf{x}_I,\mathbf{x}_R)+d^{(v,\Phi)}_{(i,P)}(\mathbf{x}_R,\mathbf{x}_S)G^{S(\Phi,h)*}_{(N,ij)}(\mathbf{x}_I,\mathbf{x}_R)\}n_{R_j}\,\mathrm{d}^2\mathbf{x}_R.
\end{aligned}
$$

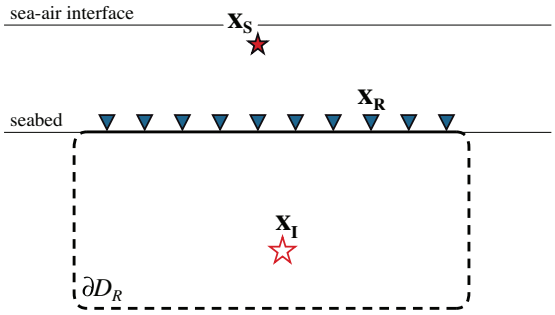

Figure 3.1: Geometry used for reciprocity-based wavefield extrapolation. A closed receiver boundary ∂D_R surrounds an imaginary source at the image point $\mathbf{x}_I$ in the subsurface, while the physical source $\mathbf{x}_S$ is located outside ∂D_R. Receivers actually used in usual acquisition scenarios are represented by blue triangles.

(3.2)

A linearized expression for Born imaging is obtained by discarding the terms describing nonlinear interaction between the recorded data and the scattered backpropagators (second line of equation 3.2), because these require velocity/density models with high spatial resolution to be computed in advance of imaging, which is usually not possible:

$$d^{S(\Phi,\Phi)}_{(N,P)}(\mathbf{x}_I,\mathbf{x}_S) \approx$$
$$-\oint_{\partial D_R}\{d^{S(\tau,\Phi)}_{(ij,P)}(\mathbf{x}_R,\mathbf{x}_S)G^{0(\Phi,f)*}_{(N,i)}(\mathbf{x}_I,\mathbf{x}_R)+d^{S(v,\Phi)}_{(i,P)}(\mathbf{x}_R,\mathbf{x}_S)G^{0(\Phi,h)*}_{(N,ij)}(\mathbf{x}_I,\mathbf{x}_R)\}n_{R_j}\,\mathrm{d}^2\mathbf{x}_R. \tag{3.3}$$

The evaluation of this integral expression requires and uses knowledge of particle velocity data in $d^{S(v,\Phi)}_{(i,P)}(\mathbf{x}_R,\mathbf{x}_S)$ and the stress tensor data in $d^{S(\tau,\Phi)}_{(ij,P)}(\mathbf{x}_R,\mathbf{x}_S)$ at the receiver locations (hence we call this *tensorial* wavefield extrapolation). These recordings are injected separately into the reference medium, respectively as deformation rate density sources ($G^{0(\Phi,h)}_{(M,ij)}(\mathbf{x}_I,\mathbf{x}_R)$ — the h backpropagator) and volume force density sources ($G^{0(\Phi,f)}_{(M,i)}(\mathbf{x},\mathbf{x}_R)$ — the f backpropagator). Finally, the results are summed together. Note that physical sources of such types are not required (see below): they must only be implemented numerically in the elastic modelling code used for extrapolation.

The main limitation at this point is the requirement that the stress tensor is known along the receiver boundary. When dense arrays of velocity receivers are available (e.g., on land), spatial derivatives of velocity can be calculated, approximating temporal derivatives of strain (Robertsson and Muyzert, 1999). If near-surface material properties can be estimated accurately it is conceivable to estimate stress from strain (e.g., Curtis and Robertsson (2002)). However, in current practice, only particle velocity data are used (stress is ignored). Velocity data are then directly injected as a boundary condition at receiver locations (*vectorial* wavefield extrapolation). This procedure can be

expressed in an integral form as

$$d^{S(\Phi,\Phi)}_{(N,P)}(\mathbf{x}_I,\mathbf{x}_S) \approx \oint_{\partial D_R} \{d^{S(v,\Phi)}_{(i,P)}(\mathbf{x}_R,\mathbf{x}_S) G^{0(\Phi,f)*}_{(N,i)}(\mathbf{x}_I,\mathbf{x}_R)\} n_{R_j}\, \mathrm{d}^2\mathbf{x}_R. \tag{3.4}$$

Equation 3.4 reveals the simplified nature of common-practice wavefield extrapolation with respect to the exact expression in equation 3.1, the best-case nonlinear expression in equation 3.2, and linearized expression in equation 3.3, all of which employ the full velocity-stress information in elastic waves.

Such a formula (equation 3.4) is not really an approximation to the exact extrapolation integrals. Rather, it is a heuristic scheme used to estimate the receiver wavefield, which contradicts the theory of reciprocity. Thus, in spite of being kinematically correct, it does not effectively represent the scattered Green's function between a physical source $\mathbf{x}_S$ and any image point $\mathbf{x}_I$ at all. This results in two types of nonphysical waves: first, during backpropagation each arrival contained in the data is injected upward and downward rather than only downward as in the true time-reversed experiment. Second, all injected energy emits compressional and shear propagating modes (e.g., even if only a recorded P-wave is injected, P and S propagating modes result and are backpropagated to any image point $\mathbf{x}_I$).

Application to ocean-bottom 4C data

At first glance, our tensorial wavefield extrapolation integral seems not to be suitable for practical applications because it requires additional information, such as stress recordings, which are not easily available. However, we now show that this method is applicable to ocean-bottom seismic acquisition systems that use 4C sensors to measure the fluid's pressure $p(\mathbf{x}_R,t)$ and the solid's particle velocity vector $\mathbf{v}(\mathbf{x}_R,t)$ (or displacement vector $\mathbf{u}(\mathbf{x}_R,t)$) at the seabed. In fact, under the assumption that the seabed can be approximately defined as a horizontal interface ($\mathbf{n}=\mathbf{i_z}$) between the fluid and solid layers as in Figure 3.2 (although a similar derivation can be obtained for any shape of seabed), only knowledge of the particle velocity vector and vertical traction vector is required to perform tensorial wavefield extrapolation (equations 3.2 and 3.3):

$$\begin{aligned} \mathbf{v}(\mathbf{x}_R,t) &= (v_x(\mathbf{x}_R,t), v_y(\mathbf{x}_R,t), v_z(\mathbf{x}_R,t)) \\ \boldsymbol{\tau}_z(\mathbf{x}_R,t) &= (\tau_{xz}(\mathbf{x}_R,t), \tau_{yz}(\mathbf{x}_R,t), \tau_{zz}(\mathbf{x}_R,t))\,. \end{aligned} \tag{3.5}$$

The boundary condition at the fluid-solid interface dictates (1) continuity of the normal component of particle velocity, (2) the normal component of the traction in the solid equals the negative of the acoustic pressure in the fluid, and (3) the tangential

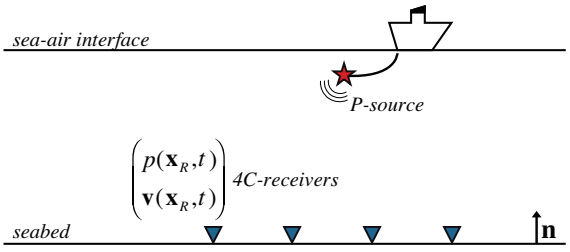

Figure 3.2: Acquisition of ocean-bottom 4C data. Four component sensors, consisting of a multicomponent geophone and a hydrophone, are placed along the seabed to record the full elastic wavefield. A boat moves over the sea surface, firing a compressional source at regular intervals. The sea-air interface generates source and receiver ghosts and higher order waterborne multiples. The seabed (liquid-solid interface) is responsible for the conversion process arising when an incident P-wave is transmitted, reflected, and converted into a shear wave.

components of the traction in the solid vanish. These constraints may be expressed as:

$$\begin{aligned}
\tau_{xz}(\mathbf{x}_R,t) &= 0 \\
\tau_{yz}(\mathbf{x}_R,t) &= 0 \\
\tau_{zz}(\mathbf{x}_R,t) &= -p(\mathbf{x}_R,t).
\end{aligned} \tag{3.6}$$

Assuming that the scattered component of the recorded wavefields can be extracted from the original recordings, 4C data therefore provide all information needed for the implementation of equation 3.2, which we can restate using only the data that are usually recorded on existing seabed systems:

$$\begin{aligned}
&d^{S(\Phi,\Phi)}_{(N,P)}(\mathbf{x}_I,\mathbf{x}_S) = \\
&\oint_{\partial D_R}\{d^{S(p,\Phi)}_{(-,P)}(\mathbf{x}_R,\mathbf{x}_S)G^{0(\Phi,f)*}_{(N,z)}(\mathbf{x}_I,\mathbf{x}_R) - d^{S(v,\Phi)}_{(z,P)}(\mathbf{x}_R,\mathbf{x}_S)G^{0(\Phi,h)*}_{(N,zz)}(\mathbf{x}_I,\mathbf{x}_R)\}\,\mathrm{d}^2\mathbf{x}_R \\
+&\oint_{\partial D_R}\{d^{(p,\Phi)}_{(-,P)}(\mathbf{x}_R,\mathbf{x}_S)G^{S(\Phi,f)*}_{(N,z)}(\mathbf{x}_I,\mathbf{x}_R) - d^{(v,\Phi)}_{(z,P)}(\mathbf{x}_R,\mathbf{x}_S)G^{S(\Phi,h)*}_{(N,zz)}(\mathbf{x}_I,\mathbf{x}_R)\}\,\mathrm{d}^2\mathbf{x}_R.
\end{aligned} \tag{3.7}$$

Thus, provided the fluid-solid boundary conditions hold at the seabed (at least in cases with a lithified seabed capable of supporting shear stress), all of the above results and learning pertains to standard seabed 4C sensors. In what follows, we provide synthetic examples that illustrate these points, and which thus demonstrate the advantages of tensorial extrapolation over vectorial extrapolation. In Chapter 7 we will instead test the validity of equation 3.7 under the acoustic assumption (Vasconcelos, 2013) on a OBC field dataset.

3.3 Examples

Elastic RTM of a single scatterer

Consider a single point scatterer embedded in a constant background medium ($V_P = 2600\,m/s$, $V_S = 1400\,m/s$, and $\rho = 1000\,kg/m^3$) at position $\mathbf{x}_{scatt} = (1000, 600)\,m$. A density perturbation of $\Delta\rho = 600\,kg/m^3$ is defined in the otherwise homogeneous density model (Figure 3.3), and an absorbing boundary condition is applied at the top of the model to prevent the construction of free-surface multiples. Such data are usually referred to as Born data; in practice, such data are the result of preprocessing steps that suppress source-side ghosts, receiver-side ghosts, and multiple scattering in the recorded data. A physical compressional source is fired at $\mathbf{x}_S = (1400, 50)\,m$, and a horizontal array of receivers is placed at $z_R = 300\,m$ with inter-receiver spacing of $dx_R = 2\,m$. The direct arrival is subtracted from the recorded data at each receiver location to give scattered fields $d^{S(v,\Phi)}_{(i,P)}(\mathbf{x}_R, \mathbf{x}_S)$ and $d^{S(\tau,\Phi)}_{(ij,P)}(\mathbf{x}_R, \mathbf{x}_S)$ only. The reference field and the full (reference plus scattered) field are computed using a 2D staggered grid elastic finite-difference algorithm (Virieux, 1986).

Particle velocity recordings are then injected along the receiver array, and the wavefield back-propagation procedure is carried out according to equation 3.4 using the homogeneous density model as the reference medium for wave propagation. Scalar and vector potentials may be recorded at any image point and crosscorrelated with the source wavefield potentials as required by the linearized imaging condition in equation 2.17. The receiver-side wavefield is then also estimated using the more accurate tensorial wavefield extrapolator (equation 3.3), and the same linearized imaging condition is used to produce a second set of elastic images.

PP imaging

Figure 3.4 shows a series of snapshots of estimated scattered P-wavefields next to the modelled scattered P-wave wavefield $d^{S(\Phi,\Phi)}_{(P,P)}(\mathbf{x}_I, \mathbf{x}_S)$. Note that although the extrapolation calculation is always carried out in reverse time, we prefer to show the wavefields according to the true propagation time in the field experiment. The left plots would (and can) be obtained exactly with a full boundary of receivers plus nonlinear tensorial extrapolation in equation 3.2. The middle column of plots is compromised by data only being recorded on part of the receiver boundary and by the use of the linearized tensorial extrapolation (equation 3.3) — in other words, by the one-sided illumination of the subsurface and by knowledge of only the background velocity model as is usually the case in seismic imaging. The right plots are further compromised by using the

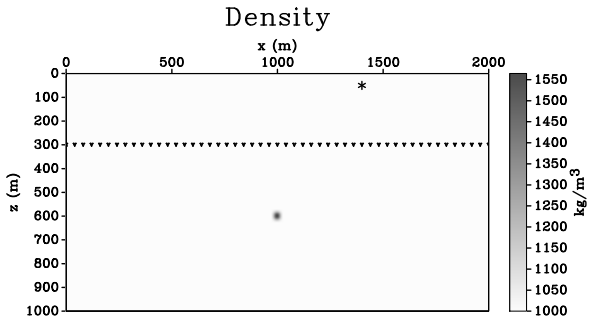

Figure 3.3: Elastic RTM geometry. A single point scatterer (gray spot in the density grid) is embedded in a homogeneous medium with velocities $V_P = 2600\,m/s$, $V_S = 1400\,m/s$, and density $\rho = 1000\,kg/m^3$. The scatterer represents a positive density perturbation of $\Delta\rho = 600\,kg/m^3$. The star indicates the location of a physical source, and every tenth receiver is marked by a triangle. Particle velocity recordings are injected at each receiver location in the wavefield extrapolation step.

usual vectorial extrapolator (equation 3.4). Comparing these plots, only the upper part of the extrapolated wavefields is obtained in seismic extrapolation because the receiver array is only available at the seabed, rather than being an ideal enclosing array. In addition, the use of only particle velocity measurements in the usual erroneous method of wavefield extrapolation in the right plots causes two types of nonphysical energy: 1) pervasive injection of down- and upgoing waves at the receiver arrays and 2) a second circular waveform that will collapse at the receiver array after the physical upgoing wave collapses. Both of these features create nonphysical wavefields at image points.

Nonphysical energy of type 1 is the same artefact that arises in the acoustic case when pressure recordings are used for wavefield extrapolation rather than the full vector acoustic (pressure plus particle velocity) data — see Vasconcelos (2013). Nonphysical energy of type 2 is peculiar to the elastic case and is due to injection in the model of the velocity displacement recordings through volume force sources; this emits both P- and S-wave propagating modes for each individual P- or S-wave arrival (Yan and Sava, 2007). In this specific case, S-wave energy, as is present in the particle velocity recordings, is erroneously injected as P-wave energy along the receiver array, causing the second circular wave in the right plots of Figure 3.4.

Tensorial versus vectorial wavefield extrapolation integrals analysis.
We now compare the tensorial integral expression for wavefield backpropagation of elastic Born data (equation 3.3) with the commonly used vectorial version (equation 3.4), and support an explanation of the nature of nonphysical waves arising in the latter. We borrow the stationary-phase approach (Snieder, 2004), commonly used to analyse seismic interferometry: this approach highlights where, along the receiver boundary

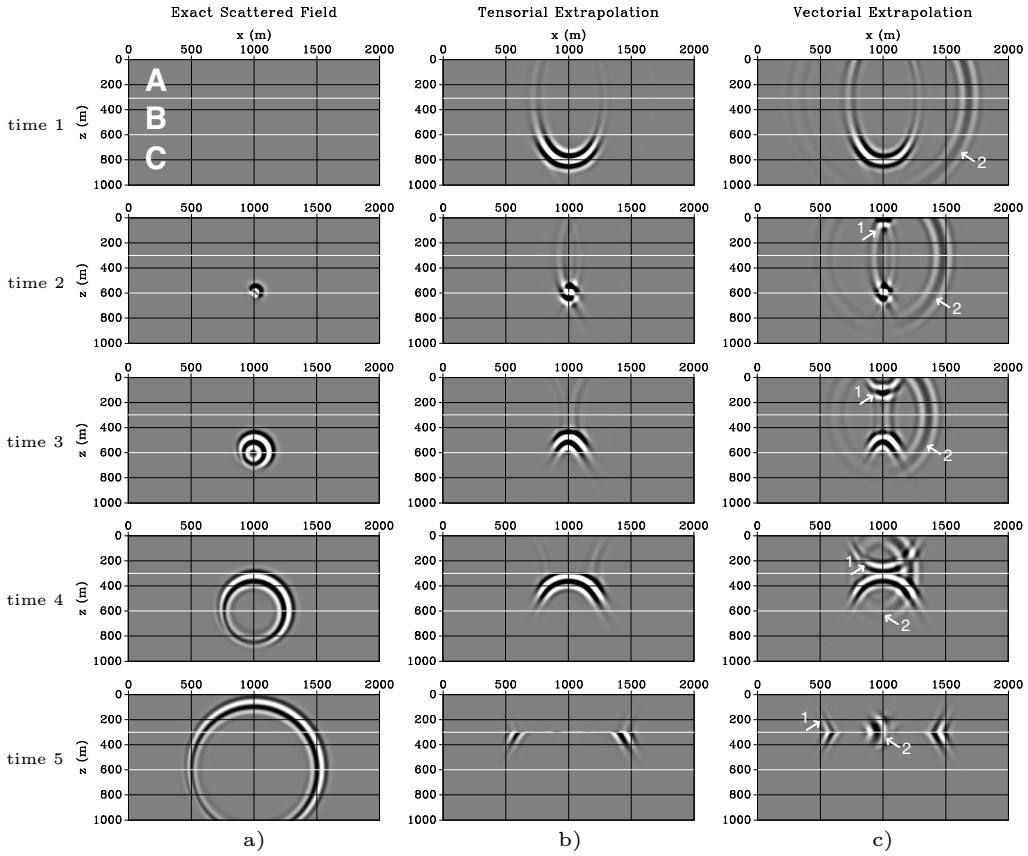

Figure 3.4: Series of snapshots of the (a) exactly modelled (b) tensorially, and (c) vectorially back-extrapolated receiver-side P-wavefield $d^{S(\Phi,\Phi)}_{(P,P)}(\mathbf{x}_I, \mathbf{x}_S)$ for the point scatterer example (Figure 3.3). Wavefields from the exact case (a) recorded at receivers in Figure 3.3 are injected at receiver locations in cases (b) and (c), and backpropagated toward earlier times (upward in this Figure). White lines at depths $z = z_R = 300m$ and $z = z_{scatt} = 600m$ define the boundaries of three regions A, B, and C of the subsurface domain where the exact, vectorial, and tensorial receiver wavefields show different features. Particularly, white arrows indicate nonphysical waves due to approximations made in the vectorial wavefield extrapolation integral (equation 3.4); types 1 and 2 are explained in the text. These nonphysical waves do not arise when the exact wavefield extrapolation integral is carried out.

∂D_R, the recorded data and the backpropagators interfere constructively and contribute to the creation of either physical or nonphysical waves in the receiver-side extrapolated wavefield. Associated boundary receivers are called stationary receivers.

The single point-scatterer example allows for the identification of three different regions of the subsurface domain (Figure 3.4): region A is located above the receiver array ($z \leq z_R$), region B is bounded between the receiver array and the scatterer ($z_R \leq z \leq z_{scatt}$), while region C is located below the scatterer depth ($z \geq z_{scatt}$). Although the receiver boundary is incomplete and the crosscorrelation between the full recorded data and the scattered receiver propagator (the second line of equation 3.2, which

is nonlinear with respect to the scattered wavefield) is not performed, the tensorial wavefield backpropagation of elastic data generates an almost correct receiver wavefield in the region between the receiver boundary and the scatterer. The stationary point on the receiver array that is needed to construct the scattered P-wave between the physical source and $\mathbf{x}_I$ is, in fact, located on the available portion of the receiver boundary. The corresponding wavefield is constructed by crosscorrelating the scattered recorded data and the reference receiver propagator (equation 3.3). However, when components of the stress tensor used for the evaluation of equation 3.3 (terms with superscript ij) are substituted (approximated) by the 'corresponding' components of the particle velocity vector (equation 3.4), the receiver wavefield shows two nonphysical waves above the receiver line and another nonphysical event below the scatterer.

Nonphysical event 1 (indicated in Figure 3.4) arises when the scattered P-wave reaches the receiver array; it is also backpropagated (erroneously) upward. Such an artefact therefore occurs only in the portion of the model above the receiver array in this case, due to the absorbing boundary condition at the top of the model. Given a generic point $\mathbf{x}_A$ in region A, this backpropagated wave reaches that location at a time equal to the time that would be obtained by effectively crosscorrelating the P-wave scattered data $d^{S(\Phi,\Phi)}_{(P,P)}(\mathbf{x}_R,\mathbf{x}_S)$ and the P-wave reference propagator $G^{0(\Phi,\Phi)}_{(P,P)}(\mathbf{x}_A,\mathbf{x}_R)$ because crosscorrelation subtracts the phase of one wavefield from another, the arrival time of the erroneous wavefield is the difference between the traveltimes of the two correlated wavefields (Figure 3.5a). An explanation of the symmetry between the backpropagation path and the physical one with respect to the receiver array comes from the fact that all the recorded energy focuses at two subsurface points, the first being at the actual scatterer location and the second being the symmetric reflection of that location through the receiver array (see Figure 3.4c at time 2). The same analysis can be carried out for any point contained in the gray cone in Figure 3.5a to identify first the corresponding stationary receiver and also the time at which this nonphysical wavefront reaches that point. Nonphysical event 2 occurs throughout the subsurface. It is caused by the crosscorrelation between the S-wave scattered data $d^{S(\Phi,\Phi)}_{(S,P)}(\mathbf{x}_R,\mathbf{x}_S)$ due to a conversion at the density perturbation and recorded at the receiver arrays, and the P-wave reference propagator $G^{0(\Phi,\Phi)}_{(P,P)}(\mathbf{x}_B,\mathbf{x}_R)$. Figure 3.5b explains the creation of this event for a point $\mathbf{x}_B$ located in region B using a stationary-phase approach.

Correctly combining velocity-stress recordings and quadrupole-dipole backpropagating sources is the key component to obtain a receiver wavefield deprived of the above two types of spurious events. Figure 3.6 shows how the scattered P-wavefield between a physical source and any point in the subsurface $d^{S(\Phi,\Phi)}_{(M,P)}(\mathbf{x}_I,\mathbf{x}_S)$ is created in equation 3.3 by summing the integral involving stress data and volume force density sources (Figure 3.6a) and the integral involving velocity data and deformation rate density

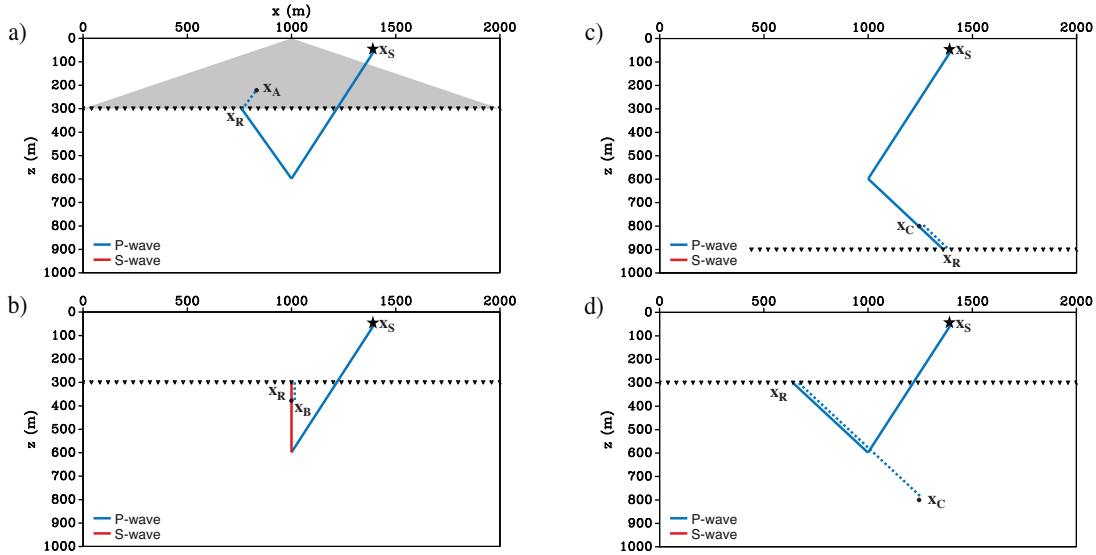

Figure 3.5: Stationary-phase analysis describing which receivers contribute to the construction of either physical or nonphysical energy in the receiver-side backpropagated wavefield. Solid lines represent the scattered Green's functions propagated forward in time during data acquisition and recorded on the receiver array. Dotted lines represent the reference Green's functions that are time reversed and injected at receiver location $\mathbf{x}_R$, propagating backwards in time during numerical back-extrapolation. Blue lines refer to P-waves, and red lines identify S-waves. (a) Nonphysical stationary path in the crosscorrelation of scattered P-wave data and the reference P-wave receiver-side propagator at $\mathbf{x}_A$. This event corresponds to an upgoing scattered P-wave, erroneously injected also as an upgoing time-reversed P-wave along the receiver array. (b) Nonphysical stationary path involved in the crosscorrelation of scattered S-wave data and the reference P-wave receiver-side propagator at $\mathbf{x}_B$. This event corresponds to a recorded scattered S-wave, erroneously injected as a P-wave along the receiver array. (c) Physical stationary path that would occur in the crosscorrelation of scattered P-wave data and the reference Pwave receiver-side propagator at $\mathbf{x}_C$; however, an array of receivers at depth $z > z_{scatt}$ is required to construct this physical event. (d) Nonphysical stationary paths in the crosscorrelation of scattered P-wave data and the reference P-wave receiver-side propagator at $\mathbf{x}_C$.

sources (Figure 3.6b). The physically scattered P-waves share the same radiation pattern between the first and the second integrands, whereas the nonphysical waves have opposite polarity resulting in a perfect cancellation (other than small numerical errors due to the presence of dispersion in finite-difference data) when they are summed together (Figure 3.6c).

Consider now the region of the subsurface below the scatterer. Here, neither the tensorial nor the vectorial wavefield extrapolation construct the scattered P-wave traveling from the physical source to any image point $\mathbf{x}_C$ because the stationary receiver lies on a portion of the receiver boundary that is not available in a usual seismic experiment (Figure 3.5c). A comparison with the exact scattered P-wave in Figure 3.4 shows how both receiver wavefields share the same spurious event at early times (i.e., before the

	Physical scattered wavefield	Nonphysical artefact 1	Nonphysical artefact 2
Region A ($z \leq z_R$)	-	X/V	X/V
Region B ($z_R \leq z \leq z_{scatt}$)	V/V	-	X/V
Region C ($z_R \geq z_{scatt}$)	X/X	-	X/V

Table 3.1: Comparison between the vectorial (left of slash) and tensorial (right of slash) receiver-side back-extrapolated wavefields with respect to the three main events discussed in the text for three different regions of the subsurface domain: V, properly handled; X, improperly handled; and X/V, improperly handled by vectorial extrapolation but properly handled by tensorial extrapolation.

scattering event occurs) due to the crosscorrelation between the scattered P-wave and the reference P-wave propagator (Figure 3.4 at time 1 and Figure 3.5d). Furthermore, after the scattering event takes place (Figure 3.4 at times 2–5), the scattered P-wave appears to propagate only upward rather than 'isotropically' in any direction (or in reverse time, the scattered P-wave collapsing onto the scatterer comes only from the direction of the receiver array). Although nonphysical events 1 and 2 pertain to using only elastic monopole sources and receivers, differences in the scattered P-wave between the exact scattered wavefield (Figure 3.4a) and the extrapolated receiver-side wavefields (Figure 3.4b and c) are due to the availability of only an incomplete (open) boundary of receivers. All of these observations are summarized in Table 3.1.

Imaging condition and artefacts.
Spurious events in receiver-side wavefield extrapolation potentially turn into artefacts in the final image. However, because an imaging condition often uses only the zero-time, zero-offset crosscorrelation between source and receiver wavefields, artefacts would only be created if the source wavefield and nonphysical waves in the receiver-side wavefield extrapolation coincide at the image point at a certain time. This is obviously not the case for nonphysical wavefield 1, which is due to the lack of directionality in the particle velocity injection because the source wavefield reaches any point $\mathbf{x}_A$ before the upward-injected P-wave. Moreover, absorbing boundary conditions are used at the top of the model in the extrapolation procedure to avoid the upgoing nonphysical wave being reflected back into the subsurface. On the other hand, because the source wavefield propagates from the source toward infinity and the nonphysical wavefield 2 starts from infinity and collapses at the receiver array (Figure 3.7), they inevitably cross at a certain time, creating artefacts in the PP image.

Figure 3.8 shows the PP images obtained from elastic RTM using the tensorial (Figure 3.8a) and vectorial (Figure 3.8b) wavefield extrapolation and the linearized imaging condition in equation 2.17. The scatterer is correctly imaged in both cases; however,

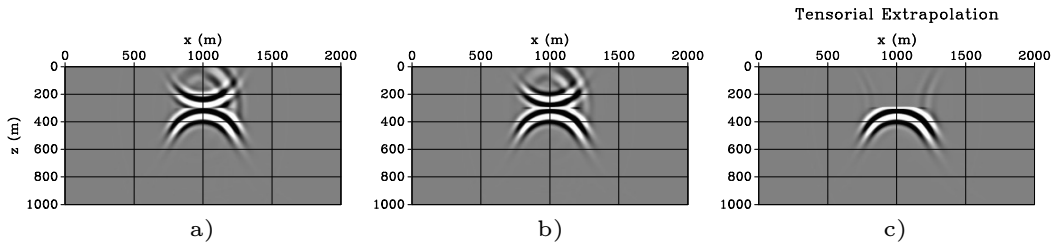

Figure 3.6: Construction of the correct backpropagated receiver-side P-wavefield using the tensorial wavefield extrapolation integral (equation 3.3) for the example in Figure 3.3: (a) first term, (b) second term, and (c) the sum of the integrals shown in (a) and (b). These wavefields share the same radiation pattern for the physical event (the downgoing scattered P-wave), whereas radiation patterns of the opposite sign cancel out in (c) for the nonphysical events (the upgoing scattered P-wave and the spurious P-wave due to the S-wave recorded at the receiver array).

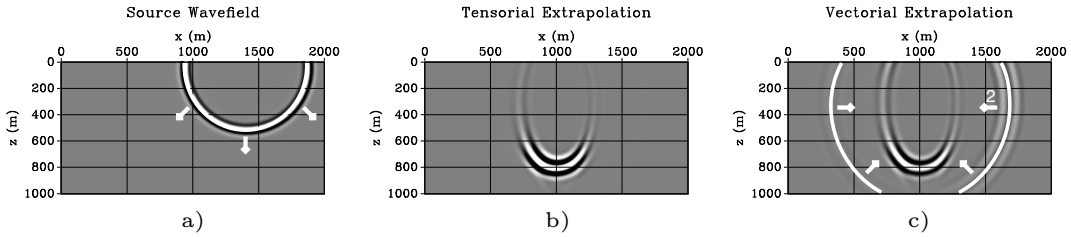

Figure 3.7: Time snapshot of (a) the source-side P-wave wavefield $G^{0(\Phi,\Phi)}_{(P,P)}(\mathbf{x}_I, \mathbf{x}_S)$, and the (b) tensorial and (c) vectorial P-wave receiver-side back-extrapolated wavefields $d^{S(\Phi,\Phi)}_{(P,P)}(\mathbf{x}_I, \mathbf{x}_S)$ for the example in Figure 3.3. The source wavefield is crosscorrelated with one of the receiver wavefields and the image is the value of the result at zero-time. This corresponds to the source wavefield snapshot being multiplied by the corresponding receiver wavefield (and the resulting panels at different times being summed together). In (a) the arrows identify the propagation direction of the source wavefield, and in (c) the arrows define propagation direction of non-physical event 2 in the vectorial receiver wavefield. Since they propagate in opposite directions and cross each other, they create an artefact in the final image (indicated in Figure 3.8b).

a strong artefact is present when the vectorial receiver wavefield is crosscorrelated with the source wavefield (Figure 3.8b). This is caused by the use of only velocity data/volume force density sources in the receiver-side extrapolation. Because the non-physical wave 2 is not present in the tensorial receiver wavefield, the artefact is strongly attenuated in the final result in Figure 3.8a, creating a much clearer image, which allows a more accurate interpretation of the subsurface structure.

PS imaging

To evaluate an imaging condition for converted- waves (a so-called PS image) the computation of the S-wave receiver wavefield is required. In this section, we analyse

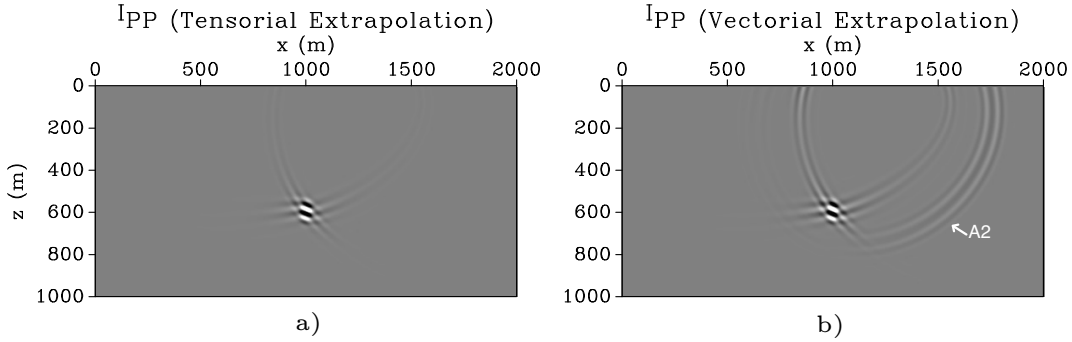

Figure 3.8: PP images resulting from elastic RTM using (a) tensorial and (b) vectorial wavefield extrapolation for the example in Figure 3.3 illuminated by a single surface source. Although the scatterer is correctly imaged in both cases (it can not be properly localized because only a single source was used in this example), artefact A2 is clearly visible below and to the right of the scatterer when only particle velocity data are injected at receiver locations during wavefield extrapolation. This results from the crosscorrelation between the source wavefield (Figure 3.7a) and nonphysical event 2 in the extrapolated receiver wavefield (Figure 3.7c).

the effect of using only particle velocity data to extrapolate the shear wavefield and describe how artefacts arise in the final image because of spurious events in the receiver-side extrapolation.

A series of snapshots of the S-wave receiver-side extrapolated field is compared to the exactly modeled scattered S-wave wavefield $d^{S(\Phi,\Phi)}_{(S,P)}(\mathbf{x},\mathbf{x}_S)$ (Figure 3.9). Nonphysical wavefields 1 and 2 are explained similarly to those of the corresponding waves in the P-wave extrapolated wavefield. The main difference concerns the shape of spurious event 2 and the chronological order at which these waves collapse at the receiver array: nonphysical wavefield 2 now arrives before the physical scattered S-wave. Wavefront 2, a scattered P-wave injected erroneously as an S-wave, has a parabolic shape: more precisely, two parabolic wavefronts propagate in opposite directions reaching the receiver array at the same time. Note that the wavefront indicated with the label 1+2 represents a recorded S-wave that was erroneously backpropagated as a P-wave, also in the wrong direction.

Figure 3.10 shows the source-side forward-propagating P-wave wavefield $G^{0(\Phi,\Phi)}_{(P,P)}(\mathbf{x}_I,\mathbf{x}_S)$ (Figure 3.10a), and the tensorially (Figure 3.10b) and vectorially (Figure 3.10c) backpropagated S-wave receiver wavefields $d^{S(\Phi,\Phi)}_{(S,P)}(\mathbf{x}_I,\mathbf{x}_S)$, which are crosscorrelated to evaluate the imaging condition in equation 2.17 (Figure 3.11). Artefact A1+2 in Figure 3.11b arises from the intersection of the source wavefield with the upper part of nonphysical wave 1+2, whereas artefact A2 is due to the lower part of spurious event 2 (Figure 3.10c).

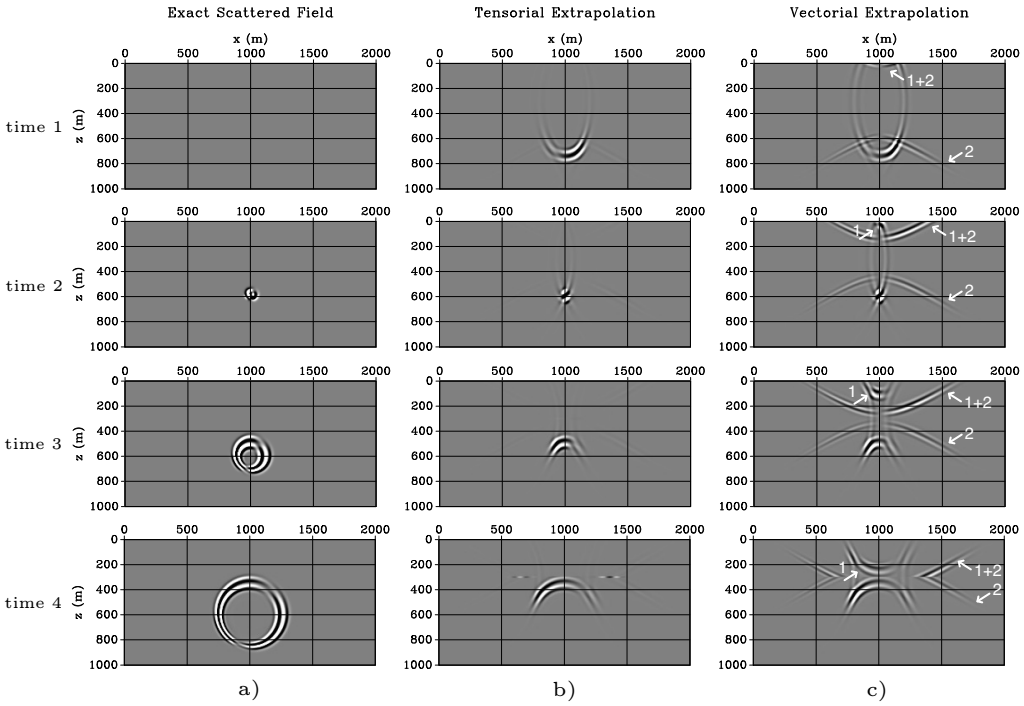

Figure 3.9: Series of snapshots of the (a) exactly modeled (b) tensorially and (c) vectorially back-extrapolated receiver-side S-wavefields $d^{S(\Phi,\Phi)}_{(S,P)}(\mathbf{x}_I, \mathbf{x}_S)$ for the point scatterer example (Figure 3.3). The white arrows indicate nonphysical waves due to approximations made in the wavefield extrapolation integral (equation 3.4). They do not arise (other than due to numerical artefacts) when the tensorial wavefield extrapolation integral is carried out in (b).

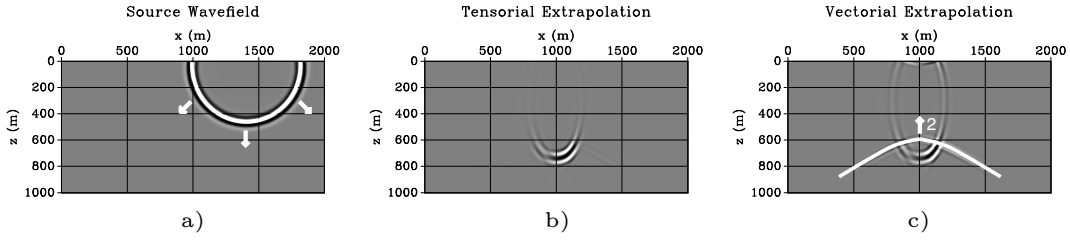

Figure 3.10: Time snapshot of (a) the source-side P-wave wavefield $G^{0(\Phi,\Phi)}_{(P,P)}(\mathbf{x}_I, \mathbf{x}_S)$, and the (b) tensorial and (c) vectorial S-wave receiver-side back-extrapolated wavefields $d^{S(\Phi,\Phi)}_{(S,P)}(\mathbf{x}_I, \mathbf{x}_S)$ for the example in Figure 3.3. In (a) the arrows identify the propagation direction of the source wavefield and, in (c) the arrows define the propagation direction of non-physical event 2 in the vectorial receiver wavefield. They cross each other and create an artefact in the final image (Figure 3.11b).

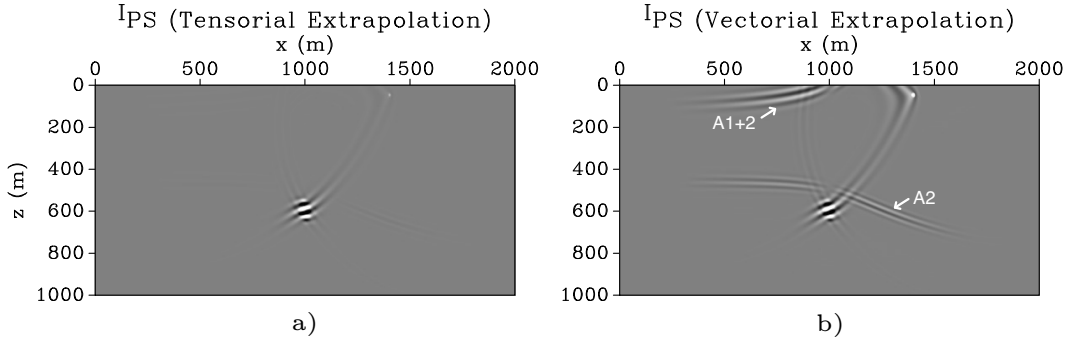

Figure 3.11: PS images resulting from elastic RTM using (a) tensorial and (b) vectorial wavefield extrapolation. Artefacts A1+2 and A2 are the result of the crosscorrelation between the P-wave source-side wavefield and spurious events in the S-wave receiver-side extrapolated wavefield when only particle velocity data are injected at the receiver locations during wavefield extrapolation.

Elastic RTM of the Marmousi 2 model

We now use a modified subset of the Marmousi2 model (Martin et al., 2002) to compare the receiver-side extrapolation formulae in a more realistic scenario. Figure 3.12a depicts the stratigraphic density model composed of a series of layers with increasing dip toward the right side. The P- and S-wave velocity models used for migration are smooth with velocities ranging, respectively from 1.6 to 3.2 km/s and 0.8 to 1.6 km/s ($V_P/V_S = 2$) (Figure 3.12b). Data are modeled using density discontinuities to generate reflections, whereas we use a constant migration density throughout the model ($\rho = 1000 kg/m^3$) to carry out Born imaging (i.e., for calculation of the source-side reference wavefield and for receiver-side back-propagation). A compressional source is fired at $\mathbf{x}_S = (6.75; 0.5)\, km$, and the wavefields are recorded by a horizontal array of receivers placed at $z_R = 0.5\, km$ with inter-receiver spacing of $dx_R = 2.5\, m$. Absorbing boundary conditions are used for modelling and migration.

Receiver-side P- and S-wave extrapolated wavefields are computed using the tensorial (Figure 3.13a and c) and vectorial (Figure 3.13b and d) wavefield extrapolation integrals. The complexity of the model results in seismic data that are densely populated by events of every kind, ranging from primary reflected P-waves to primary converted S-waves and multiply scattered and converted P- and S-waves. When the vectorial expression is used for wavefield extrapolation, the number of wavefronts injected along the line of receivers is twice the number of physical waves reaching the Earth's surface: a nonphysical S- or P-wave is erroneously generated from every physical P- or S-wave, respectively. In Figure 3.13b, several spurious waves, propagating transversally with respect to the physical ones, are indicated by white arrows: they mainly populate the right part of the model, although weak spurious energy is also visible on the left side.

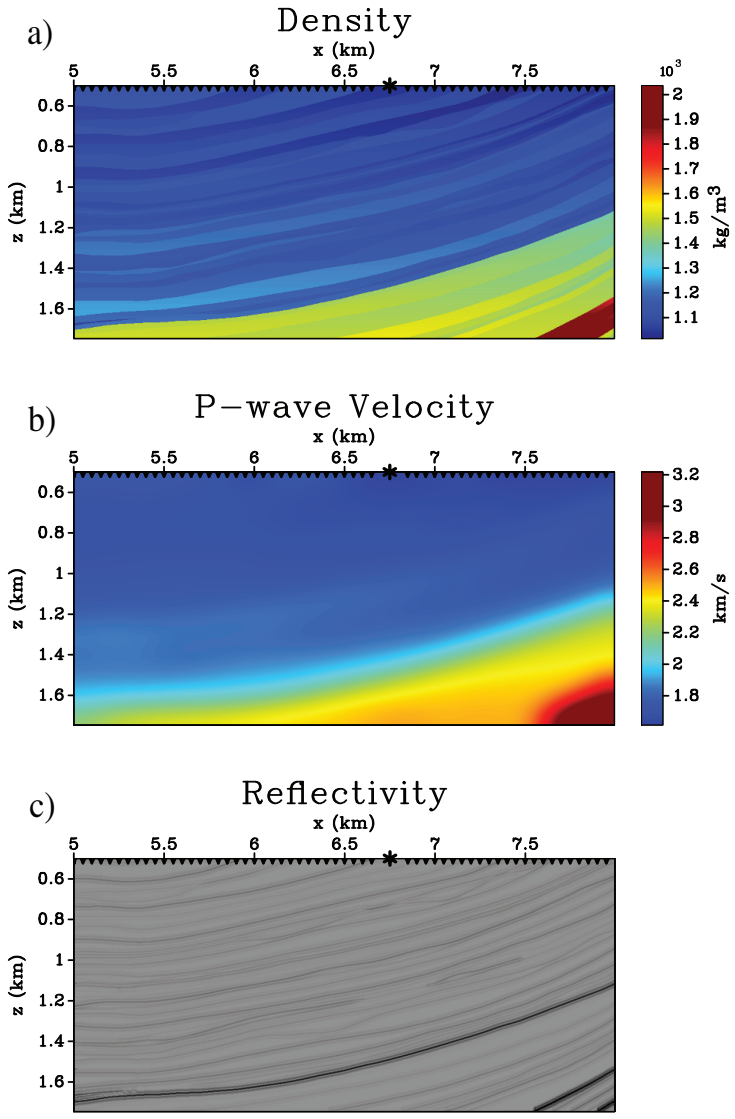

Figure 3.12: (a) Density model, (b) smoothed (migration) P-wave velocity, and (c) reflectivity ($r = |\bigtriangledown(\rho V_P)|$ models of a modified subset of the Marmousi 2 model (Martin et al., 2002) used for the second example of elastic RTM. The value of V_P ranges from 1.6 to 3.2 km/s and $V_P/V_S = 2$ and the density ranges from 1000 to 2000 kg/m^3. The star indicates the location of the physical source, and every tenth receiver is marked by a triangle.

Moreover, nonphysical events have an amplitude comparable with that of the physical events. On the other hand, the receiver-side S-wave wavefield (Figure 3.13d) seems to be less affected by nonphysical wavefronts, which propagate in a variety of different directions. The use of tensorial wavefield extrapolation integrals (Figure 3.13a and c) is necessary to generate receiver-side extrapolated wavefields deprived of artificial waves, whereas the backpropagated physical P- and S-wavefronts share the same kinematics as those obtained by the vectorial counterpart but are clearer and more discernible.

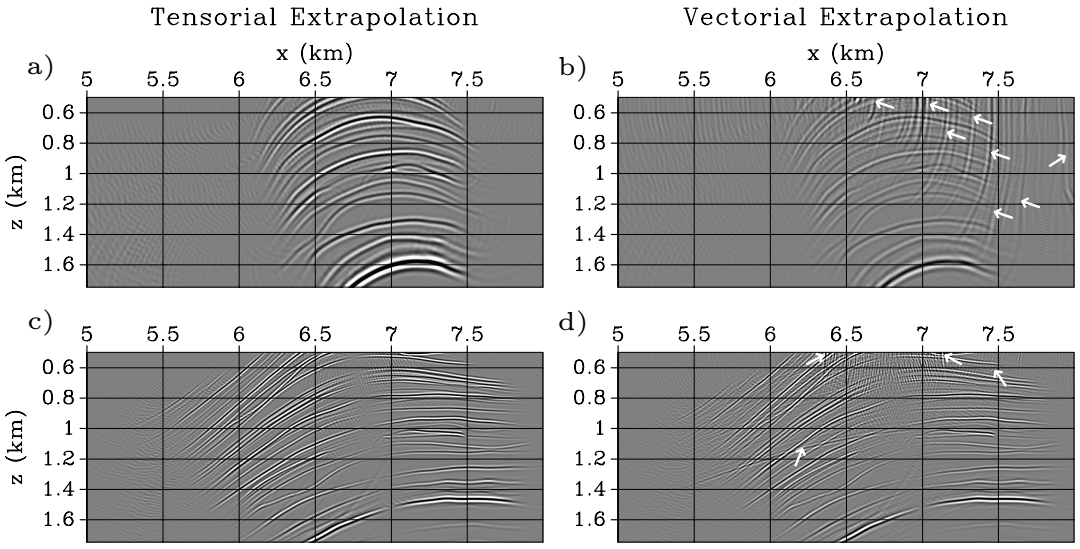

Figure 3.13: Comparison between a snapshot of the (a)/(c) tensorial and (b)/(d) vectorial receiver-side back-extrapolated wavefields $d^{S(\Phi,\Phi)}_{(P,P)}(\mathbf{x}_I, \mathbf{x}_S)$ (top) and $d^{S(\Phi,\Phi)}_{(S,P)}(\mathbf{x}_I, \mathbf{x}_S)$ (bottom). White arrows show nonphysical waves of type 2 due to approximations made in the wavefield extrapolation integral in equation 3.4.

As a last step to produce PP and PS images of the subsurface, the linearized imaging condition (equation 2.17) is applied to the source- and receiver-side extrapolated wavefields (Figure 3.14). Spurious events in the receiver-side vectorial wavefields interfere with events in the source-side wavefields to generate artefacts in the final images. They distort the structure of the layered medium, especially in the near surface around coordinates $x = 7.25\,km$ and $z = 0.8\,km$ in the PP image (Figure 3.14b) and around coordinates $x = 6.75\,km$ and $z = 0.7\,km$ in the PS image (Figure 3.14d). A clear improvement is visible when using the receiver-side tensorial wavefields either for the PP image (Figure 3.14a) or the PS image (Figure 3.14c).

Ocean-bottom 4C data

We now demonstrate the seabed extrapolation formula (equation 3.7) by adding a water layer ($V_P = 1.5\,km/s; V_S = 0\,km/s; \rho = 1000\,kg/m^3$) on top of the Marmousi 2 model of Figure 3.12 to mimic an ocean-bottom imaging experiment. Synthetic data are computed using a source at $\mathbf{x}_S = (6.75; 0.005)\,km$ and a horizontal array of pressure and particle-velocity receivers placed along the seabed ($z_R = 0.5\,km$). PP imaging using tensorial and vectorial wavefield backpropagation is performed below the receiver boundary (i.e., inside the elastic medium).

Data are initially modeled without free-surface multiples (i.e., with absorbing boundar-

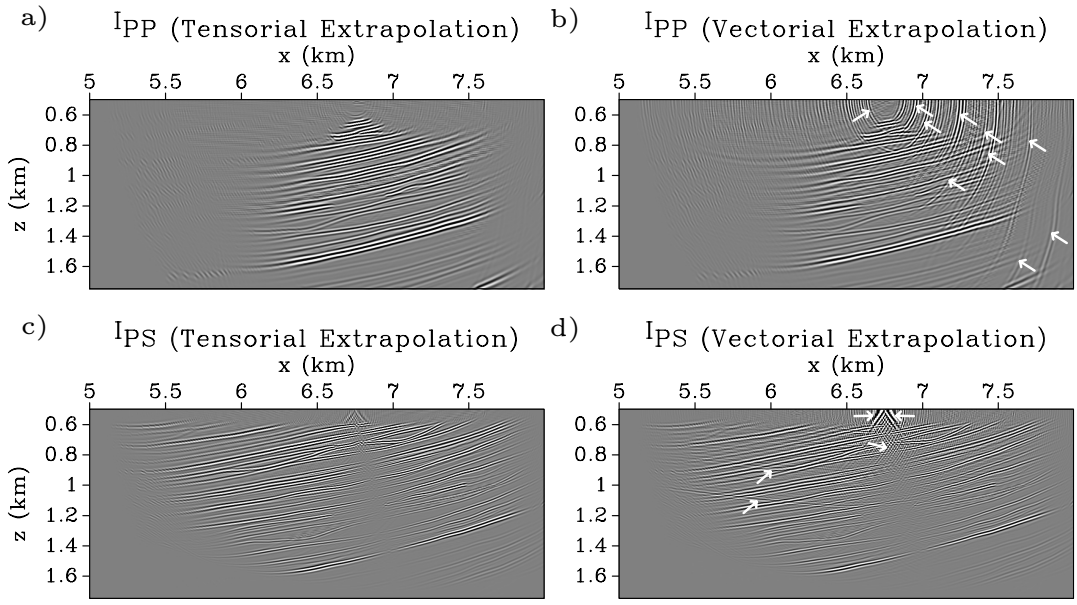

Figure 3.14: PP (top) and PS (bottom) images resulting from a single shot-profile elastic RTM of a modified subset of the Marmousi 2 model using the (a)/(c) tensorial and (b)/(d) vectorial wavefield extrapolation, respectively. Different portions of the subsurface domain are illuminated by pure- and converted-mode images because of different illumination angles of the two propagation modes for the given acquisition geometry. Nonphysical waves in the vectorial receiver-side extrapolated wavefield (Figure 3.13b and d) interfere with waves in the source wavefield to generate artefacts at the imaging stage (white arrows).

ies at the top of the water layer) to show the benefit arising from the correct injection of P- and S-waves. Figure 3.15 shows a time snapshot of the receiver-side P-wavefield computed using the tensorial and vectorial wavefield extrapolation integrals. In Figure 3.15b, analogously to Figure 3.13b, recorded S-waves are erroneously injected as P-waves and affect the vectorial wavefield (white arrows). PP images using tensorial (Figure 3.16a) and vectorial (Figure 3.16b) wavefield extrapolation are compared again showing the importance of using the pressure field along with the velocity recordings and the use of correct injectors. A clear improvement by using tensorial extrapolation is visible throughout the model and especially in the shallower part, the vectorial artefacts being almost completely suppressed.

Lastly a free surface is added at the modelling stage, so that the recorded data are composed of up- and downgoing waves at the receiver array. The same time snapshots of the receiver-side P-wavefield as in Figure 3.15 are now displayed in Figure 3.17. Apart from the same nonphysical waves indicated by white arrows, some other artefacts appear in the vectorial wavefield (black arrows in Figure 3.17b): these are downgoing wavefields from multiples in the water layer, which are erroneously treated as upgoing recorded waves and are directly backpropagated downward into the subsurface. The

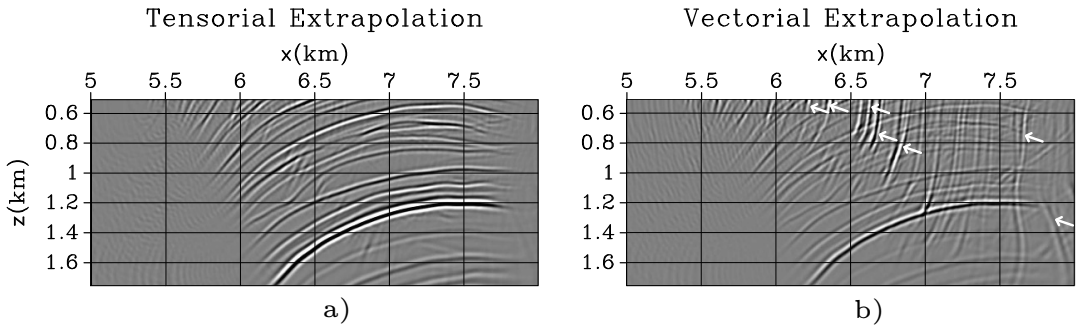

Figure 3.15: Comparison between a snapshot of the (a) tensorial and (b) vectorial P-wave receiver-side wavefields for the ocean-bottom example with absorbing boundaries at the top of the water layer. White arrows show nonphysical waves of type 2 due to approximations made in the wavefield extrapolation integral in equation 3.4.

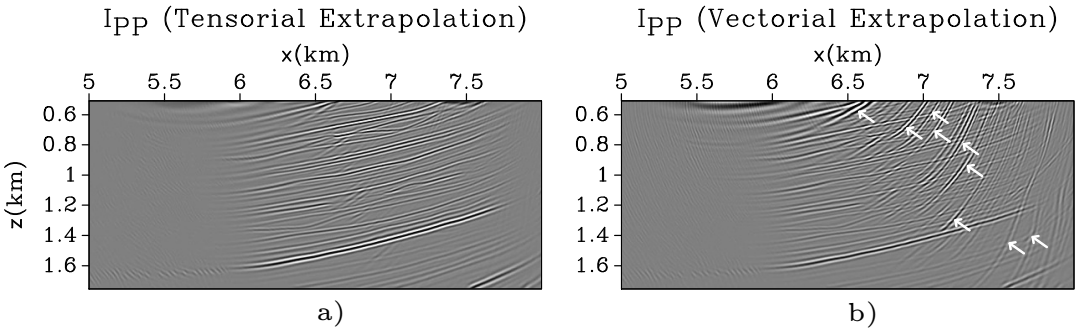

Figure 3.16: PP images resulting from a single shot-profile elastic RTM of an ocean-bottom version of the Marmousi 2 model (see main text) from data modeled with absorbing boundaries using (a) tensorial and (b) vectorial wavefield extrapolation, respectively. Nonphysical waves in the vectorial receiver-side back-extrapolated wavefield (Figure 3.15b) that interfere with waves in the source wavefield generate artefacts at the imaging stage (white arrows). These are successfully removed when tensorial wavefield extrapolation is used.

tensorial extrapolation, on the other hand, accomplishes a directional injection of the recorded wavefields and only upgoing waves are backpropagated inside the medium. Now, although the PP image constructed with the vectorial receiver wavefield (Figure 3.18b) shows further artefacts due to the interaction of the source wavefield with these downgoing waves injected in the opposite direction, the tensorial PP image (Figure 3.18a) is almost the same as that obtained earlier by migrating data without free-surface multiples (Figure 3.16a). Hence, our tensorial extrapolation proves to be capable of separating the information of downgoing free-surface multiples from upgoing reflections when wavefields are injected.

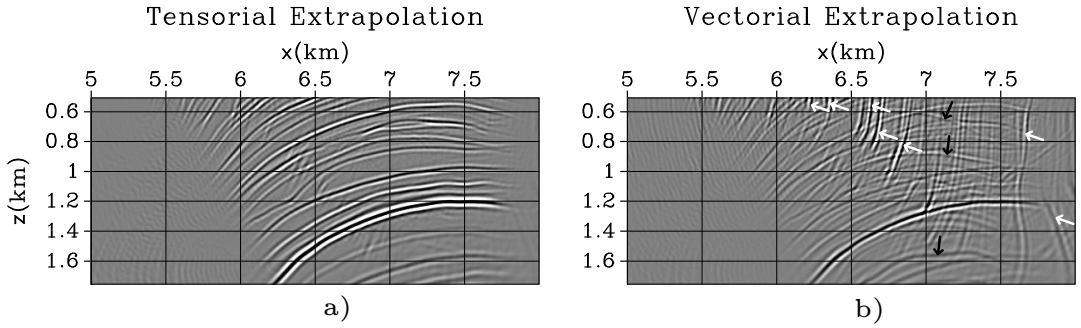

Figure 3.17: Comparison between a snapshot of the (a) tensorial and (b) vectorial P-wave receiver-side extrapolated wavefields for the oceanbottom example with data modeled using a free surface. Black arrows show nonphysical waves of type 1, and white arrows show nonphysical waves of type 2.

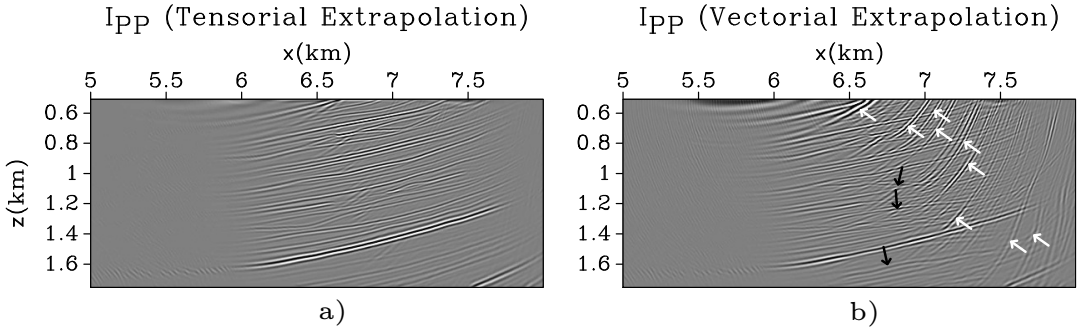

Figure 3.18: PP images resulting from a single shot-profile elastic RTM of an ocean-bottom version of the Marmousi 2 model from data modeled with a free surface using (a) tensorial and (b) vectorial wavefield extrapolation, respectively.

3.4 Discussion

Marine acquisition systems, which deploy receivers at the seabed (OBC or OBN) as an alternative to the more conventional marine streamer surveys, have created new potential but also new processing and interpretation challenges. First, the acquisition geometry is very different from that of marine and land surveys: sources and receivers are not located at approximately the same depth. Receiver depths range from tens of meters (shallow-water surveys) to hundreds of meters (deep-water surveys), and free-surface reflections modulate the spectrum more frequently than in marine streamer acquisition. Acquisition methods like over-under streamers (see Moldoveanu et al. (2007)) and processing techniques like predictive deconvolution commonly used for the suppression of receiver-side ghosts, cannot easily be translated into this context. Second, because it is impossible to record shear waves when streamers are towed behind a vessel, multicomponent ocean-bottom data contain much more information about shear velocities and reflectivity because converted shear waves are recorded directly on horizontal com-

ponent geophones at the seabed. A significant effort is needed, first, to reconcile this information with the P-wave data before the full potential of it can be exploited.

Having pressure information just above the seabed has been turned to an advantage for the separation of up- and downgoing (receiver-side ghost) waves using techniques such as PZ summation (Barr and Sanders, 1989; Soubaras, 1996; Schalkwijk et al., 1999); imaging using these separate components of the seismic data allows the reconstruction of the frequency band affected by the ghost notch effect (Godfrey et al., 1998; Grion et al., 2007; Dash et al., 2009). However, these additional data are often not used while performing elastic migration, particularly during wavefield extrapolation: receiver-side wavefields are generally obtained by backpropagation of particle velocity components at the receiver locations (Chang and McMechan, 1986, 1994; Sun and McMechan, 1986; Yan and Sava, 2008).

Here, we formulate an exact integral expression that uses a combination of velocity-stress recordings (or velocity-pressure in its application to ocean-bottom data — see above) and quadrupole-dipole backpropagating sources for wavefield extrapolation of elastic data. The numerical examples above show that direct injection of the particle displacement (or velocity) vector is not the best way to accomplish wavefield extrapolation, because it generates two types of nonphysical waves in the scattered wavefield estimate: each arrival contained in the data is injected up- and downward, and all injected energy emits compressional and shear propagating modes. When using the tensorial integral expression for the extrapolation of the receiver-side wavefield, any wavefront is backpropagated only toward the direction from which it was traveling in the physical experiment, rather than up- and downward. Imaging of the primary signal (upgoing at the receiver array) and the ghost signal (downgoing at the receiver array) can therefore be accomplished without any preliminary up/down wavefield separation. In addition, injected energy emits only compressional or shear propagating modes (e.g., if a P-wave is recorded, only a P-wave mode is backpropagated), rather than both propagating modes as is the case for the usual backpropagation procedure. This is vital for imaging with elastic data because the improvement due to the proper focusing of singly and multiply converted waves is otherwise not realized due to the introduction of spurious events. This new procedure has been proven to be effective for 2D imaging; however, it naturally extends to 3D if the Einstein's summation for repeated indices in equations equation 3.1, equation 3.2 and equation 3.3 is carried out by considering an extra coordinate (i.e., x-y-z must be used instead of only x-z). Moreover, it is important to note that the cost of our tensorial extrapolation is identical to that of conventional vectorial extrapolation because velocity and stress data can be injected together in the modelling (finite-difference) code through deformation rate density and volume force density backpropagation sources, respectively.

A practical challenge presented by the application of the ocean-bottom tensorial extrapolation (equation 3.7) to data recorded along the seabed is the fact that backpropagation sources must be placed at the seabed, where a sharp change in the medium parameters occurs. We found that this caused a degradation in the cancellation of nonphysical waves in the tensorial wavefield extrapolation when an elastic finite-difference code is used. To alleviate this problem, we used a migration velocity/density model in which the elastic layer is upward continued to substitute for the sea layer (although in doing so we cannot take advantage of the wavefield separation property of the new extrapolation formula to perform simultaneous imaging of free-surface ghosts along with primaries). The explicit handling of the fluid-solid boundary condition in a finite-difference method (van Vossen et al., 2002) or the use of a finite or spectral element modelling method (see Komatitsch and Tromp (1999)), in which the seabed properties in equation 3.6 can be represented explicitly at element boundaries, might solve this issue.

The imaging formulae in equations 2.15 to 2.18 are such that band-limited Green's functions can be retrieved for a co-located virtual, subsurface source and receiver at each image point. If the subsurface source and receiver are separated, the resulting Green's function would usually be referred to as an extended image (Sava and Vasconcelos, 2011). In acoustic media, improvements in the receiver-side extrapolated wavefields result not only in better final images, but also in more accurate extended images (Vasconcelos and Rickett, 2013), independently of the domain used for their computation, e.g., time-lag domain (Sava and Fomel, 2006), space-lag domain (Rickett and Sava, 2001), and angle domain (Sava and Fomel, 2003). Using our new extrapolation method, we would therefore expect similar improvements in elastic media. Moreover, because the penalty function usually defined for migration velocity analysis of elastic waves (Yan and Sava, 2010), which exploits the information contained in the extended images to invert for the velocity model, does not take into account the artificial events resulting from the vectorial extrapolation step, the inversion process could also benefit significantly from this new extrapolation procedure.

However, although our new wavefield extrapolation procedure improves the elastic image, the receiver wavefields still show some nonphysical waves at early times (e.g., before a scattering event occurs — see Figure 3.4c at time 1) and partial wavefronts at later times (e.g., after a scattering event occurs — see Figure 3.4c at times 3-5). These are caused first by the absence of nonlinear terms in the extrapolation and imaging steps and second by the lack of enclosing source and receiver boundaries as required by the theory of correlation-based extrapolation and imaging integrals. Note from a theoretical point of view that if both of these deficiencies would be resolved, all energy would focus on the correct locations (given a suitable velocity model, see below) and would

then be correctly transferred back to the incident field and so would not be visible in the scattered field. That is, no energy would continue to propagate to other locations causing crosstalk. The reason is that equation 3.2 then gives exactly the true scattered Green's function, which is zero before the scattering events occur.

Finally, equations 3.1 and 3.2 represent wavefield extrapolation formulae suitable for a new, final stage of elastic imaging: once we have a good estimate of the background model including high spatial frequencies (e.g., reflectors and diffractors) that introduce scattering in the back-propagation step, nonlinear terms can in principle be reintroduced to take advantage of the improved illumination offered by the energy from multiply scattered waves. These terms can alleviate illumination problems due to incomplete source and receiver aperture because the higher-order scattered waves come from a wider range of directions than primaries, as shown by Fleury and Snieder (2011) and Fleury and Vasconcelos (2012) for acoustic waves and by Ravasi and Curtis (2013b) (also Chapter 2 of this thesis) for elastic waves.

3.5 Conclusion

In this chapter we have proposed the use of interferometric relations for elastic wavefield extrapolation of land and ocean-bottom data. Reciprocity theorems are exploited to define a tensorial integral representation that allows for accurate backpropagation of the scattered wavefield between a physical source and any image point (i.e., construction of the receiver-side wavefield).

By using a combination of velocity-stress recordings and quadrupole-dipole backpropagating sources, we produce receiver-side wavefields deprived of nonphysical waves that, by contrast, arise when wavefield extrapolation is approximated by direct injection of particle velocity components as dipole backpropagating sources at the receiver locations (vectorial wavefield extrapolation). Interfaces and layers are clearly discernible in synthetic elastic images of part of the Marmousi 2 model, even for the extreme case of RTM of a single shot gather.

In a marine scenario, under the fluid-solid interface boundary conditions which may hold on the seabed, we have also shown that the wavefield extrapolation integral turns into an expression that requires only pressure and particle velocity recordings. The latter are available from standard 4C seabed acquisition systems.

4

Multidimensional deconvolution without wavefield separation

Seismic interferometry comprises a suite of methods to redatum recorded wavefields to those that would have been recorded if different sources (so-called virtual sources) had been activated. Seismic interferometry by cross-correlation has been formulated using either two-way (for full wavefields) or one-way (for directionally decomposed wavefields) representation theorems. To obtain improved Green's function estimates, the cross-correlation result can be deconvolved by a quantity that identifies the smearing of the virtual source in space and time, the so-called point-spread function. This type of interferometry, known as interferometry by multidimensional deconvolution (MDD), has so far been applied only to one-way directionally decomposed fields, requiring accurate wavefield decomposition from dual (e.g., pressure and velocity) recordings. Here we propose a form of interferometry by multidimensional deconvolution that uses full wavefields with two-way representations, and simultaneously invert for pressure and (normal) velocity Green's functions, rather than only velocity responses as for its one-way counterpart. Tests on synthetic data show that two-way MDD improves on results of interferometry by cross-correlation, and generally produces estimates of similar quality to those obtained by one-way MDD, suggesting that the preliminary decomposition into up- and downgoing components of the pressure field is not required if pressure and velocity data are jointly used in the deconvolution. Finally, as a by-product of having pressure and particle velocity measurements, we adapt one- and two-way representation theorems to convert any particle velocity receiver into its corresponding virtual dipole/gradient source by means of multidimensional deconvolution.

4.1 Introduction

In geophysical exploration, seismic interferometry comprises a set of techniques that allow a wavefield (theoretically, a Green's function) that would propagate between two receiver locations to be synthesized, as if one receiver had been replaced by an impulsive (or transient) source, generally known as a virtual source. This is usually obtained by cross-correlation of the wavefields observed at each receiver from an enclosing boundary or distribution of energy sources (Weaver and Lobkis, 2001; Campillo and Paul, 2003; Curtis et al., 2006; Schuster, 2009; Wapenaar et al., 2010a,c; Galetti and Curtis, 2012). Various authors have derived the theory for lossless (Schuster et al., 2004; Wapenaar, 2004; van Manen et al., 2005, 2006; Wapenaar and Fokkema, 2006) and dissipative media (Snieder, 2006a), and this has been applied to obtain body wave estimates from controlled-source data (Bakulin and Calvert, 2006) and in passive seismic data (Draganov et al., 2006; Forghani and Snieder, 2010; Ruigrok et al., 2010). Mehta et al. (2007) demonstrate that when sources are not uniformly distributed around the receivers (e.g., if the medium of interest is illuminated from one side only), wavefield separation of the recorded wavefields into their up- and downgoing components can improve the quality of the virtual reflection response. This mitigates artefacts associated with the limited acquisition aperture typically used in practice, and constructs a virtual wavefield response partially deprived of downgoing reflections and multiples from the overburden above a subsurface (e.g., borehole) array of receivers and virtual sources.

In the non-ideal situation of limited arrays of sources and receivers, the correlation function is proportional to the Green's function from a source that is blurred in space and time. This blurring is quantified by the so-called source point-spread function (PSF). An even more accurate estimate of the Green's function can be obtained by deconvolving the point-spread function from the correlation function. This is the essence of seismic interferometry by multidimensional deconvolution (MDD — Wapenaar et al., 2008b, 2011; Wapenaar and van der Neut, 2010; Minato et al., 2011; van der Neut et al., 2011b; Vasconcelos and Rickett, 2013; Nakata et al., 2014; van Dalen et al., 2014). The advantages of multidimensional deconvolution over interferometry by cross-correlation are: 1) removal of the source signature, 2) improved radiation characteristics of the retrieved source, and 3) relaxation of the assumptions of a closed surface of regularly sampled sources (e.g., one-sided illumination may be sufficient) and a lossless medium. On the other hand, the MDD approach also has limitations: 1) MDD requires a well-sampled array of receivers (it can not be applied to a single receiver configuration), 2) the measured wavefields must first be decomposed into up- and downgoing components for a complete cancellation of the effect of the overburden, requiring data acquisition

using dual (i.e., pressure and particle velocity) receivers — while an estimate of the first arriving downgoing wave from single component receivers via time gating (van der Neut et al., 2011a) or single-trace deconvolution (Bellezza and Poletto, 2014) can only compensate for the blurring effects and spread distortions, 3) the computational cost can be high due to the array operations involved, and 4) the inverse problem that performs the deconvolution is usually ill-conditioned and hence must be regularized.

In this chapter, we show that the preliminary step of separating measured wavefields into up- and downgoing components can be avoided. By using pressure and velocity data jointly in a system of multidimensional deconvolution equations we invert simultaneously for pressure and velocity responses. To achieve this we use a two-way (full wavefield) representation, thus differing from conventional MDD that is based on one-way (directional wavefield) representation. However, since twice the number of virtual responses are estimated using the same number of equations which depends on the number of available sources, the conditioning of two-way MDD is generally poorer than that of one-way MDD: while adding a regularization term on the solution norm is sometimes sufficient as in one-way MDD, other filters (based, for example, on the directionality of the virtual responses that we want to retrieve) or sparsity constraints (van der Neut and Herrmann, 2013) can be applied to better condition the inversion process when needed.

When used for borehole redatuming, two-way multidimensional deconvolution improves the results of interferometry by cross-correlation by suppressing the effect of medium inhomogeneities in the overburden, and produces estimates of similar quality to those obtained by one-way multidimensional deconvolution suggesting that the decomposition step is not required if pressure and velocity data are used jointly in the inversion. When two-way MDD is used for ocean-bottom multiple elimination, the virtual responses are still of good quality (clear improvements can be seen when compared to cross-correlation responses), although some interactions with the seabed are not entirely removed from the virtual gather unless directionality constraints are added to the inversion. Finally, representation theorems used for one- and two-way MDD are adapted to transform any type of available particle velocity receivers (e.g., normal or radial velocities) into their corresponding virtual dipole/gradient source. Thus we construct virtual data from virtual dipole or velocity source excitations, even though the original data are only excited by monopole sources.

4.2 One- and two-way representation theorems for seismic interferometry

Recordings of waves propagating between $\mathbf{x}_S$ and $\mathbf{x}_{VS}$ in the geometrical configuration shown in Figure 4.1 can be constructed by cross-convolution via the following two-way integral in the frequency domain (Wapenaar et al., 2011)

$$p(\mathbf{x}_{VS}, \mathbf{x}_S) = \oint_{\partial D_R} p(\mathbf{x}_R, \mathbf{x}_S) G_{v_n,q}(\mathbf{x}_R, \mathbf{x}_{VS}) - v_n(\mathbf{x}_R, \mathbf{x}_S) G_{p,q}(\mathbf{x}_R, \mathbf{x}_{VS}) \, \mathrm{d}^2\mathbf{x}_R, \quad (4.1)$$

where for each frequency, p and v_n represent the pressure and normal particle velocity recorded at the receiver boundary ∂D_R from a monopole source at $\mathbf{x}_S$, with $v_n = \mathbf{v} \cdot \mathbf{n}$ where $\mathbf{v}$ is the particle velocity vector and $\mathbf{n}$ is the outward pointing normal vector (Figure 4.1). $G_{p,q}$ and $G_{v_n,q}$ denote the Green's functions from a monopole source (q) to pressure and normal velocity receivers, respectively, and in equation 4.1 these Green's functions are from a virtual source located at $\mathbf{x}_{VS}$. Note that a more compact notation is used in this chapter since we deal with acoustic wavefields. When expressing Green's functions, the source type and observed quantity as well as their selected components are indicated in the subscript.

It is important to remember that the fields p, v_n can represent a different wave state from $G_{p,q}$, $G_{v_n,q}$ and that p, v_n can be related to $G_{p,q}$, $G_{v_n,q}$ by reciprocity theorems inside ∂D_R where the medium is assumed to be the same for both states (Fokkema and van den Berg, 1993). For example, $G_{p,q}$ and $G_{v_n,q}$ may belong to a state with different boundary conditions at ∂D_R, different sources, and/or different medium parameters outside ∂D_R, compared to those that pertain to the waves in p and v_n. Moreover, in most practical situations receivers are not available on a closed boundary, so the integration in equation 4.1 is necessarily restricted to an open receiver boundary. However, as long as the source $\mathbf{x}_S$ is located outside ∂D_R, it suffices to take the integral over an open receiver boundary such as the solid lines in Figure 4.1, as Sommerfeld's radiation conditions (Sommerfeld, 1954) may be assumed to apply on the half-sphere that would close the boundary; in other words, assuming that the half-sphere boundary radius is large, the contribution of the integral over that half-sphere vanishes. In the following we therefore replace the closed boundary integral by an open boundary integral.

The convolution-type integral in equation 4.1, which is the basic expression for two-way seismic interferometry by cross-convolution, may be converted into its one-way (directional) counterpart as follows. We assume that all fields can be locally separated into in- (+) and outgoing (-) components at the boundary (see Appendix B for a brief review of wavefield separation and for a description of the associated requirements and

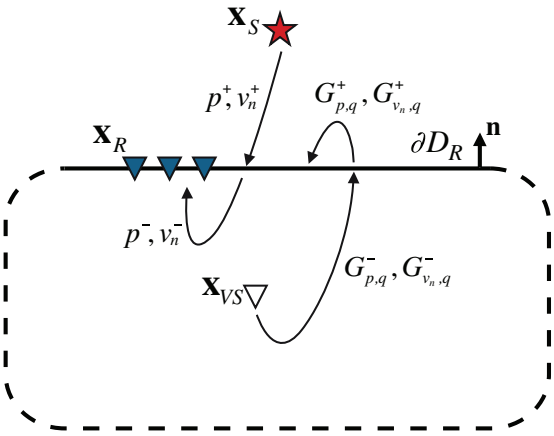

Figure 4.1: Acquisition geometry used in seismic interferometry by MDD. The red star denotes a source, blue triangles are receivers along the boundary ∂D_R and the white triangle refers to the receiver that seismic interferometry turns into a virtual source. The solid line corresponds to the portion of the surface ∂D_R where data are assumed to be available. Rays denotes the decomposition of the wavefields in terms of waves that are either ingoing (downgoing, +) or outgoing (upgoing, -) at the boundary.

limitations), such that $p = p^+ + p^-$ and $G_{v_n,q} = G^+_{v_n,q} + G^-_{v_n,q}$ (similarly for v_n and $G_{p,q}$) as illustrated in Figure 4.1. Then equation 4.1 is recast as

$$p = \int_{\partial D_R} (p^+ + p^-)(G^+_{v_n,q} + G^-_{v_n,q}) - (v_n^+ + v_n^-)(G^+_{p,q} + G^-_{p,q})\,\mathrm{d}^2\mathbf{x}_R. \tag{4.2}$$

Following the same reasoning used by Wapenaar and Berkhout (1989); Wapenaar and Fokkema (2006) and Vasconcelos et al. (2014a), the two products between purely ingoing terms at the stationary receiver locations (such receivers yield the dominant physical contributions to equation 4.2) have opposite contributions that cancel, and this also happens for the products between the two outgoing terms. Consequently, these terms do not contribute to the convolution-type integral, such that equation 4.2 can be reduced to

$$\begin{aligned} p(\mathbf{x}_{VS}, \mathbf{x}_S) = & \int_{\partial D_R} p^-(\mathbf{x}_R, \mathbf{x}_S) G^+_{v_n,q}(\mathbf{x}_R, \mathbf{x}_{VS}) + p^+(\mathbf{x}_R, \mathbf{x}_S) G^-_{v_n,q}(\mathbf{x}_R, \mathbf{x}_{VS})\,\mathrm{d}^2\mathbf{x}_R \\ & - \int_{\partial D_R} v_n^-(\mathbf{x}_R, \mathbf{x}_S) G^+_{p,q}(\mathbf{x}_R, \mathbf{x}_{VS}) + v_n^+(\mathbf{x}_R, \mathbf{x}_S) G^-_{p,q}(\mathbf{x}_R, \mathbf{x}_{VS})\,\mathrm{d}^2\mathbf{x}_R \\ & = 2 \int_{\partial D_R} p^-(\mathbf{x}_R, \mathbf{x}_S) G^+_{v_n,q}(\mathbf{x}_R, \mathbf{x}_{VS}) + p^+(\mathbf{x}_R, \mathbf{x}_S) G^-_{v_n,q}(\mathbf{x}_R, \mathbf{x}_{VS})\,\mathrm{d}^2\mathbf{x}_R, \end{aligned} \tag{4.3}$$

where we have also used the fact that terms $p^- G^+_{v_n,q}$ and $-v_n^- G^+_{p,q}$ (as well as $p^+ G^-_{v_n,q}$ and $-v_n^+ G^-_{p,q}$) give equal contributions to the integral to further reduce the number of terms involved in the integral relation 4.3.

In addition, we are free to choose convenient boundary conditions at ∂D_R and medium parameters outside ∂D_R, for G. We choose a specific type of Green's function that has only the outward propagating term —i.e. $G_{v_n,q} = G^-_{v_n,q}$, that is $G^+_{v_n,q} = 0$. Effectively then ∂D_R acts as an absorbing boundary for $G_{v_n,q}$, or equivalently the medium is homogeneous outside ∂D_R as shown in Figure 4.2. (Wapenaar et al., 2011). Equation 4.3 then simplifies to

$$p(\mathbf{x}_{VS}, \mathbf{x}_S) = 2 \int_{\partial D_R} p^+(\mathbf{x}_R, \mathbf{x}_S) G^-_{v_n,q}(\mathbf{x}_R, \mathbf{x}_{VS})\, \mathrm{d}^2\mathbf{x}_R. \tag{4.4}$$

Equations 4.1 and 4.4 are the respective starting points for two- and one-way interferometry by multidimensional deconvolution. If terms $G_{v_n,q}$ and $G_{p,q}$ (or alternatively $G^-_{v_n,q}$) inside the integrals are the unknown quantities to be estimated, these equations need to be solved by multidimensional deconvolution. For applications of MDD where $\mathbf{x}_{VS}$ is a receiver on ∂D_R, it is often useful to consider only the outward propagating part of the field at $\mathbf{x}_{VS}$ by applying decomposition also on the left hand side of equation 4.4 (the outgoing part is $p^-(\mathbf{x}_{VS}, \mathbf{x}_S)$). Whether the input is the full pressure field p or only the upgoing part of the pressure field controls whether or not the estimated Green's function from $\mathbf{x}_{VS}$ to $\mathbf{x}_R$ contains the direct wave or not (see Amundsen, 2001).

4.3 One- and two-way interferometry by multidimensional deconvolution

Interferometry by MDD essentially consists of inverting equations 4.1 or 4.4 for the unknown Green's functions. If there was a single source (and so a single equation), the inverse problem would be ill-posed. However, these equations hold for each source position $\mathbf{x}_S$ outside ∂D_R. Solving the ensemble of equations for any G is a better posed problem. Nevertheless, the existence of the relevant inverse operator is not guaranteed (indeed it seldom exists in practice) and its conditioning depends on many factors such as the number of available sources, the source array aperture, and the source bandwidth.

One-way MDD

We first consider MDD using the one-way representation. For the inversion of equation 4.4 we first define $G^-_{ow} = 2G^-_{v_n,q}$, discretise the integration along the receivers to a summation, and write the equation in matrix form for each angular frequency separately

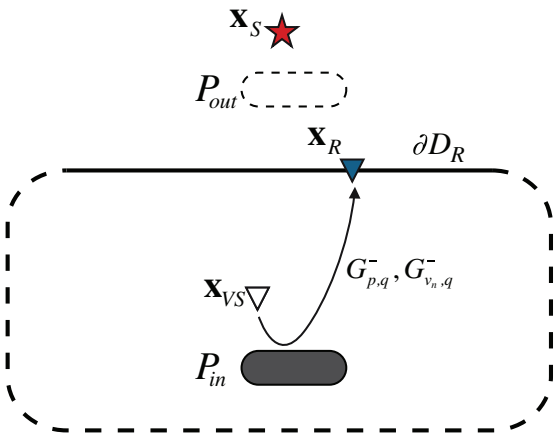

Figure 4.2: Cartoon denoting the choice of the Green's function wave state in the one-way representation (equation 4.5). Although both perturbations outside (P_{out} —white region) and inside (P_{in} —grey region) the boundary ∂D_R belong to the wave state of the recorded data, the medium is assumed to be homogeneous outside the boundary ∂D_R in the Green's function wave state, so only the perturbation inside surface ∂D_R is included in the Green's function state and hence in the solutions obtained. Keys as in Figure 1.

$$\mathbf{p} = \mathbf{p}^+ \mathbf{G}^-_{\mathbf{ow}}, \tag{4.5}$$

where $\mathbf{p}^+$ is a data matrix with rows and columns corresponding to source locations $\mathbf{x}_S$ and receiver locations $\mathbf{x}_R$, respectively. Similarly $\mathbf{p}$ is a matrix with rows and columns corresponding to source locations $\mathbf{x}_S$ and virtual source locations $\mathbf{x}_{VS}$. Finally $\mathbf{G}^-_{\mathbf{ow}}$ is a matrix with rows and columns corresponding to receiver locations $\mathbf{x}_R$ and virtual source locations $\mathbf{x}_{VS}$.

We then define our objective: to obtain a least-squares estimate of the unknown Green's functions $\mathbf{G}^-_{\mathbf{ow}}$ by minimizing the misfit

$$J^-_{ow} = \| \mathbf{p} - \mathbf{p}^+ \mathbf{G}^-_{\mathbf{ow}} \|^2, \tag{4.6}$$

where subscript 2 denotes the $\ell 2$-norm. Via some algebra (Menke, 1989), the solution of equation 4.6 can be written as the normal equation

$$\mathbf{C}^-_{ow} = \Gamma^-_{\mathbf{ow}} \mathbf{G}^-_{\mathbf{ow}} \Leftrightarrow \mathbf{G}^-_{\mathbf{ow}} = (\Gamma^-_{\mathbf{ow}})^{-1} \mathbf{C}^-_{\mathbf{ow}}, \tag{4.7}$$

where $\Gamma^-_{\mathbf{ow}} = (\mathbf{p}^+)^H \mathbf{p}^+$ and $\mathbf{C}^-_{ow} = (\mathbf{p}^+)^H \mathbf{p}$ with H denoting the conjugate transpose matrix. After Wapenaar et al. (2011) and van der Neut et al. (2011b), $\Gamma^-_{\mathbf{ow}}$ is hereafter referred to as a wavefield point-spread function, while the matrix $\mathbf{C}^-_{ow}$ is the cross-correlation function. Equation 4.7 states that the correlation function $\mathbf{C}^-_{ow}$ is

proportional to the sought Green's function $\mathbf{G}^-_{\mathbf{ow}}$, smeared in space and time by $\Gamma^-_{\mathbf{ow}}$.

Exact minimization of J^-_{ow} generally results in an unstable solution that is not desired. Numerical instability can be prevented by introducing an additional constraint on the solution norm (commonly referred to as regularization)

$$J^-_{ow} = \| \mathbf{p} - \mathbf{p}^+\mathbf{G}^-_{\mathbf{ow}} \|^2 + \lambda_G^2 \| \mathbf{G}^-_{\mathbf{ow}} \|^2 \tag{4.8}$$

and the solution of equation 4.8 is then

$$\mathbf{G}^-_{\mathbf{ow}} = (\Gamma^-_{\mathbf{ow}} + \lambda_G^2\mathbf{I})^{-1}\mathbf{C}^-_{ow} = (\Gamma^-_{\mathbf{ow}})^\dagger\mathbf{C}^-_{\mathbf{ow}}, \tag{4.9}$$

where λ_G controls the balance between minimizing the data residual (low λ_G) and the solution norm (high λ_G). Here $\dagger$ is used to identify the regularised inverse and $(\Gamma^-_{\mathbf{ow}})^\dagger$ is the regularised inverse of the one-way PSF.

Two-way MDD

The two-way representation in equation 4.1 is now converted into matrix equations suitable for inversion. Arranging the fields $p(\mathbf{x}_R, \mathbf{x}_S)$ and $v_n(\mathbf{x}_R, \mathbf{x}_S)$ into matrices $\bar{\mathbf{p}}$ and $\bar{\mathbf{v}}$ (a bar is added to emphasise that these are full data recorded by receivers $\mathbf{x}_R$ instead of virtual sources $\mathbf{x}_{VS}$ as in absence of the bar), and the Green's functions $G_{p,q}(\mathbf{x}_R, \mathbf{x}_S)$ and $G_{v_n,q}(\mathbf{x}_R, \mathbf{x}_S)$ into matrices $\mathbf{G_p}$ and $\mathbf{G_v}$ similarly to above, we can write

$$\mathbf{p} = \begin{bmatrix} \bar{\mathbf{p}} & -\bar{\mathbf{v}} \end{bmatrix} \begin{bmatrix} \mathbf{G_v} \\ \mathbf{G_p} \end{bmatrix} \Leftrightarrow \mathbf{p} = \mathbf{d}\mathbf{G_{tw}}, \tag{4.10}$$

where $\mathbf{d}$ is the first matrix composed of the concatenation of pressure and (negative) velocity data, and $\mathbf{G_{tw}}$ is the second matrix composed of the concatenation of velocity and pressure of the unknown Green's functions. The least squares solution is again obtained by minimizing the misfit

$$J_{tw} = \| \mathbf{p} - \mathbf{d}\mathbf{G_{tw}} \|^2 + \lambda_G^2 \| \mathbf{G_{tw}} \|^2, \tag{4.11}$$

and the solution is

$$\mathbf{G_{tw}} = (\Gamma_{\mathbf{tw}} + \lambda_G^2\mathbf{I})^{-1}\mathbf{C}_{tw} = (\Gamma_{\mathbf{tw}})^\dagger\mathbf{C_{tw}}, \tag{4.12}$$

where the PSF and cross-correlation matrices are block matrices composed of different combinations of pressure and velocity data

$$\Gamma_{\mathbf{tw}} = (\mathbf{d})^H\mathbf{d} = \begin{bmatrix} (\bar{\mathbf{p}})^H\bar{\mathbf{p}} & -(\bar{\mathbf{p}})^H\bar{\mathbf{v}} \\ -(\bar{\mathbf{v}})^H\bar{\mathbf{p}} & (\bar{\mathbf{v}})^H\bar{\mathbf{v}} \end{bmatrix}, \quad \mathbf{C}_{\mathbf{tw}} = (\mathbf{d})^H\mathbf{p} = \begin{bmatrix} (\bar{\mathbf{p}})^H\mathbf{p} \\ -(\bar{\mathbf{v}})^H\mathbf{p} \end{bmatrix}, \tag{4.13}$$

and $(\Gamma_{\mathbf{tw}})^\dagger$ is the regularised inverse of the two-way PSF.

Directional constraints on two-way MDD

In order to define a wave state uniquely, medium parameters, boundary conditions, and sources type need to be selected. We know that the convolution-type representation used as a starting point for seismic interferometry by MDD allows for an arbitrary choice of the Green's function wave state with possibly different boundary conditions at ∂D_R and medium parameters outside ∂D_R from those of the data. In the one-way representation, Wapenaar et al. (2011) choose the medium to be homogeneous outside boundary ∂D_R (i.e., $G^+_{v_n,q} = 0$). This implies that the sought Green's function is uniquely defined. However, this particular condition cannot be used directly for the two-way representation because full fields are used in equation 4.1 rather than up- and downgoing separated fields: the solution obtained by solving equation 4.10 via MDD thus mainly depends on the minimization criterion and regularization applied. Additional linear constraints can be applied to drive the inversion towards a desired Green's function solution.

For comparison with existing methods, here we show how we can estimate the solution of one-way MDD (in case that is what is desired) by implicitly ensuring that the downgoing Green's function components $G^+_{v_n,q} = 0$ and/or $G^+_{p,q} = 0$ go to zero. In order to do so, we first need to recall the decomposition operators in the frequency-wavenumber domain that, when applied to pressure and velocity time and space Fourier transformed fields, identify their downgoing components:

$$\mathbf{D}^+_{\mathbf{p}} = \frac{1}{2}\begin{bmatrix} \xi(k_{x_R})\mathbf{I} & \mathbf{I} \end{bmatrix}, \quad \mathbf{D}^+_{\mathbf{v}} = \frac{1}{2}\begin{bmatrix} \mathbf{I} & 1/\xi(k_{x_R})\mathbf{I} \end{bmatrix}, \tag{4.14}$$

where ξ is the so-called obliquity factor and k_{x_R} is the horizontal wavenumber at the receiver array (see Appendix B for their derivation). To be able to apply directionality constraints to the two-way representation in either equation 4.1 or its discretized version in equation 4.10, we first transform these equations from the frequency-space to the frequency-wavenumber domain by assuming that an array of receivers $\mathbf{x}_R$ is available along a horizontal line (in 2D) or plane (in 3D) and make use of Parseval's identity

(Amundsen, 2001) resulting in

$$p(\mathbf{x}_{VS},\mathbf{x}_S) = \int_{-\infty}^{\infty} p(-k_{x_R},\mathbf{x}_S)G_{v_n,q}(\mathbf{x}_R,\mathbf{x}_{VS}) - v_n(-k_{x_R},\mathbf{x}_S)G_{p,q}(k_{x_R},\mathbf{x}_{VS})\,\mathrm{d}k_{x_R}. \tag{4.15}$$

Note that the recorded data on the left-hand side of equation 4.15 remains in the frequency-space domain since we only need to transform across the receiver array. After discretizing equation 4.15 in the same way as for equation 4.1, the directionality constraints can be added to the least-squares objective function:

$$J_{tw}^{-} = J_{tw} + \lambda_{D_p}^2 \parallel \mathbf{D_p^+ G_{tw}^-} \parallel^2 + \lambda_{D_v}^2 \parallel \mathbf{D_v^+ G_{tw}^-} \parallel^2 . \tag{4.16}$$

Parameters λ_{D_p} and λ_{D_v} control the extent to which we wish the solution to contain less down- than upgoing energy (larger values of λ_{D_p} and λ_{D_v} result in less downgoing energy). The solution of the minimization problem in equation 4.16 is

$$\mathbf{G_{tw}} = (\Gamma_{\mathbf{tw}} + \lambda_G^2\mathbf{I} + \lambda_{D_p}^2(\mathbf{D_p^+})^H\mathbf{D_p^+} + \lambda_{D_v}^2(\mathbf{D_v^+})^H\mathbf{D_v^+})^{-1}\mathbf{C}_{tw} = (\Gamma_{\mathbf{tw}}^{-})^{\dagger}\mathbf{C_{tw}}. \tag{4.17}$$

Virtual dipole sources with one- and two-way MDD

Particle velocity measurements are generally required by algorithms for wavefield decomposition, both as a pre-processing step for one-way MDD as well as by two-way MDD to directly estimate virtual recordings. These measurements (or the up- and downgoing fields obtained by combining them with pressure data) are taken into account at the receiver locations $\mathbf{x}_R$ in representation theorems 4.1 and 4.4, while only pressure data are used at the virtual source location $\mathbf{x}_{VS}$. However, if we multiply each side of equation 4.1 by the operator that transforms pressure fields into particle velocity fields (i.e., $-j(\omega\rho)^{-1}\partial_i$ to obtain the i-th component of the particle velocity vector) at the virtual source location, we can create a modified representation theorem that allows us to estimate pressure and normal particle velocity Green's functions from dipolar sources (f_i) at the virtual source location, provided that we have appropriate velocity (and/or pressure array) sensors at the virtual source locations,

$$v_i(\mathbf{x}_{VS},\mathbf{x}_S) = \oint_{\partial D_R} p(\mathbf{x}_R,\mathbf{x}_S)G_{v_n,f_i}(\mathbf{x}_R,\mathbf{x}_{VS}) - v_n(\mathbf{x}_R,\mathbf{x}_S)G_{p,f_i}(\mathbf{x}_R,\mathbf{x}_{VS})\,\mathrm{d}^2\mathbf{x}_R \tag{4.18}$$

with $i = x, z$ (or any other direction obtained by combining the available velocity measurements). Similarly the one-way representation in equation 4.4 can be written as

$$v_i(\mathbf{x}_{VS}, \mathbf{x}_S) = 2 \int_{\partial D_R} p^+(\mathbf{x}_R, \mathbf{x}_S) G^-_{v_n, f_i}(\mathbf{x}_R, \mathbf{x}_{VS})\, \mathrm{d}^2\mathbf{x}_R. \tag{4.19}$$

By solving equations equations 4.18 or 4.19 via MDD, pressure and normal velocity responses from virtual dipole sources can be estimated for pressure and normal velocity recordings at virtual locations, even if only monopolar sources are available in the physical experiment.

4.4 Examples

We now use synthetic examples to explore the relative effectiveness of correlational, and one- and two-way MDD based interferometry for Green's function estimation. There are important differences between the data that can be acquired in borehole and ocean bottom, so we investigate each in turn.

Borehole redatuming

In our first example the seismic wavefield generated by sources at the Earth's surface is measured by receivers in a horizontal borehole below a complex overburden. Seismic interferometry redatums sources into virtual sources in the borehole (Bakulin and Calvert, 2006) and multidimensional deconvolution removes the effects of medium inhomogeneities between sources and receivers (Wapenaar and van der Neut, 2010). The complex overburden is here composed of fine layers and a gas cloud (white ellipse) that acts as an acoustic lens, while a target such as a hydrocarbon reservoir is located around 800 m depth (Figure 4.3a).

Data (Figure 4.3b) are generated from an array of 251 sources with spacing $dx_S = 16\,m$ firing into 101 dual receivers spaced at $dx_S = 8\,m$ using a finite-difference code which models the full set of acoustic first-order partial differential equations for pressure and particle velocity (Fokkema and van den Berg, 1993) in a staggered-grid scheme. The source excitation function is a zero-phase Ricker wavelet with a 20 Hz peak frequency, and absorbing boundaries are placed on all sides of the model. To perform wavefield separation of the recorded data in the frequency-wavenumber domain (see Appendix B for the mathematical derivation), we assume that the medium properties at the receiver level are known (here they are $V = 2100\,m/s$ and $\rho = 1000\,kg/m^3$).

Figure 4.4 shows the correlation functions for one- and two-way interferometry. The response of the reservoir is not clearly visible in the correlation functions because strong

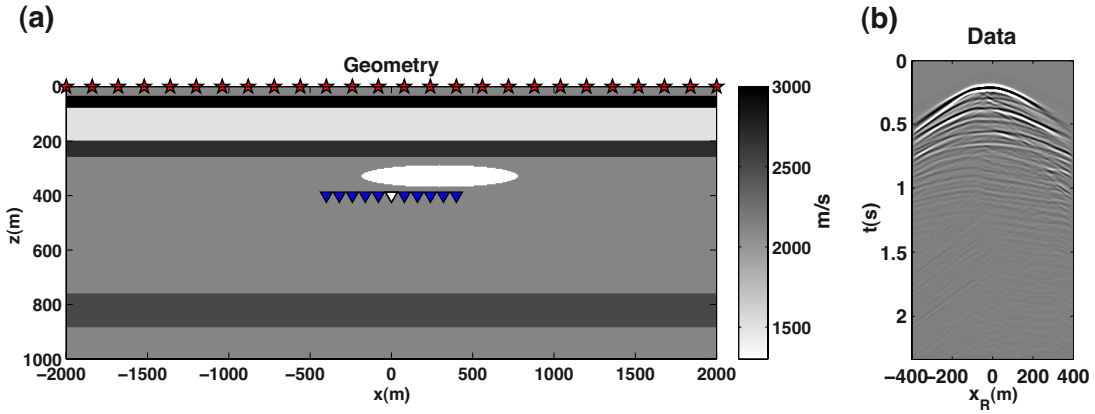

Figure 4.3: (a) Configuration for borehole redatuming. Sources (red stars) are situated at the Earth's surface, while receivers (blue triangles) and the virtual source (white triangle) are in a well below a 'complex' overburden. (b) Recorded pressure data from source at $x_S = 0\,m$.

coherent events arising from cross-talk between up- and downgoing events populate the gathers. The effect of these events can be similarly observed in the point-spread functions in Figure 4.5, which deviate from band-limited delta functions, and which need to be inverted and deconvolved by MDD: according to equations 4.7 and 4.12, the correlation functions in Figure 4.4 can be seen as the desired response convolved in space and time with the point-spread functions in Figure 4.5. Note that since in the one-way case we auto-correlate the downgoing field to construct the PSF, spurious events are fewer compared to those in the two-way case where the full field is used. This is natural because significantly more information is implicit in the one-way equations, specifically the wavefield decomposition into up- and downgoing fields.

Generally the more the PSF deviates from a band-limited delta function, the more the MDD becomes ill-posed and extra care has to be taken in the inversion. This can be observed in the singular values of the PSFs for each frequency (Figure 4.6): although two-way MDD has doubled the dimensions of the PSF, almost half of its most significant eigenvalues are very similar to those of one-way MDD (Figure 4.6a), while the remaining half are close to zero (Figure 4.6b) making the problem severely ill-posed. The benefit of deconvolving the point-spread function is illustrated in Figure 4.7: when its effect is removed from the correlation functions, the match between the directly modelled response from the reservoir (Figure 7a) and that from one-way MDD (Figure 4.7b) and two-way MDD by means of equation 4.12 (Figure 4.7c) is much improved. The retrieved responses are in fact free of multiple scattering caused by the geological layers and gas cloud in the overburden. Note also that, since the recorded pressure and normal velocity fields are used directly in the inversion, two-way MDD does not require any (accurate) estimate of medium properties along the receiver array to be successful.

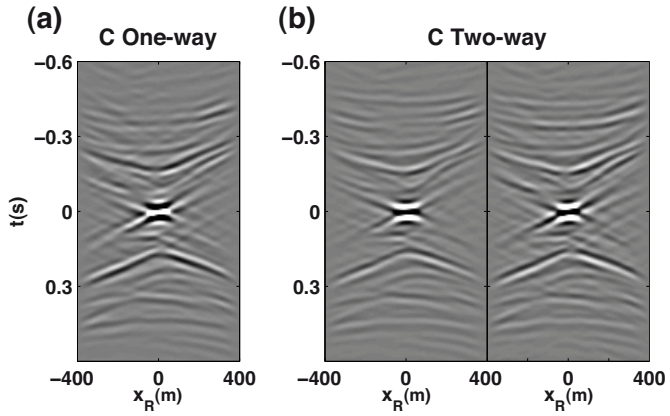

Figure 4.4: Interferometry by cross-correlation of decomposed wavefields (i.e., one-way representation), compared with (b) cross-correlation of full wavefields (i.e., two-way representation) for the configuration in Figure 4.3. In the two-way cross-correlation, each side of (b) represents a block in equation 4.13. Left is $(\bar{\mathbf{p}})^H\bar{\mathbf{p}}$ and right is $-(\bar{\mathbf{v}})^H\bar{\mathbf{p}}$.

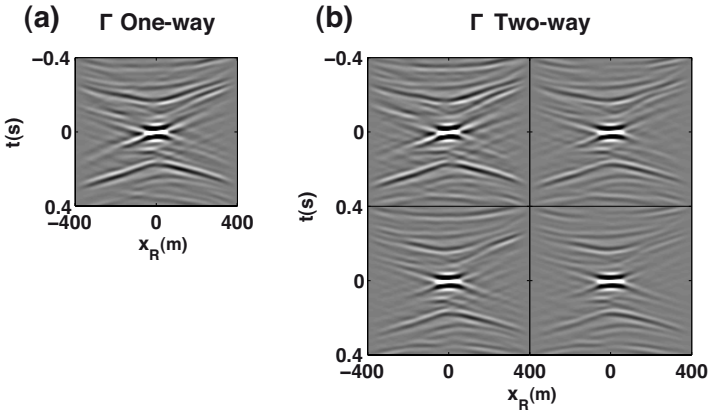

Figure 4.5: Point spread functions of (a) one-way and (b) two-way MDD for the configuration in Figure 4.3. In two-way MDD, the PSF is a block matrix and each quadrant in (b) represents a block in equation 4.13. Top left is $(\bar{\mathbf{p}})^H\bar{\mathbf{p}}$, top right is $-(\bar{\mathbf{p}})^H\bar{\mathbf{v}}$, bottom left is $-(\bar{\mathbf{v}})^H\bar{\mathbf{p}}$, and bottom right is $(\bar{\mathbf{v}})^H\bar{\mathbf{v}}$.

Interestingly, the Green's functions retrieved by two-way MDD by means of equation 4.12 shows symmetry with respect to the time axis, even though we would expect energy only in the causal part of the virtual field as stated in equations 4.1 and 4.10. Mathematically speaking, events in the anticausal part of the solution of two-way MDD are the direct consequence of choosing a regularization term that favours the minimum norm solution (i.e., $(\Gamma_{tw})^\dagger = (\Gamma_{tw} + \lambda\mathbf{I})^{-1}$): by making the Green's function real and symmetric in time, events in the anticausal part make the solution also real and symmetric in frequency, thus cancelling its imaginary component and minimizing its total energy (and hence also its norm). Moreover, as shown in Appendix C, there is also a physical reason for the retrieval of the anticausal part of the Green's function. $G^*_{v_n,q}$ and

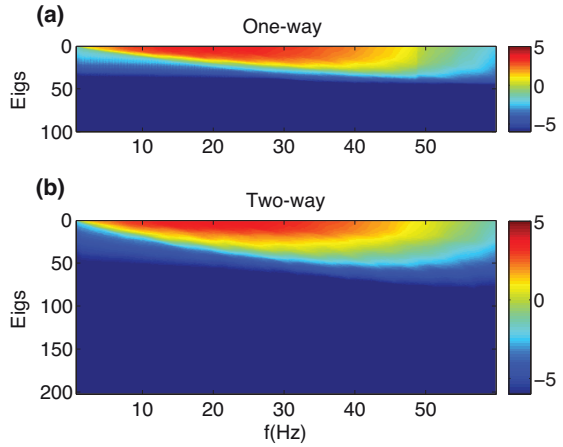

Figure 4.6: Singular values at each frequency for PSF matrices for the configuration in Figure 4.3: (a) one-way MDD (matrix $\Gamma^{-}_{\mathbf{ow}}$), and (b) two-way MDD (matrix $\Gamma_{\mathbf{tw}}$). Singular values are coloured using a logarithmic scale and re-sorted in ascending order where red indicates high values and blue low values.

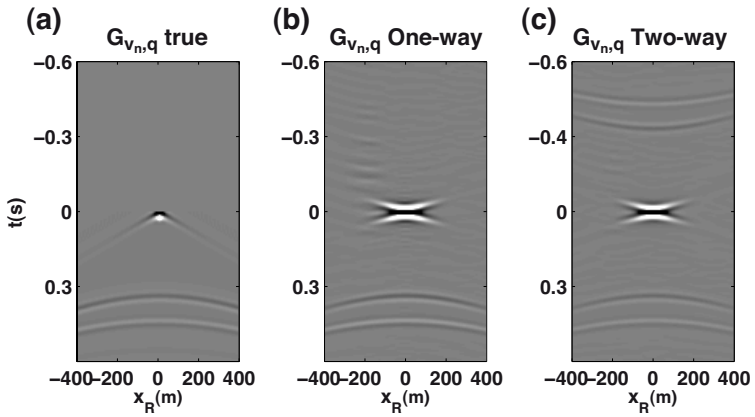

Figure 4.7: Velocity Green's function from a virtual monopole (pressure) source for the configuration in Figure 4.3. (a) Modelled response, and solutions from (b) one-way MDD, and (c) two-way MDD.

$G^{*}_{p,q}$ are in fact solutions of the correlation-type representation theorem (equation C.1) that involves the same recorded data p and v_n of the convolution-type representation theorem in equation 4.1. However, it is important to note that the contribution of the half-sphere closing the boundary ∂D_R in Figure 4.1 can not be neglected since radiation conditions can not be applied to the correlation-type representation (Wapenaar and Fokkema, 2006). Therefore we expect the anticausal estimate to be less trustworthy than the causal one in scenarios where receivers are not available on a closed boundary. We thus propose using the causal response as the estimate of the Green's function for two-way MDD. Additionally, seismic interferometry by means of two-way representations also recovers an estimate of the pressure Green's function as shown in Figure

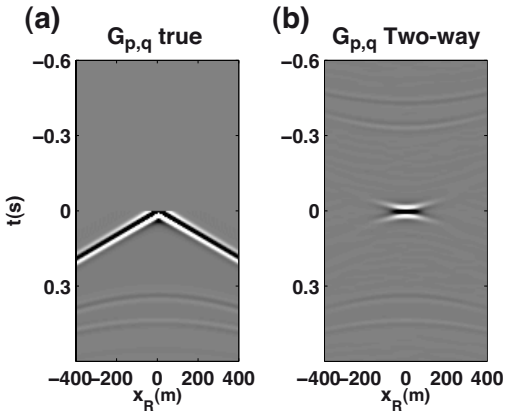

Figure 4.8: Pressure Green's function from a virtual monopole source for the configuration in Figure 4.3. (a) Modelled response and solution from (b) two-way MDD.

4.8. Note that in this case the anticausal part of the estimated Green's functions again contains arrivals from the reservoir but the polarity is reversed compared to the causal component (as expected — see Appendix C).

We then applied seismic interferometry by MDD to monopole (pressure and particle velocity) data to construct virtual dipole sources from particle velocity receivers by inverting the representation theorems in equations 4.18 and 4.19. In particular, by using the horizontal component of the recorded field ($i = x$) in the left hand side of these equations, we reconstruct Green's functions from a virtual horizontal dipole source to velocity (Figure 4.9) and pressure (Figure 4.10) receivers. The improvement arising by deconvolving the PSF from the one-way cross-correlation function ($\mathbf{C}^{-}_{\mathbf{ow}} = (\mathbf{p}^{+})^{H}\mathbf{v}_{\mathbf{x}}$ — Figure 4.9b) is shown in Figures 4.9c, d and Figure 4.10b.

When one-way MDD is used, cross-talk events that overlap the response of the reservoir in the cross-correlation gather are properly mitigated, leaving only the events of interest with their characteristic dipolar radiation pattern in the deconvolved response (Figure 4.9c). Two-way MDD is also proven to produce equally good estimates of the normal velocity Green's function (Figure 4.9d) together with the pressure Green's function (Figure 4.10b) using full (rather than decomposed) pressure and velocity fields. We refer to Appendix C for a discussion on the polarity of causal and anticausal solutions.

Ocean-bottom multiple elimination

As discussed extensively in van der Neut et al. (2011a) and Wapenaar et al. (2011), interferometry by MDD is akin to multiple elimination when applied to ocean-bottom data (Ziolkowski et al., 1999; Amundsen, 2001). Here we apply one-way and two-way

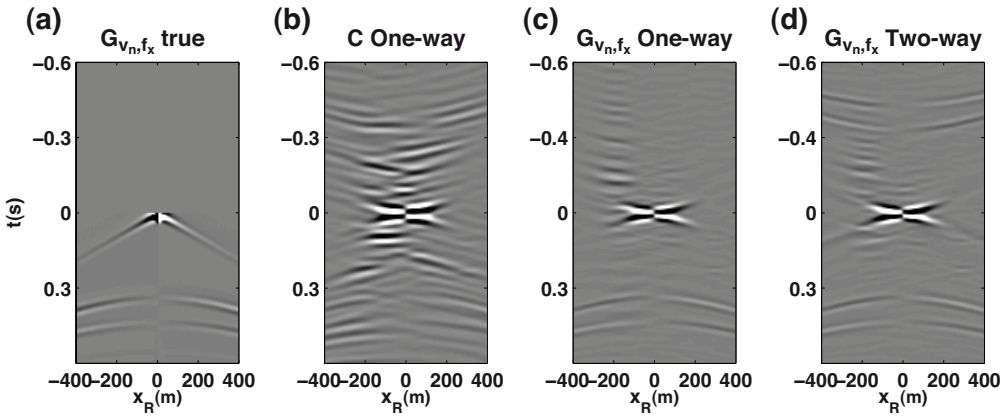

Figure 4.9: Velocity Green's function from a virtual horizontal dipole source for the configuration in Figure 4.3. (a) Modelled response, (b) result of interferometry by cross-correlation, and solutions from (c) one-way MDD, and (d) two-way MDD.

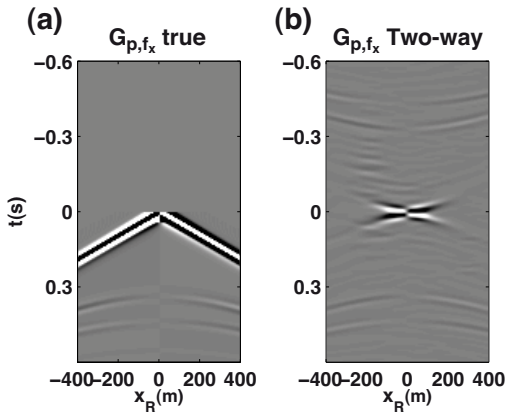

Figure 4.10: Pressure Green's function from a virtual horizontal dipole source for the configuration in Figure 4.3. (a) Modelled response and (b) solution from two-way MDD.

interferometry by MDD to synthetic acoustic data generated using an array of 126 sources with spacing $dx_S = 8\,m$ deployed just below the water surface and 101 dual receivers (recording acoustic pressure and normal particle velocity) spaced at $dx_S = 8m$ at the ocean bottom (equation 4.11a). Our objective is to synthetize the virtual response of the half-space below ∂D_R, without any multiple reflections related to the ocean bottom and the water surface that affect the recorded data (Figure 4.11b), and to test whether this is also possible using two-way MDD.

We use a model composed of three horizontal layers: the first layer is water ($V = 1500\,m/s$), while the second and third layers have velocities $1700\,m/s$ and $2200\,m/s$, respectively (Figure 4.11). Data are generated using a zero-phase Ricker wavelet with a 20 Hz peak frequency, a free-surface at the top of the model and absorbing boundaries on all other sides of the model. Wavefield decomposition is applied to the dual recordings

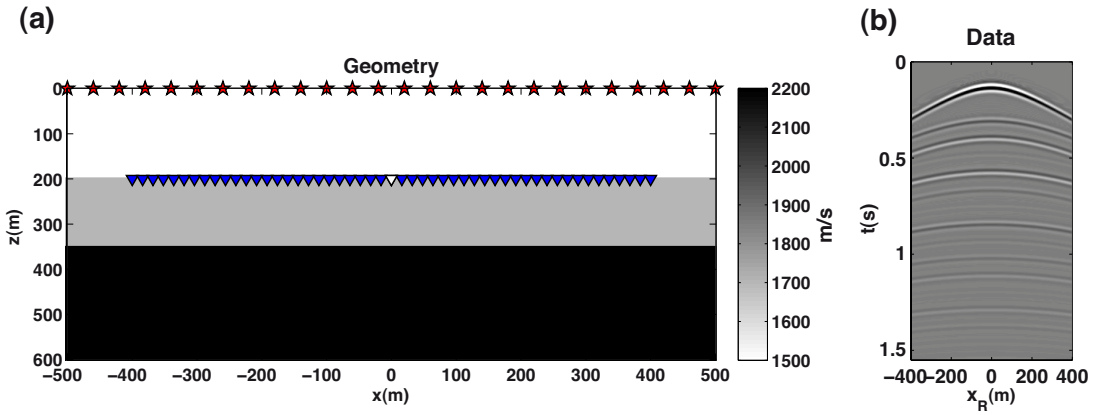

Figure 4.11: (a) Configuration for ocean-bottom multiple elimination. Sources (red stars) are situated just below the top surface, while receivers (blue triangles) and virtual source (white triangle) are at the ocean bottom. (b) Recorded pressure data from source at $x_S = 0m$.

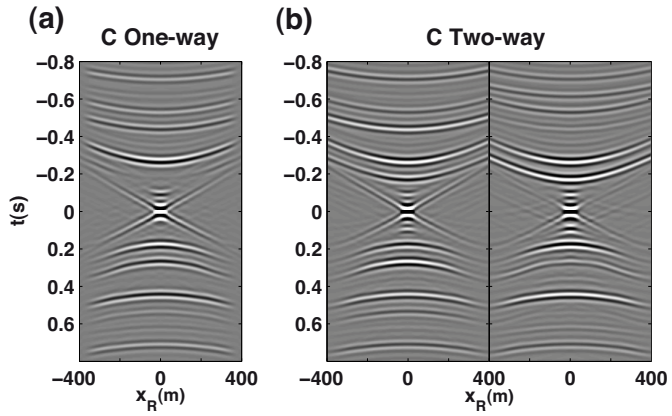

Figure 4.12: Interferometry by cross-correlation of decomposed wavefields and (b) cross-correlation of full wavefields for the configuration in Figure 4.11. In (b) the left side is $(\bar{\mathbf{p}})^H\bar{\mathbf{p}}$ and the right side is $-(\bar{\mathbf{v}})^H\bar{\mathbf{p}}$.

at the ocean bottom using the medium parameters of the first layer below the ocean bottom to obtain the downgoing pressure field $p^+(\mathbf{x}_R, \mathbf{x}_S)$ just below the ocean bottom (Amundsen and Reitan, 1995; Schalkwijk et al., 2003).

The correlation function (Figure 4.12a) and PSF (Figure 4.13a) are then computed for the one-way model by equation 4.7 and compared to those of the two-way model in equation 4.13 (Figures 4.12b and 4.13b). The match of both correlation functions with the response of the interface below the receiver array (Figure 4.14a) is reasonably good, however the correlation gathers also contain many spurious multiple reflections due to the crosstalk between up- and downgoing events in the data. Moreover, apart from band-limited delta functions around $(x_R = 0, t = 0)$, the point-spread functions also contain multiple reflections.

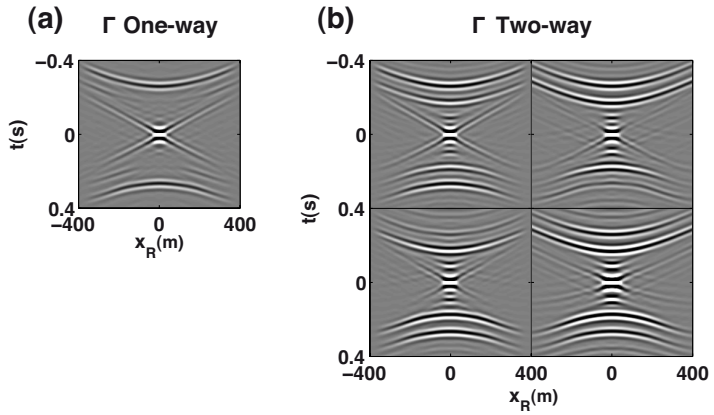

Figure 4.13: PSF of (a) one-way interferometry by MDD and (b) two-way interferometry by MDD for the configuration in Figure 4.11. In two-way MDD, the PSF is a block matrix and each quadrant in (b) represents a block in equation 4.13. Top left is $(\bar{\mathbf{p}})^H\bar{\mathbf{p}}$, top right is $-(\bar{\mathbf{p}})^H\bar{\mathbf{v}}$, bottom left is $-(\bar{\mathbf{v}})^H\bar{\mathbf{p}}$, and bottom right is $(\bar{\mathbf{v}})^H\bar{\mathbf{v}}$.

The results of the multidimensional deconvolution procedure are shown in Figure 4.14: the effect of spurious multiples in Figure 4.12 have been mitigated by either one- or two-way MDD and an estimate of the velocity Green's function (for a virtual monopole source $\mathbf{x}_{VS}$ fixed at the central receiver – the white triangle in Figure 4.11) is obtained. We notice however that when the two-way representation theorem is solved via MDD without directional constraints as in equation 4.12 (Figure 4.14c), the retrieved Green's function not only shows symmetry with respect to the time axis as in the previous example, but weak residual energy of multiple events from the seabed around $\pm 0.4\ s$ also remains in the MDD estimate. This indicates that the basic two-way MDD is less successful than one-way MDD in removing the effect of the overburden, in this seabed case.

As in the previous example, the difference in the solution of two-way MDD compared to that of one-way MDD (Figure 4.14b) is a consequence of the fact that any pair of Green's functions $G_{p,q}$ and $G_{v_n,q}$ that fit the recorded data, and which belong to a state with the same medium parameters as the recorded data p and v_n inside ∂D_R, but possibly different boundary conditions at ∂D_R and/or different medium parameters outside ∂D_R, are a valid choice of Green's functions for the representation theorem in equation 4.1. By adding boundary constraints on the directionality of the pressure and velocity Green's functions to the two-way representation (equation 4.11) as shown in equation 4.16, we define the particular Green's function that we wish to estimate and the solution of two-way constrained MDD (Figure 4.14d) becomes very similar to that retrieved by one-way MDD (Figure 4.14b). We have noted that these directionality constraints are particularly beneficial in the case of receivers sitting on a discontinuity (e.g., the seabed) that generates prominent multiples in the data. In fact, by using the

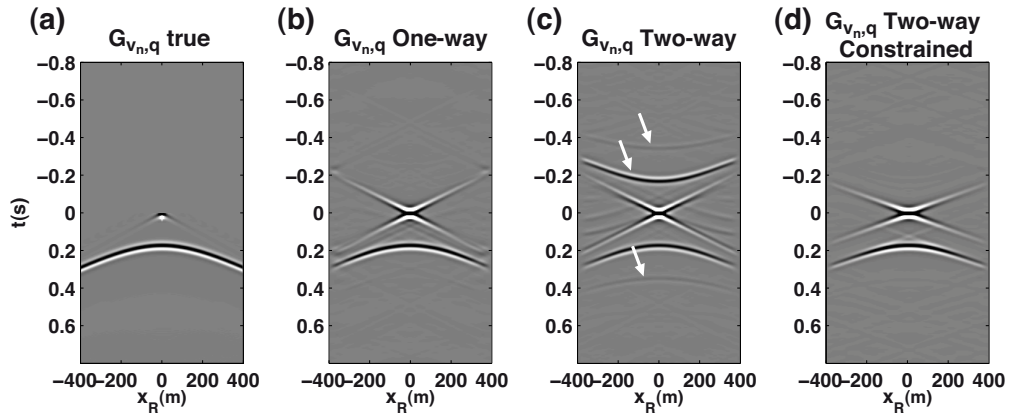

Figure 4.14: Velocity Green's function from a virtual monopole source for the configuration in Figure 4.11. (a) Modelled response, and solutions from (b) one-way MDD, (c) two-way MDD, and (d) two-way directionally-constrained MDD. White arrows indicate events that are reconstructed by two-way MDD and suppressed using a directional constraint in two-way constrained MDD.

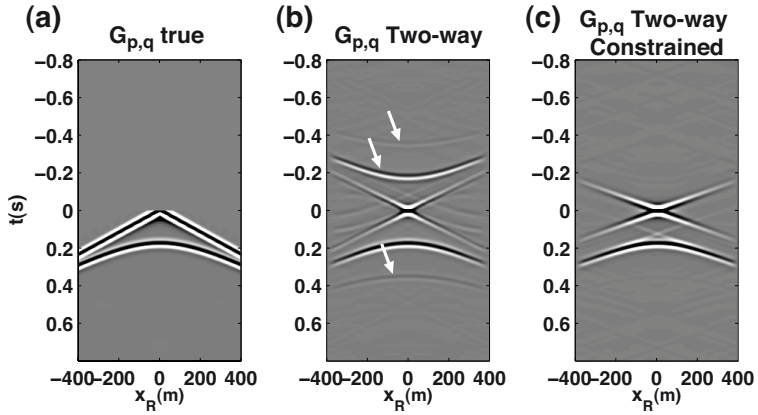

Figure 4.15: Pressure Green's function from a virtual monopole source for the configuration in Figure 4.11. (a) Modelled response, and solutions from (b) two-way MDD, and (c) two-way directionally-constrained MDD.

medium parameters of the layer below the ocean bottom in the directionality constraints (as well as in wavefield decomposition applied before one-way MDD), we have enforced the receiver line to be below the seabed, such that its effect is suppressed by MDD. This was not possible in unconstrainted two-way MDD because the recordings were directly used in the inversion process. Additionally, seismic interferometry by means of the two-way representation also recovers an estimate of the pressure Green's function as shown in Figure 4.15. Similarly to the retrieval of the velocity Green's function, two-way MDD leaves some spurious events in the pressure field (Figure 4.15b) that are suppressed in its directionally constrained counterpart (Figure 4.15c).

To further study the role of directionality constraints on two-way MDD, Figure 4.16

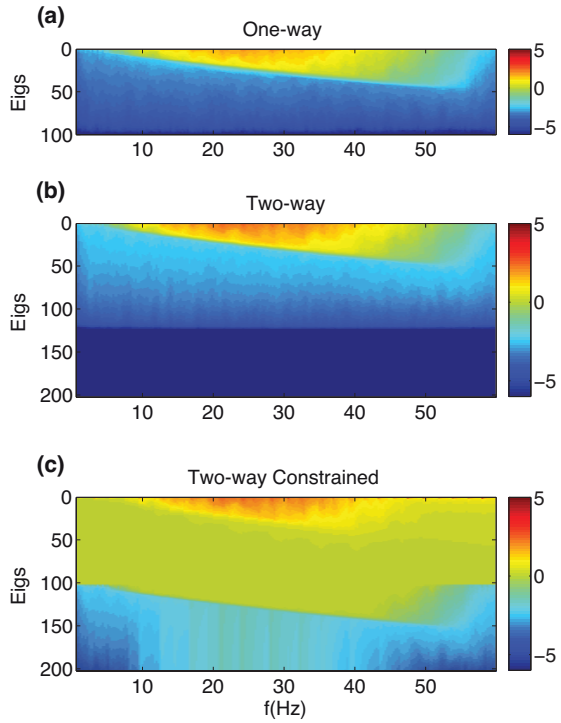

Figure 4.16: Singular values at each frequency for appropriate PSF matrices in each of the following cases for the configuration in Figure 4.11. (a) One-way MDD (matrix $\Gamma^{-}_{\mathbf{ow}}$), (b) two-way MDD (matrix $\Gamma_{\mathbf{tw}}$), and (c) two-way directionally-constrained MDD (matrix $\Gamma_{\mathbf{tw}} + \lambda^2_{D_p}(\mathbf{D}^{+}_{\mathbf{p}})^H\mathbf{D}^{+}_{\mathbf{p}}) + \lambda^2_{D_v}(\mathbf{D}^{+}_{\mathbf{v}})^H\mathbf{D}^{+}_{\mathbf{v}}$) with $\lambda^2_{D_p} = \lambda^2_{D_v} = 10$.

shows the eigenvalues of the three different PSFs for each frequency. While almost half of the most significant PSF singular values for two-way MDD (Figure 4.16b) are very similar to those of one-way MDD (Figure 4.16a) and the remaining half dramatically drop towards zero, the role of the constraint on directionally of the sought Green's functions becomes evident in Figure 4.16c. The null (or very small) singular values of the two-way PSF are increased in magnitude while the large singular values are almost unchanged. Since conditioning depends on the magnitude of the small singular values compared to the largest, this is clearly improved by the added constraints.

4.5 Discussion

Directional wavefield decomposition is a method that is used frequently in seismic processing to separate events of interest from others that are considered as noise and which affect the interpretability of the data (see Appendix B for a review on wavefield decomposition). However, the requirement of (accurate) knowledge of medium properties along a densely and uniformly sampled receiver array, together with assumptions that

the medium properties vary slowly along the receiver array and that the recorded velocity field is a measure of true ground motion (so-called vector fidelity, Norris et al., 2006) are not always fulfilled. Moreover, the decomposition matrices in equations B.3 and B.4 are unstable because of singularities near the critical angle (van der Neut and Herrmann, 2013). This introduces errors in the estimates of the decomposed fields that can propagate through the multidimensional inversion process and deteriorate the interferometric estimates.

The ability to implement seismic interferometry by MDD using full (pressure and velocity) fields rather than directionally decomposed fields is beneficial in that the knowledge of medium properties is no longer required (unless directional constraints are used). The decomposition is also directly embedded inside the regularized inverse problem leading to higher fidelity in the reconstruction around the critical angle, as similarly shown by van der Neut and Herrmann (2013) in their wavefield separation via sparsity-promoting inversion. Furthermore, the two-way MDD approach is useful in situations where one or more of the other requirements of wavefield separation are not satisfied. A first encouraging result is shown in Figure 4.17 where two-way MDD performs very well even though the receiver array intersects a sudden velocity change (hence the above requirement of slowly-varying properties is not fulfilled). A detailed comparison of our approach with one-way MDD in situations where assumptions of frequency-wavenumber wavefield decomposition are not fulfilled (i.e., medium parameter along the receiver array are not uniquely defined) is however beyond the scope of this work.

As a consequence of including velocity recordings in the two-way MDD equations, the dimension of the point-spread function doubles with respect to that of one-way MDD. The effect of this is two-fold: the inversion of the PSF is more computationally expensive for two-way than one-way MDD, and the inverse problem is also generally more poorly conditioned. However, if the inversion of the two-way PSF is performed taking advantage of its structure (a matrix that partitions into block form), two matrices of dimensions $N_R \times N_R$ need to be inverted (see Press et al. (2002) — p.77) rather than the full matrix of dimension $(2N_R \times 2N_R)$, making the computational cost of two-way MDD only twice that of one-way MDD. Moreover, additional constraints on the solution norm and the directivity of the retrieved Green's functions have been shown to be beneficial to regularize the inverse problem. As an alternative, if two-way MDD was solved in the time-domain as done by van der Neut and Herrmann (2013) for one-way MDD, we could also design a constraint that ensures the acausual solution of the problem to go to zero. While the time-domain inversion is computationally more intensive, an advantage of this regularization term with respect to our directional constraint is that no information about the medium parameters would be required.

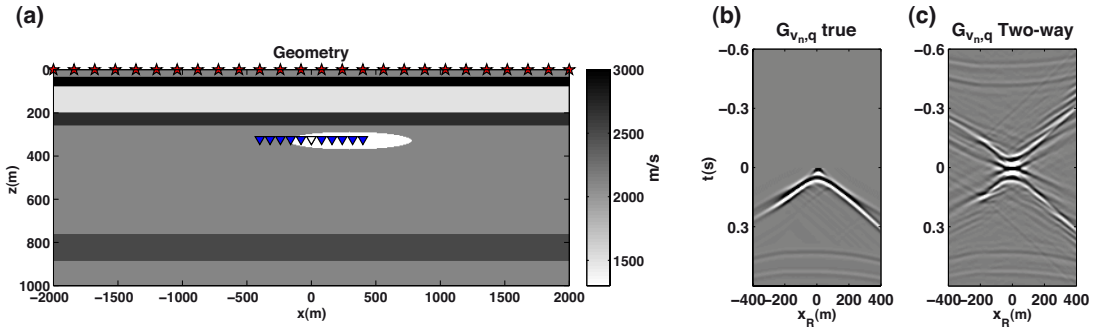

Figure 4.17: (a) Configuration for borehole redatuming with receivers (blue triangles) in a well crossing a gas cloud at depth $z_R = 328\,m$. The virtual source (white triangle) is also located inside the gas cloud and sources (red stars) are situated at the Earth's surface. Velocity Green's function from a virtual monopole source, (b) modelled response, and solution from (c) two-way MDD. An estimate of similar quality is produced for the pressure Green's function from a virtual monopole source.

Two-way MDD not only redatums the recorded data closer to the imaging target by removing some of the unwanted energy (e.g., free-surface multiples, effect of complex overburden), but also provides estimates of both pressure and particle velocity virtual fields without compromising the vector-acoustic nature of the recorded data. As a consequence, vector-acoustic migration algorithms that take advantage of directionality information contained in the velocity fields (Vasconcelos, 2013; Fleury, 2013; El Yadari and Hou, 2013; El Yadari, 2015) can be applied not only to the original recorded data but also to the virtual data, meaning that MDD redatuming and directional migration could be combined together for more accurate imaging of the target of interest.

In addition, estimates of virtual dipole sources can be produced from velocity recordings. These additional fields could aid reconstruction techniques (for example, interpolation of aliased wavefields in the crossline direction — Vassallo et al., 2010) as well as imaging algorithms, which could ultimately benefit from the directivity of dual sources in a similar way to that of dual receivers (Vasconcelos, 2013; Fleury, 2013). While we have shown that such virtual sources could readily be created by using MDD in boreholes or using ocean-bottom data, the quality of their Green's function estimates using current standard streamer data with a near-offset gap (even if we do two passes to provide split-spread data) depends strongly on the quality of interpolation of the missing traces (Ravasi et al., 2015b).

4.6 Conclusion

Seismic interferometry by multidimensional deconvolution has been formulated using a two-way representation theorem of convolution-type. This form of interferometry sim-

ultaneously estimates pressure and velocity virtual responses deprived of the effect of the overburden without requiring a preliminary up/down wavefield separation of the recorded data. However, since the underlying representation is valid for any choice of boundary conditions at the receiver boundary, and for any medium parameters outside the receiver boundary in the Green's functions wave state, the solution obtained depends on the choice of the minimization criterion and regularization employed.

A regularized least-squares solution has been shown to improve the results of interferometry by cross-correlation, and generally to produce estimates of similar quality to those obtained by one-way multidimensional deconvolution. In the special case of a receiver array sitting on an interface, as in our example of ocean-bottom multiple suppression, spurious energy is not completely suppressed by unconstrained two-way MDD and additional constraints on the directionality of the reconstructed fields can be added to improve the interferometric estimates by recasting and solving two-way MDD in the frequency-wavenumber domain. Finally, when dual recordings are available, not only estimates of velocity (and pressure) Green's functions from virtual monopole sources can be obtained via MDD, but also dipole sources can be excited virtually by deconvolving modifications of one- and two-way representation theorems in a multidimensional fashion. Thus Green's functions from dipolar sources can be estimated using data from only pressure sources.

5

Application 1: Two-sided nonlinear elastic subsalt imaging

Source-receiver interferometric imaging can be used to synthesize a subsurface acoustic or elastic image, consisting of a zero-time, zero-offset response between a co-located pseudosource and pseudoreceiver at each image point. However, if the imaging process does not properly account for multiple reflections, and enclosing boundaries of sources and receivers are not available, the image shows artefacts, poorly illuminated areas, and distorted image amplitudes. We demonstrate with numerical examples that two-sided nonlinear imaging provides the best elastic pure-mode (PP and SS) and converted-mode (PS) images, having higher resolution and more uniform illumination than those obtained from both one-sided linear imaging and other intermediate steps of imaging. We also propose practical approaches to construct the additional fields required by two-sided nonlinear imaging without the need for a detailed velocity model and receivers (and/or sources) in the subsurface. Moreover, when conversions are used for imaging, true-amplitude images should theoretically vanish because neither P-to-S nor S-to-P conversions arise at zero-time and zero-offset. Applying a correction procedure that accounts for the polarity reversal in single-shot images helps with their structural interpretation but results in an estimate of the subsurface response with uninterpretable amplitudes. This suggests that there are advantages in exploiting pure-mode SS energy because no polarity correction is required and the resulting image contains meaningful amplitudes that are proportional to the local shear-wave properties of the medium.

5.1 Introduction

An important goal of seismic processing is subsurface imaging (or migration) to estimate both the locations and amplitudes of discontinuities in subsurface properties. When the imaging problem is formulated using reciprocity theory as discussed in Chapter 1, the double surface integration over boundaries of sources and receivers allows us to identify a relationship with a specific form of seismic interferometry, called source–receiver interferometry (SRI — Curtis, 2009; Curtis and Halliday, 2010). Halliday and Curtis (2010) presented an acoustic source-receiver interferometric imaging framework where the imaging condition and wavefield extrapolation steps are expressed explicitly in terms of double integrals over source and receiver boundaries by using the scattering reciprocity theorems of Vasconcelos et al. (2009b). While in Chapter 2 and Chapter 3 we derived elastic formulations for imaging condition and wavefield extrapolation respectively, in this chapter we combine those findings and derive a formulation for fully elastic source-receiver interferometric imaging.

SRI integrals are exact and fully nonlinear, removing the single scattering assumption of Oristaglio (1989): however, they rely on the explicit evaluation of volume integrals of scattered fields to account for multiply scattered waves, which are computationally too expensive for current seismic data and computing capabilities. As discussed in detail in Chapter 2, Vasconcelos (2013) uses a modification of these reciprocity-based integrals where the volume integrals are replaced by surface integrals containing interactions of scattered fields with themselves, by invoking power conservation via the full-waveform version of the generalized optical theorem (Fleury et al., 2010; Douma et al., 2011; Fleury and Vasconcelos, 2012). Incorporating nonlinear multiple-scattering effects in the imaging process (and using fully enclosing boundaries of sources and receivers) reduces imaging artefacts, improves illumination and preserves amplitudes as shown by Fleury and Vasconcelos (2012) and Ravasi and Curtis (2013b).

Another insight derives from the connection between SRI and source-receiver imaging. On the one hand, SRI synthesizes unmeasured wavefield responses (or band-limited Green's functions) between a real source to a real receiver, using only energy recorded at a surrounding boundary of receivers and from a surrounding boundary of sources. On the other hand, source-receiver imaging generates fully nonlinear subsurface images whose amplitudes represent the zero-time, zero-offset scattered wave response between a co-located pseudosource and pseudoreceiver at each image point within the subsurface (Vasconcelos, 2008; Vasconcelos et al., 2010). This physical interpretation of an image as a scattered wavefield leads to various additional interpretation possibilities: for example, the wavefield can be observed and analysed at non-zero times and offsets, resulting in

so-called extended images (e.g., Vasconcelos et al., 2010). The next chapter is devoted to the creation of elastic extended images.

The availability of only a reference estimate of the background velocity model at the start of the imaging stage means that most imaging algorithms rely on a linear, single-scattering assumption in which all wavefields used for imaging must first have all multiples removed (Claerbout, 1971; Oristaglio, 1989; Biondi, 2006). Such methods fail to handle complex scattering effects and therefore do not produce correct amplitudes of reflecting heterogeneities. To overcome this limitation, the full wavefield propagating from any point in the subsurface to the surface receiver array (including all waves that bounce multiple times between interfaces before reaching the acquisition surface) must be determined accurately in order to backproject the recorded multiple reflections/diffractions that travel from this subsurface point to the recording surface. Similarly, an estimate of the full wavefield from the source array to any subsurface point will allow the proper imaging of waves that bounce multiple times in their path from the source to the subsurface point. Estimating these wavefields appears to require a detailed model of subsurface reflectivity heterogeneities to be known in advance of imaging (which is in general unlikely).

However, alternative approaches have recently been introduced to estimate these wavefields in acoustic media: Fleury (2013) adopts an image-based approach, while Broggini et al. (2012) and Wapenaar et al. (2012, 2013) propose an almost purely data-driven approach called autofocusing for retrieving full acoustic Green's function responses from a virtual source in the subsurface (i.e. at each image point) towards the recording array. In the former method, the linear image is used to create a (first-order) estimate of the perturbation to the background model. Unfortunately, errors in estimating small-scale features in the model, both in terms of their spatial locations and magnitudes, turn directly into dynamic and kinematic inaccuracies of the full propagators modelled in this bootstrapped stratigraphic model. The latter method does not require the structural reflectors to be known in detail, in advance of nonlinear imaging: only reflection data at the surface and an estimate of the direct arrival propagating between the virtual source location and the acquisition surface are used to estimate the full propagating Green's functions. These estimated fields are less affected by kinematic errors than those obtained by the image-based approach, however an accurate estimate of the amplitude of the direct arrival and wide-offset reflection data are necessary to achieve dynamically correct fields. Finally, note that both methods can be used with reference models that contain sharp discontinuities from interpreted salt bodies and other converting boundaries (e.g., at the seabed). By henceforth assuming that the availability of a good estimate of such full wavefields (containing also the correct internal multiples) is granted, nonlinear imaging may be applied also when initial knowledge of the medium is

limited to a reference (smooth) velocity model.

The lack of enclosing boundaries represents another challenge to applying source-receiver imaging (or any migration method) in practice: the limitation in source and receiver aperture is known to cause image distortions that can be understood as spatially varying, directionally dependent local blurring (Lecomte, 2008). van der Neut et al. (2013c) presented a novel method that transforms conventional surface seismic data (sources and receiver at the surface) into data with sources and receivers above and below a selected target zone, by inverting a series of multidimensional interferometric equations of convolution- and correlation-type. The creation of a virtual acquisition geometry at a desired depth level can therefore upgrade the seismic imaging from the conventional one-sided illumination case to the two-sided illumination case, where transmissions can be used along with underside reflections for a more uniform illumination of the target of interest.

When source-receiver imaging is formulated in elastic media as done in the following of this chapter, the tensorial nature of the elastic wave equation leads to a range of alternative imaging conditions and definitions of what a true-amplitude elastic image can be. For example, we may construct an image whose amplitudes are the zero-offset, zero-time particle velocity field due to an external volume force pseudosource, or are the compressional-wave (potential) field due to a shear-wave pseudosource. In Chapter 2, we have shown that when potential fields (or equivalently P- and S-wave fields in isotropic media) are chosen, the true-amplitude PS image (the image describing the local interactions between incident P-waves and emerging S-waves) should completely vanish (by destructive interference of images from the various sources and receivers), since P-to-S conversions cannot arise at zero-time, in zero-offset experiments.

The latter observation leads to two different possible approaches to S-wave imaging. When shear energy is used for 'structural' imaging — identification of structures in the subsurface from the images but without the need for meaningfully interpretable amplitudes of the images — then either SS reflections/transmissions or PS (and SP) conversions can be used. When SS waves are used, shear wave energy must reach each image point not only from the receiver wavefield (as is also the case for PS imaging) but also from the source wavefield. If the physical source does not generate S-wave energy such as in marine seismics, linear SS imaging requires at least one (interpreted) hard boundary in the initial estimate of the background velocity model to produce conversions in the propagation from the source to any image point. When instead PS converted waves are chosen, additional processing is required so that single-shot images interfere constructively when stacked together, rather than destructively as is the case in true-amplitude imaging. Algorithms that change the sign of the reflection coefficient

of waves arriving from different directions, thus reducing the degree of cancellation, have been proposed by various authors (Balch and Erdemir, 1994; Denli and Huang, 2008; Rosales et al., 2008; Du et al., 2012). On the other hand, if our goal is true-amplitude shear-wave imaging (where we hope to obtain physically meaningful and hence interpretable amplitudes in the image), SS energy must be preferred to converted (PS or SP) energy since no such 'non-physical' sign changes are necessary. Alternatively, as noted above, we could use extensions of the image in the time and offset domains of the subsurface pseudosources and pseudoreceivers. Such extended images do allow conversions from P-to-S or from S-to-P as the wavefield has time and space to propagate and convert, but require a further imaging or inversion step to obtain point estimates of S-wave reflectivity.

In this chapter, we first combine the findings of Chapters 2 and 3 to define an elastic scattering-based imaging framework under the formalism of source-receiver interferometry and use it to perform linear and nonlinear elastic reverse-time migration (Ravasi and Curtis, 2013b,a). We base our study on a complex geological model (a modified version of the Pluto 1.5 model) and create a synthetic experiment that includes two pairs of limited-aperture arrays of sources and receivers, the first above and the second below the imaging target. We study the potential advantages conveyed both by an ideal acquisition geometry, and by migrating multiply reflected and transmitted waves together with primary reflections. In order to focus on these aspects of imaging and not the construction of propagators discussed above, herein the full and scattered wave propagators are modelled directly and are therefore exact. We pay special attention to the contribution that the various types of waves bring to the construction of the different elastic (PP, PS and SS) images. Thus, we evaluate the potential imaging improvement that algorithms like that of Fleury (2013) and Broggini et al. (2012) could offer if extended to elastic media, by effectively enabling nonlinear imaging and providing Green's function illumination from below. In addition we use a portion of the Pluto model and full illumination of the target (i.e., an enclosing boundary of sources) to demonstrate that the true-amplitude PS image vanishes also when complex geologies are imaged.

5.2 Elastic images by source-receiver interferometric imaging

First, we define an image to be the zero-offset, zero-time sample of the scattered wavefield associated with co-located pseudosources and pseudoreceivers at each point in the subsurface as displayed in Figure 5.1 (Vasconcelos, 2008). In elastic media, a variety of different responses can be obtained by choosing different types of pseudosources and

pseudoreceivers; for example, by using the notation defined in Chapters 2 and 3 (also summarized in Table 1), an image can be defined as the zero-time, scattered wavefield from an external volume force pseudosource at $\mathbf{x}_I$ to a co-located particle velocity pseudoreceiver

$$I_{nm}(\mathbf{x}_I) = \tilde{G}^{S(v,f)}_{(m,n)}(\mathbf{x}_I, \mathbf{x}_I, t = 0). \tag{5.1}$$

This already leads to a variety of different images for different choices of m and n. Alternatively, the image can be defined as the scattered wavefield from a potential pseudosource at $\mathbf{x}_I$ to a co-located potential pseudoreceiver at time zero

$$I_{NM}(\mathbf{x}_I) = \tilde{G}^{S(\Phi,\Phi)}_{(M,N)}(\mathbf{x}_I, \mathbf{x}_I, t = 0) \tag{5.2}$$

which in an isotropic medium leads to separate analyses of PP, PS, SP and SS responses and hence to four separate images.

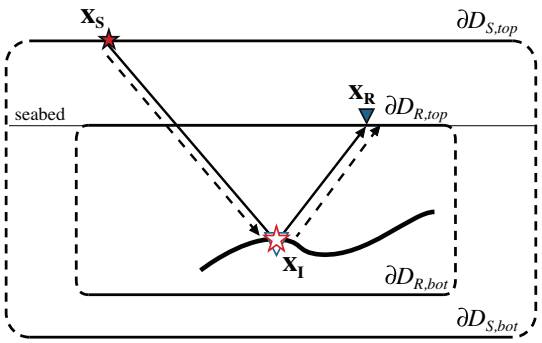

Figure 5.1: Illustration of the physical meaning of a seismic image in the context of source-receiver interferometric imaging: the zero-offset, zero-time scattered field from a pseudosource at $\mathbf{x}_I$ to a co-located pseudoreceiver in the subsurface. The image is computed using the recorded data from physical sources $\mathbf{x}_S$ along the boundary $\partial D_S = \partial D_{S,top} \cup \partial D_{S,bot}$ and physical receivers $\mathbf{x}_R$ along the boundary $\partial D_R = \partial D_{R,top} \cup \partial D_{R,bot}$, the receiver-side propagators from the image point $\mathbf{x}_I$ to physical receivers $\mathbf{x}_R$, and the source-side propagators from physical sources $\mathbf{x}_S$ to the same image point. Although enclosing boundaries are required by the theory of source–receiver imaging, sources and receivers actually used in real acquisition scenarios usually form limited aperture, truncated surface arrays (solid lines), and bottom arrays are seldom if not never available.

To construct these images we can use two-way representation theorems for elastic scattered waves (Wapenaar and Fokkema, 2006; van Manen et al., 2006; Curtis and Halliday, 2010) in a source-receiver imaging framework (Halliday and Curtis, 2010). See Figure 5.1 for a schematic illustration of this concept. Assuming the special case of ocean-bottom acquisition systems with pressure (P wave) sources and multicomponent receivers placed along a flat seabed, an imaging condition to construct potential

responses can be written by rearranging equation 2.16:

$$
\begin{aligned}
&I^{nl}_{NM}(\mathbf{x}_I) = \tilde{G}^{S(\Phi,\Phi)}_{(M,N)}(\mathbf{x}_I, \mathbf{x}_I, t=0) = \\
&\int_0^{+\infty} \left(\oint_{\partial D_S} \frac{2}{\rho(\mathbf{x}_S) V_P(\mathbf{x}_S)} \{ d^{S(\Phi,\Phi)}_{(N,P)}(\mathbf{x}_I, \mathbf{x}_S) G^{0(\Phi,\Phi)*}_{(M,P)}(\mathbf{x}_I, \mathbf{x}_S) \} \, \mathrm{d}^2\mathbf{x}_S \right) \mathrm{d}\omega \\
&+ \int_0^{+\infty} \left(\oint_{\partial D_S} \frac{2}{\rho(\mathbf{x}_S) V_P(\mathbf{x}_S)} \{ d^{(\Phi,\Phi)}_{(N,P)}(\mathbf{x}_I, \mathbf{x}_S) G^{S(\Phi,\Phi)*}_{(M,P)}(\mathbf{x}_I, \mathbf{x}_S) \} \, \mathrm{d}^2\mathbf{x}_S \right) \mathrm{d}\omega,
\end{aligned}
\tag{5.3}
$$

where G and d are the frequency domain source and receiver wavefields, respectively. As discussed in Chapter 2, in theory it is important that the boundary ∂D_S fully encloses the imaging object in order to correctly recover the amplitudes of scattered fields. However, only limited aperture, truncated source arrays are usually available in practice ($\partial D_{S,top}$ — see Figure 5.1). Note that the assumption of ocean-bottom acquisition appears in the d terms where the fields are either P- or S-wave potentials in the subsurface, due only to P-source (pure pressure) excitation functions.

In equation 5.3 the first integral performs the cross-correlation between the reference source wavefield (i.e., that computed in the reference model) and the receiver-side scattered wavefield. The second integral in equation 5.3 constitutes the nonlinear correction to the imaging condition (Fleury and Vasconcelos, 2012; Ravasi and Curtis, 2013b), which accounts for source-side multiple scattering (e.g., internal multiples occurring between the physical source $\mathbf{x}_S$ and the pseudoreceiver $\mathbf{x}_I$).

The exact expressions for reconstructing the receiver-side wavefields in equation 5.3 are

$$
\begin{aligned}
&d^{S(\Phi,\Phi)}_{(N,P)}(\mathbf{x}_I, \mathbf{x}_S) = \\
&\oint_{\partial D_R} \{ d^{S(p,\Phi)}_{(-,P)}(\mathbf{x}_R, \mathbf{x}_S) G^{0(\Phi,f)*}_{(N,z)}(\mathbf{x}_I, \mathbf{x}_R) - d^{S(v,\Phi)}_{(z,P)}(\mathbf{x}_R, \mathbf{x}_S) G^{0(\Phi,h)*}_{(N,zz)}(\mathbf{x}_I, \mathbf{x}_R) \} \, \mathrm{d}^2\mathbf{x}_R \\
&+ \oint_{\partial D_R} \{ d^{(p,\Phi)}_{(-,P)}(\mathbf{x}_R, \mathbf{x}_S) G^{S(\Phi,f)*}_{(N,z)}(\mathbf{x}_I, \mathbf{x}_R) - d^{(v,\Phi)}_{(z,P)}(\mathbf{x}_R, \mathbf{x}_S) G^{S(\Phi,h)*}_{(N,zz)}(\mathbf{x}_I, \mathbf{x}_R) \} \, \mathrm{d}^2\mathbf{x}_R
\end{aligned}
\tag{5.4}
$$

and

$$
\begin{aligned}
&d^{(\Phi,\Phi)}_{(N,P)}(\mathbf{x}_I, \mathbf{x}_S) = \\
&\oint_{\partial D_R} \{ d^{(p,\Phi)}_{(-,P)}(\mathbf{x}_R, \mathbf{x}_S) G^{(\Phi,f)*}_{(N,z)}(\mathbf{x}_I, \mathbf{x}_R) - d^{(v,\Phi)}_{(z,P)}(\mathbf{x}_R, \mathbf{x}_S) G^{(\Phi,h)*}_{(N,zz)}(\mathbf{x}_I, \mathbf{x}_R) \} \, \mathrm{d}^2\mathbf{x}_R,
\end{aligned}
\tag{5.5}
$$

where p and v_z are the pressure and vertical particle velocity recordings, respectively, and the G terms represent the receiver-side propagators. Equations 5.4 and 5.5 also come from representation theorems as described in Chapter 3. Similarly to the source boundary in the imaging condition, the receiver boundary ∂D_R should enclose the imaging object to achieve true-amplitude imaging. Finally note that, as source-side

scattered propagators G^S can be computed by subtracting the reference propagators computed in the background model from the full propagators computed in the exact model, receiver-side scattered propagators d^S can be equivalently obtained by back-propagating the required data both in the background and exact model and subtract the two extrapolated wavefields.

The first integral in equation 5.4 is linear in the relation between data and the extrapolation model: reference propagators are used to backpropagate the recorded, scattered wavefield into the subsurface. By contrast the second integral in equation 5.4 and that in equation 5.5 are nonlinear in the extrapolation model, because (full) recorded data are extrapolated through scattered and total propagators both of which include receiver-side internal multiples. Thus the latter terms include scattered recorded data interacting with scattered wave propagators resulting in a nonlinear relation between the image and the (a priori unknown) scattering perturbations. Note that if the scattered field in the first integral of equation 5.3 is obtained by means of linear wavefield extrapolation, this integral becomes equivalent to a conventional cross-correlation imaging condition (e.g., Chang and McMechan, 1994; Yan and Sava, 2008). Otherwise when nonlinear wavefield extrapolation is carried out, the imaging condition also accounts for the receiver-side multiple scattering (e.g., internal multiples occurring between the physical receiver $\mathbf{x}_R$ and the pseudosource image point $\mathbf{x}_I$).

The image given by the combination of equations 5.3 to 5.5 is thus fully nonlinear on both the acquired data and the subsurface model. It accurately focuses the energy from multiple scattering interactions along with primary scattering, provided that scattered wave propagators are available. We therefore refer to this imaging procedure as nonlinear elastic reverse-time migration (NLERTM). While the formulation proposed in this chapter is suitable for source-profile migration, in Appendix D a reciprocal formulation for receiver-profile NLERTM is discussed.

In the context of traditional elastic reverse-time migration (ERTM) where only primaries are used to map unknown discontinuities in the subsurface via knowledge of a reference model, equations 5.3 and 5.4 can be simplified under a Born approximation (i.e., single scattering assumption) and combined together, to give a linear image

$$I^l_{NM}(\mathbf{x}_I) = \int_0^{+\infty} \Bigg(\oint_{\partial D_S} \frac{2}{\rho(\mathbf{x}_S) V_P(\mathbf{x}_S)} G^{0(\Phi,\Phi)*}_{(M,P)}(\mathbf{x}_I, \mathbf{x}_S) \oint_{\partial D_R} \{ \breve{d}^{S(p,\Phi)}_{(-,P)}(\mathbf{x}_R, \mathbf{x}_S) \times G^{0(\Phi,f)*}_{(N,z)}(\mathbf{x}_I, \mathbf{x}_R) - \breve{d}^{S(v,\Phi)}_{(z,P)}(\mathbf{x}_R, \mathbf{x}_S) G^{0(\Phi,h)*}_{(N,zz)}(\mathbf{x}_I, \mathbf{x}_R) \} \, \mathrm{d}^2\mathbf{x}_R \, \mathrm{d}^2\mathbf{x}_S \Bigg) \, \mathrm{d}\omega, \tag{5.6}$$

where $\breve{d}^S$ indicates a dependance on Born data that approximate the full recorded data (d^S) by neglecting multiple scattering (Wapenaar et al., 2010b). Finally, we define

one-sided illumination when $\partial D_R = \partial D_{R,top}$ and $\partial D_S = \partial D_{S,top}$, while two-sided illumination is given by $\partial D_R = \partial D_{R,top} \cup \partial D_{R,bot}$ and $\partial D_S = \partial D_{S,top} \cup \partial D_{S,bot}$ (see Figure 5.1).

5.3 Numerical example

We now compare linear and nonlinear images in a complex medium. We present a numerical example where PP, PS, and SS images are computed using a modified version of the synthetic model Pluto 1.5 released by the SMAART JV consortium (Stoughton et al., 2001). Our model is created by flattening the seabed at a depth of $z_{seabed,1} = 760m$ and since we want to test two-sided imaging we also add a second water layer at the bottom of the model ($z_{seabed,2} = 7600\ m$). Thus we can model pure P-wave sources also along the boundary below the imaging target (otherwise additional S-wave sources would be required in the lowermost solid media by the imaging condition in equation 5.3). Figure 5.2a shows the true P-wave model and Figure 5.2b shows the reference model used for conventional (linear) imaging. The latter is obtained by smoothing the model in Figure 5.2a while keeping sharp boundaries at the fluid-solid interfaces and at the edges of the salt bodies. Figure 5.2c displays the difference between true and reference model, which represents the unknown perturbation that we would like to image. The S-wave velocity model is a scaled version of the P-wave velocity with a linearly depth-variant ratio ranging from 0.5 at $z_{seabed,1}$ to 0.7 at $z_{seabed,2}$. The ratio is, however, kept constant inside the two salt bodies ($V_S/V_P = 0.55$). Finally, the density is obtained from the P-wave velocity through the well-known Gardner's relationship $\rho = 0.23V_P^{0.25}$ (Gardner et al., 1974).

Two truncated, limited-aperture boundaries of 51 monopole P-wave sources at depths of $z_{S,1} = 40\ m$ and $z_{S,2} = 8320\ m$ with horizontal spacing $x_S = 152\ m$ are used to model the synthetic data together with two boundaries of multi-component receivers (white lines in Figure 5.2a) placed along the upper and lower seabeds throughout the extension of the model with horizontal spacing $x_R = 7.6\ m$. The modelling is carried out using a Ricker wavelet pulse with 15 Hz peak frequency and a maximum recording time of $10\ s$. Absorbing boundaries are used (to remove the effects of the free-surface), otherwise further dipole P-wave sources would be required for a proper handling of in- and out-going waves at the source boundary ∂D_S (van Manen et al., 2007; Vasconcelos, 2013; Vasmel et al., 2013).

We carry out six different imaging experiments which are represented schematically in Figure 5.3, where different combinations of sources and receivers, and linear and nonlinear terms are used. Elastic images of pure-mode reflections/transmissions (PP

and SS) and conversions (PS) are compared in terms of resolution, illumination and presence of cross-talk noise. We devote special attention to the areas just above and below one of the salt bodies where issues of illumination (below) and cross-talk (above) are usually severe. The quality of reconstruction of the complex stratigraphy around one of the faults in the subsurface will also be studied for the different imaging results.

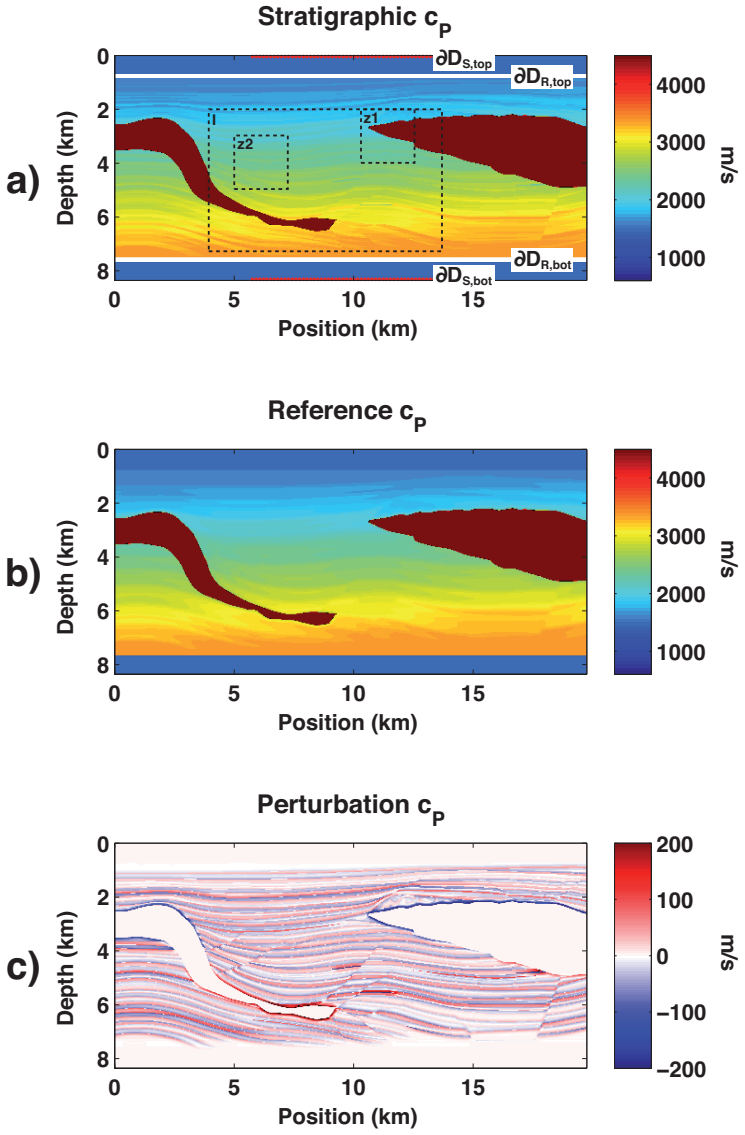

Figure 5.2: Pluto models. Stratigraphic P-wave velocity model is shown in (a) along with the shot locations (red lines) and receiver geometry (white lines). The elastic images are computed inside the windowed area $'I'$, and areas $'z_1'$ and $'z_2'$ represent a portion of one of the salt bodies and a layered structure around a fault, respectively. The P-wave migration velocity model shown in (b) is a smoothed version of the true model but with sharp boundaries around the salts and for upper and lower seabeds, while (c) shows the true P-wave velocity perturbation (the difference between (a) and (b)).

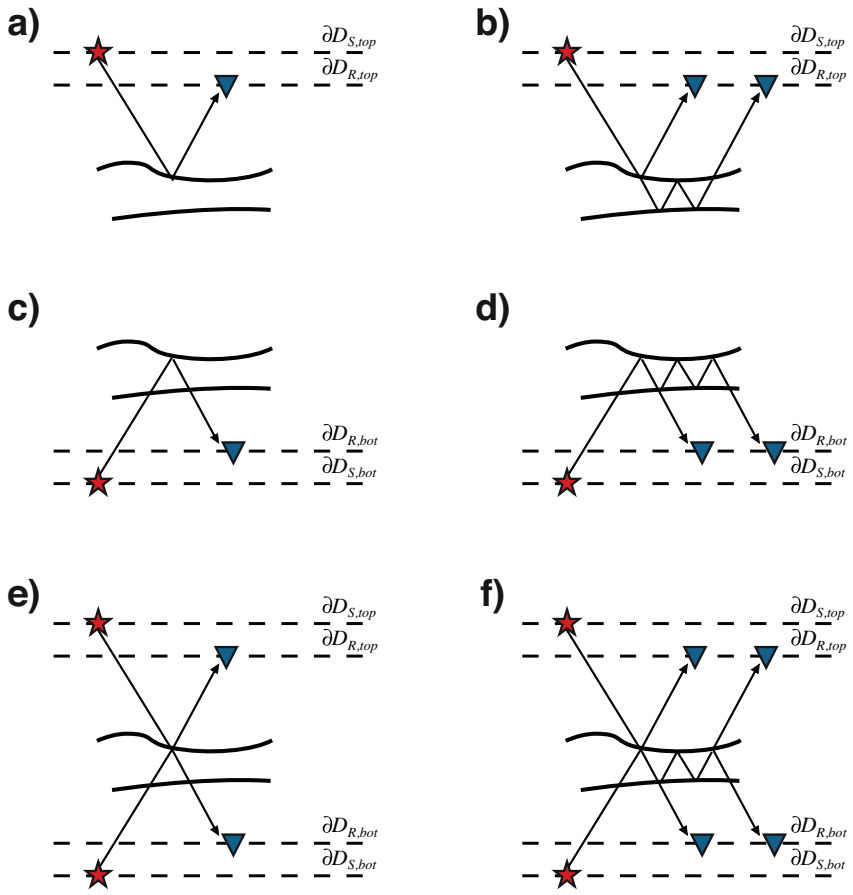

Figure 5.3: Schematic representation of the six different imaging experiments used in this study. (a) One-sided (top) elastic reverse-time migration (ERTM – which is linear), (b) one-sided (top) nonlinear elastic reverse-time migration (i.e., NLERTM), (c) one-sided (bottom) ERTM, (d) one-sided (bottom) NLERTM, (e) two-sided ERTM, (f) two-sided NLERTM. Black rays identify the type of events accounted for in each of the experiments: one-sided imaging uses reflections only, whereas two-sided imaging also uses transmissions to improve the imaging result. Moreover, linear imaging only accounts for focusing of the primary reflections and transmissions while nonlinear imaging handles also multiple reflections and transmissions with multiple reflections.

PP images

Figure 5.4 shows the PP image obtained by means of one-sided (top) reflection ERTM (i.e., conventional Born elastic reverse-time migration) juxtaposed with that of one-sided (top) reflection NLERTM. The improvement arising from the additional focusing of multiple-scattered energy (i.e., internal multiples) at any image point is remarkable. Interfaces are more clearly defined at all depths, there is a general increase in spatial resolution of the image structure, and areas that are poorly illuminated by single-scattering events are now better resolved. The artefacts affecting the top of the salt

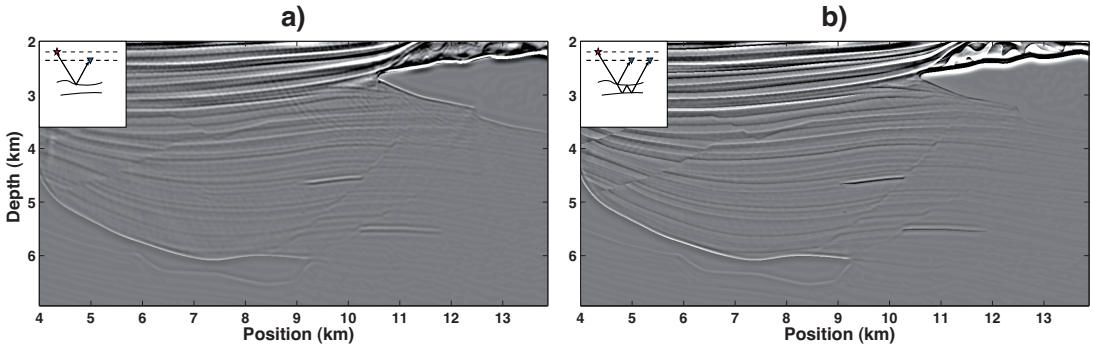

Figure 5.4: PP images obtained by means of (a) linear and (b) nonlinear source-receiver, elastic reverse-time imaging using sources and receivers only above the imaging target (i.e., $\partial D_{S,top}$ and $\partial D_{R,top}$ in Figure 5.2).

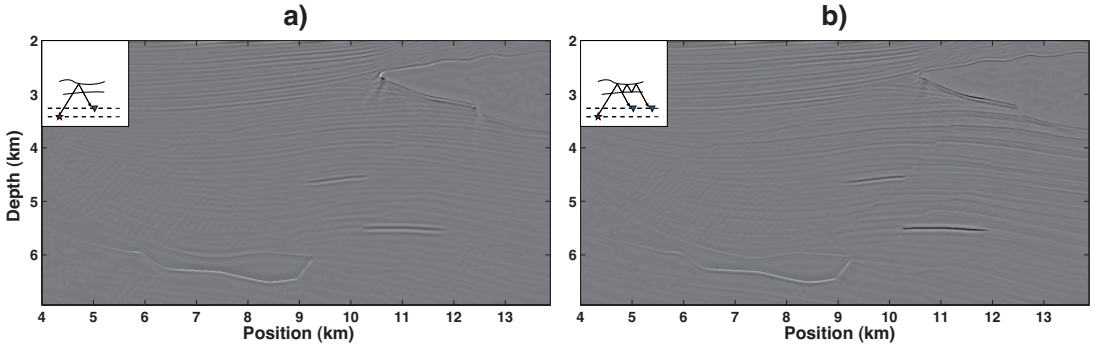

Figure 5.5: PP images obtained by means of (a) linear and (b) nonlinear source-receiver, elastic reverse-time imaging using sources and receivers only below the imaging target (i.e., $\partial D_{S,bot}$ and $\partial D_{R,bot}$ in Figure 5.2).

body on the right are significantly suppressed, and the nonlinear image (Figure 5.4b) reveals the complex structure showing the power of migrating multiples together with primaries. It is important to note that the observed improvements are not due to the multiply-scattered wavefields themselves, they are rather the result of the interplay with the singly-scattered waves at each image point.

Next, we study the value of having a second boundary of sources and receivers at the bottom of the model, but we first assume that top and bottom boundaries are used in two separate reflection imaging experiments. As a general remark, one-sided (bottom) reflection ERTM (Figure 5.5a) and NLERTM (Figure 5.5b) images have smaller amplitudes* compared to images from top sources and receivers because of the higher impedance contrast at the bottom seabed. Illumination of the imaging target from different directions helps to construct a more isotropically illuminated final image of the subsurface, and to compensate for cross-talk artefacts that arise in the elastic images when only data from top sources and receivers are migrated. Reflection events (both

*Note: all images are displayed in the same range of amplitudes.

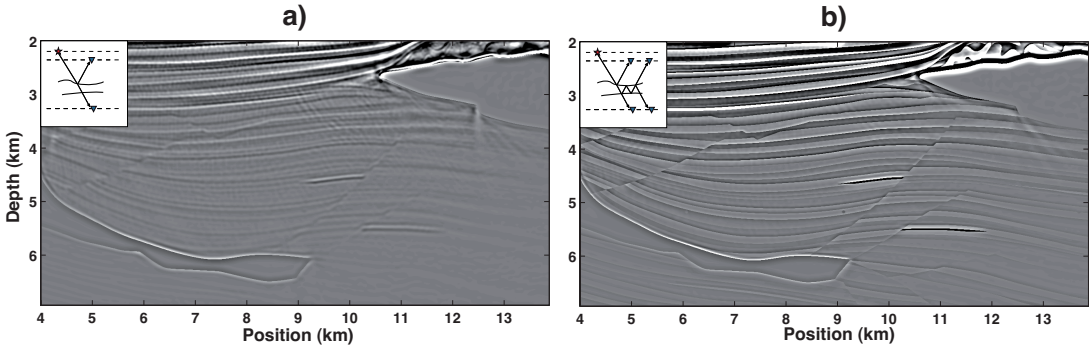

Figure 5.6: PP images obtained by means of (a) linear and (b) nonlinear source-receiver, elastic reverse-time imaging using sources above (i.e., $\partial D_{S,top}$ in Figure 5.2) and receivers both above and below the imaging target (i.e., $\partial D_R = \partial D_{R,top} \cup \partial D_{R,bot}$ in Figure 5.2).

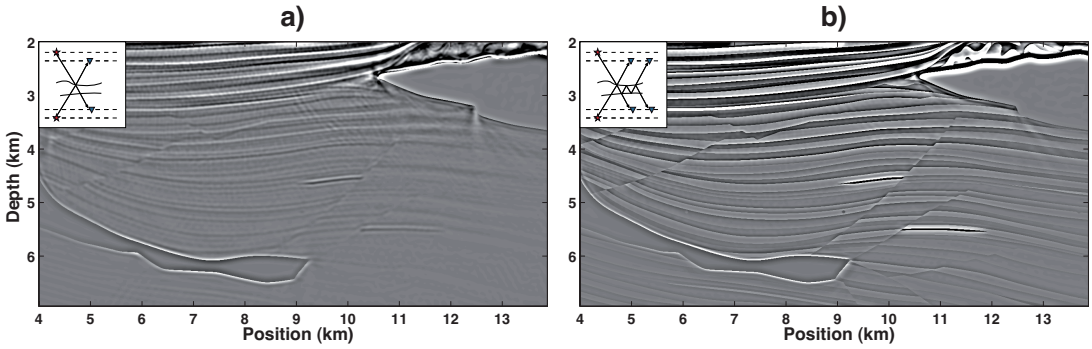

Figure 5.7: PP images obtained by means of (a) linear and (b) nonlinear source-receiver, elastic reverse-time imaging using sources and receivers both above and below the imaging target (i.e., $\partial D_S = \partial D_{S,top} \cup \partial D_{S,bot}$ and $\partial D_R = \partial D_{R,top} \cup \partial D_{R,bot}$ in Figure 5.2).

primaries and multiples) generated by sources placed within the medium below the salt bodies, for example, give rise to a better image of the layered structure below the salt on the right (Figure 5.5) compared to that of reflections from the top (Figure 5.4).

Reflections and transmissions are finally combined together by the simultaneous use of top and bottom source and receiver boundaries. Note that when we use the term 'transmissions' we refer to globally transmitted waves that are emitted on one side of the imaging target and recorded on the opposite side. In Figure 5.6 we show the advantage of recording data at two different depth levels (top and bottom panels) when only top sources are available, while in Figure 5.7 we display images that are effectively computed from a full source–receiver two-sided illumination as depicted in Figures 5.3e and f. Transmissions contain useful additional information that is responsible for more accurate imaging below salt bodies (high impedance obstructions) as is clearly visible by comparing, for example, Figure 5.6a with Figure 5.4a and Figure 5.6b with Figure 5.4b. Two-sided sources, on the other hand, add contributions throughout the imaging target that equalize the amplitudes in the final image (Figure 5.7b). The overall im-

provement provided by transmitted waves in imaging might come from the difference between the (series of) transmission and the (series of) reflection coefficients, one being high energy when the other is low energy and vice versa. Specifically for the deeper reflectors, transmitted waves have travelled a shorter path (from top to bottom) than reflections (from top to reflector to top again), thus losing less energy because of geometric spreading and scattering. Finally, the improvements in reflectors consistency below the salt bodies may occur because waves recorded at the bottom receiver array include a 'fan' of waves emitted by sources laterally far from each salt body, and hence which have travelled without interacting with strong impedance contrast of the salt bodies.

In Figures 5.8 and 5.9 close-ups of the portion of the images around the salt body on the right and one of the faults in the model are shown for the different imaging experiments discussed above. Again note the increase in spatial resolution and illumination arising from proper handling of multiple reflections. Moreover, adding sources and receivers at a given depth level results in images with more uniform amplitudes (Figures 5.8f and 5.9f).

Shear-wave (SS and PS) images

Elastic data like those recorded by ocean-bottom acquisition systems offer the possibility to image using S-wave energy, either (SS) purely reflected or (PS or SP) converted energy. The different behaviour of shear waves compared to compressional waves has, however, long presented challenges in the practice of seismic imaging. Note that in our formulation of the imaging problem, SS imaging can be performed without S-wave sources. Since converted S-wave energy reaches every point in the image and is scattered by heterogeneities, SS images are constructed by evaluating $I_{SS}(\mathbf{x})$ in equation 5.2. Similarly, PS images are obtained by evaluating $I_{PS}(\mathbf{x})$.

Here, we first use shear-wave energy for 'structural' imaging, with the primary objective of reconstructing the structure of reflectors/diffractors but not necessarily attempting to retrieve the correct dynamics of $\tilde{G}^S(\mathbf{x}_I, \mathbf{x}_I, t = 0)$ in the imaging condition. PS and SS images are compared using linear and nonlinear terms, and one- and two-sided imaging for our synthetic example. The first image displayed in Figure 5.10 is the result of PS one-sided (top) reflection ERTM when stacking over shots, without the application of any polarity correction procedure. Apart from the spurious energy just above the salt body on the right resulting from the interaction of strong converted waves in the source and receiver wavefields, we barely see any interfaces because of the destructive

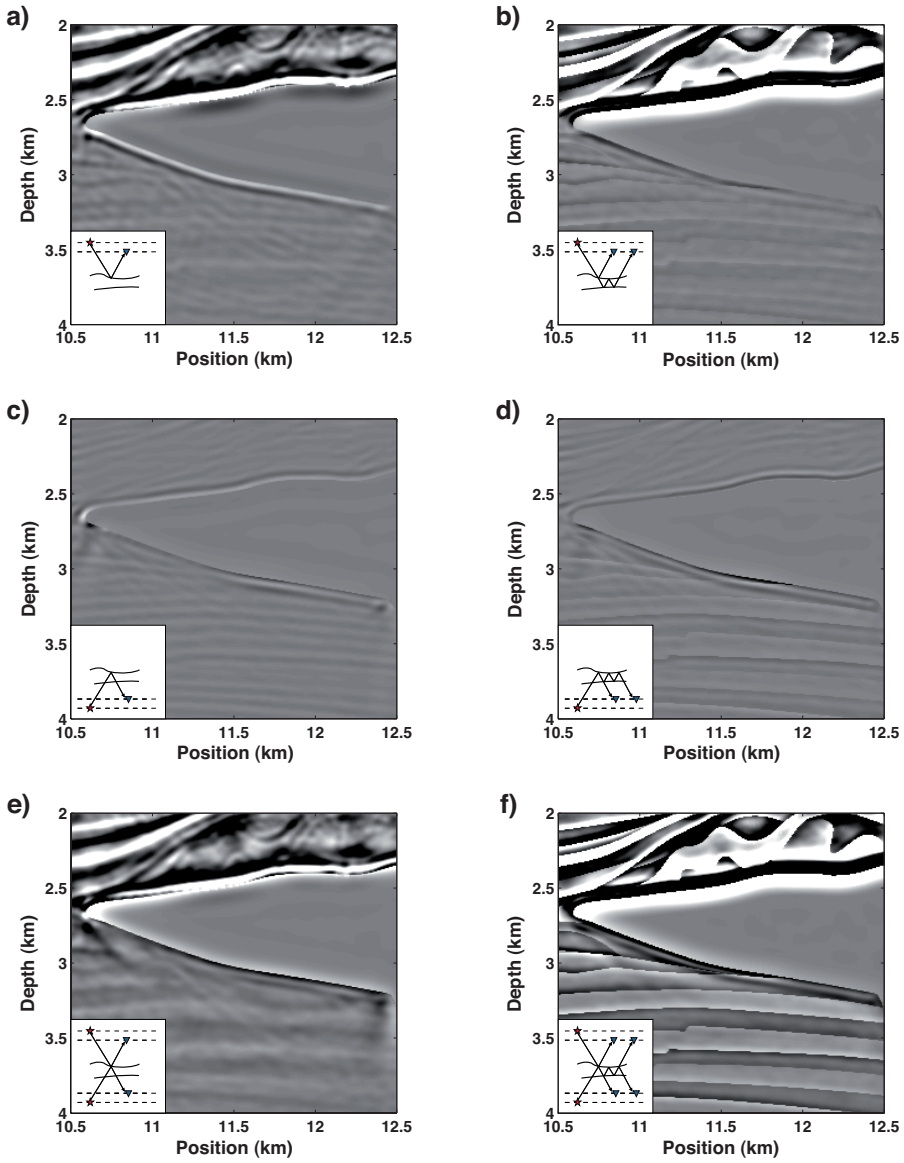

Figure 5.8: Salt body PP images for the six different imaging experiments depicted in Figure 5.3, for region z_1 in Figure 5.2a. Figures 5.8a and b are close-ups of Figures 5.4a and b, Figures 5.8c and d are close-ups of Figures 5.5a and b, and Figures 5.8e and f are close-ups of Figures 5.7a and b.

interference of single-shot images, and this effect becomes more and more apparent as we stack more and more shots.

In Figure 5.11a the same single-shot images are stacked together after correcting for the polarity change by simply multiplying by -1 the images on one side of each shot position while keeping the other side unchanged. Although the quality of the PS ERTM image is not comparable to that obtained from a PP imaging condition, some of the shallow interfaces and the two reservoirs are still resolved. Figures 5.11b to f display converted-

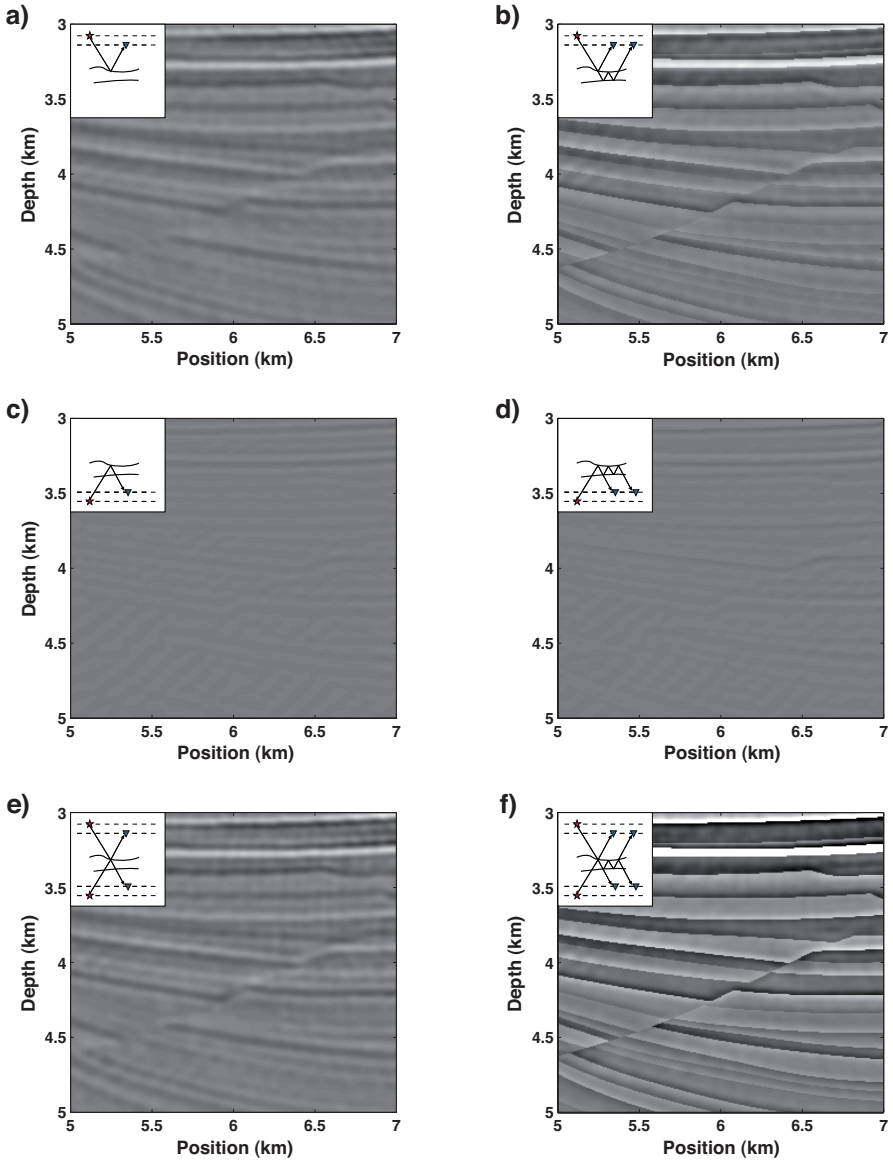

Figure 5.9: Fault PP images for the six different imaging experiments depicted in Figure 5.3, for region z_2 in Figure 5.2a. Figures 5.9a and b are close-ups of Figures 5.4a and b, Figures 5.9c and d are close-ups of Figures 5.5a and b, and Figures 5.9e and f are close-ups of Figures 5.7a and b.

wave images obtained from the other imaging experiments in Figure 5.3 after applying the polarity correction procedure. While linear (and nonlinear) reflections from the bottom acquisition geometry contribute in the same way as those in PP imaging by basically enhancing the quality of the image in areas poorly illuminated by primaries (e.g. below the salt bodies), PS transmissions show a remarkable lower frequency content (see Figures 5.11e and f) compared to their compressional-wave counterparts (Figure 5.7a and b) and converted-wave reflections (Figures 5.11a-d). While this behaviour of

nonlinear PS images is still under study, at this point we believe that the low frequency content in these images is largely non-physical in nature, and is due to the departure from the scattered field definition of the image when the polarity correction is applied.

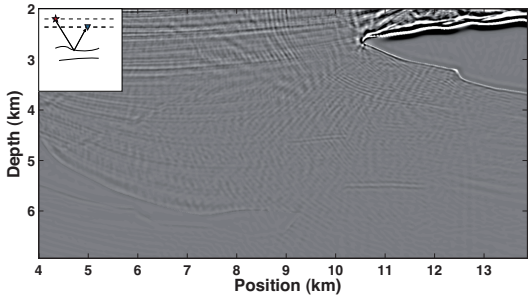

Figure 5.10: PS linear ERTM image using sources and receivers above the imaging target without correcting for converted shear wave polarity reversal.

Similarly to PP and PS imaging, in Figure 5.12 we display pure shear-wave images obtained from the different imaging experiments in Figure 5.3. Note that in marine ocean-bottom acquisition systems sources cannot directly generate shear waves because they are placed inside the water layer. SS conventional (linear) imaging thus requires the additional, accurate knowledge of one or more sharp boundaries (e.g., fluid-solid interfaces or the edge of the salt bodies) for the generation of S-wave energy in the source wavefield. By contrast, all interfaces present in the stratigraphic model are generators of shear waves in nonlinear imaging since the full (and scattered) propagators are directly modelled in the exact model. Both recorded shear wave energy and the same interfaces produce S-wave energy in the receiver wavefield for all six imaging configurations.

Pure-mode shear wave imaging does not require any additional processing step to account for positive and negative reflection coefficients because the polarity of shear reflections/transmissions is such that the procedure of stacking over shots has a naturally constructive behaviour. It is also worth noting that, although the quality of SS images (Figure 5.12) is generally higher than that of polarity-corrected PS images (Figure 5.11), the interaction between shear wave energy in the source and receiver wavefield produces prominent artefacts at strong diffractors such as at the edges of the salt bodies. Although this needs to be studied in more detail, these artefacts are likely caused by the fact that SS images rely entirely on the conversion of P-to-S transmission at the seafloor. While PP transmission occurs over the entire range of incidence angles, P-to-S transmission is therefore restricted to a subset of incident angles limited by the critical angle (which is controlled by the ratio of PS velocities at the seafloor). As a result, a pure mode S-wave image in this case can be considerably angle-limited in terms of image

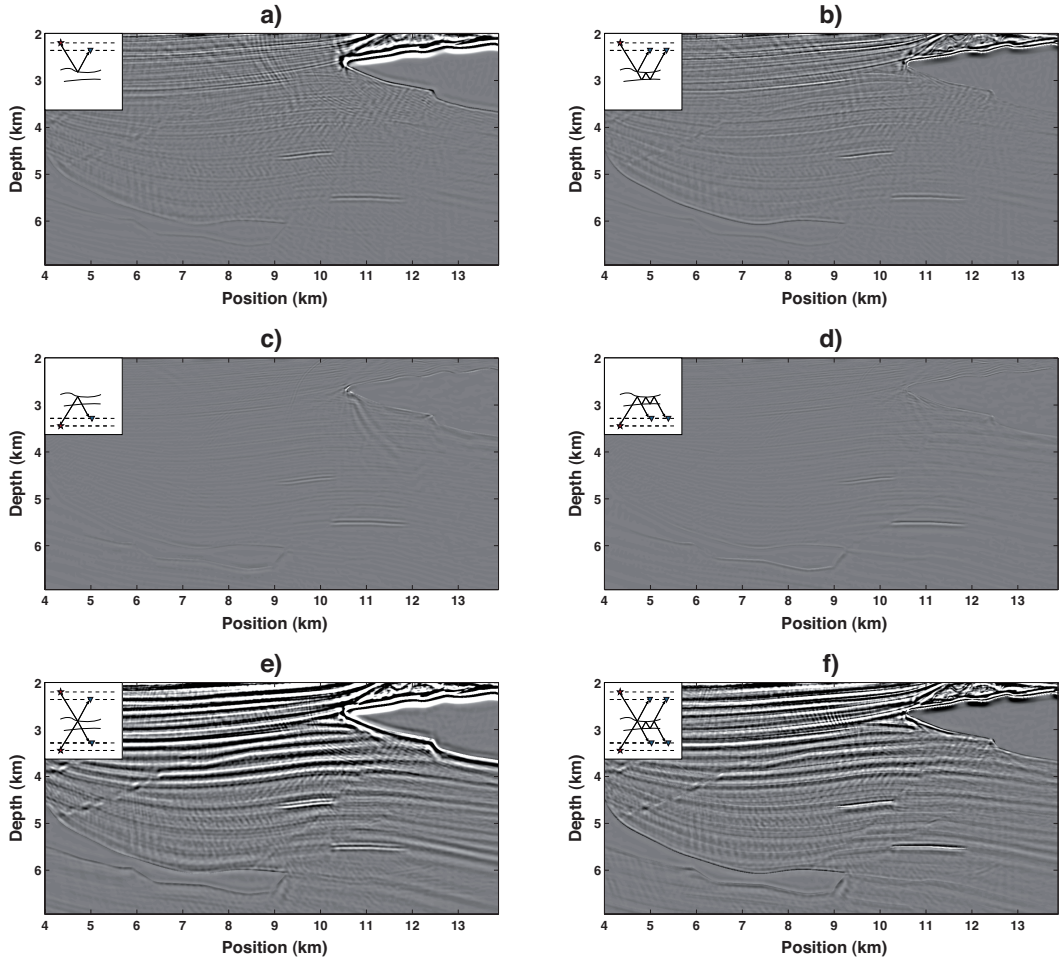

Figure 5.11: PS images obtained by applying a correction for polarity reversal for the six different imaging experiments depicted in Figure 5.3.

coverage; this in turn generates focusing artefacts of the kind observed in our SS images. Gaiser and Vasconcelos (2010) observed this angle-dependent restriction in reconstructing pure-mode shear waves in interferometry from field OBC data. Their analysis applies directly to our imaging scheme, which is a subsurface-domain interferometric reconstruction of pure-mode S-waves. An important consequence of this dependence on seafloor P-to-S velocity ratio is that, even in acquisition scenarios with very wide aperture source and receiver arrays, the pure-mode S-wave images from ocean bottom data will always be more limited in aperture compared to their P-wave counterparts, and their subsurface illumination will largely depend on the seafloor properties.

We would like to use shear-wave energy also for true-amplitude imaging in order to extract meaningful amplitudes that carry information about S-wave velocities. In Chapter 2 we have showed that in the ideal acquisition and imaging scenario (i.e., if the imaging process properly accounts for multiple scattering, and enclosing boundaries are

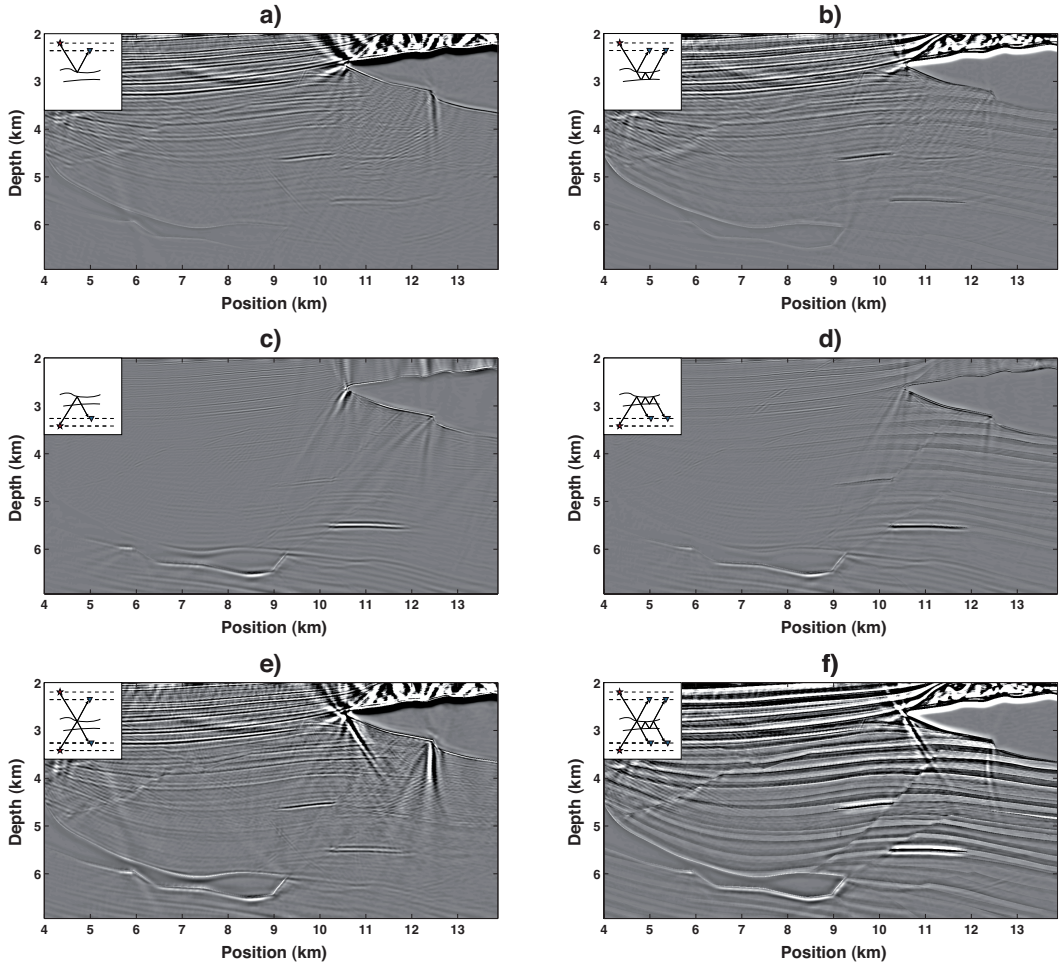

Figure 5.12: SS images for the six different imaging experiments depicted in Figure 5.3.

used) the true-amplitude PS image vanishes. Our converted-wave image arising from two-sided NLERTM without polarity correction (Figure 5.13) does however show residual non-physical energy which is not properly cancelled. This is the effect of using incomplete boundaries of receivers and, especially, sources (there are missing sources and receivers on either side of the crosssection), although the target is illuminated from both above and below.

To overcome the issues arising from limited-aperture source and receiver acquisition surfaces and check that this reasoning is correct, a local seismic experiment is carried out considering only a portion of the Pluto model embedded in an otherwise homogeneous medium (Figure 5.14a) using a full, enclosing boundary of sources. The imaging condition in equation 5.3 is evaluated by direct modelling of the required reference and full wavefields (analogously to Fleury and Vasconcelos (2012) and Chapter 2 of this thesis) and the resulting image is displayed in Figure 5.14d, as a result of summing of

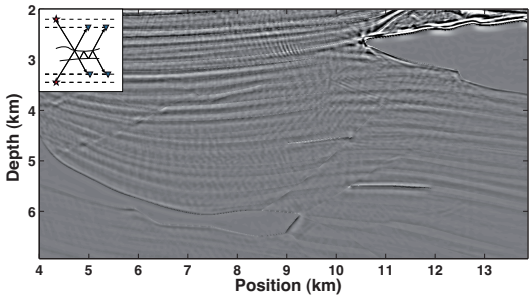

Figure 5.13: PS nonlinear image using sources and receivers both above and below the imaging target without correction for polarity reversal.

the purely linear term in equation 5.6 (Figure 5.14b) and nonlinear terms in equation 5.3 (Figure 5.14c). The linear and nonlinear contributions match and cancel out. As expected from the theory, the PS image (Figure 5.14d) is indeed close to zero everywhere.

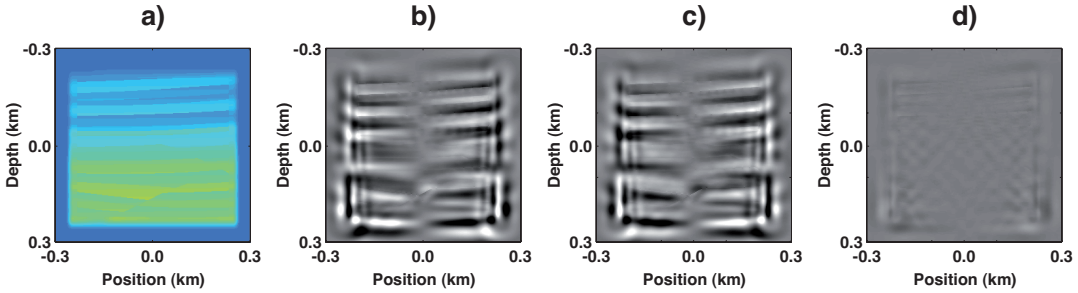

Figure 5.14: PS imaging using an enclosing boundary of sources of ray $r = 0.5\,km$ (a) P-wave velocity model. A portion of the Pluto model in Figure 5.3a is extracted and embedded in an otherwise homogeneous medium with $V_P = 2000\,m/s$, $V_S = 1000\,m/s$ and $\rho = 1000\,kg/m^3$. Shear wave properties are the same as those in the Pluto model used in the previous example. (b) Linear imaging as defined by equation 5.6, (c) nonlinear terms of the nonlinear imaging equations 5.3 to 5.5 and (d) 'full' nonlinear imaging — the sum of the linear (b) and nonlinear (c) terms.

5.4 Discussion

Multiple reflections are usually treated as noise in seismic data processing, which should be estimated and removed prior imaging (Verschuur et al., 1992; Berkhout and Verschuur, 1997; Weglein et al., 1997; Jakubowicz, 1998; Amundsen, 2001; ten Kroode, 2002). Residual energy from multiples, which is not perfectly removed by the multiple attenuation algorithm, generates imaging artefacts in standard reverse-time migration arising from cross-talk of events in the source and receiver wavefields that are not

physically related (e.g., a primary in the source wavefield interacting with a multiple in the receiver wavefield). This point of view is now moot, as geophysicists now consider multiples to be a source of useful information and attempt to use them in the imaging process (e.g., Muijs et al. (2007); Vasconcelos et al. (2008); Berkhout and Verschuur (2011); Liu et al. (2011); Davydenko and Verschuur (2012); Zhang and Schuster (2014)).

Limited aperture boundaries of sources and receivers also present a limitation to the practice of seismic imaging. One way to alleviate the illumination problem is to solve the migration problem in a least-squares sense (using least-squares migration —see Nemeth et al. (1999)). Alternatively, given that the image distortions can be thought of as local blurring filters (also called point-spread functions), an estimate of these blurring filters can be obtained by means of migration-demigration (Lecomte, 2008; Gherasim et al., 2010; Shen et al., 2011), and illumination weights can then be applied to the migrated gathers to correct these effects (Fletcher et al., 2012; Archer et al., 2013).

Despite the evident improvements when accounting for multiples and incomplete boundaries in the imaging process, fully enclosing boundaries and nonlinear interactions are not explicitly required in the original formulation of the imaging problem which was based on the concepts of the so-called adjoint-state method (Baysal et al., 1983; Tarantola, 1984). These requirements do become explicit under the SRI formalism (Halliday and Curtis, 2010; Vasconcelos, 2013; Ravasi and Curtis, 2013a), which we use here to perform linear and nonlinear ERTM: the contribution of high-order scattering interactions allows for power conservation in scattering (Fleury et al., 2010; Wapenaar et al., 2010b; Douma et al., 2011), while that of complete boundaries guarantees the presence of both stationary points that bring physical energy and those that suppress non-physical arrivals (Meles and Curtis, 2013; Loer et al., 2014).

It is worth pointing out that although our model design may not look entirely realistic, especially because of our choice to add a second water layer below the imaging target (definitely not the case for real field experiments), this does not preclude any of our observations about the increased illumination and artefact reduction given by sources (and receivers) below the imaging target. We conjecture that having P-wave only sources and a seabed acting as a P-to-S wave converter might be an alternative (approximately equivalent) approach to that of having both P- and S-wave sources in a fully elastic layer at depth, and so similar results would be obtained if we were able to record (or more likely, reconstruct) these wavefields.

In our examples data from bottom boundaries of sources and receivers and full propagators required by equations 5.3 to 5.5 are directly modelled and hence are exact. In

practice, when only a reference (smooth) version of the velocity model is available, these fields cannot be modelled directly. In acoustic media, these wavefields can be estimated by applying the autofocusing (or Marchenko redatuming) approach of Broggini et al. (2012); Wapenaar et al. (2013). This method constructs the full wavefield from a virtual source or receiver anywhere inside the medium (without needing a physical receiver or source at the location of interest), from one-sided reflection data and an estimate of the direct arriving wave-front from the virtual source to the recording surface. Whether the uplift in the image quality given by nonlinear two-sided imaging will be similar to that observed in our examples depends on the accuracy of the reconstruction of these fields in complex geologies (van der Neut et al., 2014a; Vasconcelos et al., 2014b), and when only limited-aperture arrays of sources and receivers are available. Moreover, this approach has recently been developed also for electromagnetic media (Slob and Wapenaar, 2013), and the first extension to elastic data are in da Costa et al. (2014b,c,a); Wapenaar (2014) and Wapenaar and Slob (2014).

5.5 Conclusion

In this chapter, source-receiver interferometric imaging is used to create elastic images of the subsurface that represent the local interaction between P and S waves within the subsurface. PP, PS and SS images are computed by means of linear imaging (i.e., using only primary reflections) and nonlinear imaging (i.e., exploiting also multiply scattered waves), using one- and two-sided acquisition geometries.

Conventional elastic reverse-time migration produces images that exhibit acquisition imprints and poorly illuminated areas, especially for highly complex subsurface environments. Exploiting multiple scattering in the imaging process (using nonlinear reverse-time migration) with the correct full or scattered source and receiver propagators mitigates these problems and increases the resolution of the migrated image because multiples provide better subsurface illumination. Imaging with two-sided acquisition geometries can also make use of the information contained in the transmitted component of the recorded wavefield which is shown to be beneficial, particularly for providing low wavenumber information.

When imaging with converted waves, special attention must be given to the physical meaning of the resulting image: a ‘structural’ image can be obtained from P-to-S conversions by applying one of the several available polarity correction procedures to reduce the destructive interference in the stacked image. However, true-amplitude imaging has no meaning if the response at zero-time and zero-offset is sought, because this is null by the interferometry-based definition; since the image will not be zero in real

acquisition scenarios due to their practical limitations, the amplitudes retrieved are due entirely to these limitations rather than to the subsurface properties. If used quantitatively, these amplitudes would tend to mislead subsequent geological interpretation. Other quantitative definitions of PS images are conceivable, however, those will require further research.

6

Application 2: Elastic extended images using multiple reflections and transmissions

Extended images (EIs) represent the scattered spatio-temporal response between offset subsurface pseudosources and pseudoreceivers which can be used to constrain elastic properties around each image point. However, one-sided illumination of the subsurface (from the Earth's surface), errors in the initial velocity model estimate, and the use of a linearized, single-scattering assumption (as is usual in seismic imaging) cause errors in EI gathers such as missing events, incorrect amplitudes, and spurious energy. By creating elastic (PP and PS) EIs in a synthetic example of subsalt imaging, we demonstrate the advantages of incorporating multiply-scattered waves correctly by nonlinear imaging, and of including transmitted waves by using two-sided receiver arrays, and discuss how the recently developed autofocussing methods could provide us with the various required subsurface wavefields. Pre- and post-imaging f-k filtering procedures are also introduced to further improve the quality of the EIs by (explicitly or implicitly) limiting the directions of waves arriving at the subsurface pseudo survey line. Finally, we analyse the sensitivity of elastic PP EIs to errors in the migration velocity models and show that events in the extended images are shifted in opposite directions when constructed using reflection or transmission data. In other words, velocity errors are mapped into the EIs differently in the case of one-sided from two-sided illumination. This leads to the potential for new methods of migration velocity analysis when surface and borehole seismic data are jointly acquired.

6.1 Introduction

The theory and practice of seismic processing rely on the analysis of recorded seismic data sorted into different domains. Examples include common-shot, common-receiver, common-midpoint or common-offset (Yilmaz, 1989). The structure and physical properties of the medium excited during the seismic experiment can not be inferred directly from a visual inspection of the recorded data in any of these domains. Nevertheless, important processing procedures such as noise suppression (Canales, 1984; Hampson, 1987; Jones and Levy, 1987), multiple attenuation (Foster and Mosher, 1992; Verschuur et al., 1992), velocity analysis (Taner and Koehler, 1969) and amplitude-versus-offset analysis (AVO — Ostrander, 1982; Rutherford and Williams, 1989; Castagna and Backus, 1993) are generally carried out by assuming certain kinematic behaviours of the recorded data in one or more of these domains. After decades of seismic processing experience we understand how different methods allow us to use some of the information best captured within the gathers in each of these domains.

The recent introduction of so-called extended image (EI) gathers allows recorded seismic data to be transformed into approximate time- and space-varying responses between pseudosources and pseudoreceivers located within the subsurface, without having to have such equipment actually installed there (Vasconcelos et al., 2009a; Halliday and Curtis, 2010; Vasconcelos et al., 2010; Sava and Vasconcelos, 2011). These EIs can be used as an alternative to time-lag, space-lag, or reflection-angle common image gathers (CIGs) for local velocity analysis around selected image points (Symes, 2008; Yang and Sava, 2011a,b, 2012; Fleury, 2012; Fleury and Perrone, 2012), but since they represent source to receiver responses that can be located close to targets of interest, they may also be useful for reservoir characterization (Thomson, 2011, 2012; Vasconcelos and Rickett, 2013).

Detailed analyses on the form of these gathers, carried out using a geometrical approach (Yang and Sava, 2010), asymptotic analysis (Thomson, 2011, 2012) or stationary-phase analysis (Meles and Curtis, 2013; Loer et al., 2014), show that the retrieval of the full scattered wavefield response from a pseudosource to a pseudoreceiver in the subsurface is not always successful. The imprint of finite acquisition geometries (e.g., only one-sided seismic illumination from above) and knowledge of only a smoothed estimate of the propagation velocity model (so that multiples can not easily be predicted a priori, for example) cause errors in the migration process that is used to construct EI gathers. Including multiples and transmitted arrivals in the migration process is thus fundamental if we aim to construct complete and correct EIs, as multiples add some of the missing wave vectors in upward directions, reducing associated errors.

Herein we create and analyse extended images using the source-receiver interferometry (SRI) formulation of Curtis and Halliday (2010); Halliday and Curtis (2010) and Poliannikov (2011), recently adapted to acoustic reverse-time migration by Vasconcelos (2013) and elastic reverse-time migration by Ravasi and Curtis (2013a) and Ravasi et al. (2014) (also Chapter 5 of this thesis). We construct elastic (PP and PS) EIs using a complex geological model (a modified version of the Pluto 1.5 model as in Chapter 5), and analyse the advantage of migrating multiples and transmitted waves together with primary reflections, comparing one-sided linear extended images with one-sided nonlinear extended images and those from two-sided imaging. Imaging with multiples is becoming relevant for practical imaging problems because recently-developed autofocussing methods offer the possibility to construct Green's functions from subsurface receivers without actually having to have receivers there (Broggini et al., 2012; Wapenaar et al., 2012, 2013; Wapenaar, 2014; Wapenaar and Slob, 2014; da Costa et al., 2014b,c,a). Two-sided illumination can be achieved by jointly acquiring surface and borehole data or, alternatively, the transmission data may also be estimated by autofocusing. We then introduce two f-k filtering approaches to further improve the quality of the EI gathers: the first is a pre-imaging filter that selects the directions of both incoming and emerging waves used to construct the EI (Vasconcelos et al., 2008). The second acts directly on the extended image (a post-imaging filter) and can attenuate emerging waves whose dips are outside a particular range of interest. This analysis shows that while the former more accurately removes unwanted events with possibly different dips in the source and receiver wavefields, the latter approach also performs well and is significantly less costly to apply. Finally, we study the sensitivity of the EIs to errors in the migration velocity models: while it is known that velocity errors in turn cause errors in the EIs, we demonstrate a different sensitivity of transmitted and reflected waves to such errors. We then conjecture that if data are jointly acquired at the Earth's surface and somewhere inside the medium such as in a borehole, using both transmissions and reflections in objective functions for migration velocity analysis or image-domain waveform inversion could provide more robust velocity estimates than existing methods.

6.2 Elastic extended images by source-receiver interferometric imaging

Our goal is to adapt the elastic source-receiver imaging framework presented in Chapter 5 to construct elastic extended images. Similarly to usual definition of a seismic image, an extended image can be seen as a scattered field associated with pseudosources and

pseudoreceivers inside the subsurface as displayed by the red arrow in Figure 6.1 (Vasconcelos et al., 2009a; Halliday and Curtis, 2010; Vasconcelos et al., 2010; Sava and Vasconcelos, 2011). Using the notation defined in Chapter 2, 3 and 5 (also summarized in Table 1), different combinations of pseudosource types and pseudoreceiver quantities can be taken to construct EIs. For example, the scattered wavefield from an external volume force pseudosource at $\mathbf{x}_s$ to a particle velocity pseudoreceiver at $\mathbf{x}_r$ at a given time t will be denoted $EI_{nm}(\mathbf{x}_r, \mathbf{x}_s, t) = \tilde{G}^{S(v,f)}_{(m,n)}(\mathbf{x}_r, \mathbf{x}_s, t)$, and the scattered wavefield from a potential (P- or S-wave) pseudosource at $\mathbf{x}_s$ to a potential (P- or S-wave) pseudoreceiver at $\mathbf{x}_r$ at a given time t will be denoted $EI_{NM}(\mathbf{x}_r, \mathbf{x}_s, t) = \tilde{G}^{S(\Phi,\Phi)}_{(M,N)}(\mathbf{x}_r, \mathbf{x}_s, t)$.

Extended images can be constructed via SRI (Curtis and Halliday, 2010; Halliday and Curtis, 2010; Vasconcelos, 2013; Ravasi and Curtis, 2013a) using two-way representation theorems for elastic scattered waves (Wapenaar and Fokkema, 2006; van Manen et al., 2006; Curtis and Halliday, 2010) as shown in Figure 6.1. An elastic imaging condition which preserves both the time and space correlation lags for potential-to-potential responses for ocean-bottom acquisition scenarios with pressure (P-wave) sources and multicomponent receivers can be written as

$$\begin{aligned} EI^{nl}_{NM}(\mathbf{x}_r, \mathbf{x}_s, t) &= \tilde{G}^{S(\Phi,\Phi)}_{(M,N)}(\mathbf{x}_r, \mathbf{x}_s, t) + \tilde{G}^{S(\Phi,\Phi)}_{(M,N)}(\mathbf{x}_r, \mathbf{x}_s, -t) = \\ &\int_{-\infty}^{+\infty} \left(\oint_{\partial D_S} \frac{2}{\rho(\mathbf{x}_S) V_P(\mathbf{x}_S)} \{ d^{S(\Phi,\Phi)}_{(N,P)}(\mathbf{x}_s, \mathbf{x}_S) G^{0(\Phi,\Phi)*}_{(M,P)}(\mathbf{x}_r, \mathbf{x}_S) \} \, \mathrm{d}^2\mathbf{x}_S \right) e^{j\omega t} \, \mathrm{d}\omega \\ &+ \int_{-\infty}^{+\infty} \left(\oint_{\partial D_S} \frac{2}{\rho(\mathbf{x}_S) V_P(\mathbf{x}_S)} \{ d^{(\Phi,\Phi)}_{(N,P)}(\mathbf{x}_s, \mathbf{x}_S) G^{S(\Phi,\Phi)*}_{(M,P)}(\mathbf{x}_r, \mathbf{x}_S) \} \, \mathrm{d}^2\mathbf{x}_S \right) e^{j\omega t} \, \mathrm{d}\omega. \end{aligned} \tag{6.1}$$

Note that source- and receiver-side wavefields are computed here at two different subsurface points: the former (G) is a wavefield modelled directly from the source at $\mathbf{x}_S$ to the pseudoreceiver location $\mathbf{x}_r$, while the latter (d) is the wavefield that is recorded by the receivers at $\mathbf{x}_R$ and back-extrapolated to the pseudosource location $\mathbf{x}_s$. Receiver-side extrapolation is carried out as shown in equations 5.4 and 5.5 in the previous chapter, with the only difference that $\mathbf{x}_I$ is replaced by $\mathbf{x}_s$, the pseudosource location. Finally, an elastic wavefield separation procedure is applied at each image point to both the source and the receiver wavefields to discriminate P- or S-wave potential fields from the full elastic wavefield. Helmoholtz decomposition of the particle velocity vector field can be used for the homogeneous and isotropic elastic wave equation (Aki and Richards, 1980), while a projection of the vector field onto the polarization vector is required for anisotropic media (see, for example, Yan, 2010).

Once again, the combination of equations 6.1, 5.4, and 5.5 give rise to nonlinear elastic EIs and we refer to this imaging procedure as nonlinear elastic reverse-time migration (NLERTM). In this context, nonlinearity refers to the fact that the second integral in equations 6.1 and 5.4, as well as the integral in equation 5.5 include combinations

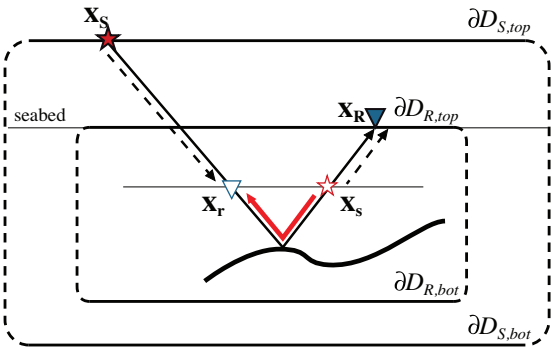

Figure 6.1: Illustration of the physical meaning of an extended image (EI): a scattered field (red arrow) from a pseudosource at $\mathbf{x}_s$ (red open star) to a pseudoreceiver at $\mathbf{x}_r$ (blue open triangle) inside the subsurface. The EI is obtained by means of source-receiver interferometry (SRI) using the recorded data from physical sources $\mathbf{x}_S$ (red star) along the boundary $\partial D_R = \partial D_{R,top} \cup \partial D_{R,bot}$ to physical receivers (blue triangle) along the boundary $\partial D_R = \partial D_{R,top} \cup \partial D_{R,bot}$ (solid ray), the receiver-side propagators from the pseudosource $\mathbf{x}_s$ to physical receivers $\mathbf{x}_R$ (right-hand dashed ray), and the source-side propagators from physical sources $\mathbf{x}_S$ to the pseudoreceiver $\mathbf{x}_r$ (left-hand dashed ray). We assume that top and bottom arrays are sufficiently extensive that contributions from arrays on the left or right (dashed) boundary segments are negligible.

of measured scattered fields with other scattered field propagators. Hence these combinations involve quadratic (hence nonlinear) contributions of the unknown scattered wavefields, and include all orders of interactions of waves with the scattering components of the medium (for example all orders of multiple scattering from non-smooth medium perturbations). Calculating these latter terms generally requires that the scattering (non-smooth) part of the medium is known prior to imaging.

When only a (usually smooth) reference model is available as is commonly the case prior to imaging, only reference Green's functions with few if any reflected or diffracted waves may be available. A linearised, approximate EI can then be obtained by simply dropping all of the nonlinear terms from the combination of equations 6.1, 5.4, and 5.5:

$$EI^{l}_{NM}(\mathbf{x}_r,\mathbf{x}_s,t) = \int_{-\infty}^{+\infty} \Bigg(\oint_{\partial D_S} \frac{2}{\rho(\mathbf{x}_S) V_P(\mathbf{x}_S)} G^{0(\Phi,\Phi)*}_{(M,P)}(\mathbf{x}_r,\mathbf{x}_S) \oint_{\partial D_R} \{ \breve{d}^{S(p,\Phi)}_{(-,P)}(\mathbf{x}_R,\mathbf{x}_S) \times G^{0(\Phi,f)*}_{(N,z)}(\mathbf{x}_s,\mathbf{x}_R) - \breve{d}^{S(v,\Phi)}_{(z,P)}(\mathbf{x}_R,\mathbf{x}_S) G^{0(\Phi,h)*}_{(N,zz)}(\mathbf{x}_s,\mathbf{x}_R) \} \, \mathrm{d}^2\mathbf{x}_R \, \mathrm{d}^2\mathbf{x}_S \Bigg) e^{j\omega t} \, \mathrm{d}\omega, \tag{6.2}$$

where multiple scattering should be neglected by the scattered data as discussed in Chapter 5. We refer to this imaging procedure as elastic reverse-time migration (ERTM). Moreover, as shown in Figure 6.1, here we adopt the following convention: one-sided illumination refers to $\partial D_R = \partial D_{R,top}$ and $\partial D_S = \partial D_{S,top}$, while two-sided illumination

refers to $\partial D_R = \partial D_{R,top} \cup \partial D_{R,bot}$ and $\partial D_S = \partial D_{S,top}$. Although having also two-sided source illumination $\partial D_S = \partial D_{S,top} \cup \partial D_{S,bot}$ as in Chapter 5 would without doubt provide further information, we have decided not to consider that case here.

Pseudo common-shot and common-receiver gathers (but also similarly common-midpoint and common-offset gathers) can be created based on different choices of pseudosources $\mathbf{x}_s$ and pseudoreceivers $\mathbf{x}_r$. It is important to remember that the field associated with a pseudosource is obtained by back-propagation of recorded elastic data (i.e., wavefield extrapolation), while the pseudoreceiver field comes from the direct forward modelling of the source wavefield. While the choice of the type of pseudogather we want to reconstruct is irrelevant for pure-mode extended images like $EI_{PP}(\mathbf{x}_r, \mathbf{x}_s, t)$ or $EI_{SS}(\mathbf{x}_r, \mathbf{x}_s, t)$ because pseudosources and pseudoreceivers can simply be swapped by invoking source-receiver reciprocity (Wapenaar and Fokkema, 2006), extra care must be taken for converted-mode extended images, especially when constructing linear PS extended images ($EI^l_{PS}(\mathbf{x}_r, \mathbf{x}_s, t)$) using migration velocity models that do not contain any sharp boundaries. This is because S-wave energy needed to construct the EI can not be generated in the source wavefield from a P-wave source without an accurate knowledge of one or more sharp boundaries in the velocity and/or density models. We notice however that a SP pseudo common-receiver gather can be constructed by exploiting the S-wave energy recorded along the receiver array in the physical experiment and back-propagating it in an elastic manner by the first term of equation 5.4 through any type of migration model, even one without sharp boundaries. Finally then, we convert this gather into a PS pseudo common-shot gather using source-receiver reciprocity (Figure 6.2). Note that, for simplicity, we follow the same procedure to construct PP EIs in the numerical example below, although pseudo common-shot gathers could have been produced directly when imaging using pure-mode waves.

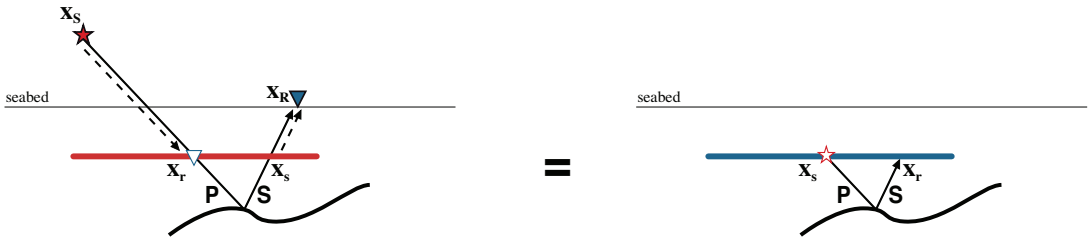

Figure 6.2: Schematic representation of the construction of the PS pseudo common-shot gather $EI_{PS}(\mathbf{x}_r, \mathbf{x}_s, t)$. The SP pseudo common-receiver gather from a line of pseudosources at $\mathbf{x}_s$ (red line) to a pseudoreceiver at $\mathbf{x}_r$ (left) is constructed by back-propagating the S-wave energy which is recorded along the receiver array in the physical experiment to position $\mathbf{x}_r$. Using source-receiver reciprocity, the latter also represents the PS pseudo common-shot gather (right) from a pseudo-source at $\mathbf{x}_s$ to a line of pseudo-receivers at $\mathbf{x}_r$ (blue line).

6.3 Pre- and/or post-imaging f-k filtering

Equations used to construct EIs contain cross-correlations (one term convolved with the conjugate of another) within all integrands, and each integrand has been shown to be equivalent to an instance of correlational seismic interferometry (Curtis, 2009; Curtis and Halliday, 2010; Halliday and Curtis, 2010). In seismic imaging, as well as in interferometry, non-physical energy arises from the crosscorrelation of source and receiver wavefields when either the wavefields that are correlated are incomplete, or they are integrated over incomplete boundaries ∂D_R and ∂D_S (Snieder et al., 2006; King et al., 2011; King and Curtis, 2012). This is especially the case in the presence of complex velocity or density models that contain sharp, dipping discontinuities such as salt flanks: in such cases, different orders of waves propagating along the pseudoreceiver line (e.g., near-horizontally propagating waves when using horizontal lines of pseudoreceivers) correlate with each other and generate strong cross-talk events in the EIs.

We can take advantage of the fact that this type of non-physical energy is constructed from, and appears in, different f-k bands from most of the desired physical energy: two different f-k filtering approaches can be used to improve the quality of the retrieved EIs in terms of mitigating non-physical (hence undesired) events. The first procedure steers the directivity of both pseudosources and pseudoreceivers. It is based on the observation that by limiting the direction of incoming waves at the pseudoreceiver location and the direction of emerging waves at the pseudosource location, we also select a range of local dips of reflectors/discontinuities whose effect will be included in the EI (Vasconcelos et al., 2008), thus eliminating, for example, the non-physical contributions from steeply dipping reflectors. We design two band-pass filters in the wavenumber domain, H_d and H_G, which respectively select a range of incident and emerging angles and filter out waves that are outside the defined ranges. Thus we prevent undesired waves (arriving at the pseudosource or pseudoreceiver from directions outside these ranges) from interacting together within the imaging condition in equation 6.1, and thus from creating artefacts in the extended image (Figure 6.3). In practice, filters H_d and H_G are applied to the receiver and source wavefield in the frequency-wavenumber domain, and the filtered responses are then transformed back to frequency-space domain via an inverse Fourier transform:

$$\hat{d}^{(\Phi,\Phi)}_{(N,P)}(\mathbf{x}_s,\mathbf{x}_S,\omega) = \int H_d(k_s) d^{(\Phi,\Phi)}_{(N,P)}(k_s,\mathbf{x}_S,\omega) e^{-jk_s x_s}\,\mathrm{d}k_s \tag{6.3}$$

and

$$\hat{G}^{(\Phi,\Phi)}_{(M,P)}(\mathbf{x}_r,\mathbf{x}_S,\omega) = \int H_G(k_r) G^{(\Phi,\Phi)}_{(M,P)}(k_r,\mathbf{x}_S,\omega) e^{-jk_r x_r}\,\mathrm{d}k_r, \tag{6.4}$$

where $\hat{d}$ and $\hat{G}$ are the filtered receiver and source wavefields, respectively. k_s is the apparent pseudosource wavenumber (wavenumber measured from the receiver wavefield at the EI survey line via a spatial Fourier transform), and k_r is the apparent pseudoreceiver wavenumber (wavenumber measured from the source wavefield at the EI survey line via a spatial Fourier transform).

Alternatively, we can act on the extended image directly and shape the directivity of pseudoreceivers. Since spurious events due to waves propagating along the EI survey line tend to occur in a particular sector of the wavenumber spectrum (near the critical angle), that is at least partially non-overlapping with physical events, waves in that sector can be removed by applying a spatial band-pass filter H_{EI} that preserves only dips inside a range of interest in the EI gather (Figure 6.3). The filter H_{EI} is applied to the frequency-wavenumber EI, and the filtered EI is then transformed back to frequency-space domain via an inverse Fourier transform:

$$\widehat{EI}_{MN}(\mathbf{x}_r, \mathbf{x}_s, \omega) = \int H_{EI}(k_r) EI_{MN}(k_r, \mathbf{x}_s, \omega) e^{-jk_r x_r} \, \mathrm{d}k_r. \tag{6.5}$$

Equations 6.3, 6.4, and 6.5 represent multidimensional inverse Fourier transforms that map $k_s \rightarrow x_s$ and $k_r \rightarrow x_r$. Note that cut-off wavenumbers in the pre-imaging approach are directly linked to cut-off incident and emerging angles, θ_d and θ_G, and can be obtained by:

$$k_{s,cut-off}(\omega) = \pm \frac{\omega}{\bar{c}_M} sin(\theta_d) \quad , \quad k_{r,cut-off}(\omega) = \pm \frac{\omega}{\bar{c}_N} sin(\theta_G), \tag{6.6}$$

where $\bar{c}_{M/N}$ is the average (P or S-wave velocity) along the pseudosurvey line, with M and N referring to the wave type at the pseudosource and pseudoreceiver, respectively. Similarly, cut-off wavenumbers in the post-imaging approach are obtained by:

$$k_{r,cut-off}(\omega) = \pm \frac{\omega}{\bar{c}_N} sin(\theta_{EI}), \tag{6.7}$$

where θ_{EI} is the cut-off dip in the EI.

6.4 Example

We present a numerical example where PP and PS EIs are reconstructed at three different subsurface locations using a modified version of the synthetic dataset Pluto 1.5 released by the SMAART JV consortium (Stoughton et al., 2001). We refer to Chapter 5 for a detailed description of the model and acquisition configuration. Note that here we use only one truncated, limited-aperture boundary of 154 monopole P-

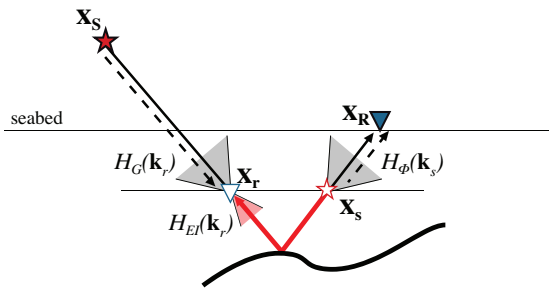

Figure 6.3: Illustration of the effect that the band-pass filters H_d, H_G and H_{EI} have on the source wavefield, receiver wavefield, and extended image respectively. For each, a range of incident or emerging angles is selected (grey cones for pre-imaging filtering and red cone for post-imaging filtering); waves that are outside the defined ranges are filtered out in order to prevent non-physical artefacts appearing in the extended image.

wave sources at a depth of $z_S = 40\,m$ with horizontal spacing of $dx_S = 76\,m$ (red dots in Figure 6.4).

We choose to place our EI pseudosurveys beside features of the model indicated in Figure 6.4. The first EI is relatively shallow ($z_{EI,1} = 2.8\,km$), at a depth comparable with the top interface of both salt bodies. Since sources provide a good illumination of the pseudosurvey line, a reasonable EI should be obtained even when only top sources and receivers are used along with conventional imaging. However strong waves propagating sub-horizontally, which bounce multiple times between the two salt bodies and pass through the pseudosurvey line, will create spurious events in the EI. This is the ideal scenario to test the effectiveness of our two f-k filtering approaches. Noting that the model contains two small reservoirs around ($x = 10\,km, z = 4.5\,km$) and ($x = 11\,km, z = 5.5\,km$), the second and third EIs are placed at $z_{EI,2} = 4.3\,km$ and $z_{EI,3} = 5.5\,km$ respectively.

In the following, four imaging experiments which are schematically visualized in Figure 6.5 (and are similar to those analysed for conventional zero-offset imaging in Chapter 5) are used to discuss the importance of both multiply reflected and transmitted waves in extended imaging. A similar analysis is performed by Meles and Curtis (2013) and Loer et al. (2014) in the context of source-receiver interferometry using a stationary-phase approach under the assumption of single-scattering by a diffractor. Loer et al. (2014); Meles and Curtis (2014a) and Meles and Curtis (2014b) also consider multiply-diffracted waves. The examples here go beyond those previous studies in that (1) they represent an imaging experiment where apart from the recorded data (fields from physical sources recorded at physical receivers), all the other fields are computed numerically and are subject to errors due to the approximate reference velocity models used; (2) they are performed in a complex model where the contribution of multiple-scattering both by reflections and diffractions is significant; (3) they go beyond the acoustic approximation and they effectively represent the first examples of elastic extended images in complex media (linear or nonlinear) presented to date.

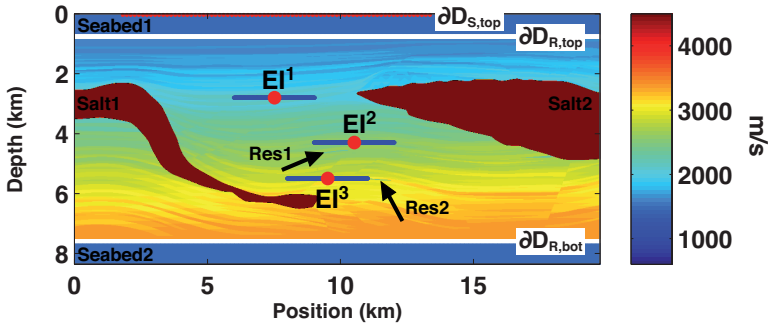

Figure 6.4: Stratigraphic P-wave velocity model, shot locations (red dots at top) and receiver geometry (white lines at top and bottom of the solid medium). Here the EIs pseudosurvey geometries are also displayed: red dots represent the pseudosources, blue lines identify the pseudoreceiver arrays. Res1 and Res2 indicate locations of the two reservoirs.

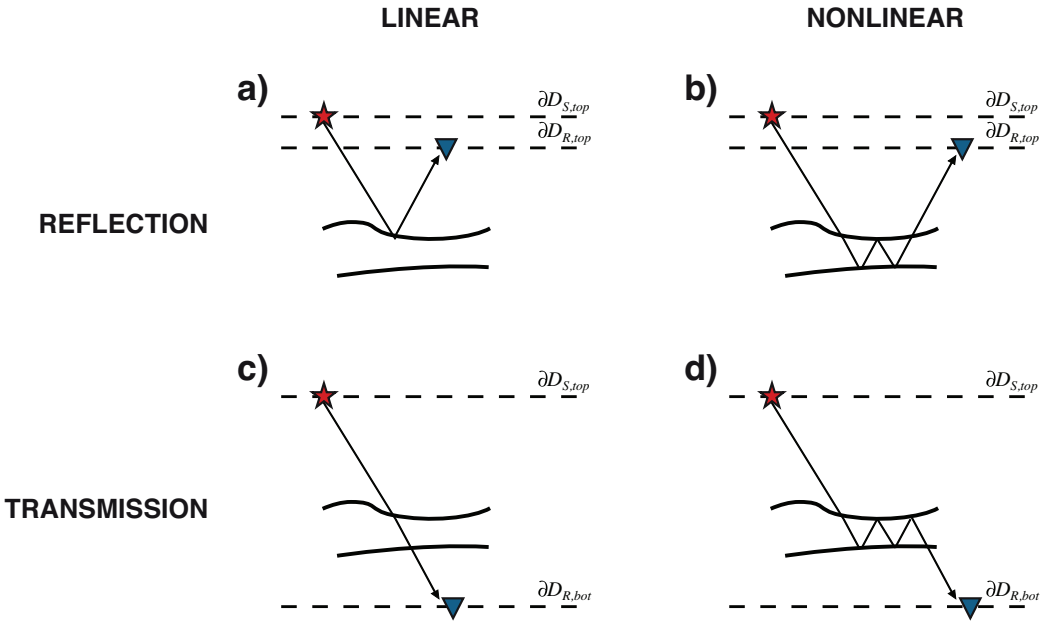

Figure 6.5: Schematic representation of the four different imaging experiments used in this study. (a) Reflection (one-sided receiver illumination from the top) ERTM. (b) Reflection NLERTM. (c) Transmission (one-sided receiver illumination from the bottom) ERTM. (d) Transmission NLERTM. Key as in Figure 5.3.

Shallow PP Extended Image

Recalling that an extended image represents (in theory) the response from a pseudosource to a pseudoreceiver inside the subsurface (Figure 6.1), we first model the exact response for the shallow pseudosurvey geometry shown in Figure 6.4 from a P-wave pseudosource to a line of P-wave pseudoreceivers (Figure 6.6a). Figure 6.6b shows the causal part of the PP extended image for the upper pseudosurvey $E^1_{PP}(\mathbf{x}_r, \mathbf{x}_s, t)$ obtained by means of reflection ERTM. We observe that dominant events mainly show

a linear moveout, which suggests that they are created by the interaction of waves propagating sideway along the pseudoreceiver array. Although some of these linear events are physical (as indicated by the labels p), the others are spurious or non-physical (np) events and strongly interfere with most of the physical waves that show much smaller amplitudes. Events exhibiting different moveouts in the t-x domain are mapped onto different wavenumbers in the f-k domain, and in this case most of the physical energy is mapped to lower wavenumbers than the non-physical (unwanted) energy (Figure 6.6c). We first apply the f-k filtering procedure which acts in the pre-imaging domain to select waves with incident and emerging angles limited to lie between $\pm 50°$, constructing the EI from the filtered source and receiver fields obtained from equations 6.3 and 6.4 (Figure 6.6d). Spurious events are successfully suppressed and the physical events in the selected range of angles are now enhanced in the extended image (see also the f-k spectrum in Figure 6.6e). This filtering approach is very effective but it is also expensive because a multi-dimensional Fourier transform has to be applied to both the source and receiver wavefields for each shot. We also apply the second f-k filtering approach which acts directly on the extended image (i.e., the post-imaging f-k filter) where we remove events with a dip higher than $\pm 50°$ (Figure 6.6f and g). This example shows that, given proper tuning of the filters H_d, H_G or H_{EI}, both the pre- and post-imaging filtering procedures provide clearer extended images compared to the original (pre-filtered) one. In the following, we apply the post-imaging filter to all PP EIs that are shown.

Figure 6.7 compares $E^1_{PP}(\mathbf{x}_r, \mathbf{x}_s, t)$ obtained from the four imaging experiments in Figure 6.5. The filtered exact response is shown in Figure 6.7a with green and magenta arrows used to indicate upgoing and downgoing waves, respectively. Starting from the reflection ERTM extended image (Figure 6.7b), we first notice how upgoing events (green arrows), such as reflections coming from the top of the salt and the seabed (salt1 and seabed2 in Figure 6.4), are generally constructed in the causal part, while downgoing events (magenta arrows) are constructed in the anticausal part. This is especially clear when we observe the first 0.5 s, where reflections from thin layers just above and below the EI survey line are constructed. To determine the origin of the events constructed it is useful to analyse the so-called correlation gather (van Manen et al., 2005; Mehta et al., 2008; Loer et al., 2014). The correlation gather is simply the set of integrands that are integrated in the imaging (and interferometric) equations 6.1 and 6.2. The dominant contribution for each source or receiver on the boundary to the summation or integration is represented by energy with zero gradient with respect to the boundary location, so-called stationary points (Snieder, 2004). In SRI two correlation gathers can be analysed: the correlation gathers for each source pair in the first step (inter-source interferometry or, equivalently, wavefield extrapolation as in equations 5.4 and 5.5), and the correlation gather for each receiver pair in the second step (inter-

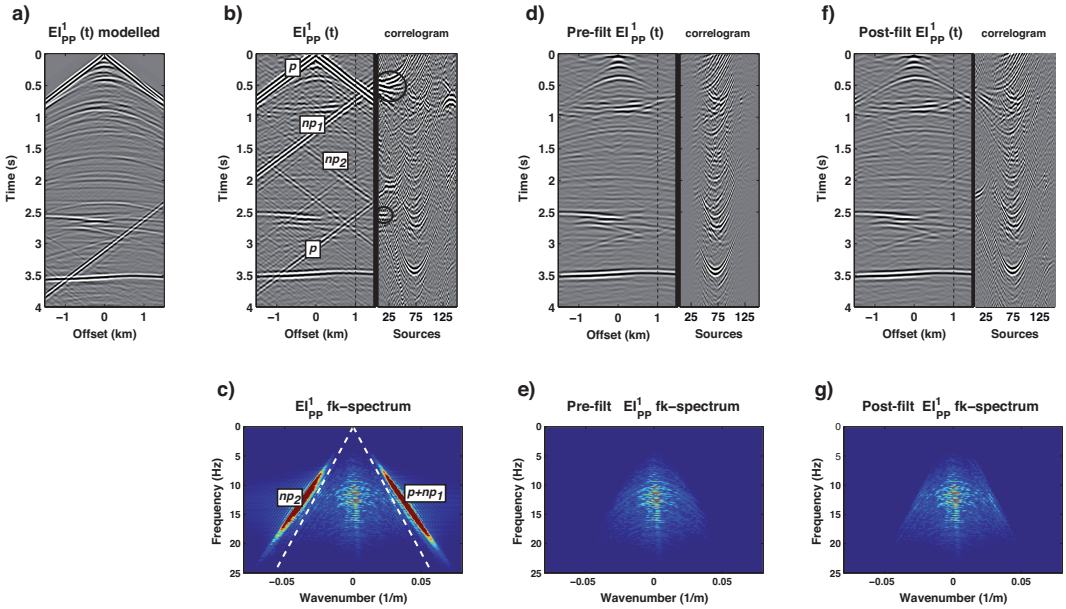

Figure 6.6: Application of the pre- and post-imaging f-k filters to the linear PP extended image shown in (b) together with its source correlation gather for the pseudo-receiver at 1000 m offset (i.e., source integrand in equation 6.2 before stacking over sources). The directly modelled EI is shown in (a) for comparison. The f-k amplitude spectrum in (c) shows that physical energy with hyperbolic moveout is present at low wavenumbers and is fairly distinct from physical energy with linear moveout (label p) and spurious energy (labels np1 and np2) populating the high wavenumbers of the spectrum. Limiting the incident and emerging angles to lie between $\pm 50°$ suppresses the linear events from the extended image as shown in gather (d), and (e) is its f-k amplitude spectrum. Applying only a post-imaging filter limiting dips to lie in the range of $\pm 50°$ (see white dashed lines in (c)) also produces a reasonable EI as displayed in (f) and (g). Note that the pre-imaging filter has suppressed more energy due to external sources in the source correlation gather (d) than has the post-imaging filter in the source correlation gather (f). Similarly the energy near the critical angle is weaker in the pre-imaging f-k spectrum than in the post-imaging one. Hence, these filters could provide fairly different results for situations where the physical stationary points are due to sources at the edge of the boundary.

receiver interferometry or, equivalently, the imaging condition as in 6.1). In the following we will limit our analysis to the source correlation gather for one pseudoreceiver, namely the pseudoreceiver at 1 km offset.

By looking at the correlation gather at positive times, we can see that stationary points of upgoing events are located in the centre of the source array. A similar observation could be drawn by looking at the correlation gather for downgoing waves at negative times: however, although the construction of upgoing events is purely physical as displayed in Figure 6.8a, downgoing events are generated in a non-physical manner (Figure 6.8b) as also noticed by Poliannikov (2011). Finally, physical events with linear moveout (Figure 6.6b) are stationary with respect to only a few sources on the left side (see black circles in the source correlation gather). The creation of these events is

only enabled by the presence of the interpreted (sharp-boundaried) salt bodies in the background models which act as secondary sources (Figure 6.8c), and by turning waves (Figure 6.8d) in the reference propagators which construct stationary paths that would otherwise have been present only if sources and receivers on the sides of the model were available (red lines in Figures 6.8c and d).

We now create the extended image from NLERTM (Figure 6.7d). We also display the purely nonlinear contributions (Figure 6.7c), obtained by subtracting from Figure 6.7d the linear term (equations 6.2), that is displayed in Figure 6.7b. The nonlinear terms are beneficial in a number of ways: first, multiples are successfully used to construct events in the pseudogather by means of scattered propagators, which add energy to those events obtained by conventional linear imaging (see, for example, that although most of the energy in the event at 3.5 s arises from linear interactions in Figure 6.7b, nonlinear interactions provide additional energy — Figure 6.7c — that cannot be discarded if we want to obtain reliable amplitudes in the EIs). Second, multiples also provide non-physical contributions that either totally or partially cancel those arising in ERTM. As a result, the energy mapped around zero-offset and zero-time is better focused for NLERTM (close-up in Figure 6.7d) than for ERTM (close-up in Figure 6.7b); this feature of the nonlinear extended image is directly linked to the overall improvement in the image resolution of nonlinear over conventional linear imaging due to proper use of multiply scattered waves (Vasconcelos, 2013; Ravasi and Curtis, 2013b; Ravasi et al., 2014) and share similarities with super-resolution effects in ultrasound imaging (Simonetti, 2006; Lerosey et al., 2007; Fink, 2008). On the other hand, the increased complexity of nonlinear source and receiver wavefields makes the cross-talk more severe and the EI noisier overall, as is also observed in acoustic nonlinear imaging by Vasconcelos (2013).

The advantage of also having receivers below the imaging target can be appreciated by inspection of the extended images from transmission ERTM (Figure 6.7e), the nonlinear part of transmission NLERTM (Figure 6.7f) and their sum (namely transmission NLERTM — Figure 6.7g). Overall, transmitted data from top sources are mainly responsible for constructing upgoing waves in the anticausal part (as demonstrated explicitly later on) and downgoing waves in the causal part. Moreover the downgoing reflection from the top seabed is reconstructed here for the first time. Interestingly this event as well as the upgoing reflections from the bottom seabed, show incorrect polarity when obtained with ERTM (Figure 6.7e), which is however correct in the nonlinear contributions present in NLERTM (Figure 6.7f). Fleury and Vasconcelos (2012) noticed a similar behavior in the image domain for acoustic waves, where the conventional image exhibits incorrect polarity for some of the reflectors which is corrected by the

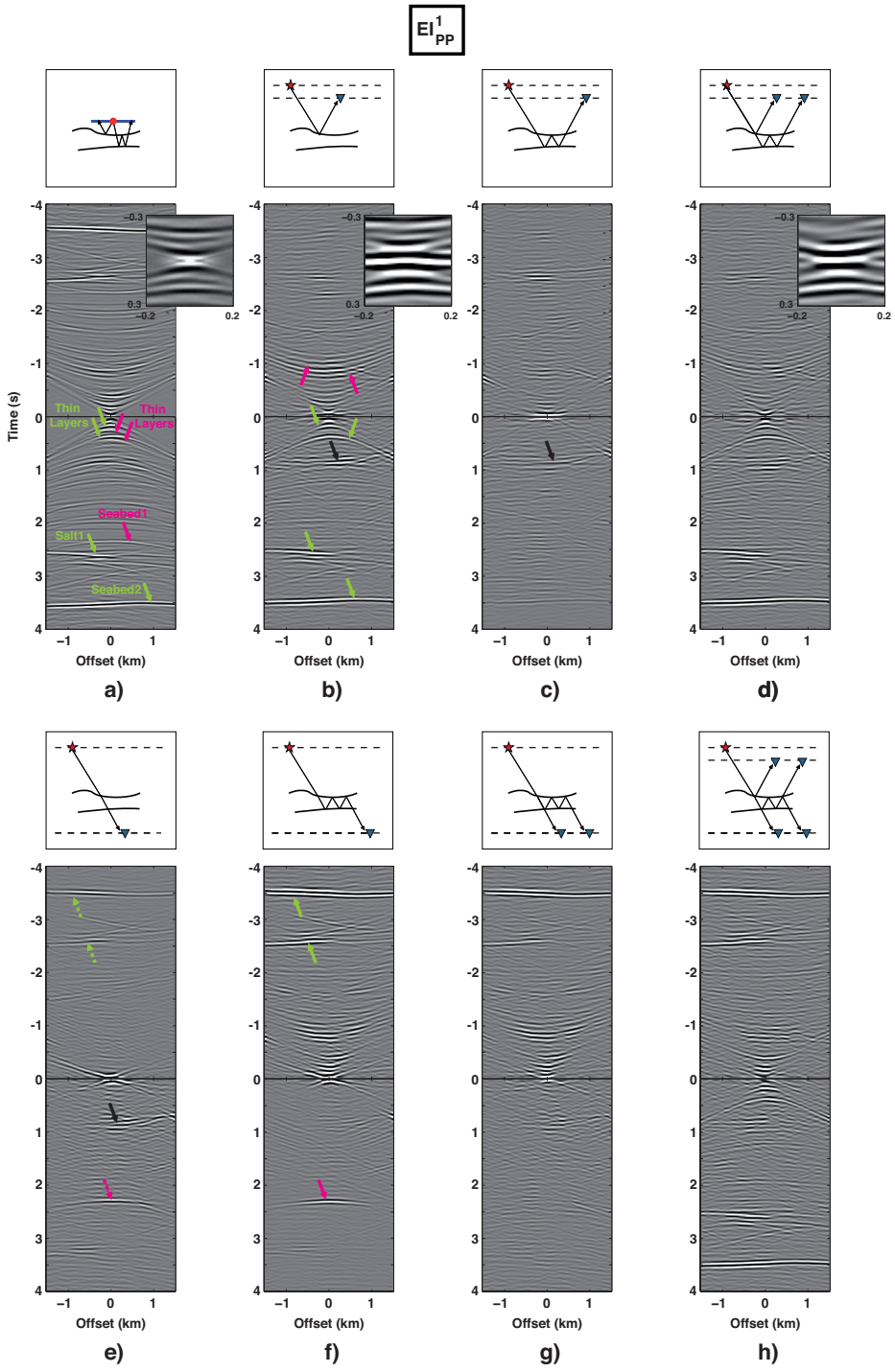

Figure 6.7: PP extended images obtained (a) via direct modelling and (b-h) from the four imaging experiments depicted in Figure 6.5 (and from various summed combinations of their contributions) for the first (shallow) survey line $EI^1_{PP}(\mathbf{x}_r, \mathbf{x}_s, t)$. The same post-imaging f-k filter has been applied to all panels. Green/magenta solid arrows point at up-/downgoing events (solid arrow: correct amplitude, dashed arrow: incorrect amplitude), and additional black arrows identify non-physical events which are not suppressed by the post-imaging f-k filters but which are suppressed by using nonlinear imaging. Close-ups in (a), (b) and (d) show focusing around the zero-time and zero-offset (imaging) point.

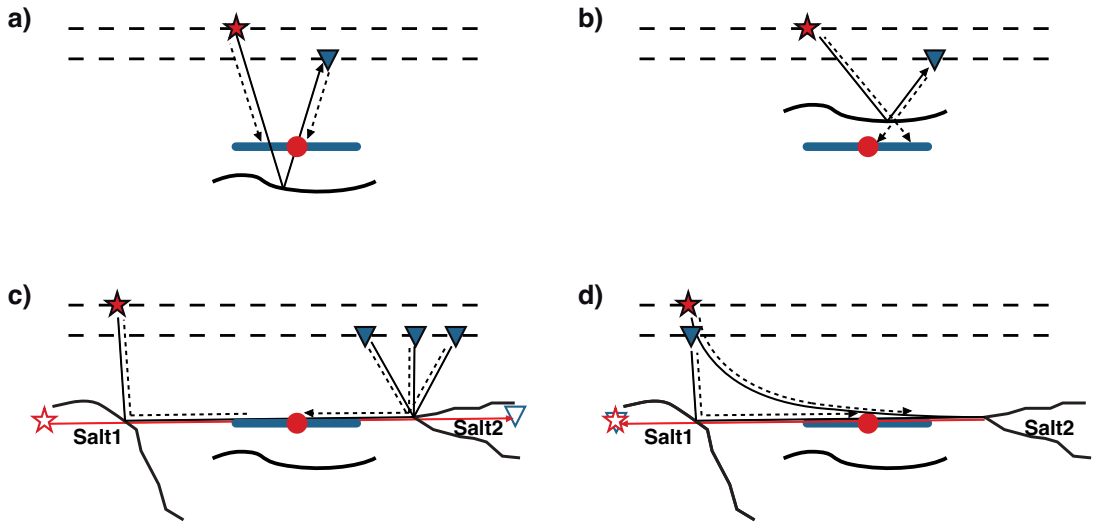

Figure 6.8: Stationary points of four different types of physical and non-physical events generated by reflection ERTM in Figures 6.6b and 6.7b. Solid lines represent the reflection event contained in the recorded data, while dashed lines are used for the propagators that are applied to the data to undo the propagation effect from and to the real sources and receivers towards the pseudosurvey line. (a) Physical construction of an upgoing event and (b) non-physical construction of a downgoing event. Construction of (c) the direct wave and (d) a diffraction from the edge of the salt enabled by the presence of sharp discontinuities and a velocity gradient creating turning waves in the background model. A red line together with an open red star and blue triangle is added to plots (c) and (d) to indicate a boundary source-receiver pair that would be needed to construct the same event in the absence of secondary scattering in the reference propagators.

addition of nonlinear imaging terms.

In our final experiment receivers are simultaneously present above and below the target. Both reflection and transmission responses are thus used to create the EIs as shown in Figure 6.7h. Note the good match between this response and the directly modelled EI in Figure 6.7a. It is also important to observe that causal and anticausal parts become very similar in terms of event construction and amplitudes when two-sided nonlinear imaging is performed. Since the final EI should converge to the causal and anticausal Green's function if both top and bottom sources and receivers were used, the degree to which time symmetry in the gather is achieved constitutes a means to assess the quality of the Green's function reconstruction, a criterion that is commonly used in seismic interferometry from ambient noise (see Stehly et al., 2006).

Shallow PS Extended Image

Analogously to our study of PP EIs, we now analyse the construction of the converted-wave PS response $E^1_{PS}(\mathbf{x}_r, \mathbf{x}_s, t)$. The directly modelled pseudo common-shot gather

from a P-wave pseudosource to a line of S-wave pseudoreceivers is displayed in Figure 6.9a. The reconstructed EIs are displayed in the other panels of Figure 6.9 (the same f-k filter is applied to each EI as discussed below). In the process of constructing PS responses from elastic data a number of differences with their PP counterparts can be observed.

First, two types of strong linear cross-talk events contaminate the converted-wave EIs (Figure 6.10a): one type has similar dip to that of PP EIs and another type has higher dip (see the f-k spectrum in Figure 6.10b). Our pre- and post-imaging f-k filters are again used to enhance the physical arrivals as shown in Figure 6.10c and e. Again the filtered EIs are clearer compared to the original (pre-filtered) one (Figure 6.10a), and the pre-imaging filter is more effective than the post-imaging filter in attenuating spurious energy while preserving the original amplitude of physical events (refer to Figure 6.9a for a comparison with amplitudes of events in the true EI).

Second, the interaction between P- and S-waves in the source and receiver wavefields generates other cross-talk events with a peculiar reverse moveout (see, for example, the event at 1 s in Figure 6.9e). These events, although clearly non-physical, cannot be removed easily by any f-k filtering approach since they are mapped to wavenumbers where physical events are also mapped. Once again nonlinear imaging provides equivalent non-physical events (Figure 6.9e) that cancel those of linear imaging (see Figure 6.9f).

Although we have shown that we are able to construct PS EIs that contain some useful information (the reflection from the top of salt1 indicated in Figure 6.9a, and from layers just above and below the EI survey line are, for example, reconstructed in Figure 6.9h), the overall quality of these pseudogathers is poor compared to that of PP gathers. Such a difference between PP and PS EIs can be explained by the fact that stationary contributions needed to construct physical events (and to cancel spurious arrivals) in their pseudogathers are distributed differently along the boundaries of sources ∂D_S and receivers ∂D_R for compressional and shear waves. While the acquisition geometry used in this imaging experiment (Figure 6.4) is sufficient to capture most of the physical stationary contributions needed for PP EIs while limiting contributions from non-physical points, many more spurious stationary contributions appear in the construction of PS EIs as discussed further below.

Another factor that could explain the deterioration in quality of the reconstruction at later times in the PS EI (especially in the anticausal panels) is the recording time for each shot; while 10 s is probably sufficient to record most of the primary (and multiple) P-wave reflections and transmissions, some of the later S-wave conversions are left out in the data (see Figure 6.9b) and consequently in the corresponding extended images.

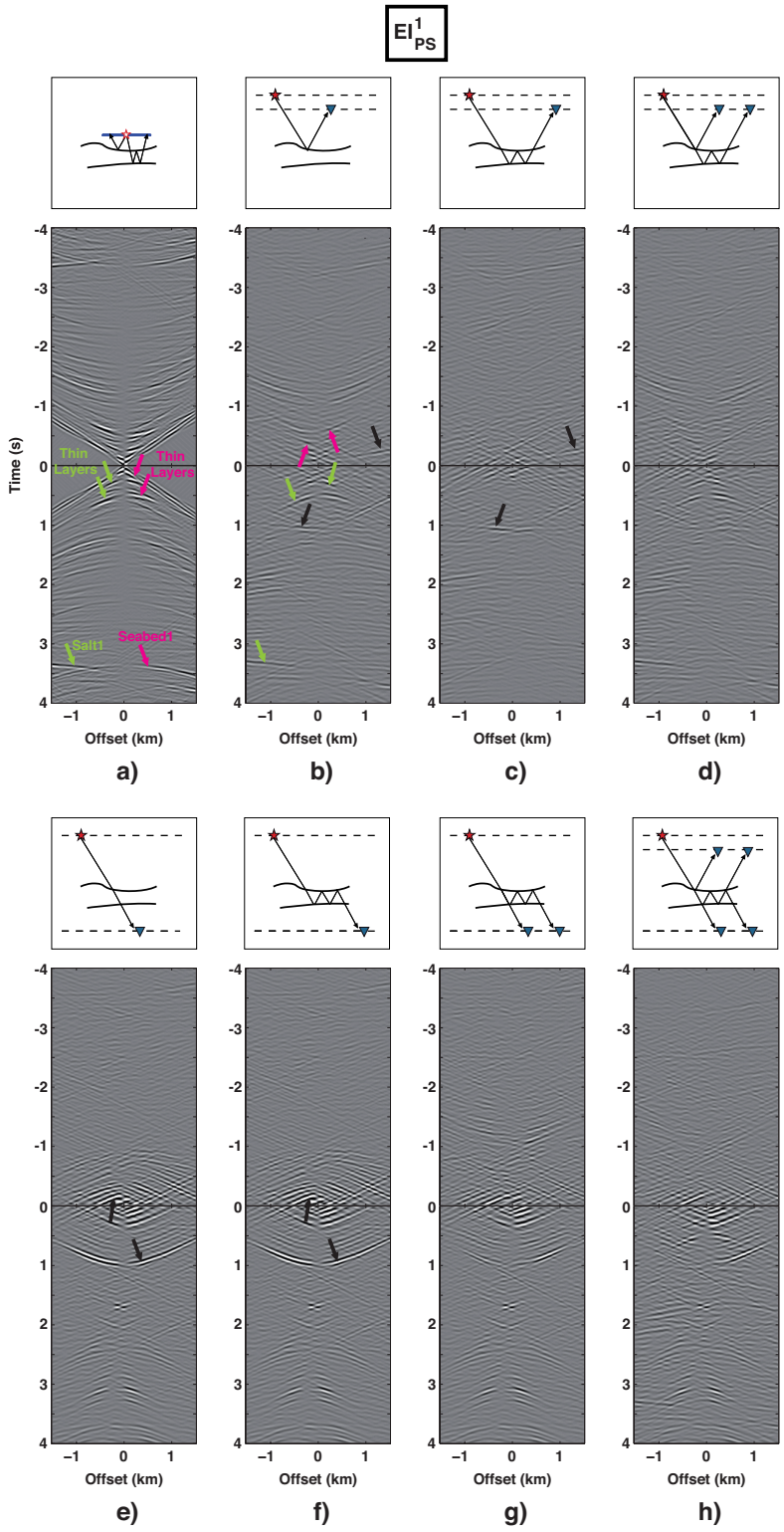

Figure 6.9: PS extended images obtained (a) via direct modelling and (b-h) from the four imaging experiments depicted in Figure 6.5 (and from various summed combinations of their contributions) for the first (shallow) survey line $EI^1_{PP}(\mathbf{x}_r, \mathbf{x}_s, t)$. Key as in Figure 6.7.

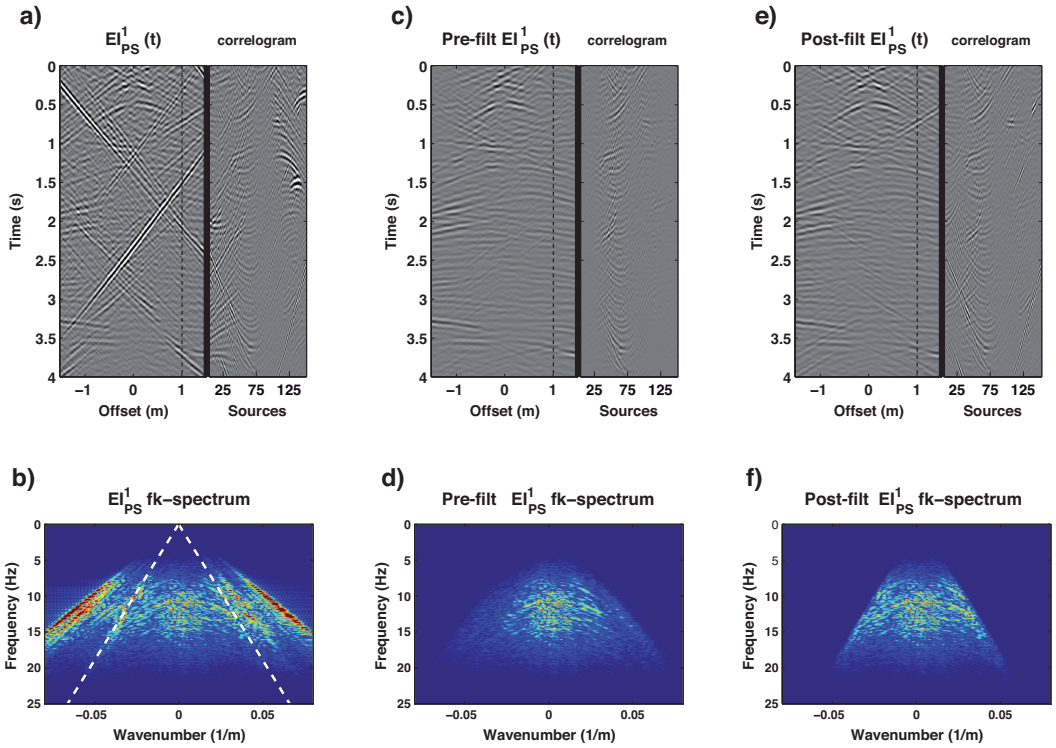

Figure 6.10: Application of the pre- and post-imaging f-k filters to the linear P-to-S extended image $EI^1_{PS}(\mathbf{x}_r, \mathbf{x}_s, t)$ shown in (a). The f-k amplitude spectrum in (b) is wider compared to that in Figure 6.6b and the distinction between physical and non-physical energy is less clear. By limiting the incident and emerging angles between $\pm 40°$ in the pre-imaging filtering procedure, the EI is successfully deprived of spurious energy as displayed in (c) (and in its f-k spectrum in (d)). The post-imaging filter, designed to limit dips to lie in the range of $\pm 40°$ (white dashed lines in (b)), is less successful in removing the artefacts due to the contribution of external sources (e), from which energy can also be seen near the critical angle in the related f-k spectrum. The added value of the pre-imaging filtering approach is that it limits dips in the source wavefield as well as in the receiver wavefield.

Given the recording time of $10\,s$ to $12\,s$ per shot in standard marine acquisition, and due to the limits of computing power available, we did not simulate longer records to test this, but it nevertheless seems reasonable. A third possibility is that marine-type P-wave source geometries provide insufficient illumination of the various shear wavefields that may be produced. For example, with horizontal seabeds at which shear tractions are zero it is impossible to generate horizontal shear energy in the solid seabed using acoustic sources above (or below) the solid model. To generate such energy would require pressure source arrays on either side of the model, or shear sources on the seabed, neither of which were included here in order to make the computational power requirements tractable.

Reservoir responses in PP and PS extended images

The importance of being able to accurately estimate both the kinematics and amplitudes of responses from reservoirs is a vital element for reservoir characterization techniques, e.g. AVO. Wavefields reflected from reservoirs are deformed by the complex overburden structure through which they propagate and the response in the recorded data is usually also complex (Figure 6.11). This is especially the case in our numerical example for the reflection of the second reservoir that, after interacting with the edge of the salt body on the right, almost disappears in the data (Figure 6.11a). On the other hand, the freedom to choose where to place an EI can convert such a complex reflection event back into a simpler one when the recorded data are back-propagated in time and space, and thus it may be rendered easier to pick and use for reservoir characterization.

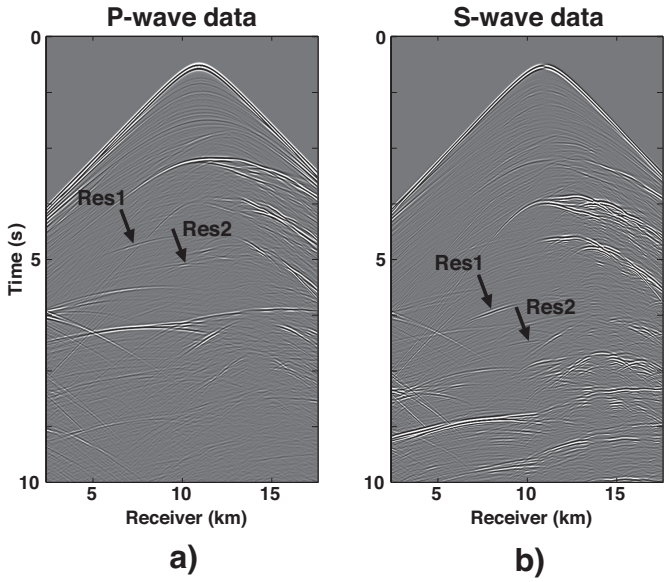

Figure 6.11: (a) P- and (b) S-wave components of the recorded data for a source at $x_S = 11km$. Black arrows are used to indicate reflections from the two reservoirs in the recorded data.

To test this, we use our second EI at $z_{EI,2} = 4.3km$, slightly above the first reservoir and a couple of kilometers away from the second reservoir. The quality of the reconstruction of both PP and PS extended image (Figures 6.12 and 6.13) is satisfactory also when the EI is placed below obstructing formations (e.g., salt bodies) as in this case. The uplift arising from properly accounting for multiply scattered waves and two-sided illumination of the pseudosurvey area is even more evident in this case than in the extended images shown before. Waves emanating from the two salt bodies create very strong spurious arrivals in the extended image from reflection ERTM (see, for example,

the event indicated by the black arrow at $t \approx 2.25\,s$ in Figure 6.12b and that at $t \approx 3\,s$ in Figure 6.13b). These unwanted events show a hyperbolic-like moveout (comparable to that of the physical events in the EI) and are thus not easily removed from the gather with a post-imaging f-k filter. Moreover, since they originate from waves with incident and emerging angles at the pseudosource and pseudoreceiver locations similar to those of waves generating physical events, also the pre-imaging filtering approach fails. The contribution coming from using the nonlinear terms to incorporate this energy into the EIs correctly is therefore fundamental to suppress these unwanted events (see Figures 6.12c and d and Figures 6.13c and d). Finally, by looking at Figure 6.11 we conclude that the P- and S-wave responses of the deeper reservoir, which were very distorted in the recorded data, have been successfully back-propagated by SRI imaging and are now easily identifiable in the extended images (event around $t = 1\,s$ in Figures 6.12h and 6.13h). This event now represents a suitable input for algorithms for amplitude analysis and reservoir characterization.

The third EI in Figure 6.4 is located at $z_{EI,3} = 5.5\,km$. Special attention is given here to the underside reflection event from the reservoir above the EI to study the additional information provided by underlying receivers (i.e., two-sided illumination), compared to the case of receivers only above targets of interest (one-sided illumination). Figures 6.14 and 6.15 show the reconstruction of PP and PS EIs, respectively, by means of the four different imaging experiments depicted in Figure 6.5 (and the combination of all of their contributions). First, we notice that reflection ERTM constructs the downgoing P-to-P and P-to-S responses of the shallower reservoir (acausal panels in Figures 6.14b and 6.15b). This construction is non-physical as schematically depicted in Figure 6.8b. As discussed also by Poliannikov (2011) in the context of SRI, non-physical events of this type generally exhibit the correct kinematic behaviour but the retrieved amplitudes are not consistent with those of the true reflection events (see Figures 6.14a and 6.15a). Multiply reflected waves (Figures 6.15c) and transmitted waves (Figures 6.14f and 6.15f) also map some of the recorded energy from the reflection event at the base of the reservoir but, since their construction is physical, the retrieved events show correct amplitudes.

In summary, multiply scattered arrivals are once again shown to be beneficial for both the quality and interpretability of the EIs. Nonlinear terms compensate for the effect of waves emanating from the two salt bodies that create very strong spurious arrivals in the extended images from reflection ERTM (see black arrows and in Figure 6.14b). In fact they create non-physical events of similar strength and opposite polarity to linear events, that once summed with the linear contributions remove those events completely (Figures 6.14c and d). Second, by providing complementary illumination of the subsurface, multiples are also beneficial to construct some physical events in the

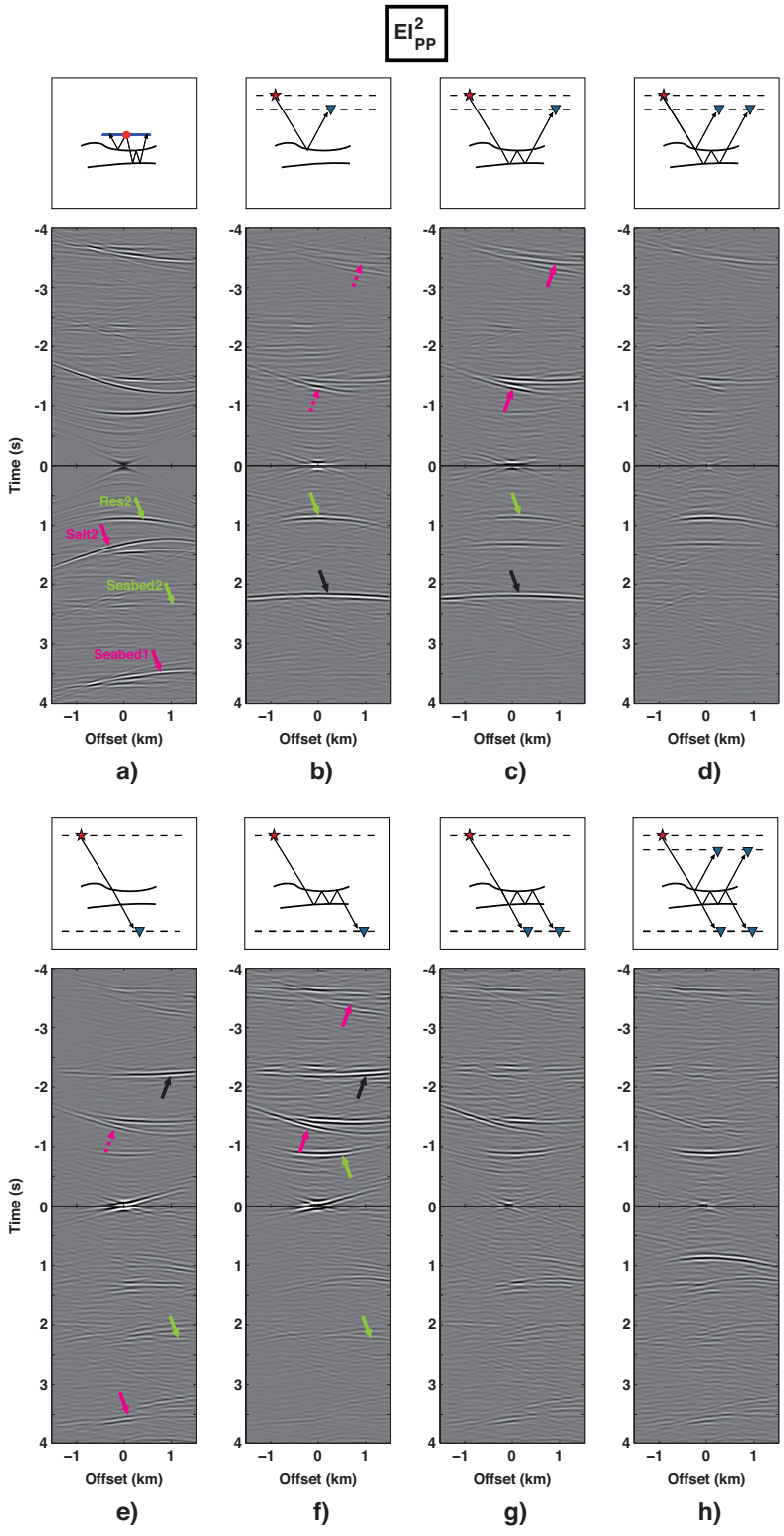

Figure 6.12: PP extended images obtained (a) via direct modelling and (b-h) from the four imaging experiments depicted in Figure 6.5 (and from various summed combinations of their contributions) for the second survey line $EI^2_{PP}(\mathbf{x}_r, \mathbf{x}_s, t)$. Key as in Figure 6.7.

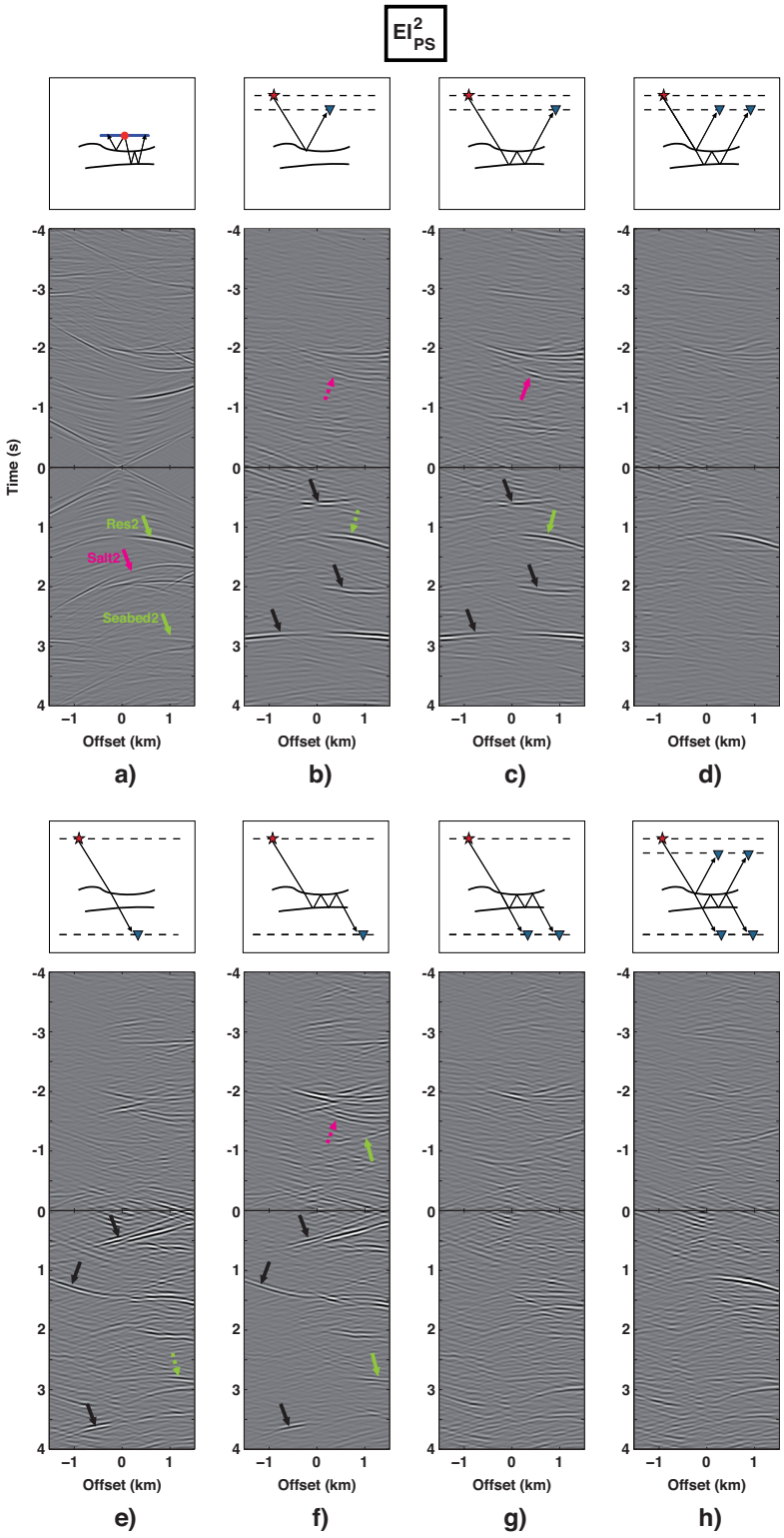

Figure 6.13: PS extended images obtained (a) via direct modelling and (b-h) from the four imaging experiments depicted in Figure 6.5 (and from various summed combinations of their contributions) for the second survey line $EI^2_{PS}(\mathbf{x}_r, \mathbf{x}_s, t)$. Key as in Figure 6.7.

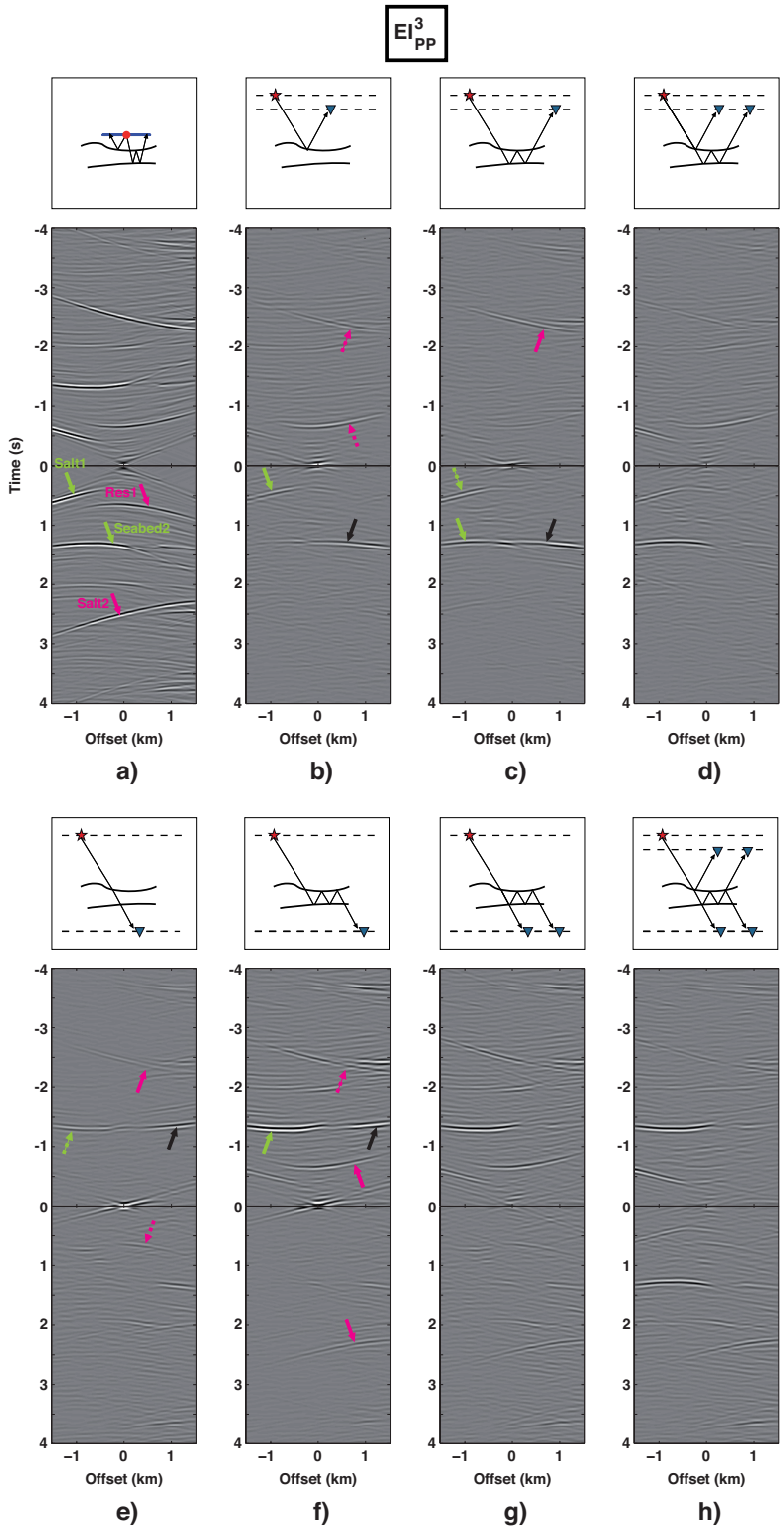

Figure 6.14: PP extended images obtained (a) via direct modelling and (b-h) from the four imaging experiments depicted in Figure 6.5 (and from various summed combinations of their contributions) for the third survey line $EI^3_{PP}(\mathbf{x}_r, \mathbf{x}_s, t)$. Key as in Figure 6.7.

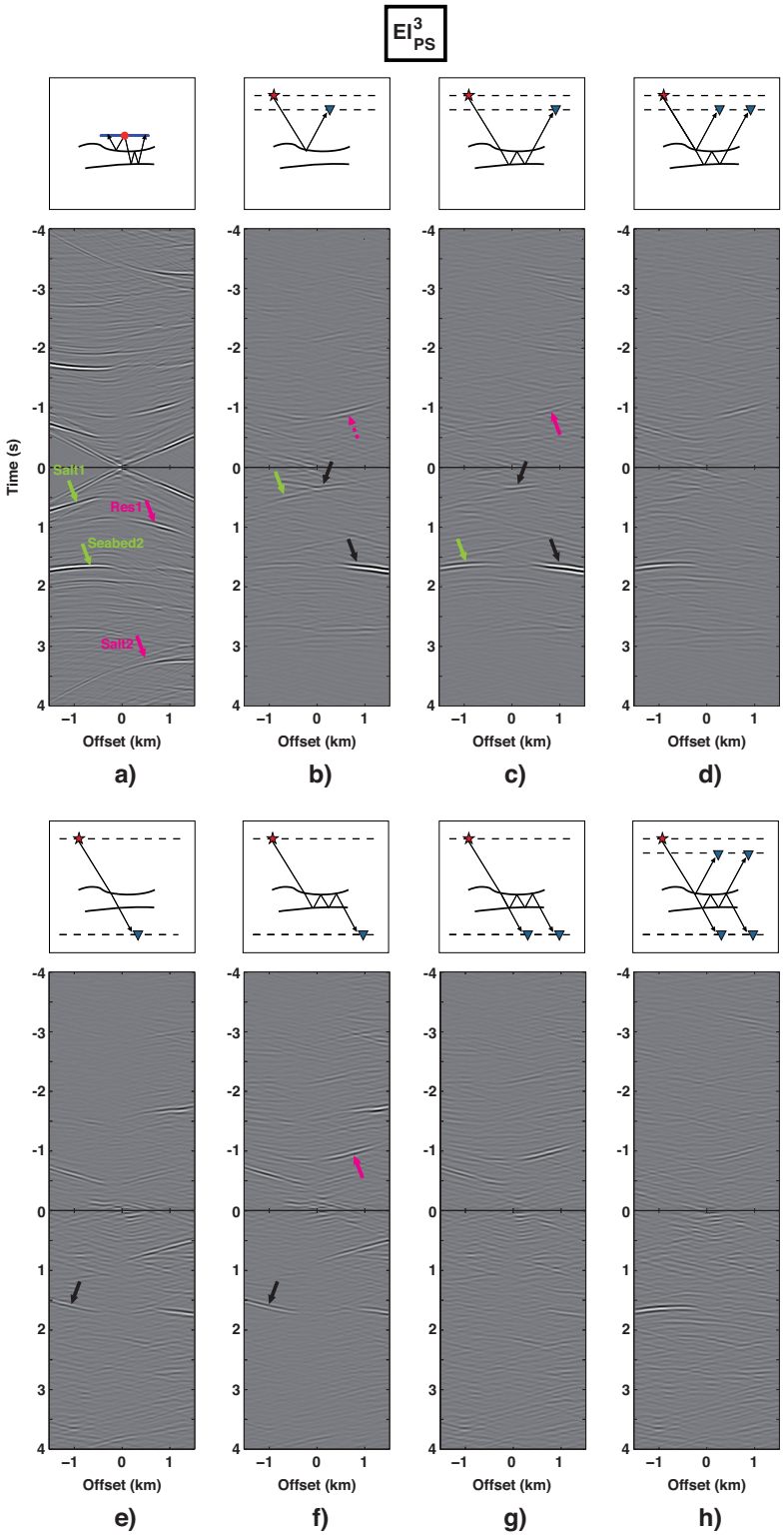

Figure 6.15: PS extended images obtained (a) via direct modelling and (b-h) from the four imaging experiments depicted in Figure 6.5 (and from various summed combinations of their contributions) for the third survey line $EI^3_{PS}(\mathbf{x}_r, \mathbf{x}_s, t)$. Key as in Figure 6.7.

pseudogather where primaries fail (see, for example, events around $t \approx 1.3\ s$ in Figure 6.14c band $t \approx 1.5\ s$ in Figure 6.15c as indicated by green arrows).

Sensitivity of the extended images to velocity errors

An extended image contains both focusing information from time-lags and moveout information from space-lags that can be employed together for migration velocity analysis (MVA) as shown for pure-mode waves by Yang and Sava (2011a,b, 2012); Fleury (2012) and Fleury and Perrone (2012) and for converted-waves by Yan and Sava (2010) and Shabelansky et al. (2013). In fact, errors in the migration velocity models lead to a departure of the focusing from zero-lag, and to deformation of the moveout in the space-lag. After we have shown that an EI is an approximation to a scattered field in the subsurface, we can move beyond these geometrical arguments and may design new migration velocity analysis objective functions based on the physical meaning of the EI as a Green's function.

To study this, new extended images are generated using incorrect P- and S-wave velocity models formed by adding a +10% error everywhere, apart from inside the salt bodies and the water layers where the correct velocities are maintained. Here we limit the source acquisition boundary to half of its original extension (i.e., ∂D_S) and sampling (i.e., $dx_S/2$). Figure 6.16 displays $EI^1_{PP}(\mathbf{x}_r, \mathbf{x}_s, t)$ for the different imaging experiments: when the extended image is obtained by means of reflection ERTM, having incorrect (too fast) migration propagators results in a shift of the events in the gather to later times: for example the event at $\sim 2.5\ s$ in Figure 6.7b (a reflection from the salt body on the left) moves to $\sim 2.7\ s$ (Figure 6.16b).

This shift can be explained by considering the construction of an upgoing reflection event by means of a stationary phase approach (Figure 6.17a): this event is created by subtracting from the traveltime of the fixed, observed reflection in the data ($t_{\mathbf{x}_S \to \mathbf{x}_R}$) the traveltimes of the propagators from the physical source to the pseudoreceiver ($t_{\mathbf{x}_S \to \mathbf{x}_r}$) and from the physical receiver to the pseudosource ($t_{\mathbf{x}_R \to \mathbf{x}_s}$):

$$t_{\mathbf{x}_s \to \mathbf{x}_r} = t_{\mathbf{x}_S \to \mathbf{x}_R} - t_{\mathbf{x}_S \to \mathbf{x}_r} - t_{\mathbf{x}_R \to \mathbf{x}_s}. \tag{6.8}$$

When the propagators are computed in the incorrect (over-estimated) velocity models their traveltimes $t^{v_{10\%}}_{\mathbf{x}_S \to \mathbf{x}_r}$ and $t^{v_{10\%}}_{\mathbf{x}_s \to \mathbf{x}_R}$ are smaller than the correct ones, so the resulting EI traveltime is larger than the one from the correct velocity models:

$$t^{v_{10\%}}_{\mathbf{x}_s \to \mathbf{x}_r} = t_{\mathbf{x}_S \to \mathbf{x}_R} - t^{v_{10\%}}_{\mathbf{x}_S \to \mathbf{x}_r} - t^{v_{10\%}}_{\mathbf{x}_R \to \mathbf{x}_s} > t_{\mathbf{x}_s \to \mathbf{x}_r}. \tag{6.9}$$

A similar exercise can be repeated to explain the shift of events in the other panels (Figure 6.16c to h).

Specifically, when we look at upgoing waves constructed from the energy of reflected waves (mainly populating the causal part in Figure 6.16b and c) and those employing the energy from transmitted waves (mainly populating the anticausal part in Figure 6.16e and f), we note that they are shifted from their original location in opposite directions with slightly different time shifts. For example the strong reflection from the bottom seabed is at time $3.5\,s$ in the EI constructed with correct velocity (Figure 6.7h), but the same event moves to $3.7\,s$ in the causal part of the EI constructed with incorrect velocity (Figure 6.16h) and to $-3\,s$ in the anticausal part of the same EI (Figure 6.16h). We now seek to understand this in more detail, and will show below that it leads to a new velocity discrimination criterion.

Meles and Curtis (2013) and Loer et al. (2014) analyse the contribution of each individual term in scattered wave SRI using a stationary phase approach. Under the assumption of a localized perturbation (e.g., a single point diffractor) located below the pseudosurvey line, they show that only two terms actually create physical energy contributions in the Green's function reconstructions (equations B1 to B3 in Loer et al., 2014). Using our notation these terms can be written as:

$$\begin{aligned} &EI^{rf}_{NM}(\mathbf{x}_r,\mathbf{x}_s,t) = \\ &\int_{-\infty}^{+\infty}\Bigg(\int_{\partial D_{S,top}}\frac{2}{\rho(\mathbf{x}_S)V_P(\mathbf{x}_S)}G^{0(\Phi,\Phi)*}_{(M,P)}(\mathbf{x}_r,\mathbf{x}_S)\int_{\partial D_{R,top}}\{d^{S(p,\Phi)}_{(-,P)}(\mathbf{x}_R,\mathbf{x}_S)\times \\ &G^{0(\Phi,f)*}_{(N,z)}(\mathbf{x}_s,\mathbf{x}_R)-d^{S(v,\Phi)}_{(z,P)}(\mathbf{x}_R,\mathbf{x}_S)G^{0(\Phi,h)*}_{(N,zz)}(\mathbf{x}_s,\mathbf{x}_R)\}\,\mathrm{d}^2\mathbf{x}_R\,\mathrm{d}^2\mathbf{x}_S\Bigg)e^{j\omega t}\,\mathrm{d}\omega \end{aligned} \tag{6.10}$$

and

$$\begin{aligned} &EI^{tr}_{NM}(\mathbf{x}_r,\mathbf{x}_s,t) = \\ &\int_{-\infty}^{+\infty}\Bigg(\int_{\partial D_{S,top}}\frac{2}{\rho(\mathbf{x}_S)V_P(\mathbf{x}_S)}G^{S(\Phi,\Phi)*}_{(M,P)}(\mathbf{x}_r,\mathbf{x}_S)\int_{\partial D_{R,bot}}\{d^{0(p,\Phi)}_{(-,P)}(\mathbf{x}_R,\mathbf{x}_S)\times \\ &G^{0(\Phi,f)*}_{(N,z)}(\mathbf{x}_s,\mathbf{x}_R)-d^{0(v,\Phi)}_{(z,P)}(\mathbf{x}_R,\mathbf{x}_S)G^{0(\Phi,h)*}_{(N,zz)}(\mathbf{x}_s,\mathbf{x}_R)\}\,\mathrm{d}^2\mathbf{x}_R\,\mathrm{d}^2\mathbf{x}_S\Bigg)e^{j\omega t}\,\mathrm{d}\omega. \end{aligned} \tag{6.11}$$

The reflection-related term EI^{rf}_{NM} contributes to the causal Green's function (Figure 6.17a) and shows how conventional imaging from above using reflection data and a background model (within the terms) maps unknown discontinuities in the subsurface. The transmission-related term EI^{tr}_{NM} constructs the anticausal Green's function (Figure 6.17b) and shows how transmitted energy is incorporated in two-sided imaging. Note that the latter is not only valid for primaries but also multiply-scattered waves

provided that all interactions between wavefield and model occur below the pseudo-source $\mathbf{x}_s$ and pseudoreceiver $\mathbf{x}_r$.

Figure 6.17c shows the causal panel of the term in equation 6.10 and Figure 6.17e shows the anticausal part of the term in equation 6.11 for $EI^1_{PP}(\mathbf{x}_r, \mathbf{x}_s, t)$. Despite the complexity of the medium and the presence of perturbations both above and below the pseudosurvey line, upgoing waves are successfully reconstructed by both terms. Moreover, comparing the panels in Figure 6.17c and e with the true EI in Figure 6.7a we notice how the two terms in equations 6.10 and 6.11 are also almost transparent to downgoing waves. We can thus see that these two terms act as an approximate up/down wavefield separation filter for primaries and possibly low-order internal multiples at the EI pseudosurvey datum surface; they also do not require any local information about the medium parameters as is usually required by wavefield separation filters (e.g., Amundsen, 1993).

The same two terms are then computed using the incorrect velocity models. When the EI is obtained by means of one-sided ERTM, having incorrect extrapolators results in a shift of the events in the gather to later times (Figure 6.17d). Upgoing events constructed from energy in the transmitted wavefield are instead shifted in the opposite direction, and generally with different time shifts (Figure 6.17f). This is explained by the fact that wavepaths used to construct EI^{rf}_{PP} (Figure 6.17a) and EI^{tr}_{PP} (Figure 6.17b) are different and thus reflected and transmitted waves have different sensitivity to velocity errors. Provided that reflection data in equation 6.10 and transmission data in equation 6.11 are effectively recorded, for example in situations where actual receivers are available at both the Earth's surface ($\partial D_{R,top}$) and somewhere inside the medium ($\partial D_{R,bot}$), such as in a borehole, this property can be directly exploited to design a new functional that is sensitive to migration velocity errors, or alternatively an additional regularization term for FWI or MVA.

We might try to quantify the time shift by temporal correlation of the two extended images, EI^{rf} and EI^{tr}

$$C(\mathbf{x}_r, \mathbf{x}_s, t) = EI^{rf}(\mathbf{x}_r, \mathbf{x}_s, t) \bar{*} EI^{tr}(\mathbf{x}_r, \mathbf{x}_s, t), \tag{6.12}$$

where $\bar{*}$ represents correlation in the time domain. It can be observed that if the migration velocity models are correct, the crosscorrelation is mainly focused around $t = 0$ (Figure 6.18a - left). Events at non-zero shift are also generated by cross-talk between events in the seismogram; these events are considered to be noise in this approach, and could be further mitigated if the correlation was replaced by deconvolution.

In the presence of velocity errors, energy is shifted instead in the time axis and so is

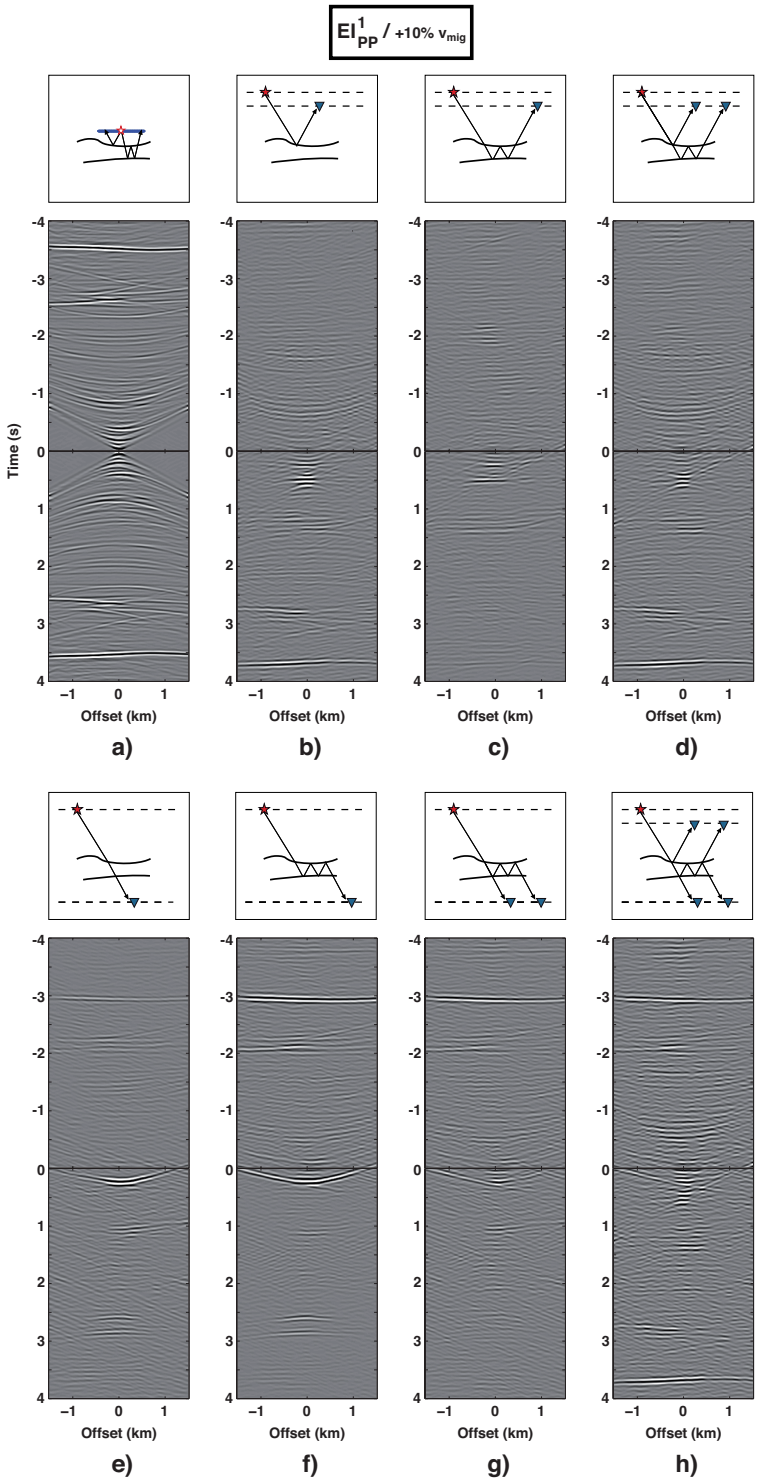

Figure 6.16: PP extended images obtained (a) via direct modelling with the correct velocity models and (b-h) from the four different experiments depicted Figure 6.5 (and from various summed combinations of their contributions) for the shallow survey line $EI^1_{PP}(\mathbf{x}_r, \mathbf{x}_s, t)$, using P- and S-wave reference and total velocity models with a +10% error in the migration propagators. Events are generally shifted downward in the causal parts and upward in the anticausal parts.

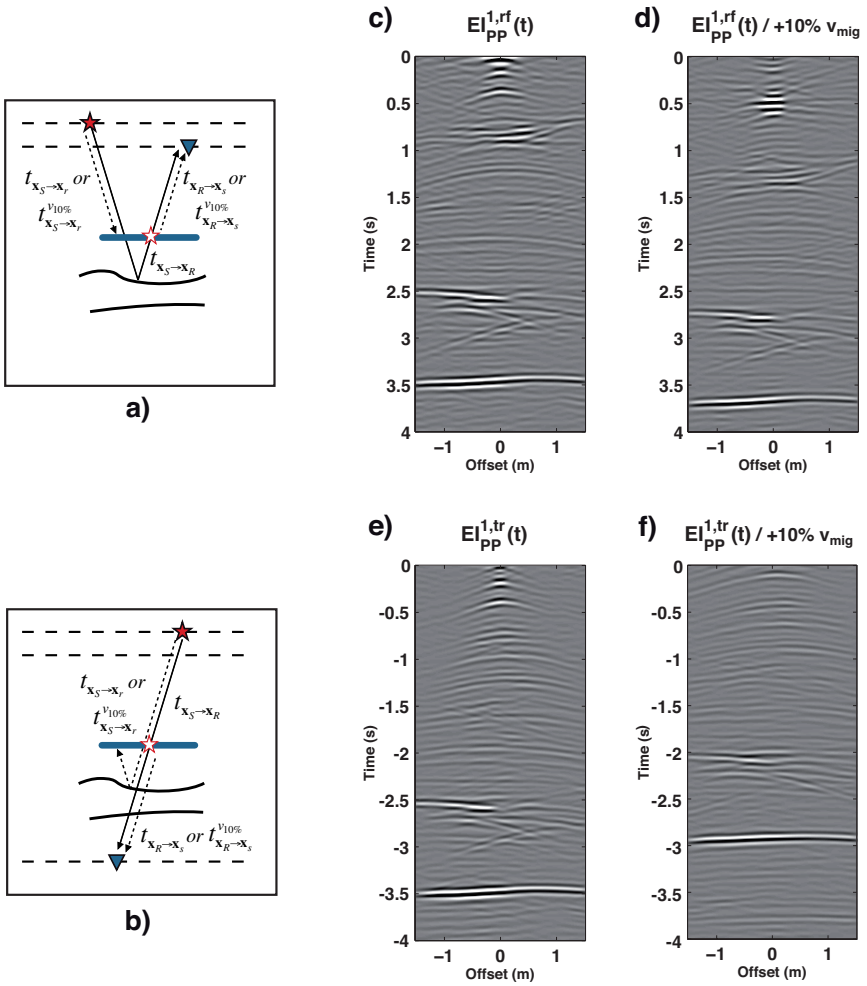

Figure 6.17: Terms that provide physical contributions to the construction of P-to-P upgoing reflections. The causal contribution comes from linear imaging of reflection data (panel (a) and equation 6.10), here shown for EI^1_{PP} with (c) correct velocity models and (d) incorrect velocity models. Nonlinear imaging of transmitted data is responsible for the creation of the anticausal contribution for (e) correct velocity models and (f) incorrect velocity models (see panel (b) and equation 6.11). Solid lines in the illustrations represent the data (reflections in top plots and transmissions in lower plots) whereas dashed lines represent the propagators that are applied to the data.

not focused at zero time (Figure 6.18a - right). We conjecture that this focusing property in the EI domain can be used for velocity analysis either by minimizing the time-shift measured by picking the time of maximum energy in the correlation gather as done by Yang and Sava (2011a) for time-lag EIs, by directly penalizing such energy as done in data correlation waveform inversion (van Leeuwen and Mulder, 2010) or in image correlation waveform inversion (Perrone et al., 2015), or by dynamic warping (Hale, 2014).

Following the second approach, a correlation-based objective function can be defined

as

$$J_C = \frac{1}{2E_C} \sum_{\mathbf{x}_s,\mathbf{x}_r,t} \parallel P(t)\mathcal{H}(C(\mathbf{x}_r\mathbf{x}_s,t)) \parallel^2, \tag{6.13}$$

where P is a penalty operator that annihilates energy at zero time and enhances energy at non-zero time lags. E_C is a normalization factor accounting for the total energy contained in the correlation defined as $E_C = \sum_{\mathbf{x}_s,\mathbf{x}_r,t} |\mathcal{H}(C(\mathbf{x}_r,\mathbf{x}_s,t))|^2$. Here we apply the Hilbert transform ($\mathcal{H}$) to the correlation to calculate its envelope and thus reduce phase-based fluctuations (see Figure 6.18a). The penalized crosscorrelations (equation 6.13) are shown in Figures 6.18b and c: the first peak at positive times in the red line carry the information about the velocity error, and it should be minimized, for example by image-domain waveform inversion.

6.5 Discussion

Estimation of seismic velocities and reservoir properties in complex geologies calls for novel imaging approaches, able to provide accurate localized information at or around points in the subsurface. Scattered responses from pseudosources to pseudoreceivers in the subsurface, known as extended images or common-image point gathers (Vasconcelos et al., 2009a, 2010; Yang and Sava, 2011a,b; Sava and Vasconcelos, 2011; Thomson, 2012) represent a candidate in the image domain that could be used for these purposes. Recent studies (King et al., 2011; King and Curtis, 2012; Meles and Curtis, 2013; Loer et al., 2014) have shown that limited aperture arrays of sources and receivers and the knowledge of only a smoothed version of the propagation velocity model (as used in linear imaging) decrease the accuracy of these scattered wave response estimates. In particular, they showed that these acquisition limitations result in significant non-physical energy being introduced into the extended images. These studies are directly linked to the theory of source-receiver interferometry (Curtis and Halliday, 2010; Halliday and Curtis, 2010; Poliannikov, 2011; Vasconcelos, 2013; Ravasi and Curtis, 2013a). SRI shows that in theory the construction of extended images requires enclosing source and receiver boundaries, and information about the location and magnitude of property perturbations in the subsurface (to construct the scattered wave propagators) in order to estimate the EI correctly. The errors that result from not satisfying these conditions are rarely negligible.

In this chapter, we demonstrate with a synthetic example the additional value arising from properly including internal multiples (in nonlinear imaging) and transmissions (from two-sided illumination) in the construction of elastic EIs in complex geologies.

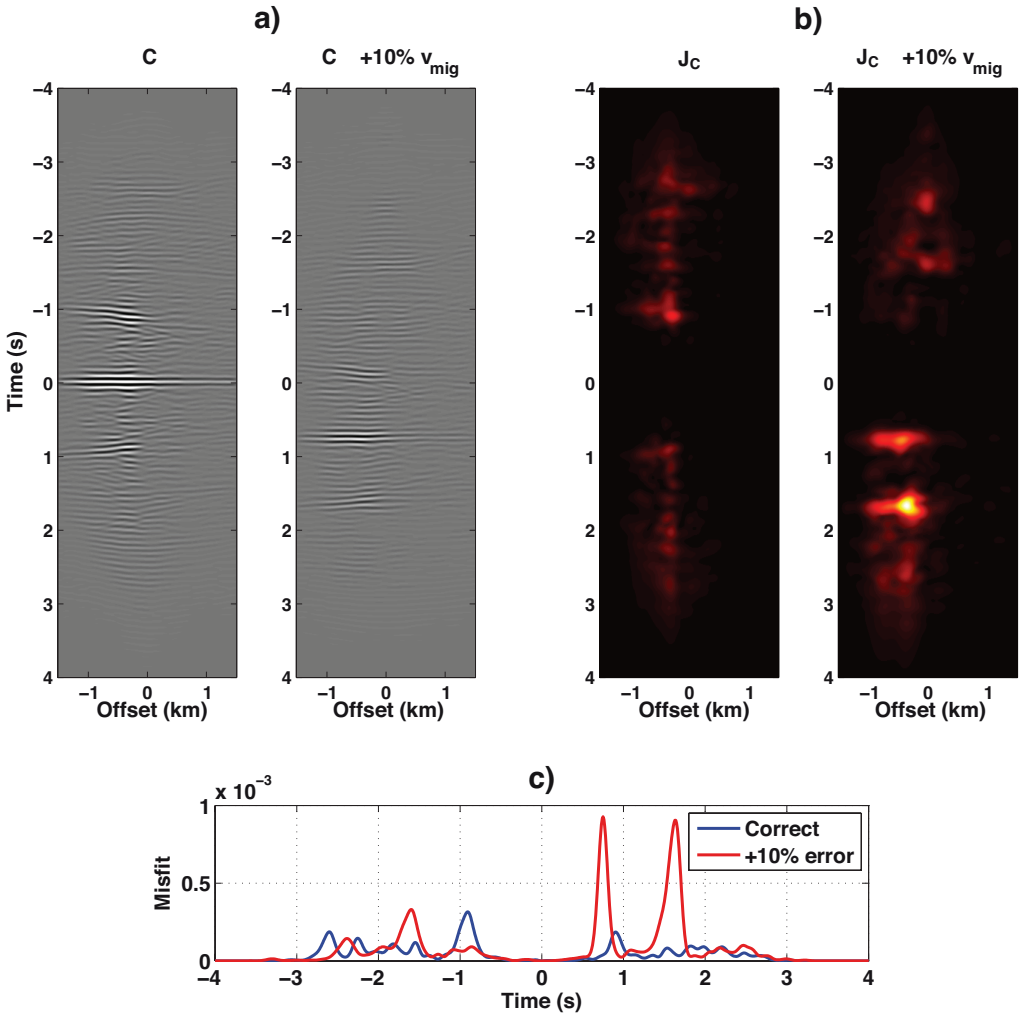

Figure 6.18: (a) Crosscorrelation of the reflection and transmission EIs (equation 6.12) and (b) penalized crosscorrelation (equation 6.13 before stacking over offset and time) for correct (left) and incorrect (right) velocity models. (c) Correlation-based objective function (equation 6.13 after stacking over space but before stacking over time) for correct (blue) and incorrect (red) velocity models.

We show how discarding one or more of these contributions results in missing events, incorrect amplitudes, and spurious energy in the reconstructed pseudogathers. We identify two different reasons for which these contributions are beneficial: first, they construct physical events in the gather which are complementary to those constructed from primaries. For example, the reflection from the top of the salt body on the right of Figure 6.4, which is reconstructed in the causal part of the first EI by means of linear ERTM (Figure 6.7b), is reconstructed in the anticausal part of the same EI only when nonlinear transmissions are accounted for in the imaging condition (Figure 6.7f). Secondly, multiply-scattered waves (either reflections or transmissions) cancel some of the non-physical or spurious energy constructed by the linear imaging conditions, as

shown by for example comparing Figure 6.9e and f for the PS case (black arrows).

However, since the acquisition geometry used in this study (Figure 6.4) is far from the ideal situation of enclosing boundaries of sources and receivers (e.g., sources are missing below the imaging target, and sources and receivers are missing along both sides of the subsurface model), we obtain PS EIs of poorer quality compared to their PP counterparts. The fact that violating the source and receiver equipartitioning requirement affects these two types of extended images in a different way is an indication of them having a different spatial distribution of stationary (physical and non-physical) contributions. As far as physical stationary points are concerned, by noting that for a fixed pseudo-offset (i.e., distance between pseudosource and pseudoreceiver) and a given interface the converted S-wave requires an incident P-wave angle that is generally larger than that of related reflected P-wave (Figure 6.19), the reconstruction of any event at large offset in the EI gather requires wider aperture acquisition (i.e., physical sources and/or receivers at farther offset) in PS imaging than in PP imaging. Furthermore, since in our example we have assumed absorbing boundaries on the sides of the subsurface model effectively creating a laterally infinite and laterally-homogeneous elastic medium outside the boundaries, P-wave sources would not suffice along the elastic portion of the enclosing source boundary and additional S-wave sources would be required to suppress all the non-physical energy generated by the available sources and receivers. On the other hand, the events that are successfully constructed in PS gathers show correct amplitudes and their characteristic radiation pattern with a polarity flip around zero-offset (normal incidence). This, together with the impossibility to extract physical (meaningful) PS zero-offset zero-time images (Ravasi and Curtis, 2013b), suggests that further research into a more suitable acquisition geometry for converted-mode extended images is necessary in future.

Although here we have assumed exact knowledge of the Earth in the models used to construct the various nonlinear migration propagators, a practical way to account for multiples in these propagators also when only a reference (e.g., smoothed) version of the velocity model is available, may be to use the autofocusing techniques proposed for acoustic media by Broggini et al. (2012); Wapenaar et al. (2012, 2013), and extended to elastic media by da Costa et al. (2014b,c,a); Wapenaar (2014); Wapenaar and Slob (2014). These authors have shown that it is possible to reconstruct an approximation to the correct Green's function (i.e., the full response including internal multiples) from a virtual source anywhere inside the medium, given only the reflection data and an estimate of the direct arrival from the pseudosource to the recording surface. This Green's function can then be interpreted as the response observed by a pseudoreceiver in the subsurface from sources at the surface by source-receiver reciprocity. In principle, such a technique might provide the full (source- and receiver-side) propagators required by

the nonlinear terms in both the wavefield extrapolation and in the imaging condition.

Similarly, given standard one-sided acquisition, the autofocusing method might also be tailored to reconstruct (and then migrate) transmission data. This is specifically true if sources and receivers at the acquisition surface are co-located, and receiver arrays are also well-sampled spatially: the same source-receiver reciprocity argument as above can then be invoked to obtain the response from each source at the acquisition surface to virtual receivers at an arbitrarily selected depth level. Finally, to enable a full two-sided illumination of the imaging target (i.e., also reflection and transmission imaging from bottom sources) a further step is required: conventional surface seismic data (i.e., sources and receivers at the surface) together with the full transmission responses obtained via autofocusing can be used to create virtual data with both sources and receivers below a selected target zone by inverting a series of multidimensional interferometric equations of convolution- and correlation-type (van der Neut et al., 2013c).

Although unwanted non-physical events are completely suppressed in the EI when enclosing boundaries are available (or in principle, when they are constructed numerically by autofocusing), two strategies can be adopted to account for those arising from the interaction of waves propagating sideways if sources and receivers are not available (or constructed numerically) on the sides of the imaging target. These spurious events can either be prevented by appropriate spectral filtering of these fields, or mitigated directly after the extended image is computed. The physical argument behind these filtering procedures is simple: any event constructed in the extended image has a characteristic slope in the t-x domain, which is intrinsically related to the local dip of the reflector/discontinuity represented. Based on some assumptions about the geological structure around the pseudosurvey line of interest, we may be able limit the direction of incoming and emerging waves at the pseudoreceiver and pseudosource locations, respectively. It is worth noting that a direct selection of the ray parameters involved in the imaging condition can also be obtained by transforming the source and receiver field in the plane-wave (τ-p) domain and crosscorrelating only the range of angles of interest, as recently implemented in seismic interferometry (Tao and Sen, 2013).

Finally, there has been a drive towards tomographic velocity analysis (either MVA or image-domain FWI) based on extended images (Yan and Sava, 2010; Yang and Sava, 2012; Fleury, 2012; Fleury and Perrone, 2012; Shabelansky et al., 2013). As demonstrated in our numerical example, adding nonlinear terms to the imaging condition (and wavefield extrapolation) results in EIs with fewer artefacts (i.e., less coherent noise) and better focusing around zero-time, zero-offset (see close-ups in Figure 6.7). We conjecture that improvements in the quality of the EIs may directly turn into a resolution

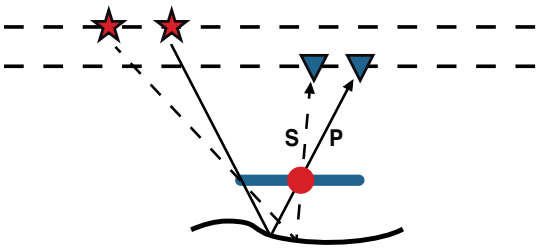

Figure 6.19: Two events (PP reflection and PS conversion) needed to generate PP and PS energy at a fixed pseudo-offset in the extended image.

improvement of these velocity analysis techniques. Moreover, since multiply-scattered waves generally travel along different paths from those of singly-scattered waves, these wavepaths can also provide additional sensitivity to the model and reduce the nullspace of the tomographic operator. Two-sided illumination may also lead to new forms of migration velocity analysis when surface and borehole seismic data are jointly acquired. In fact we can compute terms that physically contribute to a certain type of events in the EI (e.g., upgoing waves) using either reflections or transmissions and then define an objective function that minimize the relative time-shift between them. We have shown that this penalty or objective function is sensitive to a 10% velocity error in our complex reference model, but clearly it requires testing and analysis over a range of scenarios to asses its expected utility as a velocity analysis objective function in practice.

6.6 Conclusion

In this chapter we create and analyse elastic (PP and PS) extended images in a realistic Earth model using a source-receiver interferometric framework. We study how exploiting the energy emitted by a physical source during the seismic experiment, including primary reflections (i.e., linear imaging), multiple reflections (i.e., nonlinear imaging), or transmissions (i.e., two-sided imaging), impacts the reconstruction of events in extended images.

Primary reflections from a conventional acquisition setup mainly construct upgoing and downgoing physical events in the causal and anticausal part of the extended images, respectively, but also strong non-physical waves. One type of non-physical event is due to the interaction of waves propagating sideways, and is generally characterized by a linear moveout: they can be removed via f-k filtering of the source and receiver wavefields (in pre-imaging domain), or of the extended image (in post-imaging domain). In PP imaging, multiple reflections, properly included in extended images via nonlinear imaging, suppress another type of non-physical arrivals (with hyperbolic-like moveout) and correct the polarities and amplitudes of some of the physical events produced by linear imaging. Transmissions construct events that are complementary to those given

by reflection data (e.g., transmission data from top sources construct upgoing waves in the anticausal part and downgoing waves in the causal part), improving the time symmetry in the extended images. However, PS extended images are of poorer quality compared to their PP counterparts. Different factors that may affect the quality of PS imaging have been discussed, such as absence of S-wave sources, limited-aperture boundaries, and insufficient recording time.

Extended images are also proven to be sensitive to errors in the migration velocity models: in particular it is shown that different time shifts of the same event arise in the EI when it is constructed using reflection or transmission data with incorrect velocities. This suggests that the two terms provide complementary information about velocity errors, and can be combined to design velocity analysis methods with potentially greater sensitivity to model parameters than current methods.

7

Application 3: Directional acoustic extrapolation of Volve OBC data

Methods for wavefield injection are commonly used to extrapolate seismic data in reverse-time migration (RTM). Injecting a single component of the acoustic field, for example pressure, leads to ambiguity in the direction of propagation. Each recorded wavefront is propagated both up- and downward, and spurious (or ghost) reflectors are created alongside real reflectors in the subsurface image. Wavefield separation based on the combination of pressure and particle velocity data is thus generally performed prior to imaging to extract only the upgoing field from multi-component seabed or towed marine seismic recordings. By instead combining vector-acoustic (VA) data with monopole- and dipole-type propagators in the extrapolation of shot or receiver gathers, we show that wavefield separation (or deghosting) can instead be performed 'on-the-fly' at limited additional cost. This strategy is successfully applied to a line of a North Sea ocean-bottom cable dataset, acquired over the Volve field. We then evaluate additional advantages over standard RTM with decomposed fields such as improved handling of the directivity information contained in the acquired vector-acoustic data for clearer shallow sections and better focused space-lag common image gathers, and imaging of the downgoing component without the need for additional finite difference modelling via mirror migration. We finally prove the robustness of our method with respect to sparse and irregular receiver sampling.

7.1 Introduction

Recent advances in seismic streamer technology allow for the acquisition of vector-acoustic (VA) measurements by means of devices that record both pressure and multi-component (e.g., vertical and crossline) particle velocity or acceleration (Robertsson et al., 2008; Cambois et al., 2009). These new systems could represent a breakthrough in the way we process and image seismic data. Geophysical techniques that primarily focus on data-domain processing of such data have already been proposed for improved noise attenuation (Cambois et al., 2009), signal reconstruction (Vassallo et al., 2010), 3D deghosting (Ozbek et al., 2010) or multiple attenuation (Frijlink et al., 2011). Novel imaging techniques that better honour the physics of wave propagation through the use of multicomponent data are emerging. The latter are the focus of this chapter.

Current standard acoustic migration algorithms, based on either ray-theory or a wave-equation formulation (Biondi, 2006), use a single input data type that is generally the recorded pressure data or a pre-processed version of it, to create an image of the subsurface. If up/down wavefield separation (i.e., the weighted sum of pressure and velocity data, generally referred to as PZ summation — Barr and Sanders, 1989; Amundsen, 1993) is not included in the pre-processing, up- and downgoing (ghost) fields contribute to the generation of both real and spurious reflectors in the image, respectively. Ghost fields are in fact erroneously interpreted as upgoing events that travel longer in the subsurface (to compensate for bounces at the free-surface of the water layer), and interact with the directly modelled source wavefield at incorrect locations below the real reflectors from which they actually originate, generating cross-talk.

In the context of source-receiver interferometric imaging (Oristaglio, 1989; Halliday and Curtis, 2010), Vasconcelos (2013) formulates migration in a vector-acoustic fashion and shows that vector-acoustic reverse-time migration (VARTM) can produce images deprived of ghost reflectors, even when taking as input non-decomposed data. The decomposition step can be avoided because vector-acoustic fields, combined by means of two-way representation theorems (Wapenaar, 2004; van Manen et al., 2005, 2006; Wapenaar and Fokkema, 2006), enable directional wavefield injection at the receiver surface, meaning that any wavefront is back-propagated only towards the direction from which it arrived (see also Mittet, 1994; Vasconcelos, 2011; Vasconcelos et al., 2012; Blanch, 2012; Amundsen and Robertsson, 2014). Zhenhua and van der Baan (2014) have recently used VARTM for microseismic event localization. El Yadari and Hou (2013) and El Yadari (2015) have adapted the vector-acoustic framework to Kirchhoff and beam migration, respectively. Finally, in Chapter 3 (and in Ravasi and Curtis, 2013a; Ravasi et al., 2014) we have extended this methodology to elastic datasets (e.g.,

land, borehole, or hard-seabed), where wave-mode (P and S wave) separation is also embedded within wavefield extrapolation (Mittet, 1994). In Chapter 9, I discuss some of the practical limitations to the application of the elastic formulation to field datasets. A number of strategies to circumvent those limitations by means of additional recordings or data processing are then suggested.

Historically seafloor seismic data acquisition has advanced ahead of streamer acquisition in acquiring complementary data components. This was done partly with the aim of collecting converted shear-wave (PS) data together with compressional (PP) data (Maver, 2011) for improved imaging through gas clouds (Ronholt et al., 2008), density estimation (Leiceaga et al., 2010), and lithology characterization (Shahraeeni and Curtis, 2011). Moreover, given the availability of multi-component measurements at the seafloor, it is standard practice to combine pressure and particle velocity measurements in order to attenuate the effect of strong free-surface multiples on the receiver side prior to acoustic (or PP) imaging (Soubaras, 1996; Schalkwijk et al., 1999; Osen et al., 1999; Muijs et al., 2004).

Here we apply vector-acoustic migration to a receiver line of a North Sea OBC field dataset, acquired over the Volve field* (Szydlik et al., 2007). We focus primarily on evaluating its effectiveness in suppressing downgoing waves (ghosts) at the receiver array by directional injection of vector-acoustic data as an alternative to wavefield decomposition schemes. Additional advantages of VARTM over standard RTM of decomposed waves such as improved handling of directivity information for clearer shallow sections and better focused space-lag common image gathers, and imaging of the downgoing component of the recorded field without the need for additional finite-difference modelling (via mirror VARTM) are also demonstrated.

The chapter proceeds as follows: we first briefly review the theory of vector-acoustic migration with special focus on the differences that arise in wavefield extrapolation of pressure and velocity data compared to standard extrapolation of pressure data only. We then discuss the key characteristics of our field dataset and its preprocessing, and present intermediate results (e.g., receiver wavefield and single-shot images) of the application of VARTM as well as multi-shot images and their corresponding interpretation. In so doing, significant emphasis is placed on identifying and tracking key arrivals in the data that can be used to assess and illustrate the performance of vector-acoustic wavefield extrapolation.

*The dataset, property of Statoil ASA, was acquired over the Volve field in 2002. A portion of this dataset, namely a multi-component cable line, has been provided for my studies by Dr. Alexander Kritski. I would like to thank Statoil ASA and the Volve license partners ExxonMobil E&P Norway and Bayerngas Norge, for granting me permission to show this dataset.

7.2 A review of vector-acoustic migration

Define p and v_n to be the time-reversed pressure and normal particle velocity data recorded by multi-component receivers, with $v_n = \mathbf{v} \cdot \mathbf{n}$ where $\mathbf{v}$ is the particle velocity vector and $\mathbf{n}$ is the outward pointing normal vector at the recording surface. Similarly q and f_n refer to the propagators used to extrapolate the recorded data by means of monopole- and dipole-type (gradient) sources respectively, where gradients f_n are in the n-th direction. The symbol $\Rightarrow$ is used to define the back-propagation of a data component (on the left) with a specific source type (on the right), so $p \Rightarrow q$ means that recorded pressure data are back-propagated with monopole-source Green's function propagators. When implemented via finite-difference methods, $\Rightarrow$ can alternatively be seen as a boundary condition that allows a numerical injection scheme to inject the associated data components (Robertsson and Chapman, 2000; Robertsson and Amundsen, 2014).

Current practice RTM uses only monopole injection sources to estimate the receiver wavefield (w_r^{RTM}), independently of the choice of the data to be injected. If the data are the full recorded pressure field (for example, from single-component acquisition systems) we write

$$w_r^{RTM} : p \Rightarrow q \tag{7.1}$$

and each wavefront injected in the finite-difference scheme propagates both up- and downward from the injection points, irrespective of the direction from which it arrived, thus creating a wavefield artefact for every physical arrival present in the data. Although extrapolation can be done with an absorbing boundary (in place of the free-surface) to attenuate the waves propagating upward, each downgoing component of the data that is erroneously back-propagated downward instead of upward interacts with the source wavefield and generates cross-talk artefacts in the image.

Where multi-component data are recorded, up/down wavefield decomposition (Appendix B) can be applied prior to imaging to suppress some of the events that are incorrectly handled by the injection procedure in equation 7.1. Thereafter it is preferred to use only the upgoing field denoted as p^- in the extrapolation step

$$w_r^{u-RTM} : p^- \Rightarrow q. \tag{7.2}$$

Note that an image of the downgoing field denoted as p^+ can also be constructed by means of mirror imaging (Grion et al., 2007) by, for example injection of the ghost data

as if it were recorded not on the seabed but at a sea surface twice as high

$$w_r^{d-RTM} : \; p^+ \Rightarrow q. \tag{7.3}$$

Shot-profile VARTM (see Appendix E for the derivation of vector-acoustic receiver-profile migration) solves the injection limitations of standard RTM without requiring any pre-processing of the data (Vasconcelos, 2013). Simultaneous injection (indicated by the symbol '&' in the following equation) of the full pressure and (negative) normal particle velocity with two different types of injection sources, dipole and monopole respectively,

$$w_r^{VARTM} : \; (p \Rightarrow f_n) \,\&\, (-v_n \Rightarrow q) \tag{7.4}$$

enables 'on-the-fly' wavefield separation into the up- and downgoing components of the recorded field. Upgoing waves are injected only downward and downgoing waves back-propagate only upward. Intuitively, the application of dipolar injection sources on pressure data has the same effect of correcting for the different directions of arrival of seismic events in the velocity gather (by means of the so-called obliquity factor) when wavefield separation is performed in the f-k (or τ-p) domain. Finally, note that equation 7.4 is equivalent to the first line of equation 3.7. In other words, for ocean-bottom acquisitions with receivers coupled to hard seabeds, the only difference between the acoustic and elastic approaches is represented by the velocity model used to construct the q and f_n propagators, acoustic in equation 7.4 and elastic in equation 3.7.

Independently of the type of wavefield extrapolation used to construct the receiver field, before an image of the subsurface can be constructed, another wavefield (the so-called source wavefield) needs to be computed by propagating forward in time an estimate of the source wavelet (s) into the migration model:

$$w_s : \; s \Rightarrow q. \tag{7.5}$$

Note that here we use a monopole-type source but with the recent introduction of dual-source technology that combines pressure with gradient/dipole marine sources (Robertsson et al., 2012), handling of in- and outgoing waves at the source array will also be possible in the near future by combining the extrapolated receiver fields together with monopole and dipole source side propagators as explained in Vasconcelos (2013).

An imaging condition is finally employed to map the interaction of source and receiver wavefields in the subsurface and create a representation of the Earth's physical property

contrasts:

$$i: \; w_s * w_r, \tag{7.6}$$

where $*$ denotes either zero-time cross-correlation (Claerbout, 1971) or deconvolution (Guitton et al., 2007; Schleicher et al., 2008). In this chapter, we adopt a cross-correlation imaging condition.

7.3 Volve field, offshore Norway

In 2002, a 3D seismic OBC survey was acquired over the Volve field, offshore Norway in the gas/condensate-rich Sleipner area of the North Sea (Figure 7.1a). Volve is a small oil field with a dome-shaped structure formed by the collapse of adjacent salt ridges during the Jurassic period (Szydlik et al., 2007). Figure 7.1b shows the reference velocity model, together with the receiver and source line geometry selected for this study. The receiver line is a 6 km-long 4C cable placed on the seafloor about 92 m below the water surface containing 235 receivers with an interval of 25 m. The sail line is 12 km long with a shot interval of 50 m.

Pre-processing and single-shot imaging

The acquired data were preprocessed by Statoil. Pre-processing included noise suppression, source designature, and vector-fidelity corrections. Pressure (Figure 7.2a) and normal (that here we loosely call vertical because the seabed is nearly horizontal) particle velocity (Figure 7.2b) have been further scaled by the square root of time to transform the data from 3D to 2D geometrical spreading (Schalkwijk et al., 1999). We also choose a window in the common-receiver gather that contains only the direct wave, which is a downgoing field at the recording array below the seabed (Dash et al., 2009), and we calibrate the velocity component to the pressure by imposing that the upgoing field should be zero inside that window (Muijs et al., 2004). Vector-acoustic injection of the calibrated fields is then equivalent to acoustic wavefield separation and injection below the seabed. The calibration filter (Figure 7.2e) has the effect of changing amplitude and phase of the calibrated velocity data (Figure 7.2c) with respect to the recorded velocity data (Figure 7.2b): note, for example, a slight change in wavelet shape of the first arrival that improves the matching with that in the pressure data (top panel of Figure 7.2d) and the attenuation of lower frequencies (lower panel of Figure 7.2d).

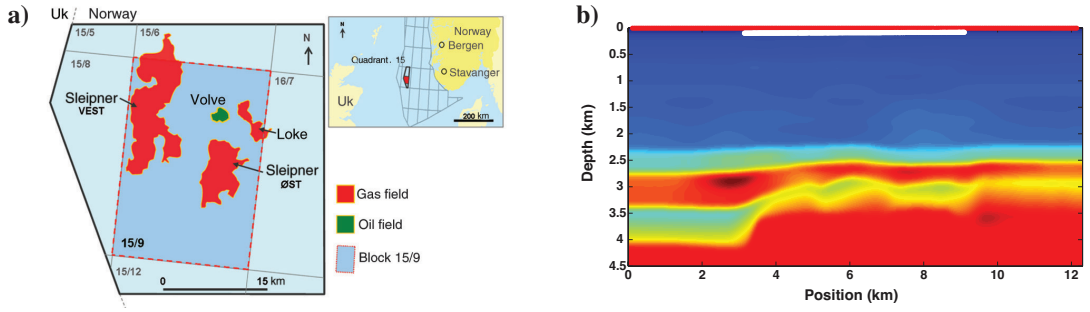

Figure 7.1: (a) Location of Volve field in the North Sea and (b) migration velocity model together with source (red line) and receiver (white line) locations.

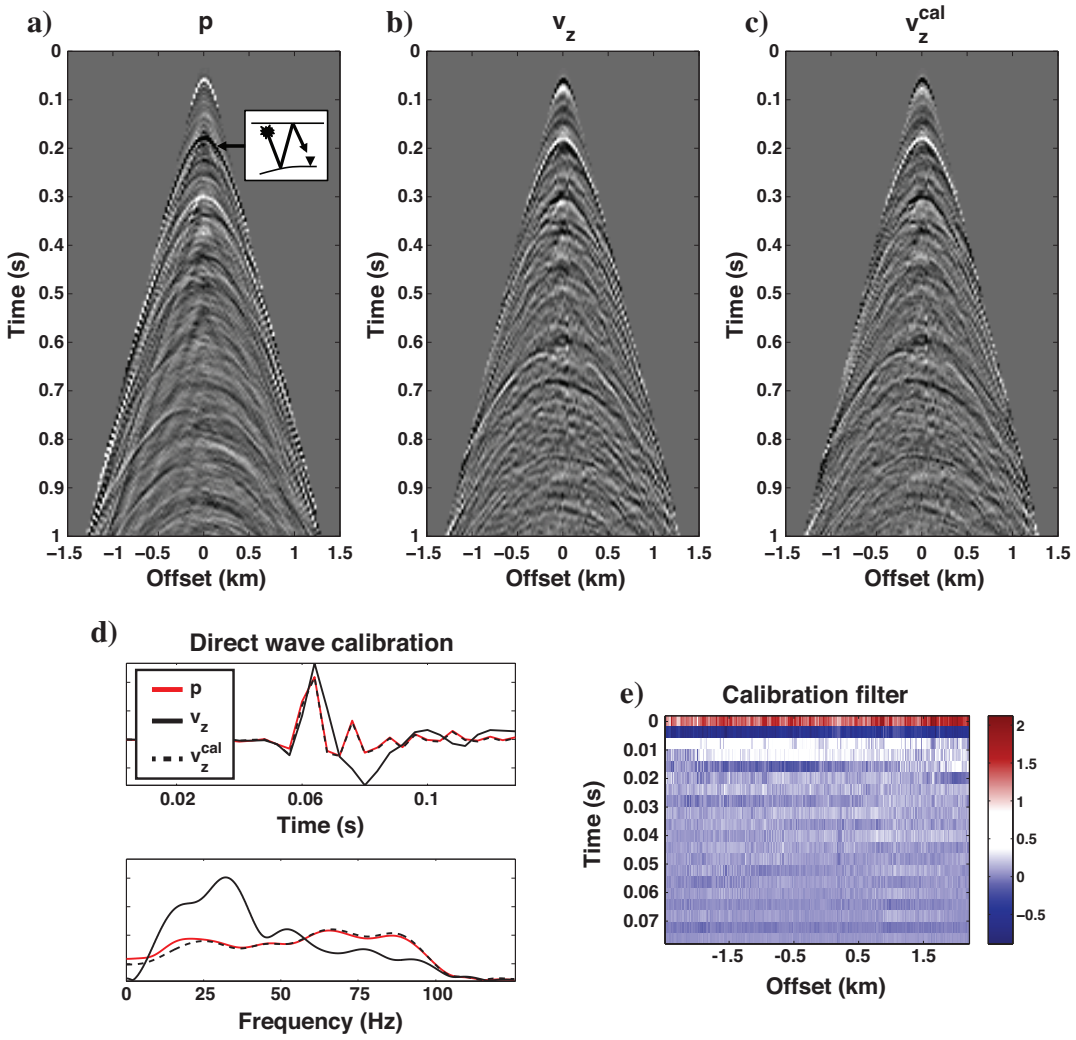

Figure 7.2: 2D slice of Volve 3D OBC dataset (the initial 1 sec of data is visualized). (a) Pressure shot-gather, (b) and (c) vertical velocity shot-gather before and after calibration. (d) Zero-offset traces of pressure (red line), vertical velocity (black line), and calibrated vertical velocity (dashed black line) inside the window where calibration is performed (top), their amplitude spectra (bottom), and (e) the calibration filter.

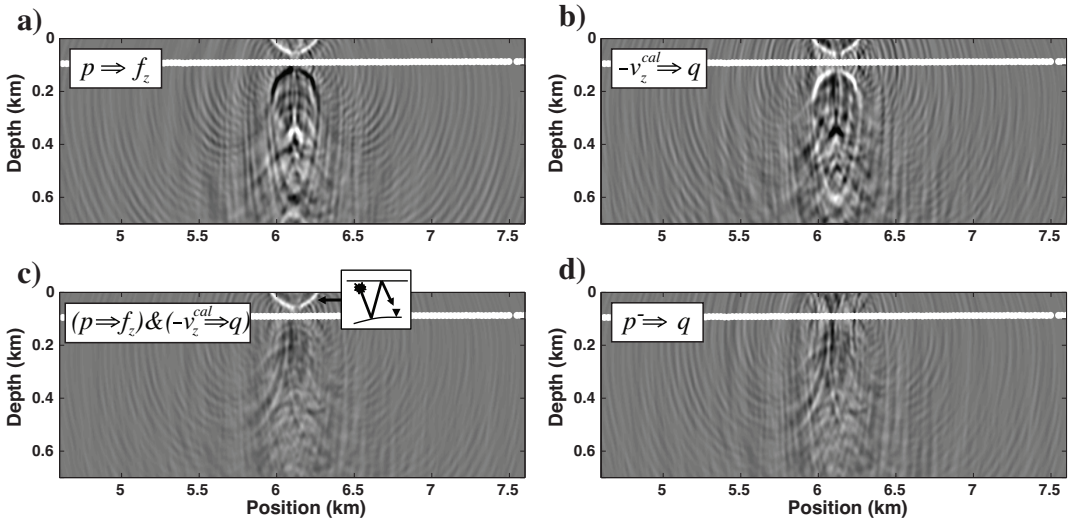

Figure 7.3: Fixed-time snapshots of reverse-time extrapolated receiver wavefields just after the injection of the first-order seabed free-surface multiple (see Figure 7.2a). VA extrapolation of (a) full pressure component, (b) full velocity component and (c) sum of the two — equation 7.4. The vector-acoustic receiver wavefield is compared to (d) standard extrapolation of the upgoing pressure field. The white line denotes the location of the receiver surface where the data are injected.

Figure 7.3 shows a time snapshot of wavefield extrapolation of the data in Figure 7.2. For illustration purposes, the pressure and velocity terms of VA extrapolation in equation 7.4 are injected separately and displayed in panels 7.3a and 7.3b. By focusing on the injection of the first-order water layer multiple (event indicated in Figures 7.2a and 7.3c), we see that each single term of VA extrapolation injects this downgoing field both upward and downward. When these terms are combined together or when vector-acoustic data are simultaneously injected as shown in Figure 7.3c, VA extrapolation almost completely suppresses the wavefront below the receiver surface and enhances that above (i.e., the direction from which this wavefront arrived at the receiver array in the physical experiment). If compared with standard extrapolation of the upgoing field (Figure 7.3d), the receiver field obtained by means of VA extrapolation is also clearer in the proximity of the receiver array because of the proper handling of local directionality information from gradients (i.e., from velocity data and dipole propagators). This is because standard extrapolation invokes a far-field radiation assumption (e.g., Halliday and Curtis, 2010; Vasconcelos et al., 2010) that yields amplitude distortions in the near fields, especially if the curvature of the wavefront approaching the receiver array is not negligible (see Wapenaar and Fokkema, 2006; Ramirez and Weglein, 2009). In fact, in the absence of particle velocity recordings, the pressure data should be scaled by a frequency-dependent factor which is a function of the angle of incidence of each recorded wavefront α, the local medium velocity V and the angular frequency ω (i.e.,

$-j\frac{\omega}{V}cos(\alpha)$ where j is the imaginary unit). This is generally avoided by assuming that the recorded wavefronts are normal to the receiver array so that $\alpha \approx 0$ (Wapenaar and Fokkema, 2006; Thorbecke and Wapenaar, 2007). On the other hand, to be able to perform VA extrapolation, a finite-difference code[†] that models the set of acoustic first-order partial differential equations for pressure and particle velocity (Fokkema and van den Berg, 1993) in a staggered-grid scheme is required. For this reason, the computational cost of such an approach is expected to be higher than that of standard acoustic extrapolation since not only the pressure component of the extrapolated field (which is visualized in Figure 7.3) but also the vertical and horizontal particle velocity fields must be computed and stored in memory.

Single-shot images are then computed for the three different choices of wavefield extrapolation in equations 7.1, 7.2 and 7.4: cross-talk between the source wavefield and the incorrectly extrapolated first-order water layer multiple in the receiver wavefield appears in the standard RTM image (indicated in the close-up of Figure 7.4a) but is suppressed when vector-acoustic injection is used (Figure 7.4b). This artefact is also not present in Figure 7.4c, because up- and downgoing fields have been properly separated in the data domain. A second strong artefact appears in the shallow section of the standard RTM image; this is caused by the improper handling of the second-order water layer multiple.

Imaging of upgoing fields

Images are then computed for the 241 shots and stacked together. Note that we use shot-profile VARTM to generate images throughout the chapter, but images of the same quality can also be produced by means of receiver-profile VARTM as shown in Appendix E. The incorrectly extrapolated downgoing events create structure that is deeper than the real interfaces in the standard RTM image (dashed white arrows in Figure 7.5a). Such ghost reflectors are significantly suppressed in both the VARTM image (Figure 7.5b) and the RTM image of upgoing field only (Figure 7.5c). A small amount of residual energy is however left around those locations: this is not due to inaccuracies in the wavefield separation or vector-acoustic injection, but is rather the effect of source-side first-order multiples that generally overlap with receiver-side ghosts in OBC data (see Figure 1 in Xia et al., 2006). Moreover, differences in the quality of the images are visible in the near surface as a consequence of invoking (RTM) or not (VARTM) a far-field radiation assumption in the extrapolation step. Close-ups of the

[†]The acoustic staggered-grid finite-difference code used for this study has been kindly provided by Dr. Ivan Vasconcelos. It is part of the Madagascar open-source package freely available from http://www.reproducibility.org.

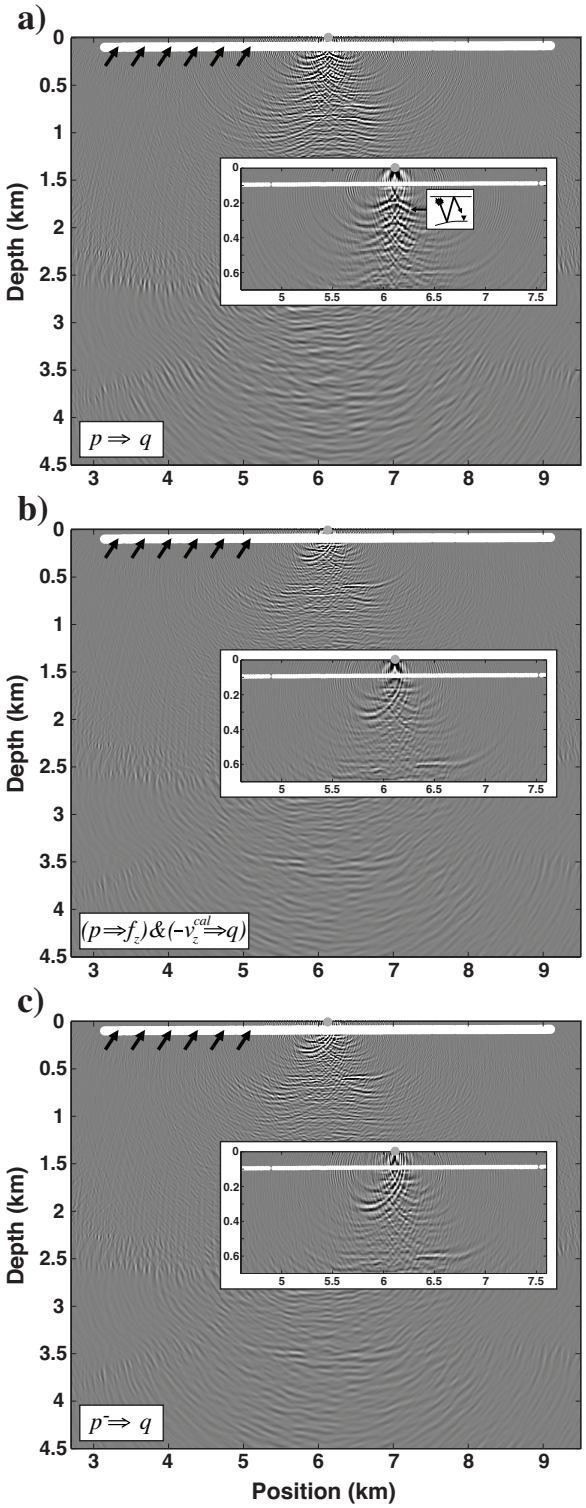

Figure 7.4: Single-shot images. (a) RTM of full pressure field (equation 7.1), (b) VARTM (equation 7.4), and (c) RTM of upgoing pressure field (equation 7.2). A line of black arrows pointing upward indicates that upgoing waves are correctly migrated, and the ghost reflectors is indicated in the RTM close-up.

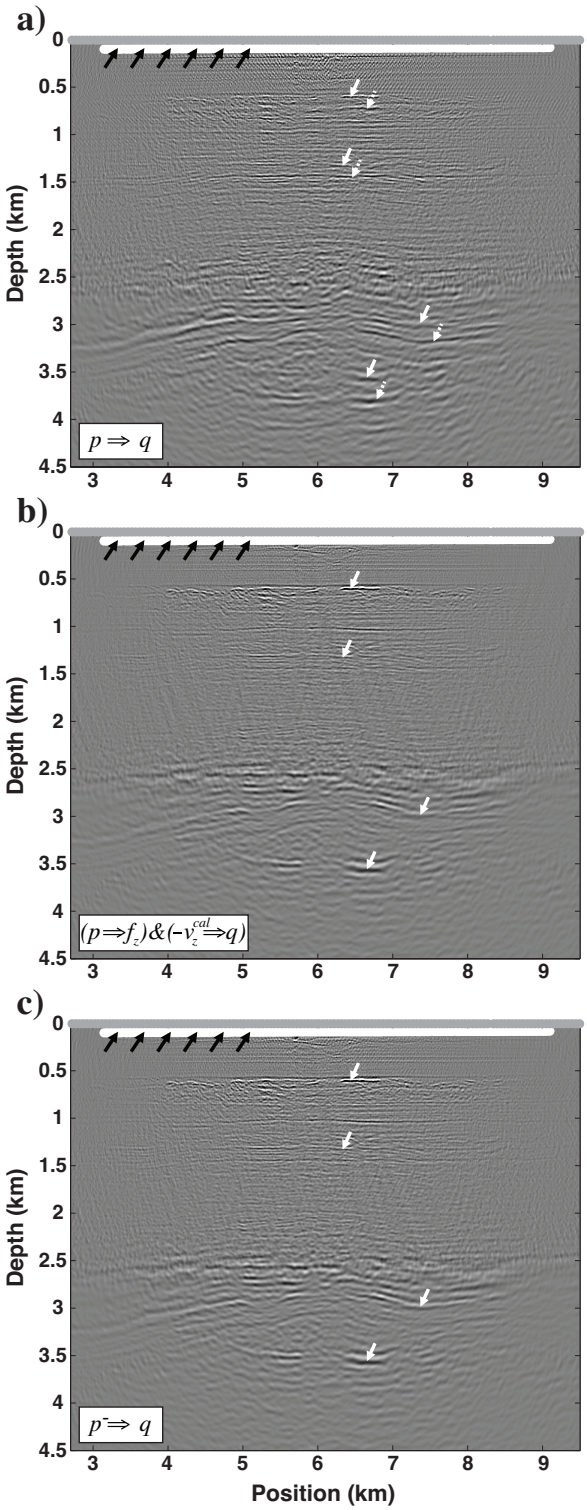

Figure 7.5: Multi-shot images. (a) RTM of full pressure field (equation 7.1), (b) VARTM (equation 7.4), and (c) RTM of upgoing pressure field (equation 7.2). A line of black arrows pointing upward indicates that upgoing waves are correctly migrated, solid white arrows indicate physical reflectors while dashed white arrows point at ghost reflectors.

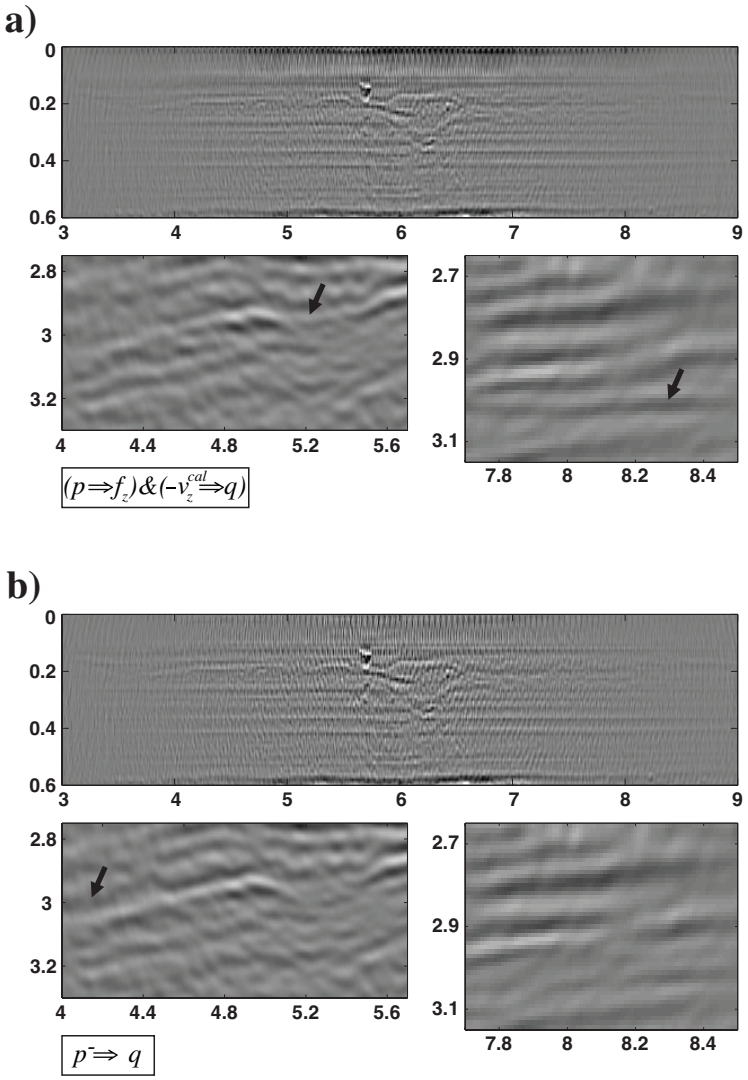

Figure 7.6: Close-ups of (a) VARTM and (b) upgoing RTM images of a shallow section and two deeper areas. Note differences in the clarity of the image in the shallow section, and in the location of some of the deeper interfaces as indicated by arrows to guide the eye.

near surface and two deeper locations are shown in Figure 7.6: the main differences between the VARTM and upgoing RTM images are indeed in the shallow section, but as a consequence of the different handling of wavefield curvature, subtle differences between the two images exist also at depths where the reservoir of interest is located. However, while most reflectors show better continuity in the VARTM image, we note that this is not the case for the reflector indicated by a black arrow in Figure 7.6b: the additional value provided by VARTM in the appraisal of the deeper structure is the subject of ongoing research.

To further study the value of imaging with VARTM with respect to standard RTM

of either full or upgoing pressure, space-lag common image gathers (CIGs — Rickett and Sava, 2002; Sava and Fomel, 2003) are computed as a function of depth at fixed surface coordinates (x = 3, 4, 5, 6, 7, 8, and 9 km). Incorrect handling of downgoing waves in RTM is reflected in additional energy in the CIG in Figure 7.7 that are generally defocused from zero-space lag (white arrows) because they are back-propagated along incorrect wavepaths. Since defocusing from zero space-lag is the criterion used to indicate velocity inaccuracies (Biondi, 2006), including such energy may affect the convergence of migration velocity analysis algorithms based on space-lag CIGs. As for images in Figure 7.5, VARTM (Figure 7.7b) and RTM of upgoing pressure (Figure 7.7c) construct space-lag CIGs that show better focusing around zero space-lag from only energy related to upgoing waves at the recording surface. In the shallow section (from 0 to 0.5 km) however, VARTM takes further advantage of the finite-frequency directivity of the vector-acoustic injection scheme and greatly attenuates events of circular shape that depart from zero space-lag in RTM of upgoing waves. As a consequence of this difference, we conjecture that velocity analysis algorithms based on VARTM CIGs such as those in Figure 7.7b could provide higher resolution models of the near surface by including also the focusing information of the shallow section that would instead be muted out from the RTM CIGs.

As extensively discussed in Chapter 6, extended images (Sava and Vasconcelos, 2011; Vasconcelos et al., 2010) have recently become an alternative tool for velocity analysis (Yang and Sava, 2011b; Fleury, 2012) and/or reservoir characterization (Thomson, 2012; Vasconcelos and Rickett, 2013; Ravasi et al., 2015d). Instead of extending the imaging condition along the space or time axis individually, EIs extend the imaging condition along both the space and time axis by constructing an estimate of the data that would have been recorded by carrying a seismic survey around or at any location of interest in the subsurface (Vasconcelos et al., 2010; Loer et al., 2014). Figure 7.8 shows a comparison between two different EIs at locations $\mathbf{x} = \{6, 2\}\ km$ and $\mathbf{x} = \{6, 2.7\}\ km$ with space extension of $\pm 1\ km$, and time extension of 1 sec only at positive times. RTM of the full pressure field creates EIs that are strongly affected by the cross-talk of downgoing waves. Similarly, f-k spectra show that the ghost effect has propagated throughout the model through of the receiver propagators and acts on the EI as well as on the recorded data. VARTM cleans up the extended images and the events representing the reflection from the top of the reservoir (white arrow in the middle plots) can be seen clearly and picked for amplitude analysis. Comparison with the EIs from RTM of the upgoing field does not show any clear difference from VARTM because the far-field assumption made by RTM algorithms holds for those waves that contribute to events in the EIs at the depth level where they are computed.

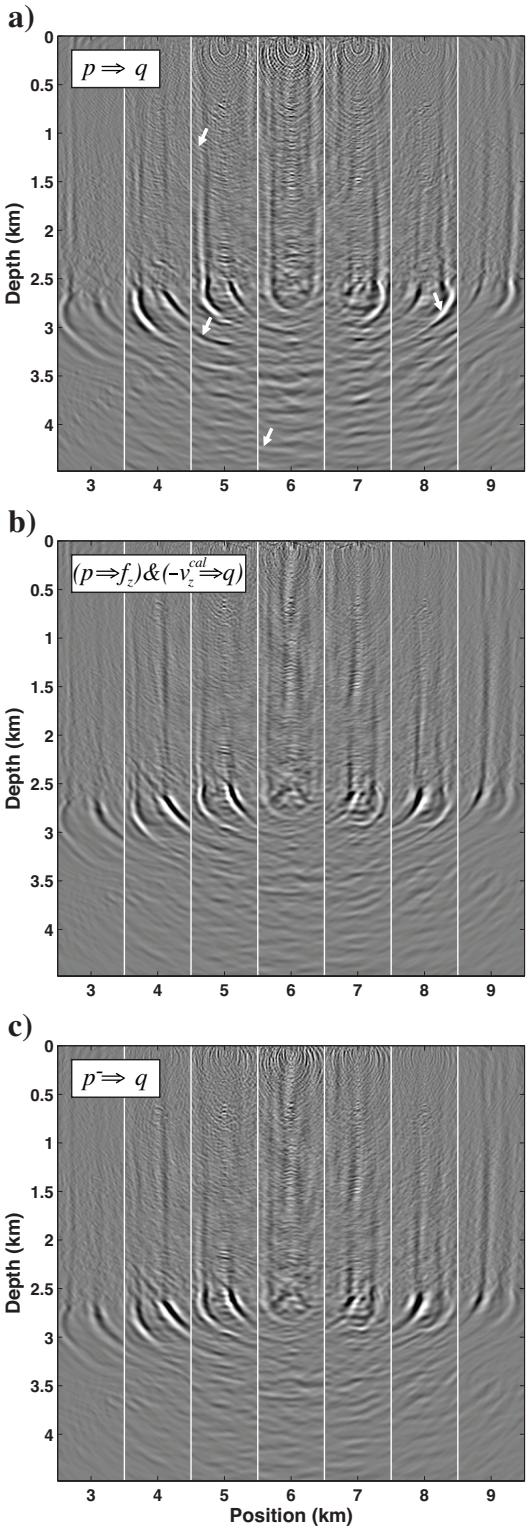

Figure 7.7: Space-lag common image gathers constructed at x = 3, 4, 5, 6, 7, 8 and 9 km for a) RTM of full pressure field, (b) VARTM, and (c) RTM of upgoing pressure field. The space-lags go from -0.5 to 0.5 km on the horizontal axis of the CIG around each surface position, and white vertical lines are used to delimit the different CIGs.

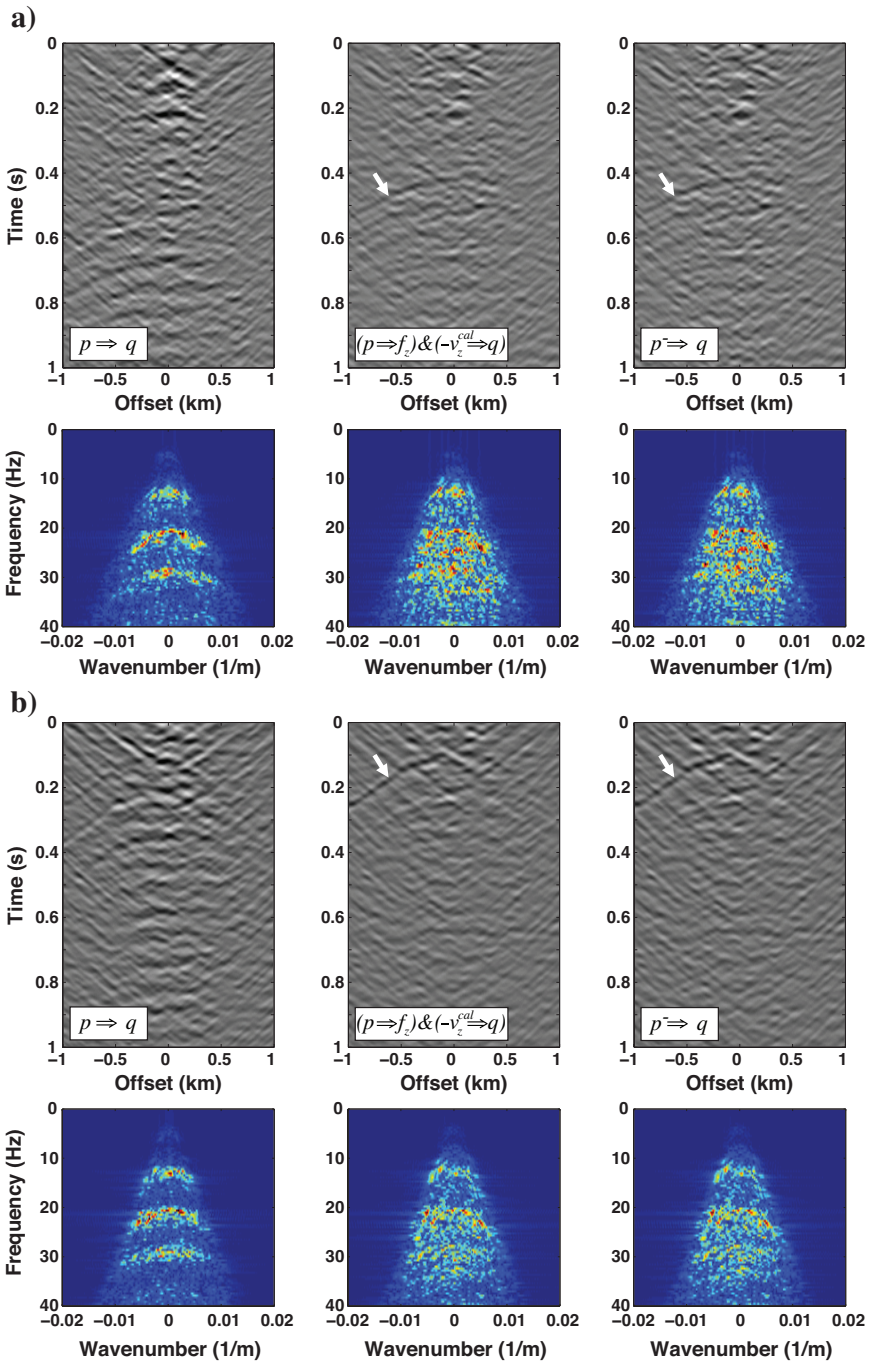

Figure 7.8: Extended images (and their f-k spectra) constructed at locations (a) $\mathbf{x} = \{6, 2\} km$ and (b) $\mathbf{x} = \{6, 2.7\}\ km$ with horizontal extension of $\pm 1\ km$, and time extension of 1 sec only at positive times for RTM of full pressure field (left), VARTM (middle), and RTM of upgoing pressure field (right). White arrows point at events with hyperbolic moveout corresponding to reflections originating at the strong velocity contrast in Figure 7.1b at 2.7 km depth.

Mirror imaging of downgoing fields

Images in Figure 7.9 correspond to imaging using only the receiver-side ghost fields via mirror RTM and mirror VARTM, respectively, and complement those of Figure 7.5. To perform mirror imaging, the free-surface is removed and the receiver extrapolation domain is extended to a depth of -4.5 km with a wavespeed model in the negative depths that is a mirrored version of the migration velocity model with respect to the free-surface (Vasconcelos, 2013). This allows the arrivals related to the ghost wavefield in Figure 7.3b to continue propagating upward toward negative depths; the final ghost receiver wavefield at negative depths is reflected to positive depths prior to imaging using the same source wavefield as that used for the upgoing images.

Mirror RTM of the full pressure data (Figure 7.9a) creates ghost reflectors that are shallower than the real interfaces: upgoing waves, in fact, instead of being only back-propagated directly in the subsurface as in standard RTM, propagates also erroneously all the way from the receiver array to the mirrored domain at negative depths. This additional path makes them coincide in time with the directly modelled source wavefield at shallower locations than those at which they are physically reflected. These spurious interfaces that are not present in the image from mirror RTM of the downgoing pressure data (Figure 7.9c) are also successfully attenuated by mirror VARTM (Figure 7.9b) meaning that the 'on-the-fly' wavefield separation into up- and downgoing waves is successful. Note however that, while mirror VARTM properly maps first-order receiver-side ghosts in the subsurface, higher-order receiver-side free-surface multiples that are recorded as downgoing waves at the receiver array generate spurious structure that is deeper than the real interfaces in any of the images in Figure 7.9 as indicated by the dashed black arrows. These artefacts may be correctly handled only by novel migration algorithms where the imaging condition is modified in order to overcome the Born (single-scattering) assumption as discussed in this thesis and in Fleury and Vasconcelos (2012); Ravasi and Curtis (2013b) and Ravasi et al. (2014).

Imaging of sparsely sampled receivers

Finally we study the ability of VARTM to migrate data that are sparsely sampled along the receiver coordinate (Figure 7.10): first we mimic a cross-line acquisition for 3D ocean-bottom cable surveys by taking 20 receivers with regular sampling of 250 m; we then further reduce the number of receivers to 7 with an irregular space sampling as in an ocean-bottom nodes systems. As previously shown by Vasconcelos (2013) on synthetic examples, we observe that the ability of vector-acoustic injection to decompose up- from downgoing is not compromised by either coarse or irregular injection

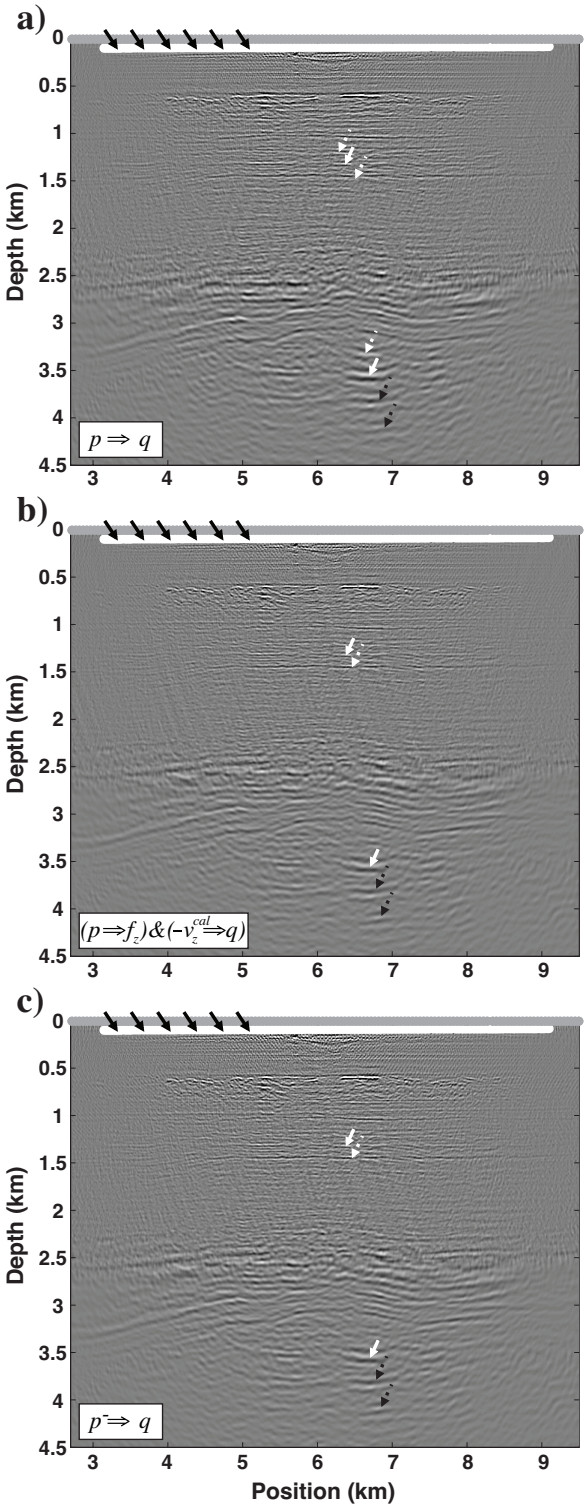

Figure 7.9: Mirror images. (a) mirror RTM of full pressure field, and (b) mirror VARTM, and (c) mirror RTM of downgoing pressure field. A line of black arrows pointing downward indicates that in these cases downgoing waves are those that are correctly migrated. Solid and dashed white arrows indicate physical and ghost reflectors, respectively, and additional dashed black arrows are used to point at spurious reflectors originated from the incorrect mapping in the subsurface of second- and higher-order free-surface multiples.

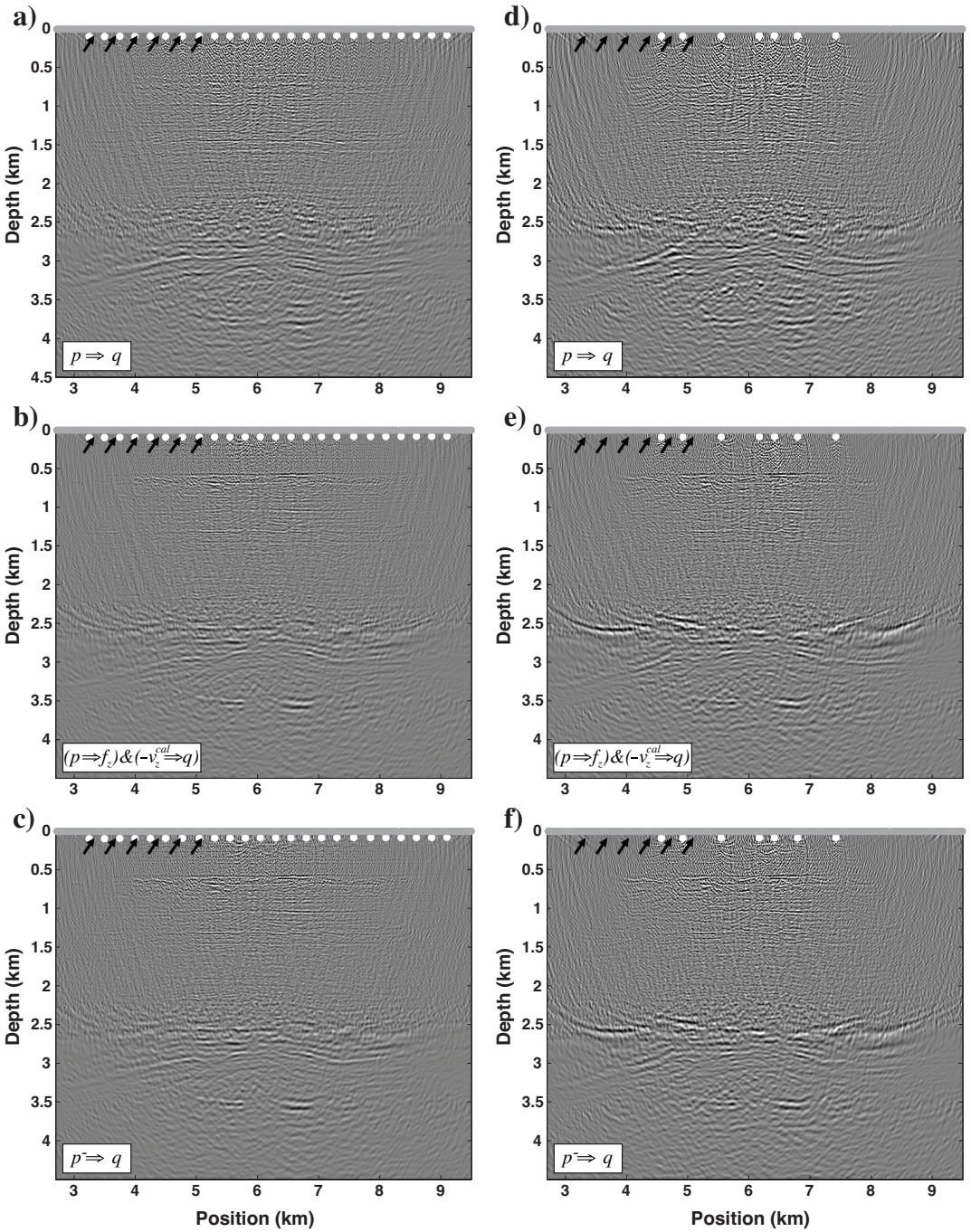

Figure 7.10: Imaging of sparse receiver acquisition mimicking cross-line in 3D ocean-bottom cable surveys (left) and ocean-bottom nodes systems (right). (a) RTM of full pressure field, (b) VARTM, and (c) RTM of upgoing pressure field. A line of black arrows pointing upward indicates that upgoing waves are correctly migrated.

grids: events that are constructed by the interaction between the downgoing component of the recorded data and the source wavefield are in fact successfully suppressed by VARTM (Figure 7.10b and e) as well as if the upgoing field is imaged by standard RTM (Figure 7.10c and f). Moreover, the use of monopole and dipole back-propagation sources together with pressure and velocity data is again beneficial in producing clearer shallow images.

We note that while approaches to up/down wavefield separation acting in the frequency-wavenumber domain could be problematic when the spatial sampling is irregular in both the source and receiver coordinates because standard implementations of the fast Fourier transform assume data to be regularly sampled (Schonewille, 2000), VARTM is not as affected by irregular sampling as former techniques in that it performs wavefield separation directly in the time-space domain without the need for any Fourier transform. On the other hand, since VA extrapolation is based on the theory of representation theorems (Wapenaar, 2004; van Manen et al., 2005, 2006; Wapenaar and Fokkema, 2006), coarse or irregular sampling may lead to spurious energy in the reconstructed wavefields at depth in a similar fashion to seismic interferometry (Mehta et al., 2008). Moreover, given the impossibility to incorporate recordings of the particle velocity component that is parallel to the acquisition surfaces in the vector-acoustic extrapolation, we only expect VARTM to slightly reduce migration swing-like artefacts due to aperture and subsampling by taking advantage of the finite-frequency directivity contained in the normal particle velocity. A more effective handling of the sampling issues may be achieved only if VARTM is applied to data that are previously interpolated by, for example, matching pursuit techniques (Vassallo et al., 2010).

To gain further insights into the accuracy of VA extrapolation with respect to the receiver sampling, we now study a single plane wave arriving at angle of incidence $\theta = 11°$ (Figure 7.11a) with maximum frequency $f_{max} = 40\,Hz$ propagating in a constant velocity medium ($V = 1500\,m/s$) and extrapolate it in three different scenarios (Figure 7.11). Even in the extreme case of a single receiver recording (Figure 7.11b), the use of vector-acoustic measurements in wavefield injection discriminates the upgoing event from the downgoing one, the latter being attenuated in the wavefield extrapolated below the receiver (and almost completely suppressed at zero-incidence). Nevertheless, the absence of neighbouring receivers prevents vector-acoustic extrapolation from sending energy only towards the correct angle of incidence of the recorded plane wave: constructive interference across groups of neighbouring receivers as in Figure 7.11c and d is crucial to identify the angle of arrival and send energy in the correct direction. It is important to note that this is also the case in the coarsely sampled receiver array ($dr = 200\,m$) in Figure 7.11c that does not satisfy the sampling criterion ($dr \leq V/(2f_{max}sin\theta) = 85\,m$). The uplift provided by a finely sampled array of receivers is visible in Figure 7.11d

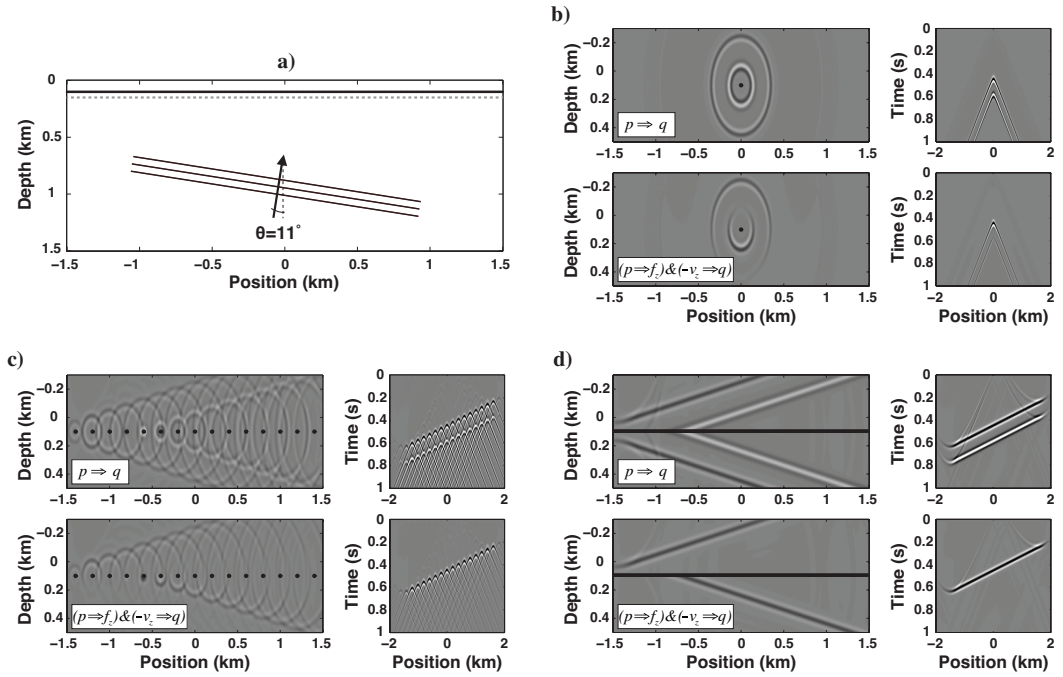

Figure 7.11: Effect of receiver sampling on wavefield extrapolation of a single plane wave arrival. (a) A plane wave with incidence angle $\theta = 11°$ is emitted in the subsurface and recorded alongside its ghost reflected off the free-surface by a horizontal array of 601 receivers with spacing of $5\,m$ (black line). (b), (c), and (d) show the extrapolation of the full recorded data using one receiver, a line of 21 receivers with spacing of $200\,m$, and the entire receiver array, respectively. Each of the left panels represents fixed-time snapshots of standard and vector-acoustic extrapolation with white dots used to identify receivers emitting the recorded data, while the right panels display the extrapolated wavefields recorded along the dashed grey line in a); the top two panels in each case are for standard monopole wavefield injection while the bottom two are for VA extrapolation.

where a coherent plane wavefront is visible in the extrapolated fields.

7.4 Discussion

Source-receiver vector-acoustic RTM is an image-domain deghosting technique that exploits the directionality information of combined pressure and vertical velocity recordings to extract the upgoing field equivalently to the effect of PZ summation (Amundsen, 1993; Soubaras, 1996) in the data-domain. The main difference between these approaches is in the handling of seismic events with different angles of incidence: data-domain deghosting balances the vertical component by first combining the information of neighbouring receivers via f-k (or τ-p) transform and subsequently applying a frequency-wavenumber correction factor, while VA extrapolation provides the same balancing directly by injection of the pressure component as a dipole source at all avail-

able receivers, thus without requiring any domain transform (f-k or τ-p) to be applied to the data.

This difference can have a significant impact for both 3D streamer and ocean-bottom seismic acquisition, which are usually characterized by fine sampling along the cable (inline direction) and by very coarse sampling in the crossline direction, due to the availability of only a limited number of cables. Consequently PZ summation, as well as other standard data-conditioning and processing techniques (e.g., Radon transform, velocity analysis) that must have access to unaliased representations of the wavefields as they are based on plane-wave decomposition, have to rely on additional approximations and assumptions, such as assuming that seismic events are linear in the crossline direction or even that the crossline component of the angle of incidence is equal to zero (2D propagation approximation). By contrast, vector-acoustic migration which is based on representation theorems that fully account for the 3D nature of the recorded wavefield (Wapenaar, 2004; van Manen et al., 2005, 2006; Wapenaar and Fokkema, 2006; Curtis and Halliday, 2010; Halliday and Curtis, 2010; Vasconcelos, 2013), does not require any assumption about the direction of arrival of events in the cross-line direction (also when poorly sampled or even when slightly aliased). Although we hypothesize that this, together with correct handling of the finite-frequency directionality, could become even more evident when vector-acoustic migration will be applied to the full 3D OBC survey, a more-in-depth study of the benefit of finite-frequency directionality on a 3D dataset will be the subject of future research.

Data-domain decomposition techniques focused on optimising signal-to-noise ratio such as optimal deghosting (ODG — Ozdemir et al., 2008; Caprioli et al., 2012), not only cancel receiver ghosts but also guarantee minimized residual noise. This is achieved at the cost of adding into the decomposition scheme information about the statistics of noise on pressure and velocity data together with their respective ghost models. While the ODG solution is very sensitive to any inaccuracy in the ghost models (e.g., cable depth, a flat sea assumption, 2-D processing), vector-acoustic migration is a suitable platform for the implementation of image-domain noise mitigation strategies that directly weight the pressure and velocity receiver wavefields or their corresponding pre-stack images (El Yadari et al., 2014) without having to rely on additional acquisition information for the construction of a reliable ghost model.

When 4C data are acquired, in- and cross-line particle velocity measurements contain useful additional information for imaging and inversion, as used by map migration methods (Kleyn, 1977) and stereo tomography (Billette and Lambare', 1998). This information can not be readily incorporated in source-receiver vector-acoustic migration for marine acquisition that deploys horizontal streamers and for ocean-bottom

acquisition with flat, horizontal seabeds: since the normal vector is directed along the vertical direction at the recording surface, the vertical particle velocity in fact becomes the only required component. While slanted cables (Soubaras and Dowle, 2010) could represent a solution in streamer acquisition to incorporate the horizontal components in source-receiver VA migration, Fleury and Vasconcelos (2013) propose an adjoint-state VA formulation that can incorporate any recording available; this is ultimately a formulation for reverse time map migration, representing also the starting point for vector-acoustic full waveform inversion.

Finally, it is important to note that while vector-acoustic injection (as well as its data-domain counterparts — PZ summation, ODG) represents an effective strategy for attenuating water-layer multiples (multiples that never leave the water column) and water-layer peg-legs that are recorded at the receiver array as downgoing waves, this approach does not address all of the effects of the free-surface in the ocean-bottom data. More specifically, source-side ghosts and any other type and order of free-surface multiples reaching the receiver array as upgoing waves generate artefacts in the final image. While no attempt to remove these events from the recorded data has been made in our field data test, there are a variety of approaches that could be applied alongside VARTM to partially or fully mitigate the effects of the free-surface (before VARTM in the pre-stack domain, or after VARTM in the post-imaging domain).

First, the source ghost can be removed from both the pressure and velocity recordings as part of the wavelet deconvolution process at an early stage in the processing chain, or directly from the image after migration (Caprioli et al., 2014) when data are acquired using only monopole sources. If over/under or dual source data are available, the source ghost attenuation can be performed either in the prestack domain by means of wavefield decomposition techniques (Moldoveanu, 2000; Egan et al., 2007) or directly while imaging by invoking an imaging condition that combines dual source data together with dual source forward propagators or source wavefields (Vasconcelos, 2013).

Other types of free-surface multiples (those that do not experience their final set of multiple bounces only within the water column before being recorded) could be attenuated by adapting the concept of surface related multiple elimination (SRME — e.g., Verschuur et al., 1992; Weglein et al., 1997) from streamer geometries to ocean-bottom geometries, where the differences between source and receiver depth levels are not negligible and need to be compensated for. The key idea behind these methods is to construct a wavefield prediction operator to compensate for the elevation difference. This can be done either analytically (Matson and Weglein, 1996; Pica et al., 2005, 2006), or by making use of the direct wave as the wavefield continuation operator (Ikelle, 1999). Since the latter procedures are not exclusively valid for pressure data, we foresee that

their application to both the pressure and velocity fields could provide a modified input dataset for VARTM deprived of free-surface multiples. Removal of the residual receiver-side ghosts and careful handling of the finite-frequency directionality contained in the velocity field will be achieved by VARTM.

Alternatively, the effects of the free-surface can be attenuated all at once by deconvolving the upgoing field with the downgoing field (Amundsen, 2001; Wang et al., 2009). If the finite-frequency directivity of the retrieved velocity field has not been affected by the deconvolution process (Ravasi et al., 2015b), VARTM of these fields could still be beneficial in terms of improving the imaging of the shallow subsurface. An attractive time-space domain extension of this demultiple approach has been recently proposed by Vasmel et al. (2014) based on time-domain finite difference propagators. Their approach relies on the ability to inject vector-acoustic field data to separate up- and downgoing fields as shown in this chapter.

Finally, free-surface multiples could instead be actively used in imaging if the full downgoing wavefield is forward propagated as the source wavefield (Muijs et al., 2007; Whitmore et al., 2010; Lu et al., 2011; Amundsen and Robertsson, 2014) and combined with the backward propagated upgoing wavefield by means of a modified imaging condition, the latter being a deconvolution imaging condition (Guitton et al., 2007; Schleicher et al., 2008). The ability to separate up- from downgoing waves 'on-the-fly' when vector-acoustic data are opportunely injected along the receiver array is not limited to back-propagation (or propagation backward in time): the downgoing component can be propagated downward (and the upgoing component upward) by injecting the full recorded vector-acoustic data forward in time and interchanging the sign of equation 7.4 (Robertsson and Chapman, 2000; van Manen et al., 2007; Amundsen and Robertsson, 2014; Vasconcelos et al., 2014a). The first application of such boundary condition for forward propagation of OBC field data has been shown in Ravasi et al. (2015a) to image free-surface multiples.

7.5 Conclusion

We have developed a workflow for the application of VARTM to a field dataset. By ensuring the matching of direct waves in the pressure and vertical velocity components by using a calibration filter, and by injecting the full recorded pressure and vertical velocity data in a vector-acoustic fashion, up/down separation is performed as part of wavefield extrapolation. The main benefit of VARTM over standard RTM of separated wavefields lies in the overall better handling of amplitudes by using a correct

combination of monopole- and dipole-type propagators, this resulting in clearer shallow sections and better focused space-lag common image gathers. Moreover, up- and downgoing fields can be jointly imaged without the need for separate finite difference modelling, and their separation is shown to be successful also in presence of sparse or irregular receiver sampling.

8

Application 4: Target-oriented Marchenko imaging of Volve field

Accurate estimate of wavefields within the Earth's interior where no real observations are available is crucial for the identification and characterization of subsurface reservoirs in complex geologies. The new method of Marchenko redatuming promises to reconstruct these full responses (including internal multiples) in an iterative fashion, by crafting wavefields that collapse at any chosen point inside of the medium. Since reflection measurements at the Earth's surface and a smooth estimate of the velocity model are taken as input, it forms a new way to create images of target zones in the subsurface with illumination from either above or below, without necessarily having to create detailed models of overburden structure. We present the first encouraging results of 2D target-oriented imaging of an ocean-bottom cable field dataset using Marchenko redatuming, and show that underside illumination has potential to reveal subsurface structure that is hidden or distorted in conventional imaging of surface data.

8.1 Introduction

Imaging the geometry and properties of complex subsurface geology, identifying and characterizing subsurface reservoirs of hydrocarbons, minerals or water, as well as monitoring of waste products stored underground such as CO_2 and nuclear waste, all require sophisticated and costly seismic imaging and monitoring. A crucial step for such imaging methods is the estimation of wavefields within the solid Earth's interior where no real observations are available. Standard redatuming approaches based on time-reversal of incomplete data (i.e., data recorded along an open boundary of surface receivers) (Berryhill, 1984), generally fail to explain how multiply scattered waves (multiples) propagate in the complex subsurface unless high-resolution seismic velocity models are available prior to imaging, as otherwise they can not accurately predict those arrival in the subsurface. This causes large errors in images and crucially in interpretation.

While extrapolation techniques like those discussed in Chapter 3 and Chapter 7 of this thesis improve upon the use of free-surface multiples, they still fail in predicting internal multiples in the subsurface. As already mentioned in Chapter 5, Marchenko redatuming (or autofocusing) is a novel technique to estimate full acoustic wavefields in the subsurface, including primary and internal multiple reflections, using seismic waves measured at the Earth's surface and only a smooth estimate of the propagation velocity (Broggini et al., 2012; Wapenaar et al., 2013). Advantages over standard redatuming methods are that the wavefield coda (or internal multiples) in the down-going fields are estimated accurately, non-physical waves in up-going fields are attenuated, amplitudes of primary and multiple events are correctly balanced. Moreover, the retrieved wavefields are separated into their up- and down-going components, which will be used to image the subsurface. Using a stationary phase analysis, van der Neut et al. (2014a) provide an insightful interpretation of the underlying mechanism by which wavefields are constructed in the subsurface, and the current challenges and limitations of the Marchenko scheme when applied to complex geologies are further discussed in Wapenaar et al. (2014b) and Vasconcelos et al. (2014b). The first attempts to extend the acoustic theory to elastic (solid) media can be found in da Costa et al. (2014a); Wapenaar (2014) and Wapenaar and Slob (2014), while Slob and Wapenaar (2013) have also derived an electromagnetic version of the Marchenko equations.

Marchenko wavefields can be used to improve subsurface imaging in areas where standard migration techniques generate spurious structures in the image caused by incorrect handling of internal reflections (Malcolm et al., 2007). Broggini et al. (2014); Behura et al. (2014) and Slob et al. (2014) construct images free from internal multiples by cross-correlating (or deconvolving) the retrieved up- and down-going fields at any point

in the subsurface. Wapenaar et al. (2014a) limit the computation of Marchenko fields to a chosen depth level, and then use methods similar to the interferometric imaging approach of van der Neut and Herrmann (2013) to create redatumed reflection responses at that depth by means of multi-dimensional deconvolution (Wapenaar et al., 2011). These responses are free of spurious events related to internal multiples in the overburden. These responses form the basis for obtaining more accurate target-oriented images of areas of the subusurface below or above the depth level of interest compared to those generated by standard reverse-time redatuming followed by cross-correlation of the subsurface responses (Dong et al., 2009).

This chapter presents the first successful application of target-oriented imaging using Marchenko redatuming on a field data. We apply the method to reflection seismic data recorded on an ocean-bottom cable dataset over the Volve oilfield, offshore Norway in 2002. One of the main obstacles to the application of such novel techniques to field datasets is the set of requirements of the reflection response (as explained below). We show that a wave-equation approach to redatuming marine sources to the seabed receiver level, sea surface multiple removal, and seismic source signature removal transforms ocean-bottom data into a suitable proxy of the reflection response required by the Marchenko scheme. We then produce images of target areas of shallow and deep subsurface structure using Marchenko wavefields, and compare these to images obtained from standard reverse-time migration (RTM) of the surface data. We conclude by showing that underside illumination may reveal additional Earth structure that is distorted or hidden in images constructed directly from surface data.

8.2 Marchenko equations

Marchenko redatuming is based on two Green's function representations (Wapenaar et al., 2014a) which uniquely relate subsurface wavefields to so-called focusing functions via the recorded seismic data. The subsurface responses ($\mathbf{G}^-$ and $\mathbf{G}^+$) belong to the wave state of the physical experiment when data are acquired, while the focusing functions ($\mathbf{F}^-$ and $\mathbf{F}^+$) are defined in a modified medium that is truncated (or homogeneous) below a chosen subsurface level. Those equations can be discretised as (van der Neut et al., 2014b)

$$\begin{aligned}\mathbf{G}^- &= \mathbf{R}\mathbf{F}^+ - \mathbf{F}^-\\ \mathbf{G}^{+*} &= -\mathbf{R}^*\mathbf{F}^- + \mathbf{F}^+,\end{aligned} \tag{8.1}$$

where $\mathbf{G}^-$ and $\mathbf{G}^+$ are matrices containing the time-space domain up- and downgoing Green's functions, with multiple sources at the acquisition surface and receivers

located at desired subsurface points. The focusing functions $\mathbf{F}^-$ and $\mathbf{F}^+$ are respectively up- and down-going acausal solutions to the wave-equation that focus at zero-time at the subsurface points, and then continue as down-going diverging fields into the homogeneous lower half-space. We suppose that $\mathbf{F}^+ = \mathbf{F}_d^+ + \mathbf{F}_m^+$, that is, $\mathbf{F}^+$ is composed of a direct wave $\mathbf{F}_d^+$ and a down-going coda $\mathbf{F}_m^+$: these quantities are also organized in matrices with concatenated traces in the time-space domain. Matrix $\mathbf{R}$ contains the real Earth's reflection response from vertical dipole sources to pressure receivers, and (left-)multiplication is equivalent to performing multi-dimensional convolution in the time-space domain, while $*$ acts on a matrix by rearranging its elements to mimic time-reversal.

To obtain a system of coupled Marchenko equations, a muting function Θ that removes the direct arrival and all subsequent events is defined. Assuming that the muting function satisfies $\Theta\mathbf{G}^- = \mathbf{0}$, $\Theta\mathbf{G}^+ = \mathbf{0}$, $\Theta\mathbf{F}^+ = \mathbf{F}_m^+$ and $\Theta\mathbf{F}^- = \mathbf{F}^-$ (Wapenaar et al., 2014a), its application to equations 8.1 yields

$$\begin{aligned} \mathbf{F}^- &= \Theta\mathbf{R}\mathbf{F}_d^+ + \Theta\mathbf{R}\mathbf{F}_m^+ \\ \mathbf{F}_m^+ &= \Theta\mathbf{R}^*\mathbf{F}^-. \end{aligned} \tag{8.2}$$

Starting from an initial focusing function $\mathbf{F}_d^+$, obtained by time-reversing an estimate of the direct wave $\mathbf{G}_d$ and assuming a null coda ($\mathbf{F}_m^+ = 0$), equations 8.2 can be iterated to convergence. As noted by van der Neut et al. (2015) and Vasconcelos et al. (2015b), the solution of the focusing functions at the iteration K can be written in a compact form by means of a Neumann series expansion:

$$\begin{aligned} \mathbf{F}^{+(K)} &= \sum_{k=0}^{K} (\Theta\mathbf{R}^*\Theta\mathbf{R})^k \mathbf{F}_d^+ \\ \mathbf{F}^{-(K)} &= \Theta\mathbf{R} \sum_{k=0}^{K} (\Theta\mathbf{R}^*\Theta\mathbf{R})^k \mathbf{F}_d^+, \end{aligned} \tag{8.3}$$

where each term in the series represents an update to the focusing function. Finally, up- and down-going Green's function can be computed from equations 8.1 using the estimated focusing functions $\mathbf{F}^-$ and $\mathbf{F}^+$.

8.3 Marchenko inputs and redatumed fields

Marchenko redatuming imposes severe requirements on the reflection response $\mathbf{R}$, and recorded reflection data can only be used as a proxy for $\mathbf{R}$ after some pre-processing.

$\mathbf{R}$ is assumed to have been obtained from large aperture, fixed-spread (pressure) receiver arrays with dense (vertical dipole) source coverage over the entire receiver array, to have broad bandwidth, and to contain only primary reflections and internal multiples (i.e., is deprived of direct waves, source and receiver ghosts, and surface-related multiples). If data are acquired with standard ocean-bottom acquisition systems, wave-equation approaches to joint source redatuming (at the receiver level), demultiple, and source designature (Ziolkowski et al., 1999; Amundsen, 2001; Amundsen et al., 2001) can transform the recorded data into a suitable estimate of the reflection response $\mathbf{R}$ for Marchenko redatuming. The essence of these methods is to solve the following frequency-domain integral relation by means of multi-dimensional deconvolution (Wapenaar et al., 2011)

$$\mathbf{p}^- = \mathbf{R}\mathbf{p}^+, \tag{8.4}$$

where the recorded up-going decomposed data ($\mathbf{p}^-$) is seen as the result of multi-dimensional convolution of the down-going data ($\mathbf{p}^+$) data and the desired reflection response ($\mathbf{R}$) that would be recorded in a hypothetical seismic experiment with no sea surface present. In this case, the decomposed data $\mathbf{p}^-$ and $\mathbf{p}^+$ are arranged in matrices with the frequency-space domain responses from multiple sources to receivers at the acquisition surface. The sought reflection response $\mathbf{R}$ is instead composed of a matrix with the frequency-space domain responses from vertical particle velocity receivers to monopole virtual sources at the acquisition surface. Each frequency is inverted separately and the time-space reflection response $\mathbf{R}$ is obtained by combining the solutions of each inversion via an inverse Fourier transform. Moreover, source-receiver reciprocity is applied to the retrieved response to obtain a reflection response from vertical dipole sources to pressure receivers as required from the theory of Marchenko redatuming. Note that although $\mathbf{R}$ is used here in spite of $\mathbf{G}^-_{\mathbf{ow}}$, equation 8.4 is equivalent to equation 4.5 in Chapter 4. An estimate of the reflection response $\mathbf{R}$ could be alternatively obtained by solving the formulation of MDD with pressure and velocity recordings in equation 4.10.

For our current study, we use data from a single line of the ocean-bottom cable array on the seabed above the Volve field located in the gas/condensate-rich Sleipner area of the North Sea, offshore Norway (Szydlik et al., 2007). We select a receiver line containing 235 receivers spaced 25 m apart, and an overlying shot line composed of 241 sources spaced 50 m apart, as shown in Figure 8.1a. Noise suppression, vector-fidelity corrections, and initial source designature are applied to the data. Further, we scale the data by $\sqrt{t}$ to account for 3D geometrical spreading and we calibrate the direct arrival of the particle velocity measurement to the pressure recording (see Chapter 7 for a more

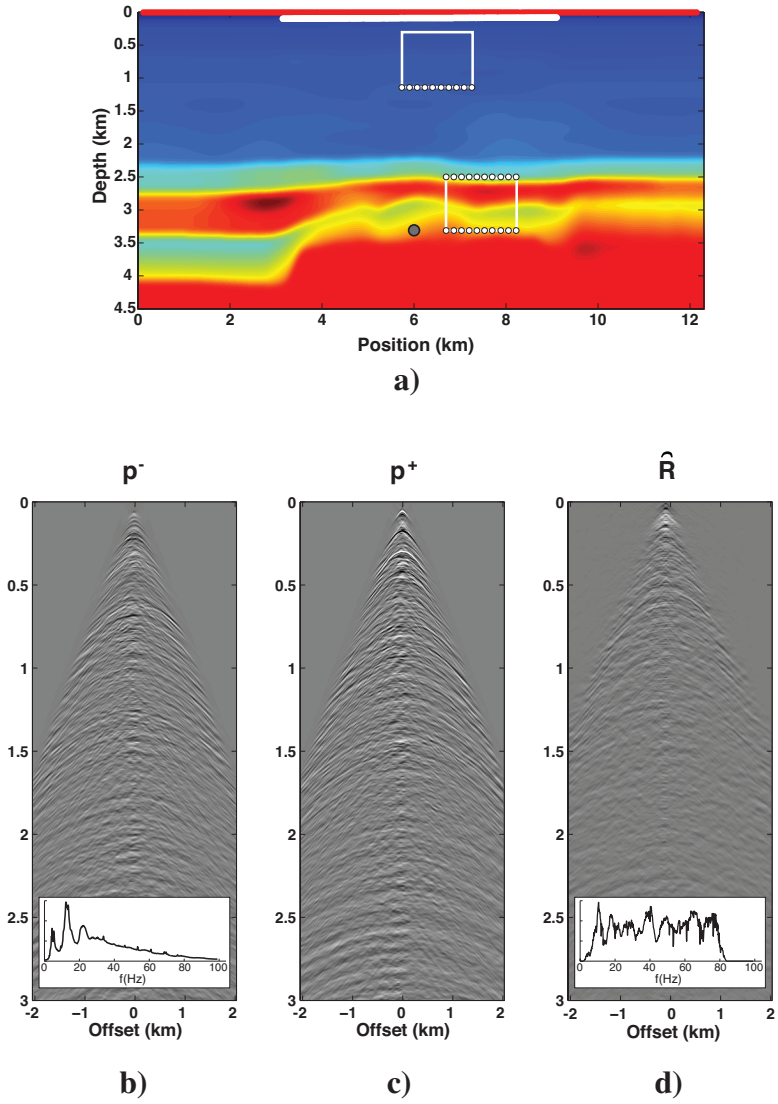

Figure 8.1: (a) Migration velocity model, source array at depth $z_S = 6\,m$ (red line) and receiver array at $z_R = 90\,m$ (white line) in the ocean-bottom cable acquisition. A grey dot represents the subsurface point where Marchenko fields are computed and shown in Figure 8.3, while two white boxes indicate the target areas where Marchenko imaging is performed. Single common-shot gather of the (b) up-going data, (c) down-going data, and (d) estimate of the reflection response $\hat{\mathbf{R}}$. Inserts in (b) and (d) show the average amplitude spectra of the gathers.

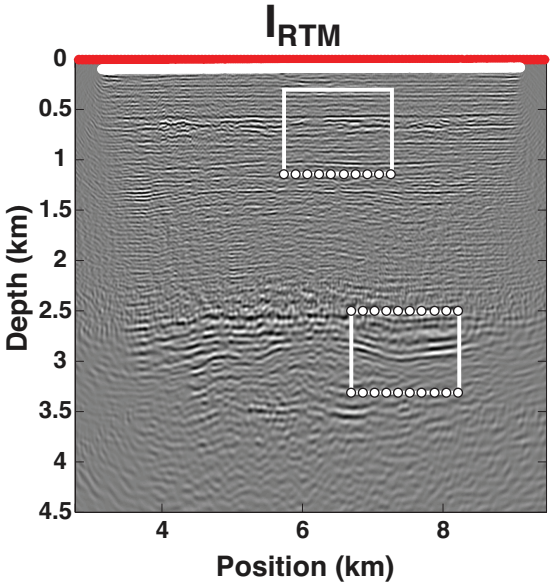

Figure 8.2: Subsurface image obtained by applying standard RTM to the proxy of the ideal reflection response $\mathbf{R}$ in Figure 8.1d.

detailed description of this procedure). After wavefield separation is carried out in the frequency-wavenumber domain (Amundsen, 1993), the up- (Figure 8.1b) and down-going (Figure 8.1c) components are used as input for multi-dimensional deconvolution (equation 8.4), and a proxy of the reflection response $\hat{\mathbf{R}}$ required as input for Marchenko redatuming is produced (Figure 8.1d). Standard reverse-time migration of our estimate of $\hat{\mathbf{R}}$ (i.e., up-going field without source and receiver ghosts and free-surface multiples) is shown in Figure 8.2 and is used in the following for comparison with Marchenko imaging.

An estimate of the direct arriving wavefront $\mathbf{G}_d$ is also required to create the initial focusing function $\mathbf{F}_d^+$. This can be computed by forward modelling (e.g., ray-tracing, finite-differences) using a smooth velocity model such as that shown in Figure 8.1a. For illustration, we compute the traveltime of the first arriving wavefront from a subsurface point $\mathbf{x}_F = \{6, 3.3\}\, km$ via ray-tracing and apply a 40 Hz Ricker wavelet with constant amplitude for all offsets (Figure 8.3a). Focusing functions $\mathbf{F}^+$ and $\mathbf{F}^-$ estimated after two iterations of the Marchenko equations ($K = 2$ in equation 8.3) are shown in Figures 8.3b and c, and used in equations 8.1 to compute Green's functions $\mathbf{G}^+$ and $\mathbf{G}^-$ (Figures 8.3d, e). Note that the iterative Marchenko scheme has retrieved the coda in the down-going field. An event with similar moveout to the direct arrival is visible at zero-offset around 1.5 s in Figure 8.3d; this may be a wave that experienced multiple bounces in the high velocity layer in between 2.6 and 2.85 km depth.

A challenge to the application of Marchenko redatuming to a field dataset is represented

by the convergence of the iterative scheme presented above. Since we do not have direct access to the real Earth's reflection response $\mathbf{R}$, it is inevitable to expect that the processed version of the recorded data $\hat{\mathbf{R}}$ may be scaled differently, such that $\hat{\mathbf{R}} = c_R\mathbf{R}$. Here c_R is at best an unknown scalar (or, more likely, a compact filter varying in time and space) that depends on the acquisition and processing chain. In this application, we have taken advantage of the observation that $\| (\Theta\mathbf{R}^*\Theta\mathbf{R})^k\mathbf{F}_d^+ \|^2 \rightarrow 0$ as $k \rightarrow \infty$ needs to be satisfied for the convergence of the Neumann series in equation 8.3. While meeting this condition does not guarantee that each update has correct amplitude and may not allow the complete cancellation of the spurious arrivals in the up-going field, we have shown that after two iterations of the Marchenko scheme we are able to produce a coda in the down-going focusing function (Figure 8.3b) and Green's function (Figure 8.3d) with non-negligible amplitudes.

An accurate deconvolution of the source wavelet from the data is however required for a correct summation of the various updates of the Neumann series. In fact, since each iteration of the Marchenko scheme involves one step of convolution and one of correlation with the reflection response $\mathbf{R}$ to obtain $\mathbf{F}^+$, and a further convolution to construct $\mathbf{F}^-$ (equation 8.3), residual source signature in the reflection response $\mathbf{R}$ may lead to the enhancements of some frequencies with respect to others. Ultimately this may prevent the successful combination of the focusing function updates from the various iterations. The problem of estimating the source wavelet from real datasets is a particularly challenging one; different approaches have been proposed, differing from each other in terms of assumptions made about the statistical nature of the response of the Earth (see, for example, Robinson and Treitel, 1980; Fokkema and Ziolkowski, 1987). Alternatively, as done in this chapter, one can attempt to remove the effect of the source signature from the data using the wave-equation demultiple approach of Amundsen (2001). While it is not possible to verify that the source wavelet has been fully deconvolved from the reflection data $\hat{\mathbf{R}}$ in our data processing, we note that that the original upgoing data shows a much higher energy content at low frequencies (see insert in Figure 8.1b) while the reflection response obtained from multi-dimensional deconvolution has a better equalized amplitude spectrum (see insert in Figure 8.1d). Finally, it is important to remember that other factors such as frequency-dependent attenuation, imperfect deghosting, unaccounted 3D effects, or noise affect the quality of the updates, and an adaptive scheme may be beneficial to further improve the robustness of Marchenko redatuming (van der Neut et al., 2014b).

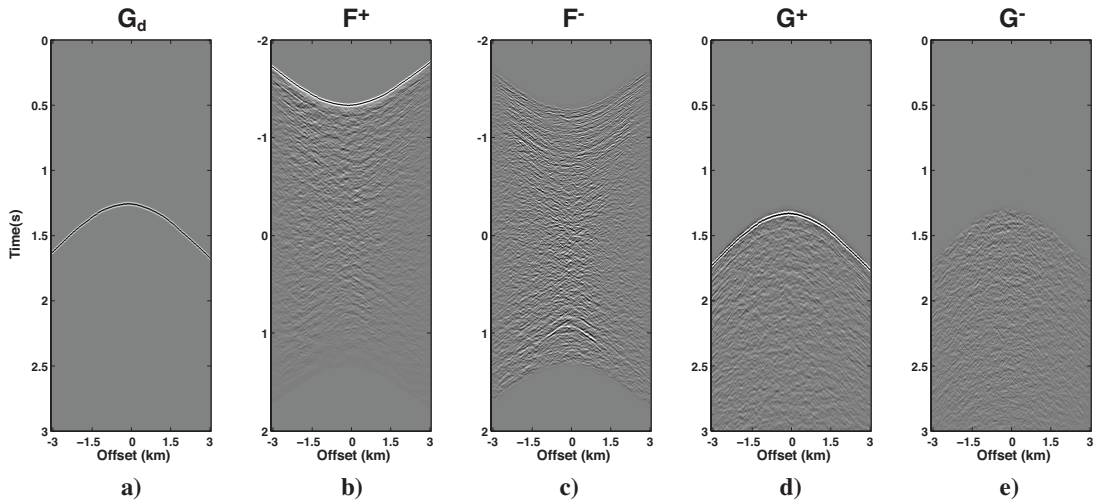

Figure 8.3: Marchenko redatuming. (a) Forward-modelled first arriving wave. (b) Down- and (c) up-going focusing functions, and d) down- and (e) up-going redatumed fields at $\mathbf{x}_F$. All panels are displayed with 50% clipping of absolute amplitudes.

8.4 Marchenko imaging

Marchenko redatuming is now used to retrieve up- and down-going Green's functions for 151 subsurface points forming a 1.5 km wide array ranging from 6.7 km to 8.2 km in the horizontal dimension, at a depth level of 2.5 km (right lower box in Figure 8.1a). From these fields we obtain an estimate of the reflection response from above the target ($\mathbf{R}_\cup$) as if both sources and receivers were located along the array of subsurface points, and were located in a modified medium with the same properties of the physical medium below the array but which is homogeneous above. We do so by solving the following equation by means of multi-dimensional deconvolution:

$$\mathbf{G}^- = \mathbf{G}^+\mathbf{R}_\cup. \tag{8.5}$$

Figure 8.4a shows an estimate of $\mathbf{R}_\cup$ for a source in the centre of the subsurface array computed by solving equation 8.5. As discussed extensively in Wapenaar et al. (2014a), the redatumed reflection response can be used as input for standard imaging in a target zone just below the redatumed level (Figure 8.4c). Comparison with standard reverse-time migration of our estimate of $\hat{\mathbf{R}}$ shows that Marchenko imaging from above is able to produce an image of similar quality of that from RTM (Figure 8.4e), slightly improving the details in between the main reflectors at 2.6 and 2.9 km and limiting the required (expensive) finite-difference computation to a much smaller subsurface area.

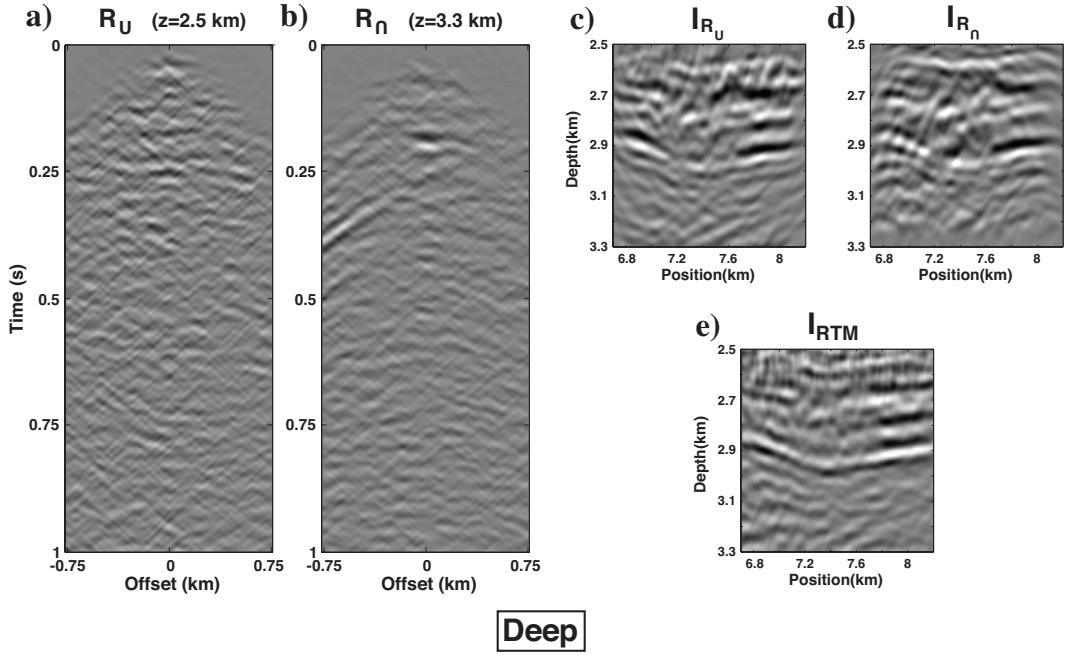

Figure 8.4: Marchenko imaging of deep subsurface. Multi-dimensional deconvolution estimates of (a) reflection response from above $\mathbf{R}_{\cup}$ at depth level $z = 2.5km$ and (b) reflection response from below $\mathbf{R}_{\cap}$ at depth level $z = 3.3\,km$. Images of the target zone from (c) above and (d) below, compared to that obtained from (e) standard RTM of the reflection response $\hat{\mathbf{R}}$.

While the computational advantage could already represent a reason to perform Marchenko imaging, by allowing target-oriented, high-resolution imaging with much higher frequencies and spatial sampling than RTM can achieve, the focusing functions $\mathbf{F}^{-}$ and $\mathbf{F}^{+}$ can also be combined to obtain a second image of the reflection response which illuminates the target area from below ($\mathbf{R}_{\cap}$) as explained by Wapenaar et al. (2014a):

$$-(\mathbf{F}^{-})^{*} = \mathbf{F}^{+}\mathbf{R}_{\cap}. \tag{8.6}$$

An estimate of $\mathbf{R}_{\cap}$ for a source in the centre of the subsurface array at a depth level of 3.3 km is shown in Figure 8.4b, and used to perform imaging of the target zone just above the lower redatumed level (Figure 8.4d). Complementary details are provided by reflections illuminating this portion of the subsurface from below and contained in $\mathbf{R}_{\cap}$. Similarly, Marchenko fields are now computed along a line at 1.13 km (upper box in Figure 8.1a) to image the complex stratigraphy in the shallow subsurface from below (Figures 8.5a and b). To improve the resolution and avoid spatial aliasing with respect to the standard RTM image (Figure 8.5c), the image is sampled (relatively cheaply) every 5 m and compared to that from RTM which was originally sampled every 10 m to save on computational cost.

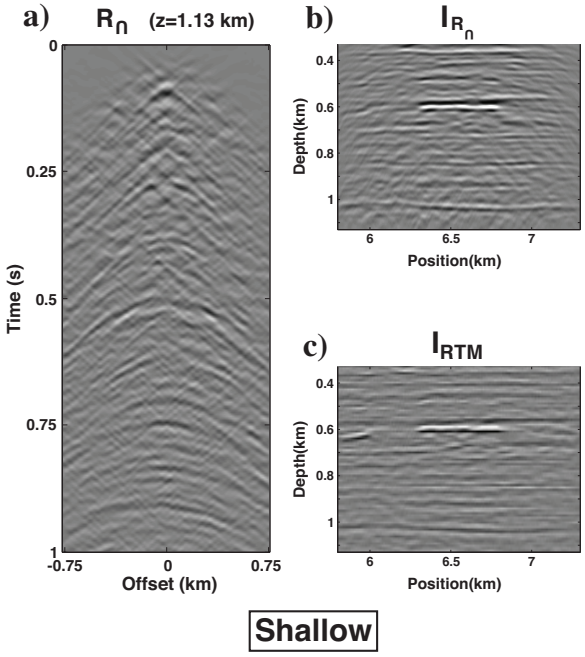

Figure 8.5: Marchenko imaging of shallow subsurface. Multi-dimensional deconvolution estimates of (a) reflection response from below $\mathbf{R}_{\cap}$ at depth level $z = 1.13\ km$. Images of the target zone from (b) below, compared to that obtained from (c) standard RTM of the reflection response $\hat{\mathbf{R}}$.

Finally, Marchenko imaging from below is performed for two additional subsurface lines with inter-receiver spacing of 10 m: the first ranges from 5.4 km to 6.9 km and is located at a depth of 3.4 km, while the second is at 3.41 km depth and extends from 4.1 km to 5.6 km in the horizontal dimension. The resulting images are merged with the image in Figure 8.4d to form Figure 8.6b. Note that since each of the reflection responses $\mathbf{R}_{\cap}$. is obtained via a multi-dimensional deconvolution process, the number of subsurface points should not exceed that of the sources at the acquisition surface for a stable inversion of equation 8.6. With the choice of the extension and sampling of the subsurface array being limited by this constraint, it is important to assure that images obtained independently from different subsurface responses $\mathbf{R}_{\cap}$, at possibly different depth levels, can be combined together. Green arrows in Figure 8.6b indicate perfect continuity of reflectors between the various images, thus showing that we may design short-aperture, finely sampled subsurface arrays that prevent spatial aliasing in the subsequent imaging step. More importantly, Marchenko imaging from below reveals a coherent structure (blue arrows in Figure 8.6b) which is not visible, or perhaps is distorted, in the RTM image of the reflection response $\hat{\mathbf{R}}$ (Figure 8.6a).

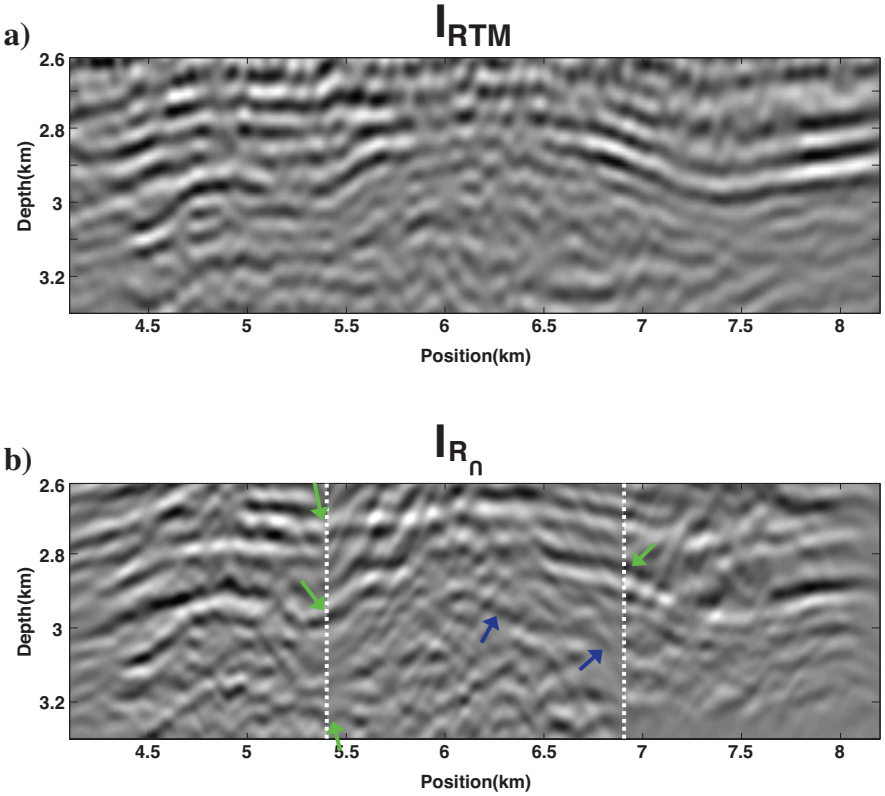

Figure 8.6: Merging of Marchenko images. (a) Standard RTM of the reflection response $\hat{\mathbf{R}}$ and (b) Marchenko imaging from below of three different subsurface redatumed responses $\mathbf{R}_\cap$ (white dashed lines delimit the three images). Green arrows in (b) indicate near-perfect continuity between images. Blue arrows in (b) refer to a clearly continuous structure revealed by Marchenko imaging that is not visible in the RTM image.

8.5 Conclusion

The novel technique of Marchenko redatuming applied to an ocean-bottom seismic data acquired over the Volve North Sea field, produces encouraging results of target-oriented imaging of both shallow and deep structures. Marchenko focusing functions also contain sufficient information to directly image the subsurface using underside reflections. Such images reveal coherent structure beneath strongly reflecting interfaces, which are distorted or invisible when imaging directly with surface data proving that the focusing functions are reliable. Therefore, other practices that require wavefield focussing such as microseismic source localization, seismic time-lapse monitoring, and non-destructive testing might also benefit from accurate estimates of focusing functions that are obtained by Marchenko redatuming.

9

Discussion

In this thesis I have considered a variety of topics centred around the theme of seismic migration using reciprocity and representation theorems to image singly and multiply scattered waves. The main focus was on extending the two-way scattering-based imaging framework to elastic media. A set of nonlinear, true-amplitude imaging conditions was derived in Chapter 2, and a procedure for directional and modally-selective extrapolation of multi-component data using finite-difference injection was proposed in Chapter 3. By applying this novel imaging approach to a realistic subsalt experiment, I further demonstrated the importance of correctly handling various components of the elastic dataset and the added value of multiply-scattered and transmitted waves on both elastic images (Chapter 5) and elastic extended images (Chapter 6). Other avenues of research that have been investigated include: seismic source redatuming by multi-dimensional deconvolution using two-way representation (Chapter 4), directional acoustic wavefield extrapolation of a field ocean-bottom dataset (Chapter 7), and target-oriented imaging by means of the novel Marchenko redatuming scheme for correct handling of the effect of multiple reverberations in the overburden (Chapter 8).

In this section, I outline potential research directions related to the range of topics covered in the thesis. In Chapters 2 and 5, for example, while we successfully verified the long-lasting conjecture that multiply-scattered waves can provide additional illumination and higher resolution to pure-mode elastic imaging, we also discovered that the contributions of singly- and multiply-scattered converted-waves tend to compensate and cancel each other. This ultimately leads to a completely null nonlinear converted wave image. Here I discuss a strategy that uses this undesired outcome as a constraint for compressional wave imaging, which may help in compensating for the lack of enclosing boundaries and sharp velocity models, as required by the theory but almost never achievable in seismological applications. Moreover, although the tensorial extrapolation procedure proposed in Chapter 3 has been proven to outperform conventional

approaches to elastic redatuming in ideal scenarios, there are still a number of questions to be answered regarding the application of this method to land, borehole, and ocean-bottom seismic acquisition scenarios. Because the information contained in the shear stress is required by the injection scheme for correct wave-mode separation, but is generally not recorded in seismic exploration, I highlight a number of possible approaches to acquire a proxy or to estimate such quantity. Finally, while throughout the thesis we have repeatedly discussed the importance of enclosing boundaries of sources and/or receivers in reciprocity-based imaging as well as in seismic interferometry, I conclude this chapter by deriving a new interferometric representation that uniquely relates data recorded along the available portion of the source boundary to an integral quantity function of the missing recordings (i.e., data that would need to be recorded to close the source boundary). By evaluating the misfit between these two quantities, I show its sensitivity to velocity errors in the model used to numerically generate the data that are not physically recorded: this observation is the first step towards the identification of an interferometric objective function for velocity model building.

9.1 Enabling nonlinear PP imaging via $I_{PS} = 0$ annihilator

In Chapters 2 and 5 we argue that when imaging is performed using a nonlinear scattering-based imaging condition and enclosing boundaries of sources and receivers, converted waves give rise to an image that is null everywhere in the subsurface, $I_{PS}(\mathbf{x}_I) = \tilde{G}^{S(\Phi,\Phi)}_{(S,P)}(\mathbf{x}_I, \mathbf{x}_I, t = 0) = 0$. Figures 2.10d and 5.14d are examples of this phenomenon.

The latter result may seem difficult to understand initially, however the explanation is actually quite intuitive. In Chapters 2 we use a *physical* argument that I restate here more in detail. P-wave energy is dilatational and it expands and contracts the medium as it propagates. As a consequence of this property, P waves do not shear homogeneous media, but they do shear the medium where they encounter heterogeneities; this is because the same P-wave energy causes different amounts of expansion on either sides of any interface separating media of differing moduli. Since differential expansion (or contraction) of the medium is the key process that generates shear wave energy, P-wave energy needs to span the medium on both sides of an interface, and hence the compressional wave has to propagate beyond a single point in space. Because propagation takes a finite length of time, this implies that there cannot be an exchange of shear energy from a P-wave point-source at zero time. Thus, $\tilde{G}^{S(\Phi,\Phi)}_{(S,P)}(\mathbf{x}_I, \mathbf{x}_I, t = 0) = 0$.

There is a also a *mathematical* way to understand this result. P waves involve volumetric expansion or contraction of the medium, which causes no rotation in the absence of

heterogeneities or anisotropy. By Helmholtz's theorem, the P wave constituent of the particle displacement field $\mathbf{u}$ can therefore be represented mathematically as the gradient of a scalar P-wave potential Φ_P, so $\mathbf{u}_P = \nabla\Phi_P$. The P-wave source at zero-time must therefore have $\nabla\Phi_P = 0$ everywhere except at the source point, where $\nabla\Phi_P \neq 0$. On the other hand, shear waves are characterized by local rotation of the medium, and in the absence of heterogeneity or anisotropy, shear waves cause no volumetric expansion as they propagate. The shear potential field Φ_{S_k} can therefore be represented mathematically by the curl of the displacement field, $\mathbf{\Phi}_{S_k} = \nabla \times \mathbf{u}$. At time zero, the curl of the wavefield is zero everywhere except at the source point. If we co-locate the source and receiver points, the shear component of the particle displacement field must be the curl of the emitted P wavefield, hence it must be $\nabla \times (\nabla\Phi_P)$. There is a mathematical identity which holds everywhere for any continuous field: the curl of the gradient of the field always equals zero. In other words, this result implies that the rotational component of a purely volumetric wavefield is zero. Hence, $\nabla \times (\nabla\Phi_P) = 0$ even at the source point; the shear wave field must therefore be zero everywhere at zero time, and $\tilde{G}^{S(\Phi,\Phi)}_{(S,P)}(\mathbf{x}_I, \mathbf{x}_I, t = 0) = 0$.

Our finding leads to some significant implications. First, it is now clear that 'true-amplitude' PS imaging is not desired when the goal is to interpret the image as a map of subsurface structure. In practice, if such an image was ever achieved our time and effort could easily have been perceived to be wasted as the image would show nothing. A critical reader may well therefore argue that the above insight has no practical use. I now suggest a framework that may allow us to utilize the physical constraint on the converted-wave image ($I_{PS}(\mathbf{x}_I) = 0$) for illumination compensation and amplitude equalization of the PP image, when imaging is performed in the presence of partial boundaries of sources and/or receivers and linear terms only (i.e., in the knowledge of only a smooth reference model).

The imaging problem may be cast as an optimization problem, where the objective is to design a set of filters that act on either the source wavefield, receiver wavefield, on both of these, or on the recorded data. Filters are estimated such that the combination of the filtered versions of the receiver and/or source fields in the imaging condition would create a null converted-wave image as if enclosing boundaries and nonlinear terms were used. I conjecture that PP imaging using the same filtered wavefields (or data) will result in higher resolution PP images similar to those from nonlinear imaging of full boundaries (see Figure 2.10c and 5.7b).

Inspired by the work of Bazargani (2014) on optimal wave focusing for seismic source imaging, I first propose an objective function where filters act only on the receiver

wavefields

$$J = \sum_{\mathbf{x}_I} \parallel I^l_{SP}(\mathbf{x}_I; a(\omega; \mathbf{x}_S)) \parallel^2 \qquad s.t. \sum_{\omega} \parallel a(\omega; \mathbf{x}_S) \parallel = 1 \quad \forall \mathbf{x}_S, \tag{9.1}$$

where each filter $a(\omega; \mathbf{x}_S)$ is function of the source location $\mathbf{x}_S$ from which each data involved in the receiver wavefield extrapolation step is generated. Moreover, by using source-receiver reciprocity, I prefer to annihilate the linear SP image (rather than PS image) such that the receiver shear wavefield is used instead of the source shear wavefield. The latter field, when produced by a P-wave source, would in fact be null at any image point unless sharp boundaries are included in the migration velocity model as discussed extensively in Chapter 6. The filtered S-wave receiver wavefield involved in the computation of the image I_{SP} is thus defined as

$$d^{S(\Phi,\Phi)}_{a(S,P)}(\mathbf{x}_I, \mathbf{x}_S, \omega) = a(\omega; \mathbf{x}_S)\, d^{S(\Phi,\Phi)}_{(S,P)}(\mathbf{x}_I, \mathbf{x}_S, \omega), \tag{9.2}$$

where the original receiver wavefield $d^{S(\Phi,\Phi)}_{(S,P)}$ is computed using the linear wavefield extrapolation formula in equations 3.3 or 3.4. The converted-wave image I_{SP} is instead obtained from the imaging condition in equation 2.17 using the filtered receiver wavefield $d^{S(\Phi,\Phi)}_{a(S,P)}$ as input. Note that a constraint on the amplitude spectrum of the filters $a(\omega; \mathbf{x}_S)$ is added to the optimization problem in equation 9.1 in order to avoid the frequency responses of those filters to be equal to zero throughout the frequency band of the signals, i.e. $a(\omega; \mathbf{x}_S) = 0\ \forall \omega, \mathbf{x}_S$. In fact, while such null filters represent a valid solution to the optimization problem, as they produce a null receiver field $d^{S(\Phi,\Phi)}_{a(S,P)}$, therefore a null SP image, they would also ultimately create a null PP image rather than the sought high-resolution image. On the contrary, we aim to find a set of non-null, frequency variant filters that produce a filtered linear receiver wavefield, propagating in the reference medium in a manner such that as far as possible the nonlinear counterpart would propagate in the real medium. Such a wavefield would in fact allow the imaging condition to remove spurious energy from the PS (or SP) image.

Similarly, an objective function that contains filters acting directly on the recorded data can be defined as

$$J = \sum_{\mathbf{x}_I} \parallel I^l_{SP}(\mathbf{x}_I; \mathbf{a}(\omega; \mathbf{x}_R, \mathbf{x}_S)) \parallel^2 \qquad s.t. \sum_{\omega} \parallel \mathbf{a}(\omega; \mathbf{x}_R, \mathbf{x}_S) \parallel = \mathbf{1} \quad \forall \mathbf{x}_S, \mathbf{x}_R, \tag{9.3}$$

where $\mathbf{1}$ is the unitary column vector and $\mathbf{a} = [a^{v_z}, a^{v_x}, a^{\tau_{zz}}, a^{\tau_{xz}}]^T$ is a column vector that contains the responses of the set of filters to be applied to the data as follows

$$\mathbf{d}^S_{\mathbf{a}}(\mathbf{x}_R, \mathbf{x}_S, \omega) = diag\left(\mathbf{d}^S(\mathbf{x}_R, \mathbf{x}_S, \omega)\right) \mathbf{a}(\omega; \mathbf{x}_R, \mathbf{x}_S). \tag{9.4}$$

Here, both data and filtered data are arranged in column vectors that contain the different components of the recorded data — e.g., $\mathbf{d}^S = \left[d^{S(v,\Phi)}_{(z,P)}, d^{S(v,\Phi)}_{(x,P)}, d^{S(\tau,\Phi)}_{(zz,P)}, d^{S(\tau,\Phi)}_{(xz,P)}\right]^T$. Finally, $diag\left(\mathbf{d}^S(\mathbf{x}_R, \mathbf{x}_S, \omega)\right)$ is square matrix such that the various elements of the vector $\mathbf{d}^S(\mathbf{x}_R, \mathbf{x}_S, \omega)$ are arranged along the main diagonal.

9.2 Tensorial elastic extrapolation in practice: the lack of data components

The directional and modally-selective elastic wavefield extrapolation presented in Chapter 3 has theoretical validity in all of the acquisition scenarios where receivers are available inside an elastic body or at the boundary between elastic and acoustic bodies. With respect to seismic applications, this includes borehole seismics in which receivers are placed inside vertical or deviated wells (Hardage, 1992) or are buried in the shallow subsurface (Bakulin et al., 2012). This also includes the so-called permanent reservoir monitoring (PRM) technologies where receivers are placed just below the ocean seabed (Nakstad et al., 2011; Bertrand et al., 2014). Standard ocean-bottom acquisition systems that comprise cables or nodes coupled to the seabed are also part of this category.

As shown in Chapter 3, the representation theorem underlying tensorial wavefield extrapolation can be simplified for ocean-bottom recordings in the presence of a hard seabed. This works by invoking the boundary condition at the fluid-solid interface (equation 3.6): only vertical particle velocity and pressure recordings are necessary to extrapolate the elastic wavefield, while the shear components of the stress tensor (i.e., τ_{xz}, τ_{yz}) are not required since they vanish at the seabed. On the other hand, when receivers are buried in the elastic medium, the information carried by τ_{xz} (and τ_{yz}) is paramount for an accurate separation of P- and S-wave modes in the injection scheme as it prevents the back-propagation of both elastic modes for each recorded arrival (see Figure 3.4b).

Limiting ourselves to the two-dimensional isotropic case, the definition of shear stress is

$$\tau_{xz}(\mathbf{x}_R, t) = \mu\epsilon_{xz} = \mu\left(\frac{\partial u_z(\mathbf{x}_R, t)}{\partial x_R} + \frac{\partial u_x(\mathbf{x}_R, t)}{\partial z_R}\right), \tag{9.5}$$

where $\mu = \rho V_S^2$ is one of the Lame's parameters and ϵ_{xz} represents the shear strain. We therefore see that an estimate of the shear stress is obtained from the local medium parameters and a measure or estimate of the shear strain along the receiver array. A

number of approaches to record or estimate both the shear strain and the medium parameters at the receiver array are discussed briefly below.

Strainmeters are devices that can record various strain components. The combination of displacement and strain measurements is becoming widely accepted in a variety of research areas in global seismology such as the analysis of episodic tremor and slip events, aseismic creep, coseismic deformation, and the study of the normal modes (Hodgkinson et al., 2013). While some of the benefits of strain measurements were already recognized in the 1930's (Benioff, 1935), many of these research areas have only become viable in recent years with improved sensor technology and the recent installation of strainmeters in continuously operating networks such as the Plate Boundary Observatory (PBO) along the western U.S. plate boundary. These recent advances have drawn new attention to the use of strainmeters alongside seismometers. Similar to other differential measurements of the Earth's motion such as the so-called rotational recordings (Lee et al., 2009; Muyzert et al., 2012; Barak et al., 2014), one of the critical issues that researchers working with strain data are constantly facing is to distinguish the signal from the noise. The high sensitivity that allows such recording devices to record small, short-term strain transients is in fact compromised by the data being inherently noisy. Therefore, strainmeters may not yet have the necessary robustness required for exploration-scale surveys, such that shear recordings could be effectively combined with measurements of pressure and particle velocity in the extrapolation of seismic data without leaking a significant amount of noise into the extrapolated wavefields. However, I foresee that improvements in the strainmeter technology may play a significant role in the implementation of tensorial wavefield extrapolation (as well as other separation techniques) in all of the acquisition scenarios described above.

Alternatively, the available particle velocity (or displacement) data can be used to numerically estimate the spatial derivatives in equation 9.5 directly. In situations where two boreholes are closely separated from each other (Cotton and Forgues, 2012; Grobbe et al., 2013; van der Neut et al., 2013a), both the longitudinal and normal derivatives may be evaluated accurately using finite-difference stencils. If recordings are available only along a single, horizontal line of receivers, an attempt to estimate such derivatives can be made in the frequency-wavenumber domain. In fact, each spatial derivative can be written in this domain as

$$\begin{aligned}\frac{\partial}{\partial x_R} &\Leftrightarrow -jk_{x_R}\\ \frac{\partial}{\partial z_R} &\Leftrightarrow -jk_{z_R}(k_{x_R};V_K) = \mp j\sqrt{\left(\frac{\omega}{V_K}\right)^2 - k_{x_R}^2},\end{aligned} \tag{9.6}$$

where k_{x_R} and k_{z_R} identify the horizontal and vertical wavenumbers, respectively, and

V_K is local medium velocity, which can be chosen to be either the P- or S-wave velocity. The frequency-wavenumber version of the shear stress therefore reduces to

$$\tau_{xz}(k_{x_R}, \omega) = -\mu \left(j k_{x_R} u_z(k_{x_R}, \omega) + j k_{z_R}(k_{x_R}; V_K) u_x(k_{x_R}, \omega) \right). \tag{9.7}$$

However, a major disadvantage of the frequency-wavenumber approach lies in the fact that while the horizontal wavenumber axis is uniquely defined given the spatial sampling of the receivers, the vertical wavenumber axis is ambiguous in two ways. First, a different sign should be applied to events that are up- or down-going at the receiver array. Second, k_{z_R} is intrinsically related to the velocities V_K of the medium along the receiver cable and different velocities (i.e., P- or S-wave velocities) should be used to correctly weight P- and S-wave events. Nevertheless, since we would like to avoid a preliminary step of wave-mode separation, only one value can be assigned to the the velocity V_K used in the computation of k_{z_R}.

As an example, the effect of choosing either P- or S-wave velocity in the evaluation of the vertical wavenumber is shown in Figure 9.1, where data have been computed via finite-difference stencil in the geometrical configuration of Figure 3.3. Figure 9.1a shows the scattered shear stress recording obtained as part of the finite-difference computation in the space-time domain (equation 9.5): the first wavefront represents the scattered P-wave while the second event is the S-wave conversion at the point scatterer. Note that by choosing the correct P-wave velocity ($V_P = 2600\, m/s$) in the computation of k_{z_R}, an accurate estimate of both the radiation pattern and absolute amplitude of the P-wave event is achieved, while the amplitude of the S-wave event is underestimated (Figures 9.1b and c). On the other hand, if k_{z_R} is computed using the correct S-wave velocity ($V_S = 1400\, m/s$) the estimate of the shear stress is very accurate in the S-wave arrival while the P-wave event is overestimated (Figures 9.1d and e).

This numerical example shows that it is generally impossible to completely resolve the velocity ambiguity, unless assumptions are made with respect to the component of the data whose vertical derivative has to be estimated. A common assumption that holds reasonably well on ocean-bottom field data is that horizontal recordings are mainly sensitive to shear waves and almost insensitive to compressional waves (Kearey et al., 1991). As a consequence, since shear waves cannot propagate in water, horizontal recordings also contain only up-going waves (alongside with the down-going seabed reflection). In this way, both ambiguities are resolved in the computation of k_{z_R}. To corroborate this point, I show the vertical (Figure 9.2a) and horizontal (Figure 9.2b) particle velocity motion of a common-shot gather of the Volve dataset presented in Chapter 7 and Chapter 8. From a visual inspection of the two gathers, it can be noticed that only the first arriving wave is clearly shared in between the vertical and the horizontal components

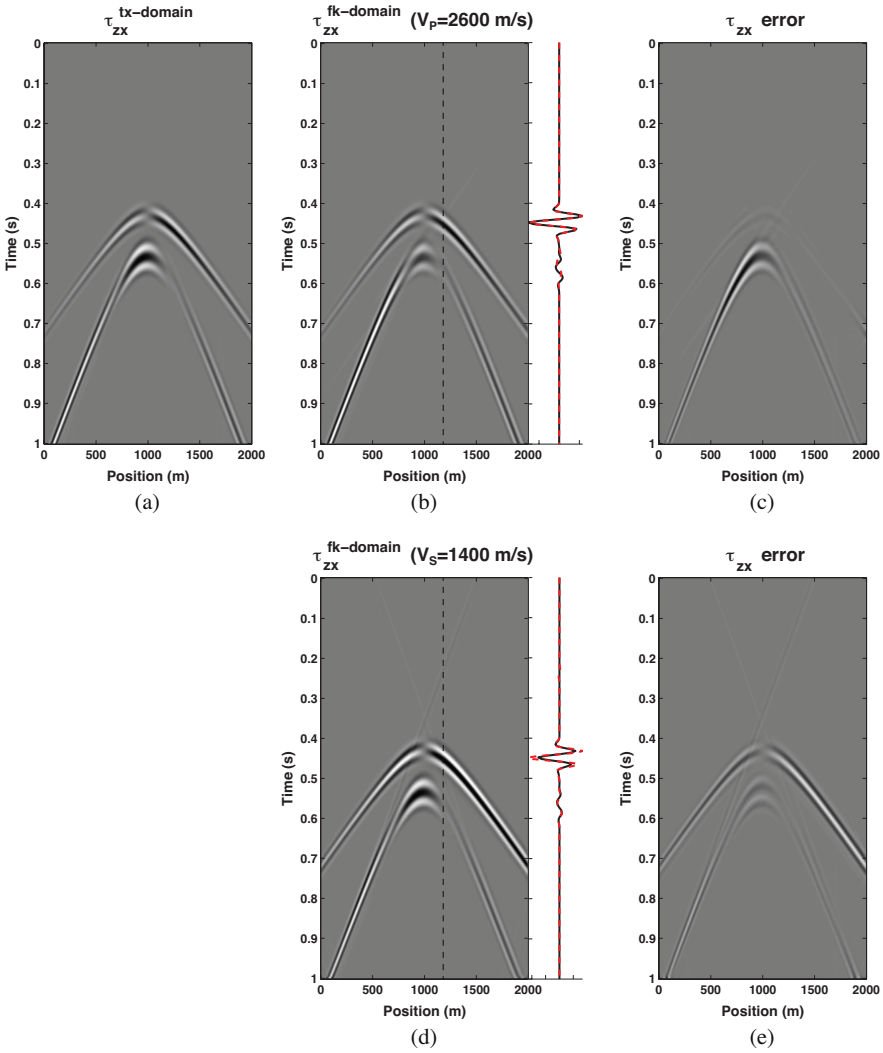

Figure 9.1: (a) Shear stress recording computed using a finite-difference stencil in the time-space domain. (b,d) Frequency-wavenumber estimates of the shear stress from particle velocity measurements as in equation 9.7, using P- and S-wave velocities in the computation of the vertical wavenumber k_{z_R}, respectively. A dashed black line is placed at position $x_R = 1200\,m$ where single trace estimates from the frequency-wavenumber (red dashed lines) and time-space (black lines) computations are compared. (c,e) Estimate errors.

(red arrows in Figures 9.2a and b). Other events in the horizontal component show instead a more pronounced moveout than those in the vertical component. This suggests that the former events can be attributed to shear waves while the latter arrivals are compressional wavefronts. We finally compute the normalized autocorrelation of the portion of horizontal particle velocity below the dashed red line such that the direct wave is removed, and we average over the receiver array (black trace in Figure 9.2c). The normalized crosscorrelation of the horizontal and vertical particle velocity (red trace in Figure 9.2c) is also computed. We observe that the two components show a

very low level of correlation meaning that their scattered parts do not present common events. This suggests that the assumption of 'natural' separation of P- and S-waves in the vertical and horizontal components may be plausible for this specific dataset.

To conclude, while we have so far focused on different approaches to evaluate the shear strain, another source of error in the process of estimating shear stress fields lies in the choice of the Lame's parameter μ, and hence in the knowledge of the S-wave velocity and density of the medium along the receiver array. Inspired by the works of Schalkwijk et al. (1999, 2003) and Muijs et al. (2004) on adaptive elastic decomposition, a possible way to identify accurate medium parameters is to calibrate an initial estimate of the shear stress component, obtained from equations 9.5 or 9.7, to the recorded pressure and particle velocity data. For example, since the first arriving wave at the receiver array is by definition a P-wave, a matching filter $a_{\tau_{xz}}(t)$ can be found such that the shear-wave energy of the forward propagated direct wave vanishes along a line (or grid) of subsurface points $\mathbf{x}_I$. This can be expressed as minimization of the following cost function:

$$J_{\tau_{xz}} = \sum_{t,\mathbf{x}_I} \parallel d^{0(\Phi,\Phi)}_{(S,P)}(\mathbf{x}_I,\mathbf{x}_S,t) + a_{\tau_{xz}}(t) * \hat{d}^{0(\Phi,\Phi)}_{(S,P)}(\mathbf{x}_I,\mathbf{x}_S,t) \parallel^2 . \tag{9.8}$$

Using the notation of Chapter 3, $d^{0(\Phi,\Phi)}_{(S,P)}(\mathbf{x}_I,\mathbf{x}_S,t)$ represents the shear-wave component of the forward propagated pressure and particle velocity data at the subsurface point $\mathbf{x}_I$:

$$d^{0(\Phi,\Phi)}_{(S,P)}(\mathbf{x}_I,\mathbf{x}_S) = \oint_{\partial D_R} \left(d^{0(\tau,\Phi)}_{(zz,P)}(\mathbf{x}_R,\mathbf{x}_S) G^{0(\Phi,f)}_{(S,z)}(\mathbf{x}_I,\mathbf{x}_R) - \{ d^{0(v,\Phi)}_{(i,P)}(\mathbf{x}_R,\mathbf{x}_S) G^{0(\Phi,h)}_{(S,ij)}(\mathbf{x}_I,\mathbf{x}_R) \} n_{R_j} \right) \mathrm{d}^2\mathbf{x}_R, \tag{9.9}$$

where propagators G^0 are computed in the reference medium and chosen to be consistent with the tensorial extrapolation formula in equation 3.3. Similarly, the initial estimate of the shear stress (indicated with $\hat{d}^{0(\tau,\Phi)}_{(xz,P)}(\mathbf{x}_R,\mathbf{x}_S)$) is forward propagated as follows:

$$\hat{d}^{0(\Phi,\Phi)}_{(S,P)}(\mathbf{x}_I,\mathbf{x}_S) = \oint_{\partial D_R} \hat{d}^{0(\tau,\Phi)}_{(xz,P)}(\mathbf{x}_R,\mathbf{x}_S) G^{0(\Phi,f)}_{(S,x)}(\mathbf{x}_I,\mathbf{x}_R)\, \mathrm{d}^2\mathbf{x}_R. \tag{9.10}$$

Once the minimization problem in equation 9.8 is solved, the filter $a_{\tau_{xz}}(t)$ can be used to improve upon the initial estimate of the shear stress data.

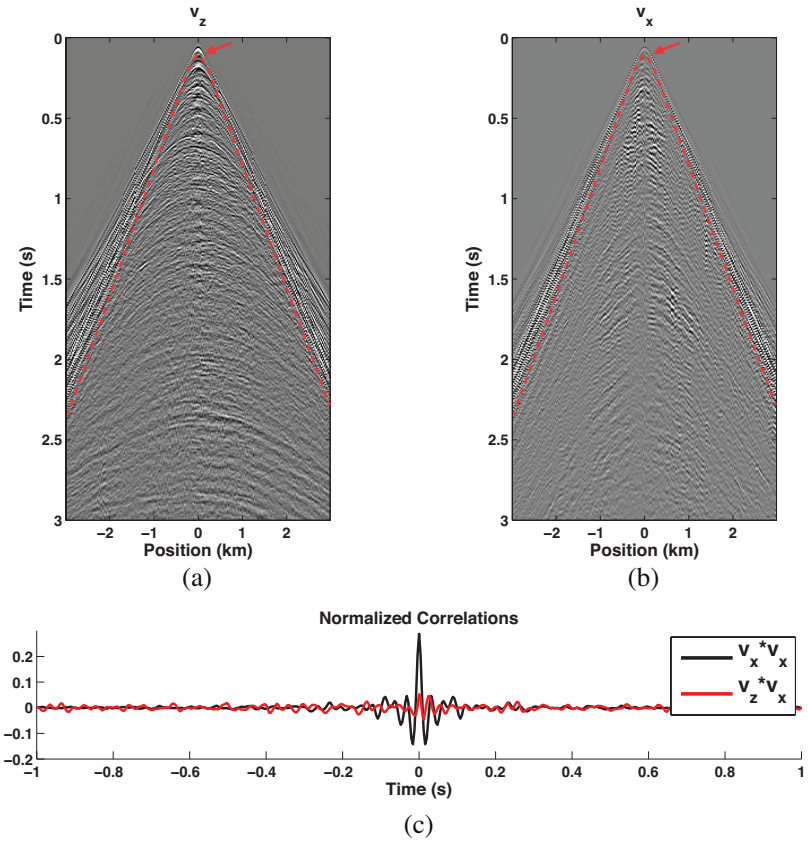

Figure 9.2: (a) Vertical and (b) horizontal particle velocity components for a common-shot gather of the Volve dataset, respectively. Red arrows indicate the direct wave arrival. (c) Normalized correlation of the horizontal particle velocity with itself (black line) and with the vertical particle velocity (red line). Red dashed lines in (a) and (b) indicate the lower bounds for the temporal parts of the portion of data used for the correlation.

9.3 Missing boundaries, our future friends?

The lack of enclosing boundaries of sources and/or receivers has long presented a challenge to the practice of seismic interferometry by cross-correlation, leading to retrieved responses that are often distorted by artefacts (Snieder et al., 2006; Wapenaar, 2006). In this thesis we have seen that limited aperture arrays of sources and receivers similarly influence the products of seismic imaging. In Chapter 2, the uneven source illumination of a square inclusion results in artefacts that prevent a clear understanding of the bottom and side interfaces of the sensed body (Figure 2.11a). Moreover, in wavefield extrapolation, one-sided illumination allows for the reconstruction of only the upper part of the receiver wavefield as shown in Figure 3.4b and c.

On one hand, when we are interested in improving the Green's function estimate, this limitation can be partially overcome by reformulating the estimation problem as a

multi-dimensional deconvolution process of the convolution-type integral representation (Wapenaar et al., 2008a, 2011; van der Neut et al., 2011b). As also discussed in Chapter 4, while the correlation-type representation holds only under the condition that the receiver boundary is a closed surface, the convolution-type representation is valid for open boundaries as long as sources are on one side of (e.g., above) the boundary of receivers.

On the other hand, as first shown in Vasconcelos et al. (2015a), representation theorems can be opportunely manipulated to obtain a set of integrals that uniquely relate the physical recordings along a limited-aperture array of sources to data that would need to be recorded to close the source boundary (so-called 'missing boundary data'). One potential application of such identities is in detecting and quantifying errors in subsurface models for inversion of model parameters (Vasconcelos et al., 2014a): the misfit between the integral term depending on the available data and that of the missing boundary data contains information about errors in the velocity model used to generate the latter data via numerical modelling (e.g., finite-difference). Building on the scattering-based relation of Vasconcelos et al. (2015a), I have derived a new metric for velocity errors detection and show with a numerical example that its evaluation with an incorrect velocity model leads to a larger misfit than when the correct velocity model is used.

To start, I consider the geometrical configuration in Figure 9.3a. A reference medium whose properties are assumed to be known is identified, and a perturbation region χ generating scattered waves is added to it. Depending on the choice of the model perturbation, the information carried by the scattered wavefield can be used for either imaging or monitoring: in imaging, we usually assume the unperturbed medium to be smooth such that it does not generate reflected waves, while discontinuities are embedded in the perturbation to account for scattering. In monitoring applications, the perturbation represents the time-lapse changes in the medium. In either case, the perturbation region and two receivers $\mathbf{x}_A$ and $\mathbf{x}_B$ are confined to be between the boundary of sources, which is here defined to be composed by two infinite integration planes $\partial D_{S,top}$ and $\partial D_{S,bot}$. Under the assumption that the perturbation is located away from the observation points and at least one of them is placed above it, Vasconcelos et al. (2009b) demonstrate that only one term of the frequency-domain scattering-based representation theorem is physical and is needed to construct the scattered response between those points

$$G^S_{p,q}(\mathbf{x}_A,\mathbf{x}_B) = \int_{\partial D_{S,top}} G^S_{p,q}(\mathbf{x}_A,\mathbf{x}_S)G^{0*}_{v_n,q}(\mathbf{x}_B,\mathbf{x}_S) + G^S_{v_n,q}(\mathbf{x}_A,\mathbf{x}_S)G^{0*}_{p,q}(\mathbf{x}_B,\mathbf{x}_S)\,\mathrm{d}^2\mathbf{x}_S, \tag{9.11}$$

where the quantities used in this and the following equations have been previously defined in Chapter 4. Superscripts 0 and S are further added to identify reference and scattered wavefields, respectively.

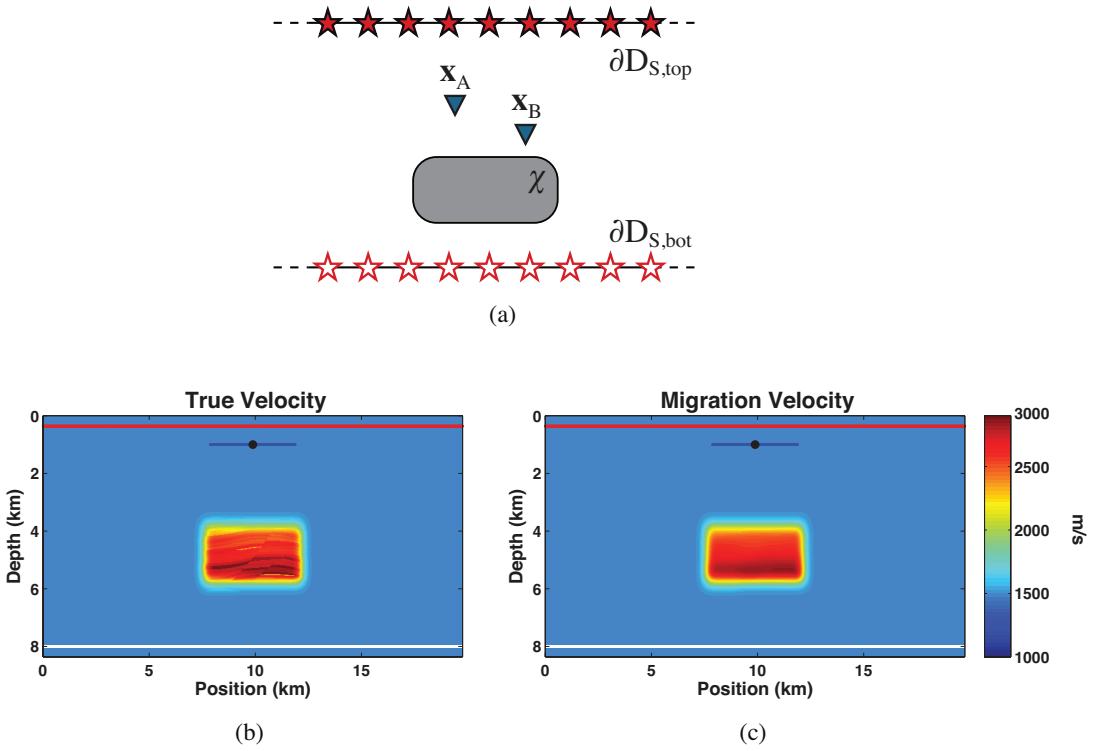

Figure 9.3: (a) Ideal geometrical configuration for the interferometric misfit function. Solid red stars denote available sources while open red stars identify missing sources. Blue triangles are receivers, and the grey square indicates the perturbation χ. True and reference velocity models used for the numerical examples are shown in (b) and (c), respectively.

As a consequence, the other terms of the scattering-based representation that do not contribute to the physical energy in $G^S_{p,q}(\mathbf{x}_A, \mathbf{x}_B)$ need to cancel each other

$$\begin{aligned}&\int_{\partial D_{S,bot}} G^S_{p,q}(\mathbf{x}_A, \mathbf{x}_S) G^{0*}_{v_n,q}(\mathbf{x}_B, \mathbf{x}_S) + G^S_{v_n,q}(\mathbf{x}_A, \mathbf{x}_S) G^{0*}_{p,q}(\mathbf{x}_B, \mathbf{x}_S)\, \mathrm{d}^2\mathbf{x}_S = \\ &\int_D G_{p,q}(\mathbf{x}_A, \mathbf{x}) \chi(\mathbf{x}) G^{0*}_{p,q}(\mathbf{x}_B, \mathbf{x})\, \mathrm{d}^3\mathbf{x}.\end{aligned} \tag{9.12}$$

Such an equation is the first component of our method. The left-hand side contains a surface integral along the bottom boundary $\partial D_{S,bot}$ which cross-correlates the reference Green's functions from each source to the receiver $\mathbf{x}_B$ and the scattered Green's functions from each source to the receiver $\mathbf{x}_A$. This is equivalent to a volume integral performed inside the perturbation subdomain which cross-correlates the reference Green's functions from each point inside the volume to the receiver $\mathbf{x}_B$ and total Green's functions from each point inside the volume to the receiver $\mathbf{x}_A$, weighted by the per-

turbation operator $\chi(\mathbf{x})$.

By noting that relations similar to equations 9.11 and 9.12 can be written for the retrieval of the anticausal Green's function $G^{S*}_{p,q}(\mathbf{x}_A, \mathbf{x}_B)$ (Vasconcelos et al., 2009b, equation 16) and by using the generalized optical theorem (Douma et al., 2011), the sum of volume integrals can be converted into an additional surface integral:

$$\begin{aligned}&\int_D G_{p,q}(\mathbf{x}_A,\mathbf{x})\chi(\mathbf{x})G^{0*}_{p,q}(\mathbf{x}_B,\mathbf{x}) + G^{0}_{p,q}(\mathbf{x}_A,\mathbf{x})\chi^*(\mathbf{x})G^{*}_{p,q}(\mathbf{x}_B,\mathbf{x})\,\mathrm{d}^3\mathbf{x} = \\ &\oint_{\partial D_{S,top}\cup\partial D_{S,bot}} G^{S}_{p,q}(\mathbf{x}_A,\mathbf{x}_S)G^{S*}_{v_n,q}(\mathbf{x}_B,\mathbf{x}_S) + G^{S}_{v_n,q}(\mathbf{x}_A,\mathbf{x}_S)G^{S*}_{p,q}(\mathbf{x}_B,\mathbf{x}_S)\,\mathrm{d}^2\mathbf{x}_S.\end{aligned} \tag{9.13}$$

Finally, after rearranging integrals over $\partial D_{S,top}$ and $\partial D_{S,bot}$ as separate terms, we can write an identity that is effectively a surface-integral-only version of the well-known generalized optical theorem (Douma et al., 2011):

$$I_{top} = I_{bot}, \tag{9.14}$$

where

$$I_{top} = \int_{\partial D_{S,top}} G^{S}_{p,q}(\mathbf{x}_A,\mathbf{x}_S)G^{S*}_{v_n,q}(\mathbf{x}_B,\mathbf{x}_S) + G^{S}_{v_n,q}(\mathbf{x}_A,\mathbf{x}_S)G^{S*}_{p,q}(\mathbf{x}_B,\mathbf{x}_S)\,\mathrm{d}^2\mathbf{x}_S \tag{9.15}$$

and

$$\begin{aligned}I_{bot} = &\int_{\partial D_{S,bot}} G^{S}_{p,q}(\mathbf{x}_A,\mathbf{x}_S)G^{0*}_{v_n,q}(\mathbf{x}_B,\mathbf{x}_S) + G^{S}_{v_n,q}(\mathbf{x}_A,\mathbf{x}_S)G^{0*}_{p,q}(\mathbf{x}_B,\mathbf{x}_S)\,\mathrm{d}^2\mathbf{x}_S \\ &+ \int_{\partial D_{S,bot}} G_{p,q}(\mathbf{x}_A,\mathbf{x}_S)G^{S*}_{v_n,q}(\mathbf{x}_B,\mathbf{x}_S) + G_{v_n,q}(\mathbf{x}_A,\mathbf{x}_S)G^{S*}_{p,q}(\mathbf{x}_B,\mathbf{x}_S)\,\mathrm{d}^2\mathbf{x}_S.\end{aligned} \tag{9.16}$$

Given the relation in equation 9.14, I here define a metric to be used to estimate the subsurface model $\mathbf{m} = [m(\mathbf{x}_1), m(\mathbf{x}_2), ..., m(\mathbf{x}_N)]$ with $\mathbf{x}_i \in D$:

$$J(\mathbf{x}_A,\mathbf{x}_B;\mathbf{m}) = \| \; I_{top}(\mathbf{x}_A,\mathbf{x}_B) - I_{bot}(\mathbf{x}_A,\mathbf{x}_B;\mathbf{m}) \; \|^2 \, . \tag{9.17}$$

Note that the first term (I_{top}) contains only recorded data from available sources along $\partial D_{S,top}$ and can be directly evaluated since it does not depend on the choice of the model $\mathbf{m}$. On the other hand, to be able to compute the second term (I_{bot}) we first need to model the required fields from missing (bottom) sources.

Since the misfit is by definition equal to zero when the velocity model used to compute fields in equation 9.16 is adequate, an optimization problem can be set up based on the

metric in equation 9.17:

$$\mathbf{m} = \min_{\mathbf{m}} \sum_{\omega, \mathbf{x}_A, \mathbf{x}_B} J(\mathbf{x}_A, \mathbf{x}_B; \mathbf{m}) \quad for\ \mathbf{m} \in D, \tag{9.18}$$

where we can sum over any combination of available receivers $\mathbf{x}_A$ and $\mathbf{x}_B$ and frequencies (or time, if we use the time-domain version of the representation theorems).

A numerical experiment is now designed to study the sensitivity of the misfit function $J(\mathbf{x}_A, \mathbf{x}_B; \mathbf{m})$ to errors in the velocity model used to compute the missing boundary data. In this case, the available data are acquired using the geometry and model in Figure 9.3b. I use a line of uniformly sampled ($dx_S = 7\,m$) monopole sources at $z_S = 360\,m$ (red line), an array of receivers at discrete positions $\mathbf{x}_A$ (blue line) recording pressure and both components of particle velocity, and a fixed-position receiver at $\mathbf{x}_B$ (black dot). The source excitation function is a zero-phase Ricker wavelet with center frequency $f_c = 15\,Hz$. In this example, the velocity model used for the computation of the reference fields is a smooth version of the true model, as shown in Figure 9.3c.

Figure 9.4a displays the time domain version of the integral I_{top}, computed using the recorded data for the single receiver $\mathbf{x}_B$ and the split-spread line of receivers $\mathbf{x}_A$ as depicted in Figure 9.3b. If we also compute the integral I_{bot} using the correct velocity model, its contribution inside the dashed lines in Figure 9.4 is in good agreement with that of I_{top} such that their sum results in small residual energy (Figure 9.4c). The imperfect cancellation of spurious arrivals outside the dashed lines is expected. It is mainly the effect of having finite aperture array of sources, lacking thus from contributions of far away sources as required by the theory in equations 9.11 to 9.16. Hence, I decide to introduce a muting function Θ, chosen to be zero for $|t| > |x_A - x_B|/V$, and I evaluate the misfit function only inside the causality cone represented by dashed white lines in Figure 9.4.

The trace-by-trace power of the windowed gather in Figure 9.4c, obtained by stacking each trace over time, is shown by the red line in Figure 9.4d: very small residual energy suggests that a correct velocity model has been used for the modelling of missing data. I now assume that our knowledge of the velocity model is limited to the smooth model in Figure 9.3c, the same model that has been used to compute the reference fields. Since each integral in equation 9.16 contains at least one scattered field, and because the reference model and the estimate of the actual model are the same in this case, each scattered field vanishes and the integral I_{bot} is thus null. The misfit function is therefore obtained by stacking the integral I_{top} over time and is represented by the blue line in Figure 9.4d. As a consequence of an incorrect knowledge of the model, larger residual energy is present throughout the extension of the receiver array when compared to

that of the correct model (red line). At this point, I hypothesize that gradient-based optimization algorithms (e.g., Tarantola (1984); Tromp et al. (2005)) may effectively use such information to improve the estimate of the velocity model. Research is required to test the performance of our metric in actual inversions in terms of regularization, pre-conditioning aspects, and parameter resolution.

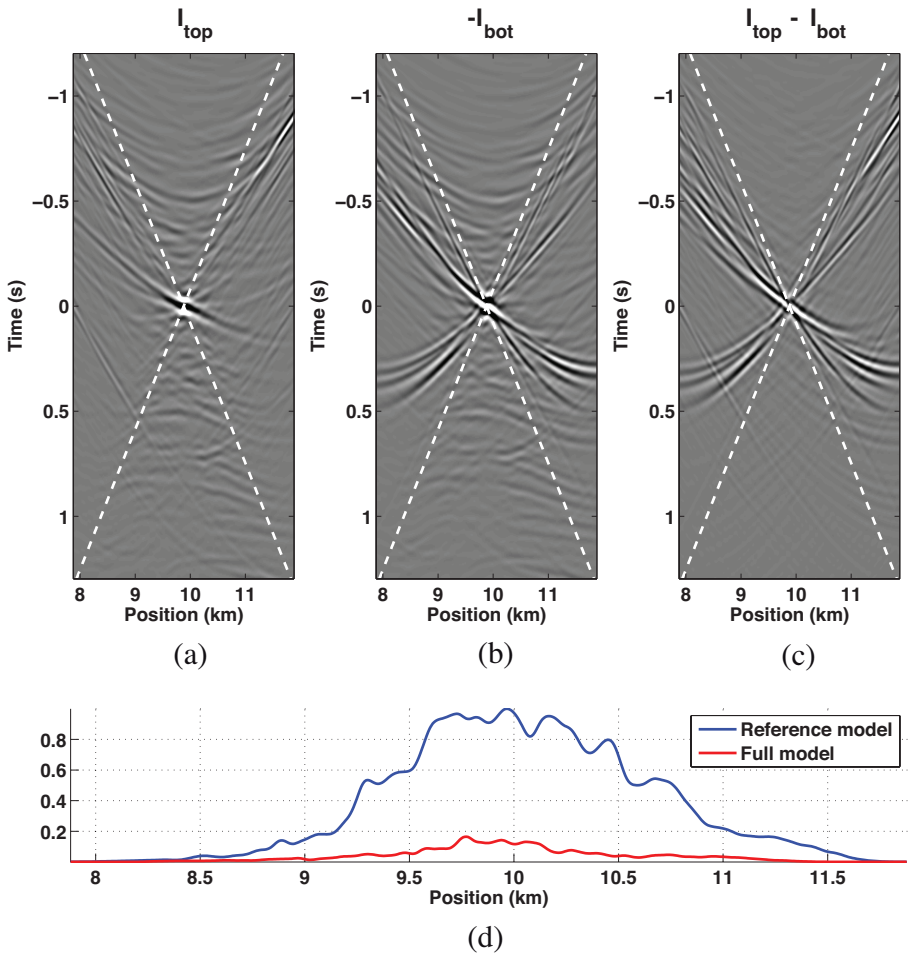

Figure 9.4: Time-domain integral contributions computed assuming the knowledge of true velocity model: (a) I_{top} (equation 9.15), (b) $-I_{bot}$ (equation 9.16), and (c) their sum. Stacking the panel (c) over the time axis within the cones defined by dashed white lines in (a) to (c) results in the red line in (d) which is compared with the misfit obtained from the knowledge of the smooth model (blue line).

■

10

Conclusion

The importance of multiply scattered wavefields has long been recognized in various imaging disciplines, but has only recently received widespread interest in the geophysical community. In this thesis I have considered a variety of topics centered around the theme of seismic migration beyond the single-scattering (Born) approximation. Reciprocity and representation theorems have been identified as a suitable platform to define physically consistent combinations of singly and multiply scattered waves in the process of constructing high-resolution, true-amplitude images of the Earth interior.

The role of Chapter 2 was two-fold: first, different representation theorems for perturbed elastic media were introduced. These were then turned into nonlinear, true-amplitude imaging conditions for migration of elastic datasets. A remarkable observation drawn from the numerical examples is that the interplay between linear and nonlinear terms is crucial to obtain images with increased illumination, higher resolution, fewer artefacts, and equalized amplitudes. While neither of those terms alone is able to provide us with a picture of the small-scale features of the medium, their destructive interference does reveal such details.

Backpropagation of recorded seismic data into the subsurface represents a key component of any imaging technique. In Chapter 3, I improved on current practice elastic wavefield extrapolation by proposing a novel formulation based on a two-way correlation-type representation theorem. The correct combination of velocity and stress data components has enabled propagation of recorded wavefields only towards their direction of arrival, with only the correct wave-mode being excited. While the application of such an approach to real land or ocean-bottom scenarios remains a challenge because of the impossibility to record reliable measurements of shear stresses, its acoustic counterpart is shown in Chapter 7 to work effectively on an ocean-bottom dataset acquired over the Volve field, North Sea. A significant advantage of correctly handling the finite-frequency directivity of particle velocity measurements in the extrapolation step, lies in

the generation of clearer shallow sections and better focused space-lag common image gathers.

By taking inspiration from wavefield extrapolation based on two-way representation, the problem of source redatuming to locations beneath a complex overburden using multi-dimensional deconvolution is reformulated in Chapter 4. While this approach was so far believed to work effectively only in the presence of up/down separated data, I showed that a two-way convolution-type representation enables redatuming of full multi-component data without the need for preliminary wavefield separation. This finding will have a significant impact for applications to borehole redatuming in the presence of subsurface properties that significantly vary along the receiver array, hence affecting standard wavefield separation procedures.

Chapter 5 was devoted to the identification of a framework for nonlinear imaging of elastic data, based on the previous theoretical findings in terms of imaging conditions (Chapter 2) and wavefield extrapolation (Chapter 3). By testing this strategy on a benchmark model that emulates deep water subsalt prospects, I analysed the additional value that multiply scattered and transmitted waves provide in imaging of shadow zones and faults. As a further step, in Chapter 6, the nonlinear elastic formulation was adapted to the construction of so-called extended images. By redatuming recorded data to a depth level much closer to small scale features of interests (e.g., reservoirs), highly distorted responses in the data were converted into much simpler and more continuous moveouts in the extended image gathers. Those responses are easier to identify and use for reservoir characterization. Moreover, it was found that when imaging with incorrect velocity models, reflection and transmission data have different sensitivity to velocity errors. This opens the way for a new family of image-domain velocity analysis methods for data that are jointly acquired at the Earth's surface and somewhere inside the medium such as in a borehole.

Finally, in Chapters 8 I further exploited the potential of extended images to perform target-oriented imaging of subsurface areas of interest of the Volve field. The novel technique of Marchenko redatuming was used to generate accurate wavefields in the subsurface from surface reflection data. Multi-dimensional deconvolution of those wavefields produced responses that could have been recorded if a seismic survey was conducted in the subsurface. Interestingly a weak coherent structure, which was not visible or was perhaps distorted in the image from surface data, was revealed by the target-oriented approach.

In light of the results presented in this thesis, I foresee that more research will be devoted in the coming years to the formulation and implementation of seismic migration and inversion algorithms that could fully benefit from the additional information carried by

multiple scattering. Free-surface and internal multiples will be more widely used with the aim of alleviating illumination issues in complex geologies. Transmitted waves and rapidly decaying fields will be exploited alongside diffractions for the identification of small scale features with superior resolution than our current capabilities. Moreover, I expect that the incorporation of acoustic and elastic wavefield separation in wavefield extrapolation and redatuming schemes will become more widely accepted, and various imaging algorithms will be reformulated by taking full advantage of multi-component data. This will limit the set of requirements and the processing steps that seismic data should have undergone before being used as input for seismic migration and inversion.

Appendices

A

Derivation of reciprocity-based elastic wavefield extrapolation

An elastodynamic wavefield in a lossless arbitrarily inhomogeneous anisotropic solid medium is uniquely defined by the stress tensor $\tau_{ij}(\mathbf{x},t)$ and the particle velocity $v_i(\mathbf{x},t)$ at position $\mathbf{x}$ and time t (Aki and Richards, 1980; Snieder, 2002). In the space-frequency domain, the stress tensor and particle velocity obey the equation of motion

$$j\omega\rho v_i - \partial_j \tau_{ij} = f_i \tag{A.1}$$

and we assume the linear stress-strain relation

$$-j\omega c_{ijkl}\tau_{kl} + (\partial_j v_i + \partial_i v_j)/2 = h_{ij}, \tag{A.2}$$

where the different quantities are defined in Chapter 2 and summarized in Table 1. Given an interaction quantity that combines these quantities (equation 2.3), the elastodynamic reciprocity theorem of the correlation-type can be identified (equation 2.4). If impulsive point sources of force/deformation type and Green's functions are substituted for the wavefields in the elastodynamic reciprocity theorems, the reciprocity theorem of the correlation-type leads to an elastodynamic Green's function representation theorem, which is the basis of seismic interferometry and of our tensorial wavefield extrapolation. Given the inter-source geometry in Figure 3.1 with a physical source $\mathbf{x}_S$ located outside of a closed boundary of receivers ∂D_R that surrounds an imaginary source at the image point $\mathbf{x}_I$ in the subsurface (Slob et al., 2007), we obtain a Green's function representation using only point sources of force type

$$d^{(v,f)}_{(n,k)}(\mathbf{x}_I,\mathbf{x}_S) = \\ -\oint_{\partial D_R}\{d^{(\tau,f)}_{(ij,k)}(\mathbf{x}_R,\mathbf{x}_S)G^{(v,f)*}_{(i,n)}(\mathbf{x}_R,\mathbf{x}_I) + d^{(v,f)}_{(i,k)}(\mathbf{x}_R,\mathbf{x}_S)G^{(\tau,f)*}_{(ij,n)}(\mathbf{x}_R,\mathbf{x}_I)\}n_{R_j}\,\mathrm{d}^2\mathbf{x}_R.$$

(A.3)

Taking advantage of source-receiver reciprocity relations

$$\begin{aligned} G^{(v,f)}_{(i,n)}(\mathbf{x}_R,\mathbf{x}_I) &= G^{(v,f)}_{(n,i)}(\mathbf{x}_I,\mathbf{x}_R) \\ G^{(\tau,f)}_{(ij,n)}(\mathbf{x}_R,\mathbf{x}_I) &= G^{(v,h)}_{(n,ij)}(\mathbf{x}_I,\mathbf{x}_R) \end{aligned} \tag{A.4}$$

an equivalent Green's function representation that mixes point sources of force and deformation types is obtained

$$\begin{aligned} &d^{(v,f)}_{(n,k)}(\mathbf{x}_I,\mathbf{x}_S) = \\ &-\oint_{\partial D_R}\{d^{(\tau,f)}_{(ij,k)}(\mathbf{x}_R,\mathbf{x}_S)G^{(v,f)*}_{(n,i)}(\mathbf{x}_I,\mathbf{x}_R) + d^{(v,f)}_{(i,k)}(\mathbf{x}_R,\mathbf{x}_S)G^{(v,h)*}_{(n,ij)}(\mathbf{x}_R,\mathbf{x}_I)\}n_{R_j}\,\mathrm{d}^2\mathbf{x}_R. \end{aligned} \tag{A.5}$$

Equations A.3 and A.5 represent two alternative ways to construct the n-th component of the particle velocity at $\mathbf{x}_I$ due to the k-th component of an external volume force density source at $\mathbf{x}_S$. A boundary ∂D_R of receivers that record the full particle velocity vector and stress tensor, and external volume force density sources at $\mathbf{x}_I$ and $\mathbf{x}_S$, respectively, are required to evaluate equation A.3. Two co-located boundaries ∂D_R of sources and receivers that fire volume force density and deformation rate density sources and record the full particle velocity vector and stress tensor are instead required to evaluate equation A.5.

Equation A.3 looks more suitable for interferometric purposes because the requirements are less severe. This is not true when the Green's function between $\mathbf{x}_S$ and $\mathbf{x}_I$ has to be estimated in an imaging context. The terms $d^{(\tau,f)}_{(ij,k)}(\mathbf{x}_R,\mathbf{x}_S)$ and $d^{(v,f)}_{(i,k)}(\mathbf{x}_R,\mathbf{x}_S)$ represent the physical recording, and the terms $G^{(v,f)}_{(n,i)}(\mathbf{x},\mathbf{x}_R)$ and $G^{(v,h)}_{(n,ij)}(\mathbf{x},\mathbf{x}_R)$ are not recorded but may be computed numerically: they are the so-called propagators because they act on the recorded data and backpropagate them into the subsurface domain. The crosscorrelation and integration (sum) over receivers can be performed implicitly by injecting recorded data at all receivers simultaneously along a boundary of virtual sources (co-located with the boundary of physical receivers).

However, equation A.5 does not represent the scalar or vectorial potentials at the image point $\mathbf{x}_I$ originating from a P- or S-wave source at $\mathbf{x}_S$. These are needed to evaluate nonlinear, reciprocity-based imaging conditions such as that in equation 2.16. Taking advantage of the P- and S-wave Green's functions defined in equations 2.9 and 2.10 we recall that the P- and S-wave components of the wavefield can be expressed as a sum of partial derivatives of the velocities. The wavefield extrapolation integral A.5 may then

be recast as

$$d^{(\Phi,\Phi)}_{(N,K)}(\mathbf{x}_I,\mathbf{x}_S) = \\ -\oint_{\partial D_R}\{d^{(\tau,\Phi)}_{(ij,K)}(\mathbf{x}_R,\mathbf{x}_S)G^{(\Phi,f)*}_{(N,i)}(\mathbf{x}_I,\mathbf{x}_R)+d^{(v,\Phi)}_{(i,K)}(\mathbf{x}_R,\mathbf{x}_S)G^{(\Phi,h)*}_{(N,ij)}(\mathbf{x}_I,\mathbf{x}_R)\}n_{R_j}\,\mathrm{d}^2\mathbf{x}_R, \tag{A.6}$$

where we use the notation $d^{(\Phi,\Phi)}_{(N,K)}(\mathbf{x}_I,\mathbf{x}_S)$ to express the received P- or S-wave (N) recorded at point $\mathbf{x}_I$, due to a P- or S-wave source (K) located at $\mathbf{x}_S$.

To conclude, nonlinear, reciprocity-based imaging conditions require also the scattered wavefield between a P- or S-wave source at $\mathbf{x}_S$ and a potential virtual receiver at the image point $\mathbf{x}_I$ (first line of equation 2.16). Following the approach that Wapenaar et al. (2010b) propose, a generic Green's function can be written as the sum of reference and scattered wavefields for any definition of the reference and scattered medium. Furthermore, because equations 2.9 and 2.10 are still valid if any Green's function is substituted by the reference Green's function G^0 we obtain

$$d^{0(\Phi,\Phi)}_{(N,K)}(\mathbf{x}_I,\mathbf{x}_S) = \\ -\oint_{\partial D_R}\{d^{0(\tau,\Phi)}_{(ij,K)}(\mathbf{x}_R,\mathbf{x}_S)G^{0(\Phi,f)*}_{(N,i)}(\mathbf{x}_I,\mathbf{x}_R)+d^{0(v,\Phi)}_{(i,K)}(\mathbf{x}_R,\mathbf{x}_S)G^{0(\Phi,h)*}_{(N,ij)}(\mathbf{x}_I,\mathbf{x}_R)\}n_{R_j}\,\mathrm{d}^2\mathbf{x}_R. \tag{A.7}$$

Subtracting equation equations A.7 from A.6, we obtain the wavefield extrapolation integral in equations 3.1.

■

B

Up/down wavefield separation

It has long been recognized that seismic recordings can be split into in- and out-going waves with respect to a chosen boundary line ∂D_R (see Figure 4.1)

$$p = p^+ + p^- \qquad v_i = v_i^+ + v_i^-, \tag{B.1}$$

where p indicates the pressure recording and v_i the particle velocity recording along the i-th direction, while superscripts $+$ and $-$ refer to in- and out-going constituents, respectively. In addition, the normal component of the particle velocity v_n is uniquely related to the normal derivative of pressure via the equation of motion

$$\frac{\partial p}{\partial n} = -j\omega\rho v_n. \tag{B.2}$$

The approach used in this thesis to obtain decomposed fields in the special case of a horizontal boundary ∂D_R, where in- and out-going constituents are generally referred as down- and up-going constituents, operates in the frequency-wavenumber domain. Up- and down-going components of pressure and normal particle velocity are in fact related to the full pressure and the normal particle velocity recordings by the matrix equations (Wapenaar and Berkhout, 1989; Amundsen, 1993; Fokkema and van den Berg, 1993)

$$\begin{bmatrix} p^+ \\ p^- \end{bmatrix} = \frac{1}{2}\begin{bmatrix} 1 & \xi \\ 1 & -\xi \end{bmatrix}\begin{bmatrix} p \\ v_n \end{bmatrix} \tag{B.3}$$

$$\begin{bmatrix} v_n^+ \\ v_n^- \end{bmatrix} = \frac{1}{2}\begin{bmatrix} 1/\xi & 1 \\ -1/\xi & 1 \end{bmatrix}\begin{bmatrix} p \\ v_n \end{bmatrix}, \tag{B.4}$$

where $\xi(k_x) = \rho\frac{\omega}{k_z(k_x)}$ is the so-called obliquity factor, $k_z(k_x) = \sqrt{(\frac{\omega}{V})^2 - k_x^2}$ is the

vertical wavenumber, k_x is the horizontal wavenumber, ρ and V are the density and the velocity at the receiver level, respectively. If we are only interested in obtaining the down-going constituents of both pressure and particle velocity as in the main text, we can define the down-going two decomposition vectors $\mathbf{D}_{\mathbf{p}}^{+}, \mathbf{D}_{\mathbf{v}}^{+}$ (in equation 4.14) by extracting the first line of the decomposition matrices in equations B.3 and B.4.

Requirements to be fulfilled for an accurate up/down wavefield separation in the f-k domain (Weglein et al., 2013) are (1) accurate knowledge of medium properties (ρ, V) at the receiver array; (2) a horizontally layered (or slowly laterally varying) medium along the receiver array; (3) horizontal (or, at least, flat) boundary ∂D_R where f-k transform and separation is carried out; (4) adequate sampling and aperture to perform an f-k transform. The number of assumptions can be reduced if more accurate separation techniques are used, such that wavefield decomposition can be performed in the frequency-space domain (Grimbergen et al., 1998; Wapenaar et al., 2008a; Weglein et al., 2013) or by means of finite-difference injection (Vasconcelos, 2013; Amundsen and Robertsson, 2014). The latter method, for example, can accommodate an arbitrary measurement surface geometry and does not require an estimate of the local medium parameters as shown in Chapter 7.

■

C

Anticausal solutions of two-way MDD

The convolution-type representation in equation 4.1 contains causal Green's functions $G_{p,p}$ and $G_{v_n,p}$, and likewise we expect to retrieve only causal (one-sided) Green's functions by inverting equation 4.10 by means of MDD (equation 4.12). However, a correlation-type representation can also be written to relate the fields in Figure 4.1 (Slob et al., 2007)

$$p(\mathbf{x}_{VS},\mathbf{x}_S) = \oint_{\partial D_R} p(\mathbf{x}_R,\mathbf{x}_S)G^*_{v_n,q}(\mathbf{x}_R,\mathbf{x}_{VS}) + v_n(\mathbf{x}_R,\mathbf{x}_S)G^*_{p,q}(\mathbf{x}_R,\mathbf{x}_{VS})\,\mathrm{d}^2\mathbf{x}_R, \quad \text{(C.1)}$$

where an enclosing boundary ∂D_R is here required since radiation conditions can not be applied to eliminate the contribution of the half-sphere that would close the boundary. In practice the quantities along the lower boundary are not available and for this reason we usually discard such contributions. Note however that this approximation is justified only if the medium is strongly reflective below $\mathbf{x}_{VS}$ (Wapenaar, 2006).

Equation C.1 can then be converted into matrix form using the same quantities defined in equation 4.10:

$$\mathbf{p} = \begin{bmatrix} \bar{\mathbf{p}} & \bar{\mathbf{v}} \end{bmatrix} \begin{bmatrix} \mathbf{G}^*_{\mathbf{v}} \\ \mathbf{G}^*_{\mathbf{p}} \end{bmatrix} = \begin{bmatrix} \bar{\mathbf{p}} & -\bar{\mathbf{v}} \end{bmatrix} \begin{bmatrix} \mathbf{G}^*_{\mathbf{v}} \\ -\mathbf{G}^*_{\mathbf{p}} \end{bmatrix} \Leftrightarrow \mathbf{p} = \mathbf{d}\mathbf{G}^*_{\mathbf{tw}} \quad \text{(C.2)}$$

and equations 4.10 and C.2 are combined to obtain

$$\mathbf{p} = \mathbf{d}\left(\alpha\mathbf{G}_{\mathbf{tw}} + \beta\mathbf{G}^*_{\mathbf{tw}}\right), \quad \text{(C.3)}$$

where α and β are constants such that $\forall\,\alpha,\beta:\ \alpha+\beta=1$. Thus we see why solving two-way MDD in fact provides both causal and anticausal Green's functions, since in the time domain $\mathbf{G}^*_{\mathbf{tw}}$ is the time-reverse of $\mathbf{G}_{\mathbf{tw}}$. Equations 4.10 and C.2 also show the

reason for the different polarity of the anticausal pressure Green's functions in Figures 4.8 and 4.15. The term $\mathbf{G_p}$ comes with a plus sign in the Green's function vector $\mathbf{G_{tw}}$ in equation 4.10 and with minus sign in the Green's function vector $\mathbf{G^*_{tw}}$ in equation C.2.

We now show that when we solve two-way MDD in a regularized sense by finding the solution at minimum norm (equation 4.11), such regularization term is responsible for choosing a specific pair of α, β namely $\alpha = \beta = 0.5$. In time domain, we first define the norm of the solution in equation C.3

$$\begin{aligned} J_G = \| \alpha \mathbf{G_{tw}}(t) + \beta \mathbf{G_{tw}}(-t) \|^2 = & < \alpha \mathbf{G_{tw}}(t), \alpha \mathbf{G_{tw}}(t) > \\ & + < \beta \mathbf{G_{tw}}(-t), \beta \mathbf{G_{tw}}(-t) > \\ & 2 < \alpha \mathbf{G_{tw}}(t), \beta \mathbf{G_{tw}}(-t) >, \end{aligned} \tag{C.4}$$

where $<,>$ represents the scalar product that here represents the product of each of the time samples, integrated over time. By noting that $\mathbf{G_{tw}}(t)$ is causal while $\mathbf{G_{tw}}(-t)$ is anticausal, their scalar products $< \mathbf{G_{tw}}(t), \mathbf{G_{tw}}(-t) >$ and $< \mathbf{G_{tw}}(-t), \mathbf{G_{tw}}(t) >$ are both zeros. Moreover, since the two Green's functions have the same energy ($< \mathbf{G_{tw}}(t), \mathbf{G_{tw}}(t) > = < \mathbf{G_{tw}}(-t), \mathbf{G_{tw}}(-t) > = k_{tw}$) we obtain

$$J_G = k_{tw} \left(\alpha^2 + \beta^2 \right). \tag{C.5}$$

Using the fact that $\alpha = 1 - \beta$ the value of β that minimizes J_G is 0.5 and so the value of α. The causal and anticausal solutions obtained by solving two-way MDD have indeed the same energy as shown in Figures 4.7, 4.8, and 4.14.

We also convert equation C.1 into a representation theorem for virtual dipole sources. By multiplying each side of the equation by the operator that transforms pressure fields into particle velocity fields (i.e., $-j(\omega\rho)^{-1}\partial_i$) at the virtual source location, we obtain

$$v_i(\mathbf{x}_{VS}, \mathbf{x}_S) = \oint_{\partial D_R} -p(\mathbf{x}_R, \mathbf{x}_S) G^*_{v_n, f_i}(\mathbf{x}_R, \mathbf{x}_{VS}) - v_n(\mathbf{x}_R, \mathbf{x}_S) G^*_{p, f_i}(\mathbf{x}_R, \mathbf{x}_{VS}) \, \mathrm{d}^2\mathbf{x}_R. \tag{C.6}$$

By comparing equation C.6 with equation 4.18 we can thus explain the change in polarity in the anticausal estimate of the velocity Green's function from a virtual dipole source (see Figure 4.9). On the other hand, the causual and anticausal estimates of the pressure Green's function from a virtual dipole share the same polarity (see Figure 4.10). The term G_{v_n, f_i} in fact comes with a plus sign in equation 4.18 and with minus sign in equation C.6, while the term G_{p, f_i} has a minus sign in both equations.

Finally, it is interesting to note that by adding directional constraints that annihilate the down-going energy of the estimated Green's functions as done in equation 4.16, the anticausal component of the estimated Green's functions goes to zero. To explain this phenomenon, we first convert the two-way correlation-type theorem (equation C.1) into its one-way (directional) counterpart. Conversely to the convolution-type theorem, the two products between in- and out-going terms at the stationary receiver locations have opposite contributions that cancel (Wapenaar and Berkhout, 1989). Consequently, equation C.1 can be written as

$$\begin{aligned} p(\mathbf{x}_{VS},\mathbf{x}_S) = &\int_{\partial D_R} p^-(\mathbf{x}_R,\mathbf{x}_S)G^{-*}_{v_n,q}(\mathbf{x}_R,\mathbf{x}_{VS}) + p^+(\mathbf{x}_R,\mathbf{x}_S)G^{+*}_{v_n,q}(\mathbf{x}_R,\mathbf{x}_{VS})d\mathbf{x}^2_R \\ &+ \int_{\partial D_R} v^-_n(\mathbf{x}_R,\mathbf{x}_S)G^{-*}_{p,q}(\mathbf{x}_R,\mathbf{x}_{VS}) + v^+_n(\mathbf{x}_R,\mathbf{x}_S)G^{+*}_{p,q}(\mathbf{x}_R,\mathbf{x}_{VS})d\mathbf{x}^2_R. \end{aligned} \tag{C.7}$$

We note that by invoking the directional constraints (i.e., $G^+_{v_n,q} = G^+_{p,q} = 0$), we are implicitly solving the following version of the one-way convolution theorem

$$p(\mathbf{x}_{VS},\mathbf{x}_S) = \int_{\partial D_R} p^+(\mathbf{x}_R,\mathbf{x}_S)G^-_{v_n,q}(\mathbf{x}_R,\mathbf{x}_{VS}) - v^+_n(\mathbf{x}_R,\mathbf{x}_S)G^-_{p,q}(\mathbf{x}_R,\mathbf{x}_{VS})\,\mathrm{d}^2\mathbf{x}_R \tag{C.8}$$

or this version of the one-way correlation theorem

$$p(\mathbf{x}_{VS},\mathbf{x}_S) = \int_{\partial D_R} p^-(\mathbf{x}_R,\mathbf{x}_S)G^{-*}_{v_n,q}(\mathbf{x}_R,\mathbf{x}_{VS} + v^-_n(\mathbf{x}_R,\mathbf{x}_S)G^{-*}_{p,q}(\mathbf{x}_R,\mathbf{x}_{VS})\,\mathrm{d}^2\mathbf{x}_R \tag{C.9}$$

which, converted into matrix equations, become

$$\mathbf{p} = \begin{bmatrix} \mathbf{p}^+ & -\mathbf{v}^+ \end{bmatrix} \begin{bmatrix} \mathbf{G}^-_{\mathbf{v}} \\ \mathbf{G}^-_{\mathbf{p}} \end{bmatrix} \Leftrightarrow \mathbf{p} = \mathbf{d}^+\mathbf{G}^-_{\mathbf{tw}} \tag{C.10}$$

$$\mathbf{p} = \begin{bmatrix} \mathbf{p}^- & \mathbf{v}^- \end{bmatrix} \begin{bmatrix} \mathbf{G}^{-*}_{\mathbf{v}} \\ \mathbf{G}^{-*}_{\mathbf{p}} \end{bmatrix} \Leftrightarrow \mathbf{p} = \mathbf{d}^-\mathbf{G}^{-*}_{\mathbf{tw}}. \tag{C.11}$$

Since the operands $\mathbf{d}^+$ and $\mathbf{d}^-$ in equations C.10 and C.11 contain different quantities, the convolution problem (i.e. causal solution) can be solved without leaking energy from the correlation problem (i.e. anticausal solution) by inputting $\bar{\mathbf{p}}$ and $-\bar{\mathbf{v}}$ together with the directional constraint to the MDD inversion scheme (see, for example, Figure 4.14).

■

D

A reciprocal source-receiver framework for elastic imaging

Imaging with ocean-bottom multicomponent data can require the application of so-called source-receiver reciprocity (Wapenaar and Fokkema, 2006) to the theory provided in the main text. Sources usually define a roughly uniformly sampled portion of a boundary because they are fired at regular times along lines by a boat moving over the sea surface at constant speed. If data are acquired by OBNs, receivers may be significantly more sparsely and less uniformly spaced on the seabed. The first step in the source-receiver imaging framework, wavefield extrapolation, requires the simultaneous injection of seismic data in a modelling code (e.g., finite-differences). To do so, a uniformly spaced boundary may be preferred because it aids error control during preliminary data interpolation along the modelling grid. Applying source-receiver reciprocity, the boundary of sources can be used at this stage (Figure D.1a), and seismic data resorted into common-receiver gathers are backpropagated into the model from source positions. Once the extrapolated wavefield is estimated, the source wavelet is injected at any receiver location to create the forward-extrapolated wavefield and the imaging condition is computed to create an image of the subsurface (Figure D.1b).

An exact elastic imaging condition with velocity-stress receivers and monopole P- or S-wave pseudosources and pseudoreceivers in the subsurface is given by

$$
\begin{aligned}
&I^{nl}_{NM}(\mathbf{x}_I) = \tilde{G}^{S(\Phi,\Phi)}_{(M,N)}(\mathbf{x}_I,\mathbf{x}_I,t=0)\} = \\
&-\int\left(\oint_{\partial D_R}\{d^{S(\tau,\Phi)}_{(ij,M)}(\mathbf{x}_R,\mathbf{x}_I)G^{0(v,\Phi)*}_{(i,N)}(\mathbf{x}_R,\mathbf{x}_I)+d^{S(v,\Phi)}_{(i,M)}(\mathbf{x}_R,\mathbf{x}_I)G^{0(\tau,\Phi)*}_{(ij,N)}(\mathbf{x}_R,\mathbf{x}_I)\}n_{R_j}\,\mathrm{d}^2\mathbf{x}_R\right)\mathrm{d}\omega \\
&-\int\left(\oint_{\partial D_R}\{d^{(\tau,\Phi)}_{(ij,M)}(\mathbf{x}_R,\mathbf{x}_I)G^{S(v,\Phi)*}_{(i,N)}(\mathbf{x}_R,\mathbf{x}_I)+d^{(v,\Phi)}_{(i,M)}(\mathbf{x}_R,\mathbf{x}_I)G^{S(\tau,\Phi)*}_{(ij,N)}(\mathbf{x}_R,\mathbf{x}_I)\}n_{R_j}\,\mathrm{d}^2\mathbf{x}_R\right)\mathrm{d}\omega.
\end{aligned}
\tag{D.1}
$$

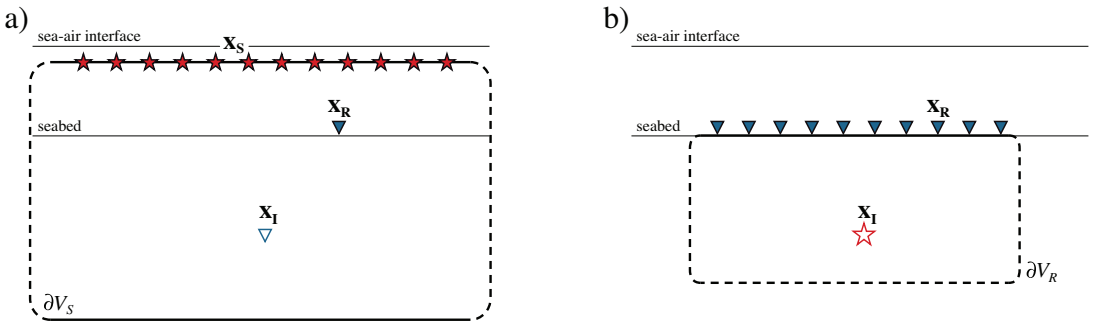

Figure D.1: Geometries used for the alternative version of scattering-based imaging condition and wavefield extrapolation. (a) A closed source boundary ∂D_S (sources actually used in the acquisition are represented by stars) is used at the extrapolation stage, whereas in (b) a closed receiver boundary ∂D_R (receivers actually used in the acquisition are represented by triangles) is used at the imaging stage.

Because no assumption about the model on and outside of ∂D_R is made up to this point, the imaging condition in equation D.1 is correct for in- and outgoing waves at the receiver boundary. Primary and ghost signals are both properly focused at the image point. However, when only monopole P-wave sources are available as in the imaging condition in equation 2.16, an approximated integral expression must be used for wavefield backpropagation by injection of the seismic data along the source array. The extrapolation of a Green's function between a P- or S-wave source fired virtually in the subsurface and a physical particle velocity receiver is

$$\begin{aligned} 2Re\{d^{S(v,\Phi)}_{(i,M)}(\mathbf{x}_R,\mathbf{x}_I)\} \approx & \oint_{\partial D_S} \frac{2}{\rho(\mathbf{x}_S)V_P(\mathbf{x}_S)}\{d^{S(v,\Phi)}_{(i,P)}(\mathbf{x}_R,\mathbf{x}_S)G^{0(\Phi,\Phi)*}_{(M,P)}(\mathbf{x}_I,\mathbf{x}_S)\}\,\mathrm{d}^2\mathbf{x}_S \\ & \oint_{\partial D_S} \frac{2}{\rho(\mathbf{x}_S)V_P(\mathbf{x}_S)}\{d^{(v,\Phi)}_{(i,P)}(\mathbf{x}_R,\mathbf{x}_S)G^{S(\Phi,\Phi)*}_{(M,P)}(\mathbf{x}_I,\mathbf{x}_S)\}\,\mathrm{d}^2\mathbf{x}_S \end{aligned} \tag{D.2}$$

whereas the Green's function between a P- or S-wave virtually fired source in the subsurface and a physical stress receiver is

$$\begin{aligned} 2Re\{d^{(\tau,\Phi)}_{(ij,M)}(\mathbf{x}_R,\mathbf{x}_I)\} \approx & \oint_{\partial D_S} \frac{2}{\rho(\mathbf{x}_S)V_P(\mathbf{x}_S)}\{d^{S(\tau,\Phi)}_{(ij,P)}(\mathbf{x}_R,\mathbf{x}_S)G^{0(\Phi,\Phi)*}_{(M,P)}(\mathbf{x}_I,\mathbf{x}_S)\}\,\mathrm{d}^2\mathbf{x}_S \\ & \oint_{\partial D_S} \frac{2}{\rho(\mathbf{x}_S)V_P(\mathbf{x}_S)}\{d^{(\tau,\Phi)}_{(ij,P)}(\mathbf{x}_R,\mathbf{x}_S)G^{S(\Phi,\Phi)*}_{(M,P)}(\mathbf{x}_I,\mathbf{x}_S)\}\,\mathrm{d}^2\mathbf{x}_S. \end{aligned} \tag{D.3}$$

The above approximations require that the model at and outside of ∂D_S is homogeneous, isotropic, and unperturbed. When this assumption is not satisfied (e.g., if source-side ghost and higher order multiples are not previously attenuated), the extrapolated wavefields will contain artificial events that erroneously crosscorrelate with the

source-side wavefield to generate artefacts in elastic images.

■

E

Receiver profile VARTM

As already discussed in Appendix D, when data are acquired with ocean-bottom acquisition systems the number of sources largely may exceeds that of receivers. Moreover ocean-bottom cables (OBCs) are poorly sampled in the cross-line direction and ocean-bottom nodes (OBNs) are coarsely and non-uniformly located across the whole survey area. Pre-stack imaging of ocean-bottom acquisition can alternatively be performed in the common-receiver domain: in terms of processing, the idea of reciprocity is applied, meaning that the common-receiver data are injected along the source array while the source wavelet is injected at the common-receiver location.

To be able to perform receiver-profile VARTM, two receiver wavefields are separately computed by injecting the common-receiver pressure and velocity data as monopole-type sources:

$$w_r^{p-VARTM} : p \Rightarrow q, \qquad w_r^{v_n-VARTM} : v_n \Rightarrow q \tag{E.1}$$

(notation is defined in Chapter 7). Similarly, two source wavefields are generated, one from a monopole source and the other from a dipole source:

$$w_s^{q-VARTM} : s \Rightarrow q, \qquad w_s^{f_n-VARTM} : s \Rightarrow f_n. \tag{E.2}$$

The resulting four wavefields are finally combined in the imaging condition:

$$i : w_s^{f_n-VARTM} * w_r^{p-VARTM} - w_s^{q-VARTM} * w_r^{v_n-VARTM}. \tag{E.3}$$

The proper handling of up- and down-going waves results in two images that show ghost reflectors with the same polarity and true reflectors with reverse polarity, such that their difference enhances the true reflectors and suppresses the ghost reflectors (Figure E.1). For a comparison with shot-profile VARTM see Figure 7.5b.

Note that while shot-profile VARTM has the same cost as shot- and receiver-profile RTM (i.e., two forward modelling steps), the cost doubles in receiver-profile VARTM (i.e., four forward modelling steps), meaning that it is convenient to switch from shot-profile to receiver-profile VARTM only when the number of sources is twice that of receivers.

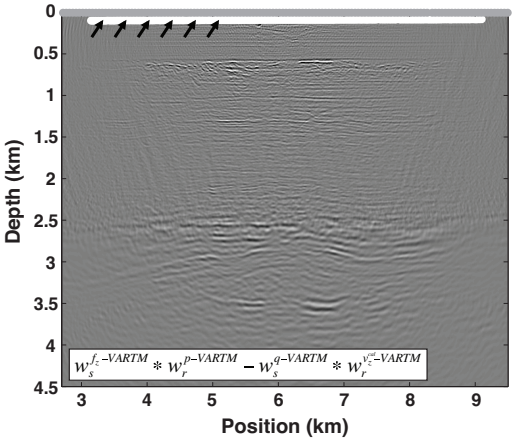

Figure E.1: Receiver-profile VARTM image for migration of up-going waves. A line of black arrows pointing upward indicates that up-going waves are correctly migrated.

References

Aki, K., and P. G. Richards, 1980, Quantitative seismology: W. H. Freeman & Co. 49, 50, 152, 243

Amal, R., N. Bertram, and D. Herron, 2005, An experimental nodal OBS acquisition from the Thunder Horse Field, Gulf of Mexico: The Leading Edge, **24**, 410–412. 76

Amundsen, L., 1993, Wavenumber-based Filtering of Marine Point Source Data: Geophysics, **58**. 175, 186, 204, 215, 247

———, 2001, Elimination of free-surface related multiples without need of a source wavelet: Geophysics, **66**, 327–341. 77, 106, 110, 115, 144, 207, 213, 216

Amundsen, L., L. Ikelle, and L. Berg, 2001, Multidimensional signature deconvolution and free-surface multiple elimination of marine multicomponent ocean-bottom seismic data: Geophysics, **66**, 1594–1604. 213

Amundsen, L., and A. Reitan, 1995, Decomposition of multicomponent seafloor data into upgoing and downgoing P- and S-waves: Geophysics, **60**. 117

Amundsen, L., and J. O. A. Robertsson, 2014, Wave equation processing using finite-difference propagators, Part 1: Wavefield dissection and imaging of marine multicomponent seismic data: Geophysics, **79**, T287–T300. 32, 186, 207, 248

Archer, S., X. Du, and R. Fletcher, 2013, Amplitude inversion of depth imaging seismic data from areas with complex geology: Presented at the 75th EAGE Conference & Exhibition, Extended Abstracts. 145

Bakulin, A., R. Burnstad, M. Jervis, and P. Kelamis, 2012, The feasibility of permanent land seismic monitoring with buried geophones and hydrophones in a desert environment: Presented at the 74th EAGE Conference & Exhibition, Extended Abstracts. 225

Bakulin, A., and R. Calvert, 2006, The virtual source method: Theory and case study: Geophysics, **71**. 102, 111

Balch, A., and C. Erdemir, 1994, Sign-change correction for prestack migration of P-S converted wave reflections: Geophysical Prospecting, **42**, 637–663. 68, 71, 129

Barak, O., P. Jaiswal, S. de Ridder, J. Giles, R. Brune, and S. Ronen, 2014, Six-component seismic land data acquired with geophones and rotation sensors: wave-mode selectivity by application of multicomponent polarization filtering: The Leading Edge, **33**. 226

Barr, F. J., and J. I. Sanders, 1989, Attenuation of water-column multiples using pressure and velocity detectors in a water-bottom cable: 59th Annual International Meeting, SEG, Expanded Abstracts, 653–656. 76, 98, 186

Baysal, E., D. Kosloff, and J. Sherwood, 1983, Reverse time migration: Geophysics, **48**, 1514–1524. 145

Bazargani, F., 2014, Optimal wave focusing for seismic source imaging: PhD thesis, Colorado School of Mines, CWP. 223

Behura, J., K. Wapenaar, and R. Snieder, 2014, Autofocus imaging: Image reconstruction based on inverse scattering theory: Geophysics, **79**, A19–A26. 210

Bellezza, C., and F. Poletto, 2014, Multidimensional deconvolution and processing of seismic interferometry Artic data: Geophysics, **79**, WA25–WA38. 103

Benioff, H., 1935, A linear-strain seismograph: The Bullettin of the Seismological Society of America, **25**, 282–309. 226

Berg, E., B. Svenning, and J. Martin, 1994, SUMIC - A new strategic toolfor exploration and reservoir mapping: 56th EAGE Conference & Exhibition, Extended Abstracts, G055. 76

Berkhout, A., and D. Verschuur, 1997, Estimation of multiple scattering by iterative inver-

sion; part i: theoretical considerations: Geophysics, **62**, 1586–1595. 144

———, 2011, Full wavefield migration, utilizing surface and internal multiple scattering: 81st Annual International Meeting, SEG, Expanded Abstracts, 3212–3216. 145

Berkhout, A. J., and D. W. van Wulfften Palthe, 1979, Migration in terms of spatial deconvolution: Geophysical Prospecting, **27**, 261–291. 36

Berryhill, J. R., 1984, Wave-equation datuming before stack: Geophysics, **49**, 2064–2066. 210

Bertrand, A., P. G. Folstad, B. Lyngnes, S. Buizard, H. Hoeber, N. Pham, S. de Pierrepont, J. Schultzen, and A. Grandi, 2014, Ekofisk Life-Of-Field Seismic: operations and 4D processing: The Leading Edge, **33**, 142–148. 225

Billette, F., and G. Lambare', 1998, Velocity macro-model estimation from seismic reflection data by stereotomography: Geophysical Journal International, **135**, 671–690. 205

Biondi, B., 2006, 3D seismic imaging: SEG. 30, 127, 186, 197

Bishop, T. N., 1985, Tomographic determination of velocity and depth in laterally varying media: Geophysics, **50**, 903–923. 68

Blanch, J., 2012, Is de-ghosting necessary with multi-component data?: Presented at the 82nd Annual International Meeting, SEG, Expanded Abstracts. 32, 186

Bleistein, N., J. K. Cohen, and J. W. Stockwell, 2001, Mathematics of multidimensional seismic imaging, migration, and inversion: Springer. 30

Boiero, D., E. Wiarda, and P. Vermeer, 2013, Surface- and guided-wave inversion for near-surface modeling in land and shallow marine seismic data: The Leading Edge, **32**, 638–646. 29

Born, M., and E. Wolf, 1999, Principles of optics: Cambridge University Press. 33

Brenguier, F., N. M. Shapiro, M. Campillo, A. Nercessian, and V. Ferrazzini, 2007, 3D surface wave tomography of the Piton de la Fournaise volcano using seismic noise correlations: Geophysical Research Letters, **34**, L02305. 29

Broggini, F., R. R. Snieder, and K. Wapenaar, 2014, Data-driven wave field focusing and imaging with multidimensional deconvolution: numerical examples for reflection data with internal multiples: Geophysics, **79**, WA107–WA115. 33, 210

Broggini, F., R. Snieder, and K. Wapenaar, 2012, Focusing the wavefield inside an unknown 1D medium - beyond seismic interferometry: Geophysics, **77**, A25–A28. 33, 127, 129, 146, 151, 180, 210

Bussat, S., and S. Kugler, 2011, Offshore ambient-noise surface-wave tomography above 0.1 Hz and its applications: The Leading Edge, **30**, 514–524. 29

Cambois, G., D. Carlson, C. Jones, M. Lesnes, W. Sollner, and H. Tabti, 2009, Dual-sensor streamer data: calibration, acquisition QC and attenuation of seismic interferences and other noises: 79th Annual International Meeting, SEG, Expanded Abstracts, 142–146. 186

Campillo, M., and A. Paul, 2003, Long-range correlations from the diffuse seismic coda: Science, **299**, 547–549. 29, 102

Canales, L., 1984, Random noise reduction: 54th Annual International Meeting, SEG, Expanded Abstracts, 525. 150

Caprioli, P. B. A., X. Du, R. P. Fletcher, and I. Vasconcelos, 2014, 3d source deghosting after imaging: 84th Annual International Meeting, SEG, Expanded Abstracts, 4092–4096. 206

Caprioli, P. B. A., A. K. Ozdemir, A. Ozbek, J. E. Kragh, D. J. van Manen, P. A. F. Christie, and J. O. A. Robertsson, 2012, Combination of multi-component streamer pressure and vertical particle velocity - theory and application to data: Presented at the 74th EAGE Conference & Exhibition, Extended Abstracts. 205

Castagna, J., and M. M. Backus, 1993, Offset-dependent reflectivity: theory and practice of AVO analysis: Presented at the 63rd Annual International Meeting, SEG, Expanded Abstracts. 150

Chang, W. F., and G. A. McMechan, 1986, Reverse-time migration of offset vertical seismic profiling data using the excitation-time imaging condition: Geophysics, **51**, 67–84. 77, 98

———, 1994, 3-d elastic prestack, reverse-time depth migration: Geophysics, **59**, 597–609. 32, 77, 98, 132

Claerbout, J. F., 1971, Toward a unified theory of reflector mapping: Geophysics, **36**, 467–481. 30, 60, 127, 190

———, 1985, Imaging the earth's interior: Blackwell Scientific Publications. 47, 60

Cotton, J., and E. Forgues, 2012, Dual-depth hydrophones for ghost reduction in 4d land monitoring: Presented at the 82nd Annual International Meeting, SEG, Expanded Abstracts. 226

Curtis, A., 2009, Source-receiver seismic interferometry: 79th Annual International Meeting, SEG, Expanded Abstracts, 3655–3658. 47, 126, 155

Curtis, A., Y. Behr, E. Entwistle, E. Galetti, J. Townend, and S. Bannister, 2012, The benefit of hindsight in observational science: Retrospective seismological observations: Earth and Planetary Science Letters, **345-348**, 212–220. 47

Curtis, A., P. Gerstoft, H. Sato, R. Snieder, and K. Wapenaar, 2006, Seismic interferometry-turning noise into signal: The Leading Edge, **25**, 1082–1092. 46, 102

Curtis, A., and D. Halliday, 2010, Source-receiver wave field interferometry: Physical Review E, **81**, 046601. 47, 70, 126, 130, 151, 152, 155, 178, 205

Curtis, A., H. Nicolson, D. Halliday, J. Trampert, and B. Baptie, 2009, Virtual seismometers in the subsurface of the earth from seismic interferometry: Nature Geoscience, 700–704. 47

Curtis, A., and J. O. A. Robertsson, 2002, Volumetric wavefield recordingand near-receiver group velocity estimation for land seismics: Geophysics, **67**, 1602–1611. 80

da Costa, C., M. Ravasi, A. Curtis, and G. A. Meles, 2014a, Elastodynamic green's function retrieval through single-sided marchenko inverse scattering: Physical Review E, **90**. 146, 151, 180, 210

da Costa, C., M. Ravasi, G. A. Meles, and A. Curtis, 2014b, Elastic autofocusing: Presented at the 76th EAGE Conference & Exhibition, Extended Abstracts. 146, 151, 180

———, 2014c, Elastic autofocusing via single-sided marchenko inverse scattering: Presented at the 84th Annual International Meeting, SEG, Expanded Abstracts. 146, 151, 180

Dash, R., G. Spence, R. Hyndman, S. Grion, Y. Wang, and S. Ronen, 2009, Wide-area imaging from obs multiples: Geophysics, **74**, Q41–Q47. 77, 98, 190

Davydenko, M., and D. Verschuur, 2012, Demonstration of full wavefield migration in 2d subsurface models: Presented at the 74th EAGE Conference & Exhibition, Extended Abstracts. 29, 33, 145

de Bruin, C. G. M., C. P. A. Wapenaar, and A. J. Berkhout, 1990, Angle-dependent reflectivity by means of prestack migration: Geophysics, **55**, 1223–1234. 37

de Hoop, A. T., 1988, Time-domain reciprocity theorems for acoustic wave fields in fluids with relaxation: Journal of the Acoustical Society of America, **84**, 1877–1882. 34

de Ridder, S., and J. Dellinger, 2011, Ambient seismic noise eikonal tomography for near-surface imaging at valhall: The Leading Edge, **30**. 29

Denli, H., and L. Huang, 2008, Elastic-wave reverse-time migration with a wavefield separation imaging condition: 78th Annual International Meeting, SEG, Expanded Abstracts, 2346–2350. 68, 71, 129

Dong, S., Y. Luo, X. Xiao, S. Chavez-Perez, and G. T. Schuster, 2009, Fast 3d target-oriented reverse-time datuming: Geophysics, **74**, WCA141–WCA151. 211

Douma, H., I. Vasconcelos, and R. Snieder, 2011, The reciprocity theorem for the scattered field is the progenitor of the generalized optical theorems: Journal of the Acoustical Society of America, **129**, 2765–2771. 126, 145, 233

Draganov, D., K. K. Wapenaar, and J. Thorbecke, 2006, Seismic interferometry: Reconstructing the earth's reflection response: Geophysics, **71**, SI61–SI70. 102

Du, Q., Y. Zhu, and J. Ba, 2012, Polarity reversal correction for elastic reverse time migration: Geophysics, **77**, S31–S41. 72, 129

Egan, M., E.-K. K. G., and N. Moldoveanu, 2007, Full deghosting of obc data with over/under source acquisition: 77th Annual International Meeting, SEG, Expanded Abstracts, 31–35. 206

El Yadari, N., 2015, True-amplitude vector-acoustic imaging: Application of gaussian beams: Geophysics, **80**, S43–S54. 122, 186

El Yadari, N., and S. Hou, 2013, Vector-acoustic kirchhoff migration and its mirror extension - theory and examples: Presented at the 75th EAGE Conference & Exhibition, Extended Abstracts. 122, 186

El Yadari, N., Y. Kamil, and M. Vassallo, 2014,

Wavefield extrapolation and imaging using single- or multi-component seismic measurements. 205

Elmore, W., and M. Heald, 1969, Physics of waves: Dover Press. 33

Fink, M., 2008, Time-reversal waves and super resolution.: Journal of Physics: Conference Series. 33, 161

Fletcher, R., S. Archer, D. Nichols, and W. Mao, 2012, Inversion after depth imaging: Presented at the 82nd Annual International Meeting, SEG, Expanded Abstracts. 145

Fleury, C., 2012, Migration velocity analysis for nonlinear reverse-time migration: Presented at the 82nd Annual International Meeting, SEG, Expanded Abstracts. 150, 173, 181, 197

———, 2013, Increasing illumination and sensitivity of reverse-time migration with internal multiples: Geophysical Prospecting, **61**, 891–906. 33, 122, 127, 129

Fleury, C., and F. Perrone, 2012, Bi-objective optimization for the inversion of seismic reflection data: Combined fwi and mva: Presented at the 82nd Annual International Meeting, SEG, Expanded Abstracts. 37, 150, 173, 181

Fleury, C., and R. Snieder, 2011, Reverse-time-migration of multiply scattered seismic waves: 81st Annual International Meeting, SEG, Expanded Abstracts, 3382. 100

Fleury, C., R. Snieder, and K. Larner, 2010, General representation theorem for perturbed media and application to green's function retrieval for scattering problems: Geophysical Journal International, **183**, 1648–1662. 126, 145

Fleury, C., and I. Vasconcelos, 2012, Imaging condition for nonlinear scattering-based imaging: Estimate of power loss in scattering: Geophysics, **77**, S1–S18. 34, 35, 38, 46, 47, 66, 67, 100, 126, 131, 143, 161, 200

———, 2013, Adjoint-state reverse-time migration of 4c data: finite-frequency map migration for marine seismic imaging: Geophysics, **78**, WA159–WA172. 206

Fokkema, J., and P. van den Berg, 1993, Seismic applications of acoustic reciprocity: Elsevier Science. 34, 104, 111, 193, 247

Fokkema, J. T., and A. Ziolkowski, 1987, The critical reflection theorem: Geophysics, **52**, 965–972. 216

Forghani, F., and R. Snieder, 2010, Underestimation of body waves and feasibility of surface-wave reconstruction by seismic interferometry: The Leading Edge, **29**, 790–794. 102

Foster, D. J., and C. C. Mosher, 1992, Suppression of multiple reflections using the radon transform: Geophysics, **57**, 386–395. 150

Frijlink, M., R. van Borselen, and W. Sollner, 2011, The free surface assumption for marine data-driven demultiple methods: Geophysical Prospecting, **59**, 269–278. 186

Gaiser, J., N. Moldoveanu, C. Macbeth, R. Michelena, and S. Spitz, 2001, Multicomponent technology: The players, problems, applications, and trends: Summary of the workshop sessions: The Leading Edge, **20**, 974–977. 76

Gaiser, J. E., and I. Vasconcelos, 2010, Elastic interferometry for ocean bottom cable data: Theory and examples: Geophysical Prospecting, **58**, 347–360. 52, 60, 142

Galetti, E., and A. Curtis, 2012, Generalised receiver functions and seismic interferometry: Tectonophysics, **532-535**, 1–26. 46, 102

Gardner, G., L. Gardner, and A. Gregory, 1974, Formation velocity and density - the diagnostic basics for stratigraphic traps: Geophysics, **39**, 770–780. 133

Gherasim, M., U. Albertin, B. Nolte, and O. Askim, 2010, Wave-equation angle-based illumination weighting for optimized subsalt imaging: Presented at the 80th Annual International Meeting, SEG, Expanded Abstracts. 145

Godfrey, R., P. Kristiansen, B. Armstrong, M. Cooper, and E. Thorogood, 1998, Imaging the foinaven ghost: 68th Annual International Meeting, SEG, Expanded Abstracts, 1333–1335. 77, 98

Granger, P. Y., M. Manin, J. L. Boelle, E. Ceragioli, F. Lefeuvre, and E. A. Crouzy, 2005, Autonomous 4c nodes used in infill areas to complement streamer data, deepwater case study: 75th Annual International Meeting, SEG, Expanded Abstracts, 84–87. 76

Gray, S. H., 1997, True-amplitude seismic migration: A comparison of three approaches: Geophysics, **62**, 929–936. 46

Grechka, V., and I. Tsvankin, 2002, PP + PS = SS: Geophysics, **67**, 1961–1971. 70

Gret, A., R. Snieder, and J. Scales, 2006, Time-

lapse monitoring of rocks properties with coda wave interferometry: Journal of Geophysical Research, **111**, B03305. 68

Grimbergen, J. L. T., F. J. Dessing, and K. Wapenaar, 1998, Modal expansion of one-way operators in laterally varying media: Geophysics, **63**, 995–1005. 248

Grion, S., R. Exley, M. Manin, X. Miao, A. Pica, Y. Wang, P. Granger, and S. Ronen, 2007, Mirror imaging of obs data: First Break, **25,**, 37–42. 77, 98, 188

Grobbe, N., J. V. der Neut, and C. A. Vidal, 2013, Flux-normalized elastodynamic wavefield decomposition using only particle velocity recordings: 83rd Annual International Meeting, SEG, Expanded Abstracts, 4693–4698. 226

Guitton, A., A. Valenciano, D. Bevc, and J. Claerbout, 2007, Smoothing imaging condition for shot-profile migration: Geophysics, **72**, S149–S154. 190, 207

Hale, D., 2014, Dynamic warping of seismic images: Geophysics, **78**, S105–S115. 177

Halliday, D., and A. Curtis, 2009, Generalized optical theorem for surface waves and layered media: Physical Review E, **79**, 056603. 47, 71

———, 2010, An interferometric theory of source-receiver scattering and imaging: Geophysics, **75**, SA95–SA103. 35, 46, 47, 60, 61, 126, 130, 145, 150, 151, 152, 155, 178, 186, 192, 205

Halliday, D., A. Curtis, and K. Wapenaar, 2012, Generalized PP + PS = SS from seismic interferometry: Geophysical Journal International, **189**, 1015–1024. 56, 70

Hampson, D., ., 1987, The discrete radon transform: A new tool for image enhancement and noise suppression: 57th Annual International Meeting, SEG, Expanded Abstracts, 141–143. 150

Haney, M., and H. Douma, 2012, Rayleigh wave tomography at coronation field, canada: The topography effect: The Leading Edge, **31**, 54–61. 29

Hardage, B. A., 1992, Crosswell seismology and reverse vsp: Geophysical Press. 225

Hodgkinson, K., D. Agnew, and E. Roeloffs, 2013, Working with strainmeter data: Presented at the Transactions American Geophysical Union. 226

Hong, T.-K., and W. Menke, 2006, Tomographic investigation of the wear along the san jacinto fault, southern california: Physics of the Earth and Planetary Interiors, **155**, 236–248. 47

Hughes, P., O. H. Hatland, J. M. Haynes, M. Oygaren, and G. Drivenes, 2010, De-risking a palaeocene amplitude anomaly prospect using multi component seismic and controlled source electromagnetics: Presented at the NPF Biennial Geophysical Seminar, Expanded Abstracts. 76

Ikelle, L. T., 1999, Using even terms of the scattering series for deghosting and multiple attenuation of ocean-bottom cable data: Geophysics, **64**, 579–592. 206

Jakubowicz, H., 1998, Wave equation prediction and removal of interbed multiples: 68th Annual International Meeting, SEG, Expanded Abstracts, 1527–1530. 144

Jones, I., and S. Levy, 1987, Signal-to-noise ratio enhancement in multichannel seismic data via the karhunen-loeve transform: Geophysical Prospecting, **3**, 12–32. 150

Kearey, P., M. Brooks, and I. Hill, 1991, An introduction to geophysical exploration: Blackwell Scientific Publications. 227

King, S., and A. Curtis, 2012, Suppressing nonphysical reflections in green's function estimates using source-receiver interferometry: Geophysics, **77**, Q15–Q25. 35, 155, 178

King, S., A. Curtis, and T. Poole, 2011, Interferometric velocity analysis using physical and non-physical energy: Geophysics, **76**, SA35–SA49. 155, 178

Kleyn, A., 1977, On the migration of reflection time contour maps: Geophysical Prospecting, **25**, 125–140. 205

Knapp, S., N. Payne, and T. Johns, 2001, Imaging through gas clouds: A case history from the gulf of mexico: 71st Annual International Meeting, SEG, Expanded Abstracts, 776–779. 76

Komatitsch, D., and J. Tromp, 1999, Introduction to the spectral-element method for 3-D seismic wave propagation: Geophysical Journal International, **139**, 806–822. 99

Lecomte, I., 2008, Resolution and illumination analyses in PSDM: a ray-based approach: The Leading Edge, **27**, 650–663. 128, 145

Lee, W. H. K., H. Igel, and M. D. Trifunac, 2009, Recent advances in rotational seismology: Seismological Research Letters, **80**, 479–490. 226

Leiceaga, G. G., J. Silva, F. Artola, E. Marquez, and J. Vanzeler, 2010, Enhanced density estimation from prestack inversion of multicomponent seismic data: The Leading Edge, **29**, 1220–1226. 76, 187

Lerosey, G., J. de Rosny, A. Tourin, and M. Fink, 2007, Focusing beyond the diffraction limit with far-field time reversal: Science, **315**, 1120–1122. 33, 161

Li, X.-Y., 1998, Fracture detection using P-P and P-S waves in multicomponent seafloor data: 68th Annual International Meeting, SEG, Expanded Abstracts, 2056–2059. 76

Liu, Y., X. Chang, D. Jin, R. He, H. Sun, and Y. Zheng, 2011, Reverse time migration of multiples for subsalt imaging: Geophysics, WB209–WB216. 31, 145

Loer, K., G. A. Meles, A. Curtis, and I. Vasconcelos, 2014, Diffracted and pseudo-physical waves from spatially-limited arrays using source-receiver interferometry (sri): Geophysical Journal International, **196**, 1043–1059. 35, 145, 150, 157, 159, 174, 178, 197

Lu, L., Z. Ding, R. S. Zeng, and Z. He, 2011, Retrieval of green's function and generalized optical theorem for scattering of complete dyadic fields: Journal of the Acoustical Society of America, **129,**, 1935–1944. 52, 207

Lu, R., J. Yan, J. E. Anderson, and T. Dickens, 2010, Elastic RTM: Anisotropic wave-mode separation and converted-wave polarization correction: 80th Annual International Meeting, SEG, Expanded Abstracts, 3171–3175. 68, 72

Lu, S., D. Whitmore, A. A. Valenciano, and N. Chemingui, 2014, Enhanced subsurface illumination from separated wavefield imaging: First Break, **32**, 87–92. 29

Malcolm, A. E., M. V. de Hoop, and H. Calandra, 2007, Identification of image artifacts from internal multiples: Geophysics, **72**, S123–S132. 31, 210

Malcolm, A. E., M. V. de Hoop, and B. Ursin, 2011, Recursive imaging with multiply scattered waves using partial image regularization: A north sea case study: Geophysics, **76**, 33–42. 33

Margerin, L., and H. Sato, 2011, Generalized optical theorems for the reconstruction of green's function of an inhomogeneous elastic medium: Journal of the Acoustical Society of America, **130**, 3674–3690. 71

Martin, G. S., K. J. Marfurt, and S. Larsen, 2002, Marmousi-2: An updated model for the investigation of avo in structurally complex areas: 72nd Annual International Meeting, SEG, Expanded Abstracts, 1979–1982. 92, 93

Matson, K., and A. B. Weglein, 1996, Removal of elastic interface multiples from land and ocean-bottom data using inverse scattering: 66th Annual International Meeting, SEG, Expanded Abstracts, 1526–1530. 206

Maver, K. G., 2011, Ocean bottom seismic: Strategic technology for the oil industry: First Break, **29**, 75–80. 76, 187

Mehta, K., A. Bakulin, J. Sheiman, R. Calvert, and R. Snieder, 2007, Improving the virtual source method by wavefield separation: Geophysics, **72**, V79–V86. 102

Mehta, K., R. Snieder, R. Calvert, and J. Sheiman, 2008, Acquisition geometry requirements for generating virtual-source data: The Leading Edge, **27**, 620–629. 159, 203

Meles, G. A., and A. Curtis, 2013, Physical and non-physical energy in scattered wave source-receiver interferometry: Journal of the Acoustical Society of America, **133**, 3790–3801. 35, 145, 150, 157, 174, 178

———, 2014a, Discriminating physical and non-physical diffracted energy in source-receiver interferometry: Geophysical Journal International, **197**, 1642–1659. 157

———, 2014b, Fingerprinting ordered diffractors in multiply diffracted waves: Geophysical Journal International, **198**, 1701–1713. 157

Menke, W., 1989, Geophysical data analysis: Academic Press. 107

Minato, S., T. Matsuoka, T. Dickens, J. H. D. Draganov, and K. Wapenaar, 2011, Seismic interferometry using multidimensional deconvolution and crosscorrelation for cross-well seismic reflection data without borehole sources: Geophysics, **76**, SA19–SA34. 102

Mittet, R., 1994, Implementation of the kirchhoff integral for elastic waves in staggered-grid modelling schemes: Geophysics, **59**, 1894–1901. 79, 186, 187

Moldoveanu, N., 2000, Vertical source array in marine seismic exploration: 70th Annual International Meeting, SEG, Expanded Abstracts, 53–56. 206

Moldoveanu, N., L. Combee, M. Egan, G. Hampson, L. Sydora, and W. Abriel, 2007,

Over/under towed streamer acquisition: A method to extend seismic bandwidth to both higher and lower frequencies: The Leading Edge, **26**, 41–58. 97

Mordret, A., M. Landes, N. M. Shapiro, S. C. Singh, P. Roux, and O. I. Barkved, 2013, Near-surface study at the valhall oil field from ambient noise surface wave tomography: Geophysical Journal International, **193**, 1627–1643. 29

Muijs, R., J. Robertsson, and K. Holliger, 2004, Data-driven adaptive decomposition of multicomponent seabed recordings: Geophysics, **69**, 1329–1337. 187, 190, 229

Muijs, R., J. O. A. Robertsson, and K. Holliger, 2007, Prestack depth migration of primary and surface-related multiple reflections: Part i - imaging: Geophysics, **72**, S59–S69. 29, 77, 145, 207

Muyzert, E., A. Kashubin, E. Kragh, and P. Edme, 2012, Land seismic data acquisition using rotation sensors: Presented at the 74th EAGE Conference & Exhibition, Extended Abstracts. 226

Nakata, N., R. Snieder, and M. Behm, 2014, Body-wave interferometry using regional earthquakes with multidimensional deconvolution after wavefield decomposition at free surface: Geophysical Journal International, **199**, 1125–1137. 102

Nakstad, H., J. Langhammer, and M. Eriksrud, 2011, Permanent reservoir monitoring technology breakthrough in the north sea: Presented at the 73rd EAGE Conference & Exhibition, Extended Abstracts. 225

Neidell, N., and M. Taner, 1971, Semblance and other coherency measures for multichannel data: Geophysics, **36**, 482–497. 68

Nemeth, T., W. Chengjun, and G. Schuster, 1999, Least-squares migration of incomplete reflection data: Geophysics, **64**, 208–211. 145

Norris, M., M. Johnson, and M. Walsch, 2006, Obc signal fidelity: Geophysical Prospection, **54**, 793–815. 121

Oristaglio, M. L., 1989, An inverse-scattering formula that uses all the data: Inverse Problems, **5**, 1097–1105. 31, 46, 47, 126, 127, 186

Osen, A., L. Amundsen, and A. Reitan, 1999, Removal of water-layer multiples from multicomponent sea-bottom data: Geophysics, **64**, 838–851. 187

Ostrander, W., 1982, Plane-wave reflection coefficients for gas sands at nonnormal angles of incidence,: 52nd Annual International Meeting, SEG, Expanded Abstracts, 216–218. 150

Ozbek, A., M. Vassallo, K. Ozdemir, D.-J. van Manen, and K. Eggenberger, 2010, Crossline wavefield reconstruction from multicomponent streamer data: Part 2-joint interpolation and 3d up/down separation by generalized matching pursuit: Geophysics, **75**, WB69–WB85. 186

Ozdemir, K., P. Caprioli, A. Ozbek, E. Kragh, and J. Robertsson, 2008, Optimized deghosting of over/under towed-streamer data in the presence of noise: The Leading Edge, **27**, 190–199. 205

Perrone, F., P. Sava, and J. Panizzardi, 2015, Wavefield tomography based on local image correlations: Geophysical Prospecting, **63**, 35–54. 177

Pica, A. L., M. Manin, P. Y. Granger, D. Marin, E. Suaudeau, B. David, G. Poulain, and P. H. Herrmann, 2006, 3d srme on obs data using waveform multiple modelling: 76th Annual International Meeting, SEG, Expanded Abstracts, 2659–2663. 206

Pica, A. L., G. Poulain, B. David, M. Magesan, S. Baldock, T. Weisser, P. Hugonnet, and P. H. Herrmann, 2005, 3d surface-related multiple modeling, principles and results: 75th Annual International Meeting, SEG, Expanded Abstracts, 2080–2083. 206

Plessix, R., 2006, A review of the adjoint-state method for computing the gradient of a functional with geophysical applications: Geophysical Journal International, **167**, 495–503. 34

Poliannikov, O., 2011, Retrieving reflections by source-receiver wavefield interferometry: Geophysics, **76**, SA1–SA8. 151, 160, 168, 178

Pratt, R., 1999, Seismic waveform inversion in the frequency domain, part 1: Theory and verification in a physical scale model: Geophysics, **64**, 888–901. 68

Press, W. H., B. P. Flannery, S. A. Teukolsky, and W. T. Vetterling, 2002, Numerical recipes in c: The art of scientific computing: Cambridge University Press. 121

Ramirez, A. C., and A. B. Weglein, 2009, Green's theorem as a comprehensive framework for data reconstruction, regularization, wavefield separation, seismic interferometry,

and wavelet estimation: A tutorial: Geophysics, **74**, W35–W62. 192

Ravasi, M., and A. Curtis, 2013a, Elastic imaging with exact wavefield extrapolation for application to ocean bottom 4c seismic data: Geophysics, **78**, S265–S284. 9, 129, 145, 151, 152, 178, 186

———, 2013b, Nonlinear scattering based imaging in elastic media: Theory, theorems and imaging conditions: Geophysics, **78**, S137–S155. 9, 76, 100, 126, 129, 131, 161, 180, 200

Ravasi, M., A. C. I. Vasconcelos, and A. Kritski, 2015a, A practical approach to vector-acoustic imaging of primaries and free-surface multiples: Presented at the 77th EAGE Conference & Exhibition, Extended Abstracts. 207

Ravasi, M., G. A. Meles, A. Curtis, Z. Rawlinson, and L. Yikuo, 2015b, Seismic interferometry by multi-dimensional deconvolution without wavefield separation: Geophysical Journal International, **202**, 1–16. 9, 122, 207

Ravasi, M., I. Vasconcelos, and A. Curtis, 2014, Beyond conventional migration: nonlinear elastic subsalt imaging with transmissions and two-sided illumination: Geophysical Journal International, **198**, 1187–1199. 9, 151, 161, 186, 200

Ravasi, M., I. Vasconcelos, A. Curtis, and A. Kritski, 2015c, Vector-acoustic reverse time migration of volve obc dataset without up/down decomposed wavefields: Geophysics. 9

Ravasi, M., I. Vasconcelos, A. Curtis, and G. Meles, 2015d, Elastic extended images and velocity sensitive objective functions using multiple reflections and transmissions: Geophysical Journal International. 9, 197

Ravasi, M., I. Vasconcelos, A. Kritski, A. Curtis, C. da Costa Filho, and G. Meles, 2015e, Target-oriented marchenko imaging of a north sea field: Geophysical Research Letters; In Preparation. 9

Rickett, J., and P. Sava, 2001, Offset and angle domain common-image gathers for shot-profile migration: 71st Annual International Meeting, SEG, Expanded Abstracts, 1115–1118. 99

———, 2002, Offset and angle-domain common image-point gathers for shot-profile migration: Geophysics, **67**, 883–889. 197

Robertsson, J., and C. Chapman, 2000, An efficient method for calculating finite-difference seismograms after model alterations: Geophysics, **65**, 907–918. 188, 207

Robertsson, J. O. A., and L. Amundsen, 2014, Wave equation processing using finite-difference propagators, part 2: Deghosting of marine hydrophone seismic data: Geophysics, **79**, T301–T312. 188

Robertsson, J. O. A., J. O. Blanch, and W. W. Symes, 1994, Viscoelastic finite-difference modeling: Geophysics, **59**, 1444–1456. 53

Robertsson, J. O. A., D. Halliday, D.-J. van Manen, I. Vasconcelos, R. Laws, K. Ozdemir, and H. Gronaas, 2012, Full-wavefield, towed-marine seismic acquisition and applications: Presented at the 74th EAGE Conference & Exhibition, Extended Abstracts. 70, 189

Robertsson, J. O. A., I. Moore, M. Vassallo, K. Ozdemir, D.-J. van Manen, and A. Ozbek, 2008, On the use of multicomponent streamer recordings for reconstruction of pressure wavefields in the crossline direction: Geophysics, **73**, A45–A49. 186

Robertsson, J. O. A., and E. Muyzert, 1999, Wavefield separation using a volume distribution of three component recordings: Geophysical Research Letters, **26**, 2821–2824. 80

Robinson, E. A., and S. Treitel, 1980, Geophysical signal analysis: Prentice-Hall, Inc. 216

Ronen, S., L. Comeaux, and J. Miao, 2005, Imaging downgoing waves from ocean bottom stations: 75th Annual International Meeting, SEG, Expanded Abstracts, 963–966. 77

Ronen, S., A. Ratcliffe, P. Nicholls, K. Mills, R. Leggott, K. Hawkins, and L. Scott, 2003, Combined ocean bottom stations and surface-towed seismic streamers: Presented at the 65th EAGE Conference & Exhibition, Extended Abstracts. 76

Ronholt, G., H. Aronsen, T. Hellmann, and S. Johans, 2008, Improved imaging of the snohvit field through integration of 4c obc and dual-azimuth streamer seismic data: First Break, **26**. 187

Rosales, D. A., S. Fomel, B. L. Biondi, and P. Sava, 2008, Wave-equation angle-domain common-image gathers for converted waves: Geophysics, **73**, S17–S26. 72, 129

Rose, J. H., 2002, Single-sided autofocusing

of sound in layered materials: Inverse Problems, **18**, 1923–1934. 33

Ruigrok, E., X. X. Campman, D. Draganov, and K. Wapenaar, 2010, High-resolution lithospheric imaging with seismic interferometry: Geophysical Journal International, **183**, 339–357. 102

Rutherford, S. R., and R. H. Williams, 1989, Amplitude-versus-offset variations in gas sands: Geophysics, **54**, 680–688. 150

Sava, P., and S. Fomel, 2003, Angle-domain common-image gathers by wavefield continuation methods: Geophysics, **68**, 1065–1074. 72, 99, 197

———, 2006, Time-shift imaging condition in seismic migration: Geophysics, **2006**, S209–S207. 99

Sava, P., and I. Vasconcelos, 2011, Extended imaging condition for wave-equation migration: Geophysical Prospecting, **59**, 35–55. 37, 46, 47, 72, 99, 150, 152, 178, 197

Schalkwijk, K. M., C. P. A. Wapenaar, and D. J. Verschuur, 1999, Application of two-step decomposition to multicomponent ocean-bottom data: Theory and case study: Journal of Seismic Exploration, **8**, 261–278. 76, 98, 187, 190, 229

———, 2003, Adaptive decomposition of multicomponent ocean-bottom seismic data into downgoing and upgoing P- and S-waves: Geophysics, **68**, 1091–1102. 117, 229

Schleicher, J., J. C. Costa, and A. Novais, 2008, A comparison of imaging conditions for waveequation shot profile migration: Geophysics, **73**, S219–S227. 190, 207

Schonewille, M., 2000, Fourier reconstruction of irregularly sampled seismic data: PhD thesis, Delft University of Technology. 203

Schuster, G. T., 2009, Seismic interferometry: Cambridge University Press, New York. 102

Schuster, G. T., J. Yu, J. Sheng, and J. Rickett, 2004, Interferometric/daylight seismic imaging: Geophysical Journal International, **157**, 838–852. 102

Shabelansky, A. H., A. Malcolm, M. Fehler, X. Shang, and W. Rodi, 2013, Converted phase elastic migration velocity analysis: 83rd Annual International Meeting, SEG, Expanded Abstracts, 4732–4737. 173, 181

Shahraeeni, M., and A. Curtis, 2011, Fast probabilistic nonlinear petrophysical inversion: Geophysics, **76**, E45–E58. 76, 187

Shahraeeni, M., A. Curtis, and G. Chao, 2012, Fast probabilistic petrophysical mapping of reservoirs from 3d seismic data: Geophysics, **77**, O1–O19. 76

Shapiro, N., M. Campillo, L. Stehly, and M. Ritzwoller, 2005, High-resolution surface-wave tomography from ambient seismic noise: Science, **307**, 1615–1618. 29

Shen, H., S. Mothi, and U. Albertin, 2011, Improving subsalt imaging with illumination-based weighting of RTM 3D angle gathers: Presented at the 81st Annual International Meeting, SEG, Expanded Abstracts. 145

Simmons, J., and M. Backus, 2003, An introduction - multicomponent: The Leading Edge, **22**, 1227–1262. 76

Simonetti, F., 2006, Multiple scattering: The key to unravel the subwavelength world from the far-field pattern of a scattered wave: Physical Review E, **73**. 33, 161

Simonetti, F., M. Fleming, and E. A. Marengo, 2008, Illustration of the role of multiple scattering in subwavelength imaging from far-field measurements: Journal Optical Society of America, **25**, 292. 34

Simonetti, F., L. Huang, N. Duric, and O. Rama, 2007, Imaging beyond the born approximation: An experimental investigation with an ultrasonic ring array: Physical Review E, **76**. 33

Slob, E., D. Draganov, and K. Wapenaar, 2007, Interferometric electromagnetic green's functions representations using propagation invariants: Geophysical Journal International, **169**, 60–80. 46, 243, 249

Slob, E., and K. Wapenaar, 2013, Coupled marchenko equations for electromagnetic green's function retrieval and imaging: Presented at the 83rd Annual International Meeting, SEG, Expanded Abstracts. 146, 210

Slob, E., K. Wapenaar, F. Broggini, and R. Snieder, 2014, Seismic reflector imaging using internal multiples with marchenko-type equations: Geophysics, **79**, S63–S76. 210

Snieder, R., 2002, Scattering and inverse scattering in pure and applied science: Academic Press, Inc. 49, 50, 243

———, 2004, Extracting the green's function from the correlation of coda waves: A derivation: Physical Review E, **69**, 046610. 84, 159

———, 2006a, Retrieving the green's function of the diffusion equation from the response

to a random forcing: Physical Review E, **74**. 102

———, 2006b, The theory of coda wave interferometry: Pure and Applied Geophysics, **163**, 455–473. 68

Snieder, R., K. van Wijk, M. Haney, and R. Calvert, 2008, The cancellation of spurious arrivals in green's function extraction and the generalized optical theorems: Physical Review E, **78**. 47, 71

Snieder, R., K. Wapenaar, and K. Lerner, 2006, Spurious multiples in seismic interferometry of primaries: Geophysics, **71**, SI111–SI12. 35, 155, 230

Socco, L. V., S. Foti, and D. Boiero, 2010, Surface-wave analysis for building near surface velocity models - established approaches and new perspectives: Geophysics, **75**, A83–A102. 29

Sommerfeld, A., 1954, Optics: Academic Press. 104

Sonneland, L., and L. Berg, 1987, Comparison of two approaches to water layer multiple attenuation by wave field extrapolation: 57th Annual International Meeting, SEG, Expanded Abstracts, 276–277. 77

Soubaras, R., 1996, Ocean-bottom hydrophone and geophone processing: 66th Annual International Meeting, SEG, Expanded Abstracts, 24–27. 76, 98, 187, 204

Soubaras, R., and R. Dowle, 2010, Variable depth streamer-a broadband marine solution: First Break, **28**, 89–96. 206

Stehly, L., M. Campillo, and N. Shapiro, 2006, A study of the seismic noise from its long-range correlation properties: Journal of Geophysical Research, **111**. 163

Stewart, R. R., J. E. Gaiser, R. J. Brown, and D. C. Lawton, 2003, Converted-wave seismic exploration: Application: Geophysics, **68**, 40–57. 76

Stolt, R., and A. Weglein, 1985, Migration and inversion of seismic data: Geophysics, **50**, 2458–2472. 31

Stork, C., 1992, Reflection tomography in the postmigrated domain: Geophysics, **57**, 680–692. 68

Stoughton, D., J. Stefani, and S. Michell, 2001, 2-d elastic model for wavefield investigations of subsalt objectives, deep water gulf of mexico: Presented at the 71st Annual International Meeting, SEG, Expanded Abstracts. 133, 156

Strobbia, C., A. Laake, P. Vermeer, and A. Glushchenko, 2011, Surface waves: use them then lose them. surface-wave analysis, inversion and attenuation in land reflection seismic surveying: Near Surface Geophysics, **9**, 503–514. 29

Sun, R., and G. A. McMechan, 1986, Pre-stack reverse-time migration for elastic waves with application to synthetic offset vertical seismic profiles: Proceedings of the IEEE, **74**, 457–465. 32, 77, 98

Symes, W., 2008, Migration velocity analysis and waveform inversion: Geophysical Prospecting, **56**, 765–790. 37, 150

Szydlik, T., P. Smith, S. Way, L. Aamodt, and C. Friedrich, 2007, 3d pp/ps prestack depth migration on the volve field: First Break, **25**, 43–47. 187, 190, 213

Taner, M., and F. Koehler, 1969, Velocity spectra, digital computer derivation applications of velocity functions: Geophysics, **34**, 859–881. 68, 150

Tao, Y., and M. K. Sen, 2013, On a plane-wave based cross-correlation type seismic interferometry: Geophysics, **78**, Q35–Q44. 181

Tarantola, A., 1984, Inversion of seismic reflection data in the acoustic approximation: Geophysics, **49**, 1259–1266. 34, 145, 235

ten Kroode, F., 2002, Prediction of internal multiples: Wave Motion, **35**, 315–338. 144

Thomsen, L., O. Barkved, B. Haggard, J. Kommedal, and B. Rosland, 1997, Converted-wave imaging of valhall reservoir: Presented at the 59th EAGE Conference & Exhibition, Extended Abstracts. 76

Thomson, C., 2011, On the space-time domain form of the reflection operator for a simple flat-lying interface: Geophysical Prospecting, **60**, 49–63. 150

———, 2012, The form of the reflection operator and extended image gathers for a dipping plane reflector in two space dimensions: Geophysical Prospecting, **60**, 64–92. 37, 150, 178, 197

Thorbecke, J., and K. Wapenaar, 2007, On the relation between seismic interferometry and the migration resolution function: Geophysics, **72**, T61–T66. 47, 193

Tromp, J., C. Tape, and Q. Liu, 2005, Seismic tomography, adjoint methods, time reversal and banana-doughnut kernels: Geophysical Journal International, **160**, 195–216. 34, 235

van Dalen, K., K. Wapenaar, and D. Halliday,

2014, Surface wave retrieval in layered media using seismic interferometry by multidimensional deconvolution: Geophysical Journal International, **196**, 230–242. 102

van der Neut, J., A. Bakulin, and D. Alexandrov, 2013a, Acoustic wavefield separation using horizontal receiver arrays deployed at multiple depth on land: Presented at the 83rd Annual International Meeting, SEG, Expanded Abstracts. 226

van der Neut, J., and F. Herrmann, 2013, Interferometric redatuming by sparse inversion: Geophysical Journal International, **192**, 666–670. 103, 121, 211

van der Neut, J., E. Slob, K. Wapenaar, J. Thorbecke, R. Snieder, and F. Broggini, 2013b, Interferometric redatuming of autofocused primaries and internal multiples: Presented at the 83rd Annual International Meeting, SEG, Expanded Abstracts. 36

van der Neut, J., M. Tatanova, J. Thorbecke, E. Slob, and K. Wapenaar, 2011a, Deghosting, demultiple and deblurring in controlled-source seismic interferometry: International Journal of Geophysics, 870819. 103, 115

van der Neut, J., J. Thorbecke, K. Mehta, E. Slob, and K. Wapenaar, 2011b, Controlled-source interferometric redatuming by crosscorrelation and multidimensional deconvolution in elastic media: Geophysics, **76**, SA63–SA76. 102, 107, 231

van der Neut, J., J. Thorbecke, K. Wapenaar, and E. Slob, 2015, Inversion of the multidimensional marchenko equation: Presented at the 77th EAGE Conference & Exhibition, Extended Abstracts. 212

van der Neut, J., I. Vasconcelos, and K. Wapenaar, 2014a, An interferometric interpretation of marchenko redatuming: Presented at the 76th EAGE Conference & Exhibition, Extended Abstracts. 146, 210

van der Neut, J., C. A. Vidal, N. Grobbe, and K. Wapenaar, 2013c, Turning one-sided ilumination into two-sided illumination by target-enclosing interferometric redatuming: Presented at the 75th EAGE Conference & Exhibition, Extended Abstracts. 128, 181

van der Neut, J., K. Wapenaar, J. Thorbecke, and I. Vasconcelos, 2014b, Internal multiple suppression by adaptive marchenko redatuming: 84th Annual International Meeting, SEG, Expanded Abstracts, 4055–4059. 211, 216

van Leeuwen, T., and W. A. Mulder, 2010, A correlation-based misfit criterion for wave-equation traveltime tomography: Geophysical Journal International„ **182**, 1383–1394. 177

van Manen, D.-J., A. Curtis, and J. O. A. Robertsson, 2006, Interferometric modeling of wave propagation in inhomogeneous elastic media using time reversal and reciprocity: Geophysics, **71**, SI47–SI60. 46, 48, 51, 102, 130, 152, 186, 203, 205

van Manen, D.-J., J. O. A. Robertsson, and A. Curtis, 2005, Modeling of wave propagation in inhomogeneous media: Physical Review Letters, **94**, 164301. 46, 102, 159, 186, 203, 205

———, 2007, Exact wavefield simulation for finite-volume scattering problems: Journal of the Acoustical Society of America, **122**, EL115–EL121. 133, 207

van Vossen, R., J. O. A. Robertsson, and C. H. Chapman, 2002, Finite-difference modeling of wave propagation in a fluid-solid configuration: Geophysics, **67**, 618–624. 99

Vasconcelos, I., 2008, Generalized representations of perturbed fields - applications in seismic interferometry and migration: 78th Annual International Meeting, SEG, Expanded Abstracts, 2927–2941. 35, 52, 126, 129

———, 2011, Source-receiver reverse-time imaging of vector-acoustic seismic data: Presented at the 81st Annual International Meeting, SEG, Expanded Abstracts. 32, 46, 186

———, 2013, Source-receiver reverse-time imaging of dual-source, vector-acoustic seismic data: Geophysics, **78**, WA147–WA158. 32, 34, 35, 82, 84, 122, 126, 133, 145, 151, 152, 161, 178, 186, 189, 200, 205, 206, 248

Vasconcelos, I., M. Ravasi, and A. Curtis., 2015a, Constraints on missing boundary data in wavefield interferometry and imaging: Journal of the Acoustical Society of America; Submitted. 231

Vasconcelos, I., M. Ravasi, and J. van der Neut, 2014a, An interferometry-based, subsurface-domain objective function for waveform inversion: Presented at the 76th EAGE Conference & Exhibition, Extended Abstracts. 105, 207, 231

Vasconcelos, I., and J. Rickett, 2013, Broadband extended images by joint inversion of multiple blended wavefields: Geophysics, **78**,

WA123–WA145. 36, 37, 99, 102, 150, 197

Vasconcelos, I., J. Robertsson, M. Vassallo, and D.-J. van Manen, 2012, Reverse-time imaging of dual-source 4c marine seismic data using primaries, ghosts, and multiples: Presented at the 74th EAGE Conference & Exhibition, Extended Abstracts. 46, 186

Vasconcelos, I., P. Sava, and H. Douma, 2009a, Wave-equation extended images via image-domain interferometry: 79th Annual International Meeting, SEG, Expanded Abstracts, 2839–2843. 37, 47, 60, 61, 150, 152, 178

———, 2010, Nonlinear extended images via image-domain interferometry: Geophysics, **75**, SA105–SA115. 34, 36, 37, 46, 126, 127, 150, 152, 178, 192, 197

Vasconcelos, I., and R. Snieder, 2008a, Interferometry by deconvolution: Part 1 - theory for acoustic waves and numerical examples: Geophysics, **73**, S115–S128. 46

———, 2008b, Interferometry by deconvolution: Part 2 - theory for elastic waves and application to drill-bit seismic imaging: Geophysics. 47

Vasconcelos, I., R. Snieder, and H. Douma, 2009b, Representation theorems and green's function retrieval for scattering in acoustic media: Physical Review E, **80**, 036605. 35, 36, 46, 126, 231, 233

Vasconcelos, I., R. Snieder, and B. Hornby, 2008, Imaging internal multiples from subsalt vsp data examples of target-oriented interferometry: Geophysics, **73**, S157–S168. 145, 151, 155

Vasconcelos, I., D.-J. van Manen, M. Ravasi, K. Wapenaar, and J. van der Neut, 2014b, Marchenko redatuming: advantages and limitations in complex media: Presented at the 84th annual SEG meeting, Workshop W-11: Using Multiples as Signal for Imaging. 146, 210

Vasconcelos, I., K. Wapenaar, J. van der Neut, C. Thomson, and M. Ravasi, 2015b, Using inverse transmission matrices for marchenko redatuming in highly complex media: Presented at the 85th Annual International Meeting, SEG, Expanded Abstracts; Submitted. 212

Vasmel, M., J. Robertsson, D.-J. van Manen, and A. Curtis, 2013, Immersive experimentation in a wave propagation laboratory: Journal of the Acoustical Society of America, **134**, EL492–EL49. 133

Vasmel, M., J. O. A. Robertsson, and L. Amundsen, 2014, A new solution to eliminate free surface related multiples in multicomponent streamer recordings: Presented at the 76th EAGE Conference & Exhibition, Extended Abstracts. 207

Vassallo, M., A. Ozbek, K. Ozdemir, and K. Eggenberger, 2010, Crossline wavefield reconstruction from multicomponent streamer data: Part 1 - multichannel interpolation by matching pursuit (mimap) using pressure and its crossline gradient: Geophysics, **75**, WB53–WB67. 122, 186, 203

Verschuur, D., A. Berkhout, and C. Wapenaar, 1992, Adaptive surface-related multiple elimination: Geophysics, **75**, 1166–1177. 144, 150, 206

Virieux, J., 1986, P-SV wave propagation in heterogeneous media: velocity-stress finite-difference method: Geophysics, **51**, 889–901. 65, 83

Wang, Y., S. Grion, and R. Bale, 2009, What comes up must have gone down: The principle and application of up-down deconvolution for multiple attenuation of ocean bottom data: Presented at the CSEG Recorder. 77, 207

Wapenaar, C., and J. Grimbergen, 1996, Reciprocity theorems for one-way wave fields: Geophysical Journal International, **127**, 169–177. 36

Wapenaar, C., G. Haimé, and A. Berkhout, 1991„ Elastic wave field decomposition: before or after downward extrapolation?: 61st Annual International Meeting, SEG, Expanded Abstracts, 1001–1004. 78

Wapenaar, C. P. A., and G. C. Haimé, 1990, Elastic extrapolation of primary seismic P- and S-waves: Geophysical Prospecting, **38**, 23–60. 48, 55

Wapenaar, K., 2004, Retrieving the elastodynamic green's function of an arbitrary inhomogeneous medium by cross correlation: Physical Review Letters, **93**. 34, 46, 102, 186, 203, 205

———, 2006, Green's function retrieval by cross-correlation in case of one-sided illumination: Geophysics, **71**, SI33–SI46. 230, 249

———, 2014, Single-sided marchenko focusing of compressional and shear waves: Physical Review E, **90**, 063202. 146, 151, 180, 210

Wapenaar, K., and A. Berkhout, 1989, Elastic wave field extrapolation: Redatuming of single- and multi-component seismic data: Elsevier Science. 105, 247, 251

Wapenaar, K., F. Broggini, E. Slob, and R. Snieder, 2013, Three-dimensional single-sided marchenko inverse scattering, data-driven focusing, green's function retrieval, and their mutual relations: Physical Review E, **110**, 084301. 33, 127, 146, 151, 180, 210

Wapenaar, K., F. Broggini, and R. Snieder, 2012, Creating a virtual source inside a medium from reflection data: heuristic derivation and stationary-phase analysis: Geophysical Journal International, **190**, 1020–1024. 127, 151, 180

Wapenaar, K., D. Draganov, R. Snieder, X. Campman, and A. Verdel, 2010a, Tutorial on seismic interferometry: Part 1 - basic principles and applications: Geophysics, **75**, 75A195–75A209. 46, 102

Wapenaar, K., and J. Fokkema, 2006, Green's function representations for seismic interferometry: Geophysical Research Letters, **33**, L19304. 35, 46, 48, 50, 51, 55, 59, 79, 102, 105, 114, 130, 152, 154, 186, 192, 193, 203, 205, 253

Wapenaar, K., and E. Slob, 2014, On the marchenko equation for multicomponent single-sided reflection data: Geophysical Journal International, **199**, 1367–1371. 146, 151, 180, 210

Wapenaar, K., E. Slob, and R. Snieder, 2008a, Seismic and electromagnetic controlled-source interferometry in dissipative media: Geophysical Prospecting, **56**, 419–434. 34, 36, 231, 248

———, 2010b, On seismic interferometry, the generalized optical theorem, and the scattering matrix of a point scatterer: Geophysics, **75**, SA27–SA35. 132, 145, 245

Wapenaar, K., E. Slob, R. Snieder, and A. Curtis, 2010c, Tutorial on seismic interferometry: Part 2 - underlying theory and new advances: Geophysics, **75**, 75A211–75A227. 46, 102

Wapenaar, K., J. Thorbecke, J. V. der Neut, F. Broggini, E. Slob, and R. Snieder, 2014a, Marchenko imaging: Geophysics, **79**, WA39–WA57. 33, 211, 212, 217, 218

Wapenaar, K., J. Thorbecke, and D. Draganov, 2004, Relations between reflection and transmission responses of three-dimensional inhomogeneous media: Geophysical Journal International, **156**. 36

Wapenaar, K., J. Thorbecke, J. van der Neut, I. Vasconcelos, and E. Slob, 2014b, Marchenko imaging below an overburden with random scatterers: Presented at the 76th EAGE Conference & Exhibition, Extended Abstracts. 210

Wapenaar, K., and J. van der Neut, 2010, A representation for green's function retrieval by multidimensional deconvolution: Journal of the Acoustical Society of America, **128, no. 6, EL366-EL371.**, EL366–EL371. 36, 102, 111

Wapenaar, K., J. van der Neut, and E. Ruigrok, 2008b, Passive seismic interferometry by multidimensional deconvolution: Geophysics, **73**, A51–A56. 102

Wapenaar, K., J. van der Neut, E. Ruigrok, D. Draganov, J. Hunziker, E. Slob, J. Thorbecke, and R. Snieder, 2011, Seismic interferometry by crosscorrelation and by multidimensional deconvolution: A systematic comparison: Geophysical Journal International, **185**, 1335–1364. 36, 102, 104, 106, 107, 109, 115, 211, 213, 231

Weaver, R. L., and O. I. Lobkis, 2001, Ultrasonics without a source: Thermal fluctuation correlations at mhz frequencies: Physical Review Letters, **87**, 134301. 102

Weglein, A., 2014, Multiples: signal or noise?: 84th Annual International Meeting, SEG, Expanded Abstracts, 4393–4399. 46

Weglein, A., F. Gasparotto, P. Carvalho, and R. Stolt, 1997, An inverse-scattering series method for attenuating multiples in seismic reflection data: Geophysics, **62**, 1975–1989. 144, 206

Weglein, A. B., J. D. Mayhan, L. Amundsen, H. Liang, J. Wu, L. Tang, Y. Luo, and Q. Fu, 2013, Green's theorem de-ghosting algorithms in k,w (e.g., P-Vz de-ghosting) as a special case of x,w algorithms (based on Green's theorem) with: (1) significant practical advantages and disadvantages of algorithms in each domain, and (2) a new message, implication and opportunity for marine towed streamer, ocean bottom and onshore acquisition and applications: Journal of Seismic Exploration, **22**, 389–412. 248

Whitmore, N. D., A. A. Valenciano, W. Sollner, and S. Lu, 2010, Imaging of primaries and multiples using a dual-sensor towed

streamer: Presented at the 80th Annual International Meeting, SEG, Expanded Abstracts. 29, 207

Wong, M., B. Biondi, and S. Ronen, 2010, Joint least-squares inversion of up- and down-going signal for ocean bottom data sets: Presented at the 80th Annual International Meeting, SEG, Expanded Abstracts. 29, 77

———, 2011, Least-squares reverse time migration/inversion for ocean bottom data: A case study: 81st Annual International Meeting, SEG, Expanded Abstracts, 2369–2373. 77

Wu, R. S., and A. Ben-Menahem, 1985, The elastodynamic near field: Geophysical Journal of the Royal Astronomical Society, **81**, 609–621. 56

Xia, G., R. Clarke, J. Etgen, N. Kabir, K. Matson, and S. Michell, 2006, Obs multiple attenuation with application to the deepwater gom atlantis obs nodes data: Presented at the 76th Annual International Meeting, SEG, Expanded Abstracts. 193

Yan, J., 2010, Wave-mode separation for elastic imaging in transversely isotropic media: PhD thesis, Colorado School of Mines. 152

Yan, J., and P. Sava, 2007, Elastic wavefield imaging with scalar and vector potentials: 77th Annual International Meeting, SEG, Expanded Abstracts, 2150–2154. 78, 84

———, 2008, Isotropic angle-domain elastic reverse-time migration: Geophysics, **73**, S229–S239. 32, 48, 61, 64, 65, 67, 69, 71, 77, 98, 132

———, 2010, Analysis of converted-wave extended images for migration velocity analysis: Presented at the 80th Annual International Meeting, SEG, Expanded Abstracts. 99, 173, 181

Yang, T., and P. Sava, 2010, Moveout analysis of wave-equation extended images: Geophysics, **75**, 151–161. 150

———, 2011a, Wave-equation migration velocity analysis with time-shift imaging: Geophysical Prospecting, **59**, 635–650. 150, 173, 177, 178

———, 2011b, Waveform inversion in the image domain: Presented at the 73rd EAGE Conference & Exhibition, Extended Abstracts. 37, 150, 173, 178, 197

———, P., 2012., Image-domain wavefield tomography for complex geologic structures: Presented at the EAGE/ACGGP First Latin American Geophysics Workshop. 150, 173, 181

Yilmaz, O., 1989, Seismic data processing: SEG. 46, 76, 150

Zhang, D., and G. Schuster, 2014, Least-square reverse time migration of multiples: Geophysics, **79**, S11–S21. 145

Zhenhua, L., and M. van der Baan, 2014, Acoustic representation theorem based time-reversal extrapolation for microseismic event localization: Presented at the 84th Annual International Meeting, SEG, Expanded Abstracts. 186

Zhu, X., S. Altan, and J. Li, 1999, Recent advances in multicomponent processing: The Leading Edge, **18**, 1283–1288. 76

Ziolkowski, A., D. B. Taylor, and R. G. K. Johnston, 1999, Marine seismic wavefield measurement to remove sea surface multiples: Geophysical Prospecting, **47**. 115, 213